4557

VALIDATION OF THE COUPLED NCEP MESOSCALE SPECTRAL MODEL AND AN ADVANCED LAND SURFACE MODEL OVER THE HAWAIIAN ISLANDS

A DISSERTATION SUBMITTED TO THE GRADUATE DIVISION OF THE UNIVERSITY OF HAWAI'I IN PARTIAL FULFILLMENT OF THE REQUIREMENTS FOR THE DEGREE OF

DOCTOR OF PHILOSOPHY

IN

METEOROLOGY

DECEMBER 2004

By

Yongxin Zhang

Dissertation Committee:

Yi-Leng Chen, Chairperson
Thomas A. Schroeder
Yuqing Wang
Hann-Minn Henry Juang
Mark A. Merrifield

ACKNOWLEDGMENTS

I would like to thank my advisor, Prof. Yi-Leng Chen, for his encouragement and guidance during the course of my Ph.D. program. He made my time at the University of Hawaii an outstanding learning experience. I am also grateful to the other members of my Ph.D. committee, Prof. Thomas A. Schroeder, Prof. Yuqing Wang, Prof. Mark A. Merrifield, Prof. Shang-Ping Xie, and Dr. Hann-Ming Henry Juang, for all their encouragement, discussions and feedback.

I was fortunate to work closely with Dr. Song-You Hong at the Yonsei University, Korea, and Kevin Kodama at the Weather Forecast Office, Honolulu, who gave me much of their time.

Many thanks also go to my friends at the Department of Meteorology, University of Hawaii, particularly Xian'an Jiang, Andrew Levine, Linlin Pan, Zhou Wang, Bo Yang, Qinghua Ding, Bing Fu, Xuyang Ge, Mary Ann Esteban, Anthony Reynes, Luis Bejarano-Avendano, Chuh-Hsin Chang, Hideki Okajima, Bunmei Taguchi, Sean Daida, Rebecca Schneider, Yang Yang, Haiyan Teng, Brandon Kerns, Christopher Chambers, Eric Lau, Justin Ventham, Ian Morrison, Claus Dolling, Sam Houston, and Ryan Lyman. My friends at the East-West Center, particularly Soonjung Kwon, Isao Nakasone, Satomi Yamashiro, Amporn Jirattikorn, Jon Ross, and Napat Settachai are also thanked.

I owe an enormous amount of gratitude to my wife, Lhamtso, and my son, Dorjee, for their love, encouragement and support throughout my Ph. D. program.

ABSTRACT

The National Centers for Environmental Prediction (NCEP) Mesoscale Spectral Model (MSM) coupled with an advanced Land Surface Model (LSM) is used in assessing the impact of the improved representation of island terrain and surface boundary conditions on simulating orographic effects and local circulations under various large-scale settings.

The surface variables predicted by the operational 10-km Regional Spectral Model (RSM) during a one-month period of 20 May through 20 June 2002 agree well with observations over the buoy stations in the Hawaiian waters. Over land with adequate representation of the terrain, the 1.5-km MSM provides better forecasts of surface variables than the 10-km RSM. Further improvements are achieved by coupling the MSM with the LSM. In particular, over-estimation of the surface wind speed and daytime cold biases in the MSM are largely corrected in the coupled MSM/LSM. The observed composite diurnal cycles of surface variables are also better forecasted by the MSM/LSM than the MSM.

Evaluations of the 3-km MSM/LSM simulations are performed for sea breeze cases during 23 June to 28 June 1978 over northwest Hawaii. Except for 27 June, the model predicted onset time, duration and vertical extent of the sea breezes agree with observations. Sensitivity tests using the MSM/LSM demonstrate the non-trivial effects of surface properties and initialization processes on sea breeze behavior.

Heavy rainfall and high wind events over the Hawaiian Islands display a large variability in rainfall and wind distribution related to complex terrain and local winds. The 10-km RSM/LSM reasonably resolves regional-scale weather features associated

with significant synoptic systems but fails to accurately reproduce rainfall distribution and rate, and orographically amplified strong winds. The MSM/LSM, with its higher resolution ($\leq$ 3 km), has better capability in simulating localized rainfall distributions and airflows associated with these heavy rainfall and high wind events.

Major model bias is that the MSM/LSM produces excessive rainfall on the windward side of steep mountains with little rainfall downstream of the mountain ranges.

TABLE OF CONTENTS

LIST OF TABLES

LIST OF FIGURES

CHAPTER 1

Introduction

The effects of mountain barriers on a steady flow have received considerable attention in the past (Smith 1979; Blumen 1990; Schar and Smith 1993 and others). Besides mechanically forcing the approaching airflow to deflect and ascend on the windward slopes, the mountains also interact with the large-scale airflow and generate circulations ranging from planetary waves to minor perturbations over very small obstacles. The wave perturbations can be divided into those occurring over the mountains (mountain waves) and those occurring to the lee of the mountains (lee waves) (Corby 1954; Scorer 1978). A wake of weak winds and the associated vortices downstream of isolated mountains have long been recognized (Bowley et al. 1962; Hubert and Krueger 1962; Chopra and Hubert 1965; Lyons and Fujita 1968 and others). In addition, the mountains also act as a heat source (sink) during the day (night) and induce thermally driven diurnal circulations (Banta 1990). Under the presence of significant synoptic forcing, localized strong winds (Lilly and Zipser 1972; Ramage et al. 1977; Schroeder 1977a; Baines 1980; Overland and Walter 1981; Li and Chen 1998) and heavy rainfall (Schroeder 1977b; Akaeda et al. 1995; Li et al. 1997; Yeh and Chen 1998, 2002) are frequently recorded in regions with complex terrain.

The Hawaiian Islands, located in the central North Pacific with different sizes (< 140 km in diameter), shapes and mountain heights (500 m – 4 km), are ideal for the study of island-induced flow response under undisturbed and disturbed synoptic conditions.

During the summer months (May-September), trade winds are persistent with an occurrence frequency of more than 85% (Schroeder 1993). During the cool season (October-April), extratropical and subtropical weather systems are able to penetrate southward and disrupt the summer trade-wind weather of the island chain (Schroeder 1993; Kodama and Businger 1998). Heavy rains and high winds are usually spawned from these synoptic disturbances related to the island terrain and local winds. Despite their relatively small sizes, the Hawaiian Islands have profound influences on the weather and circulations over the adjacent waters (Smith and Grubišić 1993; Feng and Chen 2001). Xie et al. (2001) document far-field effects of the Hawaiian Islands on wind curl and cloud liquid water that persist for several thousand kilometers downstream.

Heavy rainfall and high winds associated with synoptic- and meso-scale disturbances affecting the Hawaiian Islands pose a significant hazard to the society, including severe property damage and human casualties. On average, seven to eight flash floods and numerous high wind events (> 20 m s^{-1}) occur each year (Schroeder 1977a, b). Significant weather over the Hawaiian Islands is associated with synoptic/mesocale disturbances; however, heavy rainfall and high winds are frequently localized in nature due to the presence of steep mountains and complex terrain. Orographic effects and local winds create a large spatial variability in rainfall distribution during heavy rain events (Haraguchi 1977; Schroeder 1977b; Dracup et al. 1991; Kodama and Barnes 1997). With small watersheds and narrow stream basins, the time between peak rain and peak discharge may be as short as 15 minutes (Schroeder 1977b). Response time is limited since fifty percent of the state is within five miles of the shore. It is extremely important to have the timely detection of heavy rains.

Forecasting the occurrence and location of heavy rains and high winds in Hawaii is particularly challenging due to sparse upper-air and surface observations in mid-Pacific (Kodama and Businger 1998). Compounding this problem is the lack of routine mesoscale observational network in the state of Hawaii. Clouds that produce heavy rains may be deep cumulonimbus clouds (Schroeder 1977b) or shallow warm rain clouds (Cram and Tatum 1979), therefore, satellite infrared and visible images alone cannot identify the cloudy areas with heavy precipitation. Strong local winds associated with orographic effects are also frequently undetected by routine National Weather Service (NWS) observations. The recent deployment of four WSR-88D (Weather Surveillance Radar 88 Doppler) radars across the Hawaiian Islands has largely improved the capability to monitor heavy rainfall and high wind events around the state. However, high mountains limit their effectiveness in some areas. It is thus desirable to use a high resolution meoscale model in conjunction with the analyses of available data to investigate orographic effects and local circulations during the heavy rainfall and high wind events and to explore the benefit of high-resolution guidance in forecasting local weather.

The primary operational models for the WFO-HFO (Weather Forecast Office – Honolulu) are the Aviation (AVN) and the Medium Range Forecast (MRF) runs of the Global Spectral Model (GSM), which were combined to become the Global Forecast System (GFS) in early 2003. These model runs are generally able to provide forecast guidance on the synoptic-scale systems that affect the Hawaiian Islands; however, they are unable to resolve the mesoscale weather features related to the complex local terrain because of their coarse horizontal resolution. In a collaborative effort among the

University of Hawaii, NCEP (National Centers for Environmental Prediction) and WFO-HFO, the hydrostatic version of the Regional Spectral Model (RSM) (Juang and Kanamitsu 1994; Juang et al. 1997) with a 10-km resolution was implemented operationally in early 1997 for the state of Hawaii by NCEP. From preliminary analyses (Wang et al. 1998) and feedback from forecasters at the WFO-HFO, it is apparent that the RSM forecasts show improvements over the AVN and MRF runs in simulating heavy rainfall and high wind events. Nevertheless, statistical evaluations of the RSM forecasts at four surface sites (Hilo on the island of Hawaii; Lihue on the island of Kauai; Kahului on the island of Maui; and Honolulu on the island of Oahu) during the 1997 warm season (May – September) show that the RSM outperforms the AVN at Hilo and Lihue but not at Kahului and Honolulu (Kodama and Juang 1999). The disappointing results at Kahului and Honolulu are likely caused by the poor representation of the local topography for these two sites by the 10-km grid of the RSM.

Recently, the nonhydrostatic version of the Regional Spectral Model (referred to as the Mesoscale Spectral Model; MSM) was developed at NCEP (Juang 2000). Preliminary applications of the MSM at high resolutions ($\leq$ 3 km) over the Hawaiian Islands show encouraging results in simulating localized heavy rainfall and high winds (Chen et al. 1999). Nevertheless, under the summer trade wind conditions, the lower boundary conditions appear inadequate with weaker than normal diurnal cycles of temperature and wind in the nested MSM forecasts in Hawaii (Zhang et al. 2000).

In addition to the existence of complex terrain, large variations in local microclimate, ranging from humid tropical on the windward lower slopes to hot desert over bare lava soil, with different vegetation covers are typical for the Hawaiian Islands (Juvik et al.

1978; Giambelluca et al. 1986). It is well known that land surface processes in association with heterogeneous vegetation and soil properties play a critical role in influencing the diurnal and vertical structure of the planetary boundary layer (PBL) and the associated clouds and precipitation processes (Avissar and Pielke 1989; Chen and Avissar 1994a, b; Chen and Dudhia 2001a, b). However, in the current implementation of the RSM and MSM, only one vegetation type (broadleaf tree) is considered, with a constant vegetation fraction of 70%. It also has only one soil type, sandy clay loam. Thus, it is desirable to couple the RSM and MSM with an advanced Land Surface Model (LSM) with improved lower boundary conditions to better resolve surface processes. In a collaborative effort among the University of Hawaii, the Yonsei University in Korea, WFO-HFO and NCEP, the modified Oregon State University LSM originally developed by Pan and Mahrt (1987) (Chen et al. 1996; Chen and Dudhia 2001a) was implemented in early 2002 into the RSM and MSM with improved lower boundary conditions.

The goal of this study was to examine and understand the island effects on the atmosphere including local circulations, heavy rainfall and strong winds, using the coupled MSM/LSM at high resolutions ($\leq$ 3 km) over the Hawaiian Islands, in conjunction with observational analyses. Model performance under undisturbed and disturbed synoptic conditions is evaluated using observations. The dissertation is organized in seven chapters, as outlined below.

Chapter 2 contains a brief description of the coupled MSM/LSM and its adaptation over the Hawaiian Islands.

Chapter 3 documents the evaluation of the coupled MSM/LSM forecasts under summer trade wind conditions from 20 May through 20 June, 2002 (32 days).

Observations collected at three NWS surface sites on the island of Oahu are used to validate the model simulations. This chapter was aimed at assessing the impact of improved representation of the terrain and surface boundary conditions on simulating the orographic effects and local circulations under weak synoptic conditions. Since the RSM provides the initial conditions and boundary conditions for the MSM, the RSM simulations in the regional domain are evaluated using observations at two buoy stations over the adjacent waters of the Hawaiian Islands.

Chapter 4 presents numerical simulations of the sea breeze circulations over northwest Hawaii during 23-28 June 1978 (Schroeder 1981) using the coupled MSM/LSM. This chapter was aimed at investigating the performance of the coupled MSM/LSM in simulating the observed sea breeze development with improved surface boundary conditions. Model sensitivity tests of the effect of surface properties on sea breeze behavior are also performed.

In Chapter 5, four heavy rainfall cases over the Hawaiian Islands are simulated using the coupled MSM/LSM. These heavy rainfall events occur during the passage of significant synoptic-scale weather disturbances over the Hawaiian Islands: troughs or closed lows in the upper troposphere (Sadler 1967), cold fronts, and kona storms (Simpson 1952; Ramage 1962). The 10-km RSM/LSM forecasts are presented alongside the MSM/LSM simulations for comparison.

In Chapter 6, a high wind event (14-15 February 2001) over the Hawaiian Islands associated with a cold front is investigated using the coupled MSM/LSM. A strong high-pressure cell moved to the northeast of the Hawaiian Islands following the passage of the cold front. The cell then merged with the semi-permanent subtropical high and resulted in

windy conditions across the state of Hawaii. The model performance in simulating the localized high winds over the island chain is evaluated. The possible mechanisms for the development of downslope windstorms at various locations over the Hawaiian Islands are also examined.

Chapter 7 summarizes the major conclusions of this study. Future work is also outlined.

CHAPTER 2

Model description and experimental design

2.1 RSM model and domain

A comprehensive description of the NCEP RSM is presented in Juang and Kanamitsu (1994). The primitive equations in sigma coordinates employed in the GSM are used in the RSM. While the GSM uses spherical harmonics functions, the RSM uses sine and cosine series as horizontal basis functions. The dependent variables in the regional domain are divided into a time-dependent base field and a perturbation part in terms of their spectral representation. The RSM then predicts deviations from the forecasts of the global model component. A time filtering (Asselin 1972) is applied to the perturbations in order to eliminate the computational mode resulting from a leapfrog time scheme during the model integration. A semi-implicit adjustment is applied to the perturbations in the regional domain to permit numerical stability with a large time step. An implicit horizontal diffusion was originally applied to the perturbations on sigma surfaces; however, such a numerical treatment was found to cause cold mountain-top air to spread downward and outward with model integration time in areas of steep terrain (Juang et al. 2004). This problem was largely corrected by implementing the horizontal diffusion for temperature and humidity on pressure surfaces instead (Juang et al. 2004). Horizontal diffusion for wind is still performed on sigma surfaces. To reduce noise from the lateral boundaries, a lateral boundary relaxation is performed on the total tendency computed by the RSM.

The model physics used are the same as the GSM including short- and long-wave radiation with diurnal variation, radiation-cloud interaction, gravity-wave drag, simplified Arakawa-Schubert convective parameterization scheme, shallow convection, and large-scale precipitation (Juang and Kanamitsu 1994). The boundary layer physics employs the MRF (Medium-Range Forecast) diffusion scheme with nonlocal diffusion for the mixed layer, and local diffusion for the free atmosphere (Hong and Pan 1996). There are 28 sigma layers in the RSM: 0.995, 0.982, 0.964, 0.942, 0.915, 0.883, 0.845, 0.801, 0.750, 0.693, 0.632, 0.568, 0.501, 0.435, 0.372, 0.312, 0.258, 0.210, 0.168, 0.132, 0.102, 0.078, 0.058, 0.041, 0.028, 0.017, 0.009 and 0.002. Seven of these 28 sigma layers are below 1.5 km. The lowest level corresponds to about 30-50 m above the surface.

The entire RSM system designed for Hawaii consists of two components: the GSM and the RSM (Wang et al. 1998). The GSM component is a version of the operational NCEP Global Spectral Model. A 97×76-point grid domain is used for the RSM at a 10-km resolution (Fig. 2.1a). High-resolution (~ 1 km) Navy-NCAR terrain data for the Hawaiian Islands are used in the RSM.

2.2 MSM model and domain

The MSM was developed on the basis of fully compressible nonhydrostatic equations which were transformed from height coordinates to sigma coordinates under a hydrostatic base state (Juang 2000). Besides the hydrostatic perturbation related to the external hydrostatic state as perturbation nesting, the nonhydrostatic perturbation in association with the internally evolved hydrostatic state was also introduced in the MSM. The major model physics employed in the RSM are used in the MSM without the hydrostatic

assumption. A new precipitation physics package (Hong et al. 1998) was implemented into the MSM. This package incorporates a prognostic cloud scheme for the grid-resolvable precipitation and a parameterization convection scheme with a convective trigger function (Hong and Pan 1998). The same 28 sigma layers used in the RSM are also used in the MSM.

The MSM is set up for three sub-regions of the state of Hawaii: the Oahu domain at a 1.5-km resolution (Fig. 2.1b), the Molokai-Maui-Hawaii domain at a 3-km resolution (Fig. 2.1c), and the Kauai domain at a 1.5-km resolution (Fig. 2.1d). The choice of the resolution for the MSM domains is based on considerations of both cost-effectiveness and representation of terrain features. In the 1.5-km Oahu domain, the model terrain adequately represents the two narrow mountain ranges (Koolau Range on the east and Waianae Range on the west) on the island of Oahu (Fig. 2.1b). The peak height is 0.6 km for both mountain ranges, which is about 0.2-0.5 km lower than the actual height. In the 3-km Molokai-Maui-Hawaii model domain (Fig. 2.1c), both Mauna Kea and Mauna Loa over the Big Island are evident with a peak height of 3.9 km, which is about 0.2-0.4 km lower than the actual height. Another small mountain range, the Kohala mountains, is located over the northern part of the island with a peak height of 1.2 km in the model, ~ 0.3 km lower than the actual height. The Waimea Saddle is situated between Mauna Kea and the Kohala mountains. The peak height of the Haleakala mountain on the island of Maui is roughly 2.3 km in the MSM domain, ~ 0.7 km lower than the actual height. The West Maui mountains have a peak height of 0.8 km in the model, ~ 0.7 km lower than the actual height. These large differences over West Maui between the model terrain and the actual may be related to the fact that the West Maui mountains are characterized by steep

slopes and narrow mountain ranges and the MSM appears to have difficulties in resolving these steep terrains at 3-km grid spacing. Two small islands in this area (Lanai and Kahoolawe) are also evident in the 3-km model domain (Fig. 2.1c). In the 1.5-km Kauai domain (Fig. 2.1d), the model terrain reasonably resolves the mountain shape with a peak height of 1.3 km, comparable to the actual height of 1.5 km. This model domain also shows the Waimea Canyon southwest of the mountain ridge and another small mountain over the island of Niihau, located southwest of the island of Kauai (Fig. 2.1d).

2.3 Land surface model

The RSM and MSM use the two-layer soil model of Mahrt and Pan (1984), Pan and Mahrt (1987), with modifications based on Pan (1990). The soil model includes soil thermodynamics and soil hydrology, both modeled as a diffusion process. The evaporation process in the surface energy balance is modeled by three components: direct evaporation from the bare soil surface, transpiration through the leaf stomata, and evaporation of precipitation intercepted by the leaf canopy. The earlier version of the LSM in the RSM and MSM assumed a homogeneous vegetation category (broadleaf tree) and soil category (sandy clay loam) in the entire model domain. The vegetation fraction was constant at 70%. Albedo and roughness lengths were taken from the global model (Briegleb et al. 1986).

In early 2002, the land surface model in the RSM and MSM was updated to represent heterogeneous soil and vegetation types. Corresponding surface albedo and surface roughness length as well as soil parameters are derived based on Chen and Dudhia

(2001a). The roughness length over the oceans uses the Charnock formula for flux computation (Charnock 1955):

$$z_0 = 0.0144 \times u_*^2 / g \tag{2.1}$$

where z_0 is the roughness length, u_* the friction velocity of air, and g the acceleration of gravity. This formula gives z_0= 1 mm for u_*=1 m s^{-1}. Since the threshold values for direct evaporation in Pan and Mahrt (1984) are unavailable in the USGS (US Geological Survey) datasets, the direct evaporation formulation from Mahfouf and Noilhan (1991) is adapted, as done by Chen and Dudhia (2001a). There are 13 vegetation categories and 16 soil categories employed in the LSM. Vegetation fraction ranges from 0 to 100%.

The vegetation types and vegetation fraction for the major Hawaiian Islands were compiled from the USGS 1:100,000-scale Land Use Land Cover Level II Data for Hawaii (DOI USGS 1986). The soil types were also compiled from the USGS data with reference to the soil surveys in Hawaii (Foote et al. 1972; Sato et al. 1973). The USGS Land Use Land Cover data for Hawaii were prepared and distributed at a resolution of 200 m. Our compiled data have a resolution of 30", or roughly 1 km at 20 °N. The vegetation type at every grid box in our compiled datasets was specified as the dominant vegetation type within the USGS grids. The vegetation fraction was computed as the ratio of the numbers of the USGS grids containing vegetation to the total number of the USGS grids within the grid box. The USGS Land Use Land Cover data for Hawaii do not contain soil information. We first established a correspondence between the soil types in Foote et al. (1972) and Sato et al. (1973) and the USGS Land Use Land Cover Level II data based on direct comparisons. We then obtained the soil types from the USGS Land

Use Land Cover data using this correspondence. Because of small seasonal changes in vegetation for the Hawaiian Islands, we consider the vegetation type and vegetation fraction at every grid point as constant year-round.

2.4 Experimental design

Evaluations of the RSM/MSM coupled with the LSM in simulating orographic effects and local circulations under summer trade wind conditions are being made at NWS surface sites for a one-month period of May 20 through June 20 2002 using our archived model data from daily experimental forecasts. Further evaluations of the coupled MSM/LSM in simulating local sea breeze circulations are performed over northwest Hawaii during 23-28 June 1978. Observational analyses of these sea breeze circulations are presented in Schroeder (1981). We have also assessed the impact of improved representation of the terrain and surface boundary conditions on simulating localized rainfall and orographically amplified high winds based on a few cases.

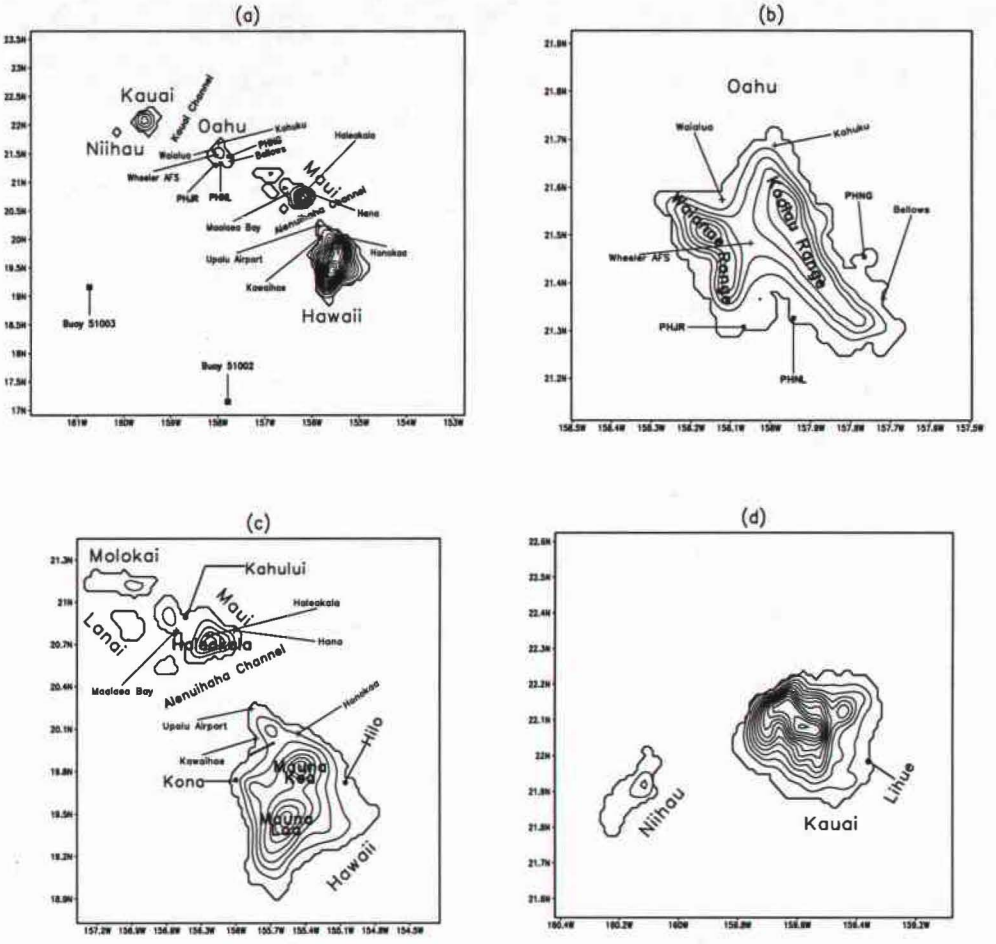

Figure 2.1. (a) The RSM model grids at a 10-km resolution for the Hawaiian Islands with the contour interval of 200 m; (b) the MSM model grids (1.5 km × 1.5 km) for the Oahu domain with the contour interval of 100 m; (c) the MSM model grids (3 km × 3 km) for the Molokai-Maui-Hawaii domain with the contour interval of 500 m; and (d) the MSM model grids (1.5 km × 1.5 km) for the Kauai domain with the contour interval of 100 m. Two buoy stations (51002 and 51003) and three surface sites over Oahu (PHNL, PHJR, and PHNG) are denoted by closed squares. The surface sites where model forecasted 10-m winds are validated are denoted by crosses. The thick solid line over Northwest Hawaii in (a) and (c) denotes the transection for sea breeze simulations.

CHAPTER 3

Summer trade-wind conditions over Oahu

3.1 Introduction

Under same large-scale trade-wind conditions, each island in the Hawaiian island chain would experience a different flow regime due to large variations in the mountain heights (ranging from about 500 m for Oahu to over 4 km for the Big Island). The island-induced flow response of each island is also different under different trade-wind speeds, wind directions, and trade-wind inversion height. It is ideal to validate high-resolution simulations of local effects over the Hawaiian Islands under undisturbed, persistent synoptic conditions (e.g., summer trade-wind weather).

During the summer months, orographic clouds and local showers are frequent over the Hawaiian Islands without the presence of significant synoptic/mesoscale disturbances, despite the fact that the trade-wind belt has a minimum in the global distribution of rainfall. Leopold (1949) first described qualitatively the interactions between the prevailing trade-wind flow and the island-induced circulations over the Hawaiian Islands including orographic lifting, thermally driven land-sea breeze circulations, flow deceleration and deflection, and the lid effect of the trade-wind inversion. Using data updated through 1983, Giambelluca et al. (1986) compiled a rainfall atlas for the six largest islands of Hawaii (Big Island, Maui, Kauai, Oahu, Molokai, and Lanai). Rainfall maxima correspond to regions with persistent orographic lifting of moisture-laden northeast trade winds along the windward slopes. Areas of low rainfall are found in

leeward areas and atop the highest mountains. For mountains with tops well below the inversion (~ 2 km), the rainfall maximum occurs near or just downstream of the summits.

In addition to orographic lifting, the island airflow and weather is also affected by dynamic blocking as the trade-wind flow encounters island obstacles and by the diurnal heating cycle. Modeling studies (Smolarkiewicz et al. 1988; Rasmussen et al. 1989; Rasmussen and Smolarkiewicz 1993) predict flow deceleration and deflection on the windward side of the Big Island if the Froude number (Fr = U/Nh, where U is the upstream wind speed, N is the Brunt-Väisälä frequency, and h is the height of the barrier) is less than unity. For islands with Fr<1 because of the presence of high mountains (i.e., Maui and the Big Island), the incoming trade-wind flow is deflected by the terrain (Leopold 1949; Chen and Nash 1994). For airflow approaching those islands with low mountains such as Molokai and Oahu with Fr>1, the trade-wind flow is able to move over the islands. In regions of weak winds because of island blocking, thermally driven diurnal circulations (Leopold 1949; Lavoie 1967; Garrett 1980; Schroeder 1981; Chen and Nash 1994; Chen and Wang 1994; Feng and Chen 1998) become significant. Thermally driven diurnal circulations may contribute to rainfall by reinforcing trade-wind orographic lifting (Garrett 1980), generating areas of low-level convergence when interacting with the prevailing trade winds (Leopold 1949; Schroeder 1981; Takahashi 1977; Austin et al. 1996; Carbone et al. 1998; Feng and Chen 1998; Wang and Chen 1998; and Li and Chen 1999) or initiating orographic lifting of onshore flow in areas not exposed to trade winds (e.g., lee-side coast of the Big Island) (Yang and Chen 2003). Schroeder et al. (1977) show distinct diurnal rainfall patterns for the major Hawaiian Islands. Local rainshowers also affect the surface airflow (Wang and Chen 1995; Chen

and Wang 1995; Carbone et al. 1995, 1998). Recent modeling work (Feng and Chen 2001) shows that the diurnal heating cycle affects the upstream flow deceleration. They show that the simulated upstream flow deceleration for the Big Island is most significant early in the morning when the simulated offshore flow has the largest horizontal extent (20 km) and a maximum depth (300 m).

Perturbations induced by airflow past isolated mountains include a variety of phenomena, ranging from bow-shaped ship waves to wake vortices (Scorer 1986; Sun and Chern 1993; Lin et al. 1992). The composite wind field based on ship reports (Patzert 1970) suggests the existence of quasi-stationary structure with two counterrotating vortices forming the wake of the Big Island. The first aircraft probing of Hawaii's wake was made in the summer of 1980 during the Hawaiian Mesoscale Energy and Climate (HAMEC) Project (Nickerson and Dias 1981). Their work contained the first direct evidence for the existence of atmospheric vortices in Hawaii's wake. During the Hawaiian Rainband Project (HaRP) conducted in July and August of 1990, five NCAR Electra flights were designated to depict the mesoscale airflow downstream of the Big Island. Smith and Grubiŝić (1993) show that the wake consists of two elongated counterrotating eddies that give rise to a wide region of strong reverse flow along the wake axis. In addition, wave clouds in the lee of the island of Oahu have been reported from satellite imagery (Schroeder 1977; Burroughs and Larson 1979). Lavoie (1974) simulates hydraulic jumps over Oahu.

Even though trade winds are persistent during the summer, there are large day-to-day variations in the island-induced flow response and rainfall (Chen and Feng 1995; Ramage and Schroeder 1999; Frye and Chen 2001). Occasionally, there are trade-wind

disturbances embedded in the trade-wind flow without the presence of large-scale forcing (Raymond and Lewis 1995). Forecasting summer trade-wind rainfall and weather over the Hawaiian Islands and the adjacent waters remains a significant challenge.

Our daily experimental MSM run has been conducted for the Oahu domain at a 1.5-km resolution since the summer of 2001 and then changed to the coupled MSM/LSM since April 30, 2002. We chose Oahu for carrying out the daily experimental MSM run because the island has more than 80% of the state's population. It is desirable to assess the impact of the improved representation of the terrain and surface boundary conditions on simulating orographic effects and local circulations. In contrast to the 1.5-km MSM Oahu domain which shows two narrow mountain ranges (Koolau on the east and Waianae on the west) (Fig. 2.1b), the 10-km operational RSM resolves only one mountain range with peaks ~ 0.3 km (Wang et al. 1998; Fig. 2.1a).

This chapter documents the evaluations of the coupled MSM/LSM forecasts under summer trade-wind conditions from 20 May through 20 June 2002 (32 days). Observations collected at three NWS surface sites on the island of Oahu are used to validate the model simulations. Since the RSM provides the initial conditions and boundary conditions for the MSM, the RSM simulations in the regional domain are evaluated using observations at two buoy stations over the adjacent waters of the Hawaiian Islands. This chapter is organized as follows. Synoptic conditions and model initializations are discussed in section 3.2. Comparisons between model simulations and observations are described in section 3.3. Conclusions and discussions are presented in section 3.4.

3.2 Synoptic conditions and model initialization

The subtropical high shifted east from its normal summertime position and was located off the west coast of the United States following the inland movement of an intense low system along the California coast around May 20, 2002 (Fig. 3.1a). This movement placed the Hawaiian Islands under the influence of the trailing ridge of the subtropical high with weak trade winds. At first the winds were southeasterlies. Later, there was virtually no large-scale wind flow when the ridge axis was over the Hawaiian Islands (Fig. 3.1b). Under this synoptic situation, nighttime land breezes and daytime sea breezes prevail over the islands (Leopold 1949; Lyons 1979; Garrett 1980; Schroeder 1981; Chen and Nash 1994). Towards the end of May, the subtropical high was strengthened after merging with a high pressure system coming from the northwest Pacific (Fig. 3.1c). Normal trade wind weather returned to the Hawaiian Islands for the next two weeks. Around June 12 the high was pushed southeastward towards the islands by a mid-latitude frontal system which tightened the pressure gradient over the islands and resulted in strong trade winds for the last week of the study period (Fig. 3.1d). Although there were occasional interruptions, the entire period of May 20 through June 20 can be generally characterized by weak synoptic winds during the first week followed by normal trade wind weather.

The model runs are started at 1400 HST (Hawaiian Standard Time; UTC = 10 h + HST) each day (referred to as day 0). For the RSM/LSM runs, the initial conditions and lateral boundary conditions are interpolated from the AVN data of the operational NCEP GSM forecasts; whereas the initial soil conditions (soil temperature and soil moisture) are given by the 24-h forecasts of the previous RSM/LSM run. The 24-h forecasts of the previous

MSM/LSM run are also used to provide the initial soil conditions for the daily MSM/LSM run. The initial conditions and lateral boundary conditions for the MSM (MSM/LSM) runs are interpolated from the RSM (RSM/LSM) forecasts. The RSM/LSM and MSM/LSM integrations are carried out for 48 hours and 36 hours, respectively. Model data are output every three hours. The restart hour from the coarse-resolution model to the fine-resolution model (i.e., the nesting period) is 6-hour from AVN to RSM and 3-hour from RSM to MSM, respectively. The current system employs a one-way nesting from the coarse-resolution model to the fine-resolution model.

3.3 Results

3.3.1 Comparisons with buoy data

Since the RSM/LSM provides the base fields for the nested MSM/LSM runs, it is important to evaluate the performance of the RSM/LSM in the regional domain over the open ocean. There are four buoy stations over the adjacent waters of the Hawaiian Islands. Among them, only two buoy stations (51002 and 51003) are within our RSM model domain (see Fig. 2.1a). Therefore, model validations are carried out at these two stations during the one-month period including surface pressure, 2-m temperature, 10-m wind direction and 10-m wind speed. These two buoy stations do not report observations for dew point temperature and in the case of buoy station 51003 observations for temperature were missing for the analysis period. Four times are chosen for the model validations: 0200 HST (day 0, 12-h forecast), 1400 HST (day 1, 24-h forecast), 0200 HST (day 1, 36-h forecast), and 1400 HST (day 2, 48-h forecast). Comparisons are made with and without the advanced LSM for the RSM forecasts. It is apparent that the model forecasted

surface pressures from the 12-h, 24-h, 36-h and 48-h forecasts at these two buoy stations agree well with observations in terms of magnitude and temporal variations during the one-month period (Fig. 3.2). Except for a few outliers, the differences between the model forecasts and observations are generally less than 0.5 hPa.

For the 2-m temperatures at buoy station 51002 (Figs. 3.3a and 3.3b), the RSM and RSM/LSM forecasts agree reasonably well with observations for 24-h (valid at 1400 HST, day 1), 36-h (valid at 0200 HST, day 1) and 48-h forecasts (valid at 1400 HST, day 2). The 12-h forecast (valid at 0200 HST, day 0) persistently produces slightly higher surface temperature than the observations. The reason for this overestimation of surface temperature by both models may be related to initialization data or air-sea processes. Note that over the ocean, the forecasted 2-m temperatures from RSM and RSM/LSM are almost identical for the entire period.

The model forecasts of the 10-m wind speeds from RSM and RSM/LSM at the two buoy stations are similar and are consistent with observations in terms of magnitude and temporal evolution at the four validation times (Fig. 3.4). Both models also did a decent job in forecasting the observed surface wind directions at the two buoy stations (Fig. 3.5). Note that surface wind direction changes much more significantly from day to day at buoy station 51003 than at buoy station 51002, both in observations and model simulations. Considering that buoy station 51003 is affected by the wakes of the island of Hawaii (Smith and Grubiŝić 1993; Xie et al. 2001), daily changes in surface wind direction at this station may reflect the unsteadiness of the wakes.

In summary, the RSM forecasts agree well with observations for surface pressure, 10-m wind speed and 10-m wind direction over the two buoy stations, and for 2-m

temperature over buoy station 51002. The RSM/LSM simulations are quite similar to those of the RSM at the two buoy stations since the LSM only affects model simulations over land.

3.3.2 Model verifications over land

There are three main airports on the island of Oahu that report observations on an hourly basis: PHNL (Honolulu International Airport), PHNG (Kaneohe Marine Corps Base Hawaii), and PHJR (Kalaeloa Airport) (see Fig. 2.1b). A fourth site, PHHI (Wheeler Air Force Base), collects observations during the daytime on weekdays only. We do not perform model validations at this site. PHNG, with a terrain height of 2 m, is located near the eastern coastline on the windward side of the Koolau Range. The other two sites, PHNL and PHJR, are situated in urban areas near the southern coastline and on the lee side of the Koolau Range, with respective terrain heights of 4 m and 9 m (see Fig. 2.1b). Meteograms from the MSM/LSM model output are produced daily at these sites for the forecasters at WFO-HFO. In this study, comparisons between model simulations and observations are conducted at three forecast times: 0200 HST (day 0), 1400 HST (day 1) and 0200 HST (day 1), which correspond to 12-h, 24-h and 36-h model forecasts, respectively. Adjustments for surface variables are applied to model simulations based on the terrain difference between the model domain and the real terrain, using the standard lapse rate of the atmosphere.

The 12-h, 24-h and 36-h sea-level pressure forecasts at PHNL from RSM, MSM and MSM/LSM are compared with observations in Figure 3.6. It is evident that all three models forecast the magnitude and temporal variations of the observed sea level pressure rather well. This is also the case for the other two surface sites (not shown).

Figure 3.7 shows the observed and forecasted 2-m temperatures from RSM, MSM and MSM/LSM at PHNL. At 0200 HST, the RSM forecasts higher surface temperature than observed (Figs. 3.7a and 3.7c). We found that in the RSM domain with a 10-km resolution, PHNL is treated as an ocean point instead of as a land point. The forecasted nighttime surface temperatures from MSM and MSM/LSM are generally consistent with observations under normal trade wind conditions from May 31 to June 20 (Figs. 3.7a and 3.7c). Nevertheless, discrepancies between the MSM and MSM/LSM forecasts and observations are noted during the weak wind days (May 20 through May 30).

At 1400 HST (Fig. 3.7b), the RSM, MSM and MSM/LSM forecasts at PHNL diverge considerably. For almost the entire study period the RSM persistently forecasts lower 2-m temperature than observations, with the differences as large as 4 °C (2 °C) during normal trade wind (weak wind) days, due to its treatment of PHNL as an ocean point. The MSM forecasts still contain cold biases (~ 2 °C) even though PHNL is treated as a land point in the MSM domain. In comparison, the 2-m temperatures forecasted by the MSM/LSM agree reasonably well with observations for the entire period. The improved performance of the MSM/LSM over the MSM at 1400 HST is due to better representation of land surface processes by the LSM. As noted earlier, there is only one vegetation type (broadleaf tree) with a constant vegetation fraction of 70% over the Hawaiian Islands in the MSM. However, in reality, PHNL is located in an urban area with less than 10% vegetation cover.

The RSM persistently forecasts higher 2-m dew point temperatures than observations at PHNL during both nighttime and daytime, probably due to its treatment of PHNL as an ocean point (Fig. 3.8). The MSM simulated 2-m dew point temperature is close to

observations at nighttime (Figs. 3.8a and 3.8c) but is about 3 °C higher than observations during the daytime (Fig. 3.8b). In comparison, the 2-m dew point temperatures from MSM/LSM forecasts are close to observations during both nighttime and daytime. One salient feature in Figure 3.8 is that the observed 2-m dew point temperature is lower during the normal trade wind period than during the weak wind period, at both 0200 HST and 1400 HST. The lowest daytime 2-m dew point temperature occurs during the strong wind period of June 12 through June 18. This is likely related to the increased vertical mixing in the afternoon hours under strong wind conditions which bring down the drier air aloft. This feature is captured by the MSM/LSM but not by the RSM and MSM.

All three models capture the temporal evolution in 10-m wind speed at PHNL reasonably well (Fig. 3.9); however, the RSM simulations are about 5 m s^{-1} (3 m s^{-1}) higher at 0200 HST (1400 HST) than observations, whereas the MSM simulations are about 4 m s^{-1} (3 m s^{-1}) higher at 0200 HST (1400 HST) than observations. The slightly higher wind speed in the RSM as compared with the MSM is likely related to the differences in the model terrain. There is only a single mountain range with much lower mountain heights in the RSM domain as compared with the MSM domain (Fig. 2.1). As noted earlier, the surface at PHNL is specified as water and tropical forest with broadleaf trees (70% vegetation cover) in the RSM and MSM, respectively, with unrealistic small roughness lengths over the island of Oahu (0.005 – 0.01 m). As a result, the 10-m wind speed is overestimated by the RSM and MSM. In comparison, the MSM/LSM provides quite consistent surface wind speed with observations not only during the weak wind period (May 20 to May 30) but also during the normal trade wind period (May 31 to June 20). This is largely due to the realistic representation of surface roughness (0.5 m as an

urban site) by the LSM. All three models produce similar forecasts for 10-m wind direction at PHNL during normal trade wind days which agree reasonably well with observations (Fig. 3.10). However, during the weak wind period, there are discrepancies between model forecasts and observations. At 1400 HST (Fig. 3.10b), the MSM/LSM captures the observed onshore wind component (wind direction $\geq 90°$) during weak wind days while the RSM and MSM do not.

PHJR is located in an urban area with relatively flat terrain (see Fig. 2.1b). Figure 3.11 shows the observed and forecasted 2-m temperature from the RSM, MSM and MSM/LSM at PHJR. With 70% vegetation cover over the island, the RSM and MSM provide almost identical forecasts during the entire period. However, in the MSM/LSM, PHJR and the adjacent areas are treated as urban areas with less than 10% vegetation cover. At 0200 HST (Figs. 3.11a and 3.11c), the RSM and MSM forecasted 2-m temperatures are slightly higher than those observed during May 20 to June 12. At 1400 HST (Fig. 3.11b), the RSM and MSM provide much lower (~ 3 °C lower) 2-m temperatures than observations. In comparison, the MSM/LSM forecasted 2-m temperatures are consistent with observations both at 0200 HST and at 1400 HST for the entire period.

The RSM and MSM forecast higher dew point temperatures than observations at 0200 HST and 1400 HST for the entire period at PHJR (Fig. 3.12) due to the specification of this site as tropical forest with 70% vegetation cover. In comparison, the MSM/LSM forecasted 2-m dew point temperatures agree with observations reasonably well. Similar to PHNL, the MSM/LSM also captures the observed lower dew point temperature in the afternoon hours during the stronger trade wind days.

The RSM and MSM overestimate the surface wind speeds by as much as 4 m s^{-1} at 0200 HST and 1400 HST at PHJR during the normal trade wind period (Fig. 3.13). This is related to the small surface roughness used in both models. The forecasted 10-m wind speeds from the MSM/LSM are generally consistent with observations for the entire period. For the 10-m wind direction at PHJR, all three models provide similar forecasts during the normal trade wind period that agree with observations reasonably well (Fig. 3.14). However, during the weak wind period, the MSM/LSM forecasted 10-m wind directions are closer to observations than the RSM and MSM forecasts.

We will next examine the model forecasts at PHNG which is located on the windward side of the island of Oahu. In the MSM/LSM model, PHNG and the adjacent areas are specified as broadleaf shrubs with perennial ground cover (~ 80% vegetation fraction). This surface site is well exposed to marine air due to its proximity to the ocean and the constant influences from the incoming trade winds. At nighttime (Figs. 3.15a and 3.15c), the MSM and MSM/LSM generate identical but closer fits to observations than the RSM. At 1400 HST (Fig. 3.15b), cold biases are evident in the RSM and MSM forecasts but not as significant as at PHNL (see Fig. 3.7b) and PHJR (see Fig. 3.11b). This is probably due to the fact that daytime heating at PHNG is not as significant as at PHNL and PHJR due to marine air influence at PHNG. Overall, the MSM/LSM provides a better fit to observations at 1400 HST when compared to the RSM and MSM forecasts.

For the 2-m dew point temperature forecasts at PHNG, the RSM and MSM provide identical forecasts at nighttime that agree reasonably well with observations (Figs. 3.16a, 3.16c). The MSM/LSM also captures the observed daily variations in 2-m dew point temperature during the nighttime reasonably well. During the daytime (Fig. 3.16b), the

MSM/LSM provides a better fit to observations while the forecasted 2-m dew point temperatures from the RSM and MSM are persistently higher than observations.

The forecasted 10-m wind speeds from the MSM/LSM at PHNG are close to observations both at 0200 HST and at 1400 HST during normal trade wind period, whereas the RSM and MSM forecasts are about 2 m s^{-1} (1 m s^{-1}) higher than observations at 0200 HST (1400 HST) (Fig. 3.17), primarily related to small surface roughness over the entire island as previously mentioned. The MSM/LSM also captures the persistent calm conditions recorded at PHNG at 0200 HST during May 21 through May 28 (Figs. 3.17a and 3.17c). However, the model underestimates the surface wind speed at 1400 HST by about 1 m s^{-1} during the same period (Fig. 3.17b). For the 10-m wind direction (Fig. 3.18), model forecasts from the RSM, MSM and MSM/LSM are identical and are consistent with observations during normal trade wind days (May 31 to June 20). During the weak wind period, model forecasts diverge from observations.

Based on observations and model forecasts from the RSM, MSM and MSM/LSM, statistics of surface variables are computed at the three surface sites for 12-h, 24-h and 36-h forecasts. They are summarized in Tables 3.1, 3.2 and 3.3 which contain (1) the 32-day mean, (2) the correlation coefficient of model simulations with observations, and (3) forecasting errors for 2-m temperature, 2-m dew point temperature, and 10-m wind speed, respectively. The forecasting error is defined as

$$fe = \frac{\sum_{i=1}^{N} \left| A_o^i - A_m^i \right|}{N} \tag{3.1}$$

where A refers to any of the four surface variables, N is the number of days of observations (N = 32), subscripts o and m respectively denote observations and model simulations, and superscript i ranges from 1 to 32.

For 2-m temperature (Table 3.1) and 2-m dew point temperature (Table 3.2), the MSM/LSM forecasts consistently show the highest correlation coefficient with observations, with fewer forecasting errors than the RSM and MSM forecasts. The 32-day mean in the MSM/LSM forecasts is also the closest to the observed mean. Cold biases are evident in the 24-h RSM and MSM forecasts. In addition, the forecasted 2-m dew point temperatures form RSM and MSM are negatively correlated with observations at PHJR for the 24-h forecast.

The overestimation of 10-m wind speed by the RSM and MSM is reflected in the 32-day means at all three surface sites (Table 3.3). It is more severe in the RSM simulations than in the MSM simulations. The correlation coefficients of the RSM, MSM and MSM/LSM forecasted surface wind speeds with observations are only slightly different at each surface site. However, the MSM/LSM simulations persistently provide the fewest forecasting errors. Amongst the three surface sites, correlation coefficients are higher at PHNL and PHNG than at PHJR.

At all three surface sites, the largest variations and forecasted uncertainties in wind direction occur mainly during the period with weak trades (20-30 May) (Figs. 3.10, 3.14 and 3.18). Except for the 12-h and 36-h forecasts at PHJR, the simulated wind directions agree fairly well with observations during the normal trade wind period (31 May to 20 June) (Figs. 3.10, 3.14 and 3.18). The impact of the incorporation of the advanced land surface model with improved surface boundary conditions on the simulated thermally

driven circulations when trades are weak will be evaluated from the composite analysis in the next section. Additional evaluations of the MSM/LSM performance in simulating the observed thermally driven circulations over northwest Hawaii (Schroeder 1981) will be discussed in the following chapter.

In summary, the 1.5-km MSM provides better forecasts for surface variables than the 10-km RSM over the surface sites; however, there are still large discrepancies between the MSM simulations and observations. Further improvements have been achieved by coupling the LSM with the MSM. In particular, overestimation of surface wind speed and daytime cold biases experienced by the MSM are largely corrected in the MSM/LSM.

3.3.3 Diurnal cycle and precipitation

To further explore the performance of the MSM/LSM in comparison to the MSM in simulating the diurnal cycles of surface variables under different weather regimes, we selected three weak trade wind days (5/24, 5/25, and 5/26) and five strong trade wind days (6/13, 6/16, 6/17, 6/18, and 6/19) from May 20 through June 20, 2002 for composite analyses. We examined the RSM forecasted 10-m winds at an upstream point (21.5 °N, 157.5 °W) for a weak trade wind day or a strong trade wind day, when easterly trade winds are present. For weak (strong) trade wind days, the wind speed at the upstream point is less than 5 m s^{-1} (greater than 8 m s^{-1}).

a) Diurnal cycles of surface variables

We constructed composites of the diurnal cycles of 2-m temperature, 2-m dew point temperature, 10-m wind speed and 10-m wind direction at the three surface sites for the three weak trade wind days and the five strong trade wind days. The MSM/LSM and MSM 12-h (valid at 0200 HST, day 0) through 36-h (valid at 0200 HST, day 1) forecasts

at 3-h intervals are examined in comparison to observations. Figures 3.19a-f show the observed and forecasted composite diurnal cycles of 2-m temperatures from MSM/LSM and MSM at the three surface sites for the weak trade wind days (left column) and the strong trade wind days (right column). The MSM/LSM and MSM capture the observed diurnal cycles of 2-m temperature reasonably well during both the weak and the strong trade wind days. The MSM/LSM does a much better job than the MSM in reproducing the observed magnitude. The MSM forecasts persistently show cold biases during the daytime.

Both the MSM/LSM and MSM capture the daytime maximum and nighttime minimum in the observed 2-m dew point temperatures at PHNL and PHJR during the weak trade wind days (Figs. 3.20a, 3.20c). These dew point temperature extremes are due to daytime moist sea breezes and nighttime dry land breezes when synoptic winds are weak. At PHNG which is exposed to the incoming trade wind flow, the diurnal variation in the 2-m dew point temperature is smaller than the other two sites with higher values at nighttime under weak trades. The MSM/LSM reproduces the observed maxima and minima in 2-m dew point temperatures at PHNG better than the MSM during the weak trade wind days (Fig. 3.20e); however, the magnitude of the morning maximum in the MSM/LSM forecasts is much lower than observations.

During the strong trade wind days (Figs. 3.20b, 3.20d and 3.20f), the MSM persistently forecasts higher dew point temperature than observations, especially during the daytime hours. Furthermore, at PHNL and PHJR (Figs. 3.20b and 3.20d), the observed 2-m dew point temperatures have a daytime minimum possibly related to vertical mixing as a result of solar heating over the urban areas. The observed daytime minimum in the dew

point temperature is not forecasted by the MSM. In comparison, the MSM/LSM forecasts at PHNL and PHJR are not only in phase with observations throughout most of the day, but also agree with the observed magnitude. At PHNG which is located on the windward side, the MSM/LSM and MSM reasonably capture the diurnal cycles in the observed 2-m dew point temperature with a daytime maximum (Fig. 3.20f). However, the simulated magnitude is about 0.5 °C (1.0 °C) lower (higher) than observations from the MSM/LSM (MSM) forecasts.

During the strong trade wind days (Figs. 3.21a, 3.21c and 3.21e), both the MSM/LSM and MSM forecast higher wind speed in daytime hours and reduced wind speed in nighttime hours as shown in the observations. However, the MSM simulated surface wind speed is persistently 3 m s^{-1}, 5 m s^{-1} and 2.5 m s^{-1} higher than observations at PHNL, PHJR and PHNG, respectively. The MSM/LSM forecasted surface wind speed is generally close to observations at PHNL and PHJR but is about 0.5 m s^{-1} higher than observations at PHNG. Both models also reproduce the observed diurnal cycles in 10-m wind direction at PHNL and PHNG during the strong trade wind days reasonably well (Figs. 3.21b and 3.21f).

To evaluate the performance of the MSM/LSM and MSM in forecasting the diurnally driven land/sea breeze circulations under weak synoptic wind conditions, the horizontal maps of the simulated surface wind for the weak trade wind days are plotted. In the early morning (Figs. 3.22a, 3.22b), both the MSM/LSM and MSM forecast weak land breezes on both sides of the Koolau Range and Waianae Range. In the afternoon (Fig. 3.23), the MSM/LSM produces onshore wind component (sea breezes) along the coastlines surrounding the islands (Fig. 3.23a), whereas the MSM provides weak onshore flow only

along the eastern and western coastlines (Fig. 3.23b). Considering that there are considerable cold biases in the MSM simulations over land at 1400 HST, it is not surprising that the daytime sea breezes are more pronounced in the MSM/LSM model than in the MSM model.

In summary, diurnal cycles of 2-m temperature, 2-m dew point temperature and 10-m wind are better forecasted by the MSM/LSM over the three surface sites during both the weak and strong trade wind days as compared with the MSM forecasts. The daytime minima in 2-m dew point temperatures during the strong trade wind days at the two urban sites are also reproduced by the MSM/LSM. In addition, the sea breezes in the nested Oahu domain are better forecasted by the MSM/LSM than MSM during the weak trade wind days.

b) Precipitation field

We have constructed composite horizontal maps of 6-h accumulated rainfall during the early morning period (0200 HST – 0800 HST) and the afternoon period (1100 HST – 1700 HST) based on observations and the MSM/LSM and MSM forecasts under the weak and strong trade wind conditions. The results are presented in Figures 3.24, 3.25 and 3.26. During the early morning hours of the three weak trade wind days, both observations and model simulations show little or no rainfall for the entire island (not shown). This is consistent with local circulations during the early morning hours when the downslope/offshore flow dominates. During the afternoon hours of the three weak trade wind days (Fig. 3.24a), appreciable rainfall occurs along the west and east slopes of the Waianae Range, and along the west slope of the Koolau Range, consistent with local afternoon sea breeze/upslope flow circulations. The daytime rainfall is forecasted by the

MSM/LSM but is about twice of the observed values in those areas (Fig. 3.24b). The MSM also produces some rainfall along the east slope of the Waianae Range (Fig. 3.24c); nevertheless, it largely misses the observed rainfall along the west slope of the Waianae Range.

During the five strong trade wind days, the MSM/LSM and MSM produce considerable rainfall on the windward side of the Koolau Range during the early morning as well as afternoon hours which is consistent with observations (Figs. 3.25 and 3.26). However, two deficiencies are noted in both the MSM/LSM and the MSM forecasts: (1) the forecasted rainfall amount is more than three times the observed amount, and (2) the models fail to produce the observed heavy rainfall located near or slightly downstream of the Koolau Range ridge. Furthermore, the MSM produces questionable rainfall in the wake area of the island (Figs. 3.25c and 3.26c).

In summary, rainfall patterns for the weak trade wind days are better reproduced by the MSM/LSM than the MSM when compared to observations. However, during the strong trade wind days both the MSM/LSM and the MSM produce excessive rainfall on the windward side of the island with less or no rainfall over the ridge axis. This is in contrast to observations which show maximum rainfall occurring near or slightly downstream of the mountain ridge. Under strong trades, the condensates produced on the windward slopes or near the mountain tops may drift downstream with the winds. This process is not well simulated in the high resolution models.

3.4 Conclusions and discussion

We have validated the RSM forecasts at two buoy stations in the regional domain with a 10-km grid and the coupled MSM/LSM forecasts at three surface sites in the nested Oahu domain with a 1.5-km grid for the period of May 20 through June 20 2003. Major results are summarized as follows.

1) Over the two buoy stations, the RSM 48-h forecasts of surface pressures, 2-m temperatures and 10-m wind speeds compare favorably with observations. The RSM predicted 10-m wind direction is generally consistent with observations at these buoy stations as well. The RSM/LSM simulations over the two buoy stations are similar to those of the RSM since the LSM only affects model simulations over land.

2) Over the surface sites on the island of Oahu, the inclusion of the advanced LSM improves the performance of the MSM over the RSM in forecasting 2-m temperature, 2-m dew point temperature, 10-m wind speed and 10-m wind direction when compared with observations. The daytime cold biases and overestimation of surface wind speed by the MSM are largely corrected by coupling the MSM with the LSM with improved surface boundary conditions.

3) Under weak trades, the sea breezes in the nested Oahu domain are better forecasted by the MSM/LSM than the MSM. The MSM/LSM also captures the observed diurnal cycles in 2-m temperature, 2-m dew point temperature and 10-m wind at the three surface sites reasonably well. The daytime minima in the 2-m dew point temperatures during the strong trade wind days at the two urban sites are also reproduced by the MSM/LSM.

4) Rainfall distribution in association with local sea breeze circulations under weak synoptic wind conditions are better reproduced by the MSM/LSM than the MSM.

However, one major deficiency in the MSM/LSM simulations is that in contrast to observations it produces excessive rainfall on the windward side of the island with less or no rainfall near or downstream of the mountain ridge under normal trade wind conditions.

Our results demonstrate that over land the 1.5-km MSM model provides better forecasts of the surface variables and local circulations as compared with the 10-km operational RSM model. Further improvements of the MSM forecasts are made by coupling the MSM with the advanced land surface model with improved surface boundary conditions. In the next chapter, we examine the MSM/LSM simulations in resolving the observed sea breeze circulations over northwest Hawaii during 23 June to 28 June 1978 (Schroeder 1981). The results indicate generally satisfactory performance of the MSM/LSM in simulating the sea breezes. We also used the coupled MSM/LSM to simulate localized heavy rainfall and high wind events over the Hawaiian Islands. Our analyses show that the MSM/LSM has a better capability than the 10-km operational RSM in simulating localized rainfall distribution and airflows associated with these events because of its better representation of the orographic effects and the lower boundary conditions at the surface. Results from our case studies of these events will be presented in Chapters 5 and 6.

Table 3.1. 32-day mean (°C), correlation coefficient of model forecasts with observations, and forecasting error (°C) of 2-m temperature for the period of May 20 through June 20, 2002 computed from observations and the MSM/LSM and MSM simulations at the three surface sites on the island of Oahu. Correlation coefficient is denoted by "cc" and forecasting error by "fe". Computation of forecasting error is given by equation (3.1) in the text.

		12-h forecast			24-h forecast			36-h forecast		
		Mean	cc	fe	mean	cc	fe	mean	cc	Fe
PHNL	OBS	24.19			29.19			24.19		
	RSM	24.95	0.61	0.87	26.00	0.60	3.20	24.65	0.59	0.69
	MSM	24.24	0.60	0.59	26.97	0.67	2.25	24.05	0.27	0.76
	MSM/LSM	23.83	0.78	0.64	28.86	0.82	0.72	23.40	0.76	0.90
PHJR	OBS	22.31			28.79			22.31		
	RSM	23.01	0.51	0.99	26.98	0.54	1.86	22.91	0.01	1.06
	MSM	23.17	0.51	1.09	26.78	0.66	2.06	23.06	0.03	1.13
	MSM/LSM	22.18	0.69	0.77	28.86	0.63	0.75	22.29	0.64	0.67
PHNG	OBS	23.94			27.17			23.94		
	RSM	23.07	0.64	0.91	26.54	0.20	0.78	23.00	0.61	0.99
	MSM	24.30	0.63	0.65	26.49	0.19	0.85	24.32	0.58	0.57
	MSM/LSM	24.02	0.67	0.65	26.90	0.32	0.69	23.88	0.76	0.43

Table 3.2. As in Table 3.1 except for 2-m dew point temperature. Unit is °C for the mean and the forecasting error.

		12-h forecast			24-h forecast			36-h forecast		
		Mean	cc	fe	mean	cc	fe	mean	cc	Fe
PHNL	OBS	19.43			19.39			19.43		
	RSM	21.34	0.59	1.92	21.79	0.67	2.38	21.03	0.49	1.62
	MSM	19.93	0.79	0.64	21.56	0.47	2.53	19.53	0.58	0.66
	MSM/LSM	19.23	0.77	0.58	18.89	0.67	0.95	19.01	0.71	0.65
PHJR	OBS	18.43			19.18			18.43		
	RSM	20.07	0.77	1.69	21.81	-0.03	2.67	19.68	0.58	1.35
	MSM	20.03	0.74	1.64	21.63	-0.15	2.54	19.60	0.58	1.30
	MSM/LSM	18.78	0.72	0.63	18.96	0.72	0.96	18.56	0.69	0.56
PHNG	OBS	20.13			20.69			20.13		
	RSM	20.43	0.73	0.64	22.00	0.23	1.47	20.03	0.60	0.74
	MSM	20.23	0.76	0.60	21.63	0.29	1.19	19.93	0.59	0.78
	MSM/LSM	19.74	0.79	0.71	20.54	0.49	0.79	20.17	0.70	0.65

Table 3.3. As in Table 3.1 except for 10-m wind speed. Unit is m s^{-1} for the mean and the forecasting error.

		12-h forecast			24-h forecast			36-h forecast		
		mean	cc	fe	mean	cc	fe	mean	cc	Fe
PHNL	OBS	3.41			6.41			3.41		
	RSM	6.51	0.84	3.17	7.43	0.77	1.97	7.63	0.77	4.27
	MSM	5.75	0.82	2.43	7.64	0.74	2.08	6.57	0.66	3.25
	MSM/LSM	2.92	0.78	0.94	5.87	0.78	1.01	3.07	0.62	1.18
PHJR	OBS	2.24			4.98			2.24		
	RSM	5.53	0.42	3.56	7.55	0.16	3.36	6.56	0.48	4.35
	MSM	5.49	0.46	3.47	7.43	0.23	3.21	6.55	0.47	4.42
	MSM/LSM	2.21	0.39	1.17	4.48	0.18	1.29	2.66	0.52	1.03
PHNG	OBS	2.52			4.31			2.52		
	RSM	5.25	0.84	2.75	7.59	0.68	3.46	6.19	0.76	3.78
	MSM	4.88	0.83	2.40	6.54	0.69	2.54	5.59	0.75	3.21
	MSM/LSM	2.53	0.78	0.86	4.80	0.71	1.49	3.80	0.79	1.49

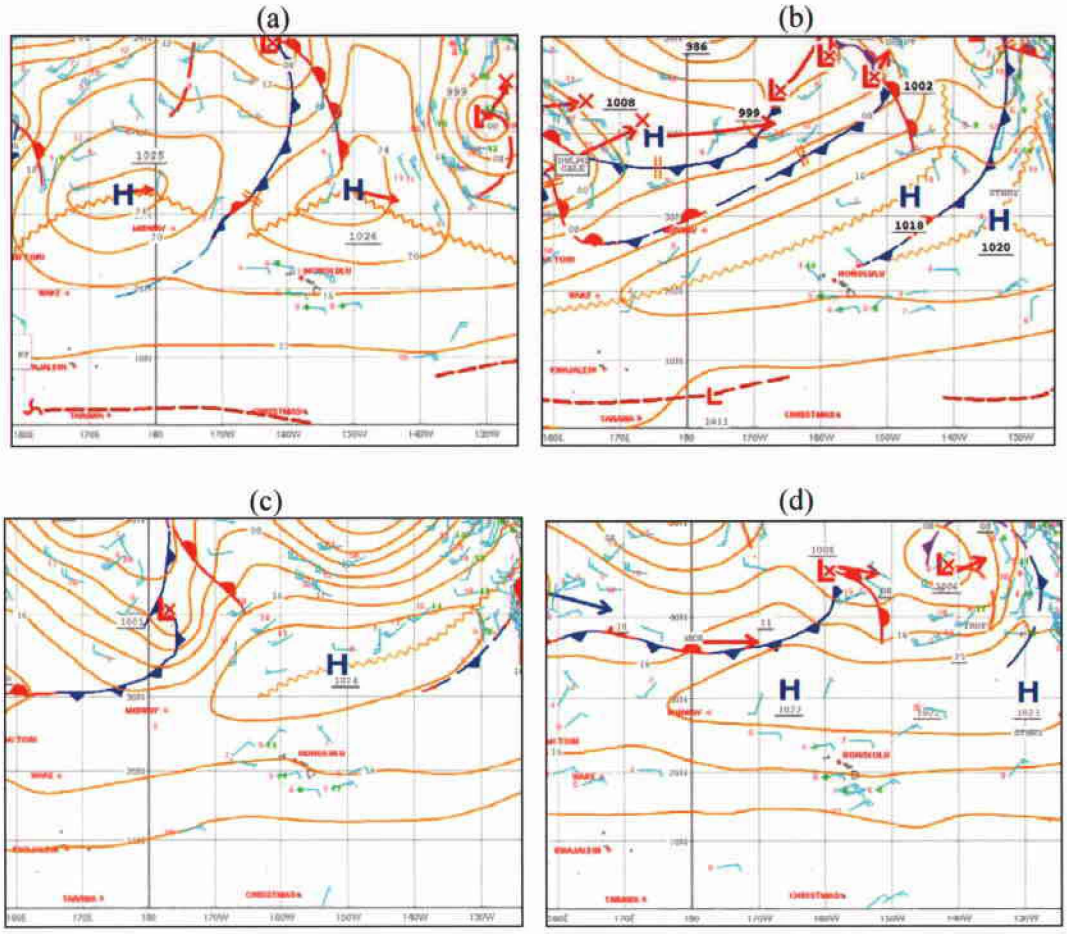

Figure 3.1. Surface analyses for 0000 UTC on (a) May 20, (b) May 25, (c) May 30, and (d) June 16, 2002 (adapted from the subjective analyses by forecasters at the Weather Forecast Office Honolulu). Isobars are plotted every 4 hPa.

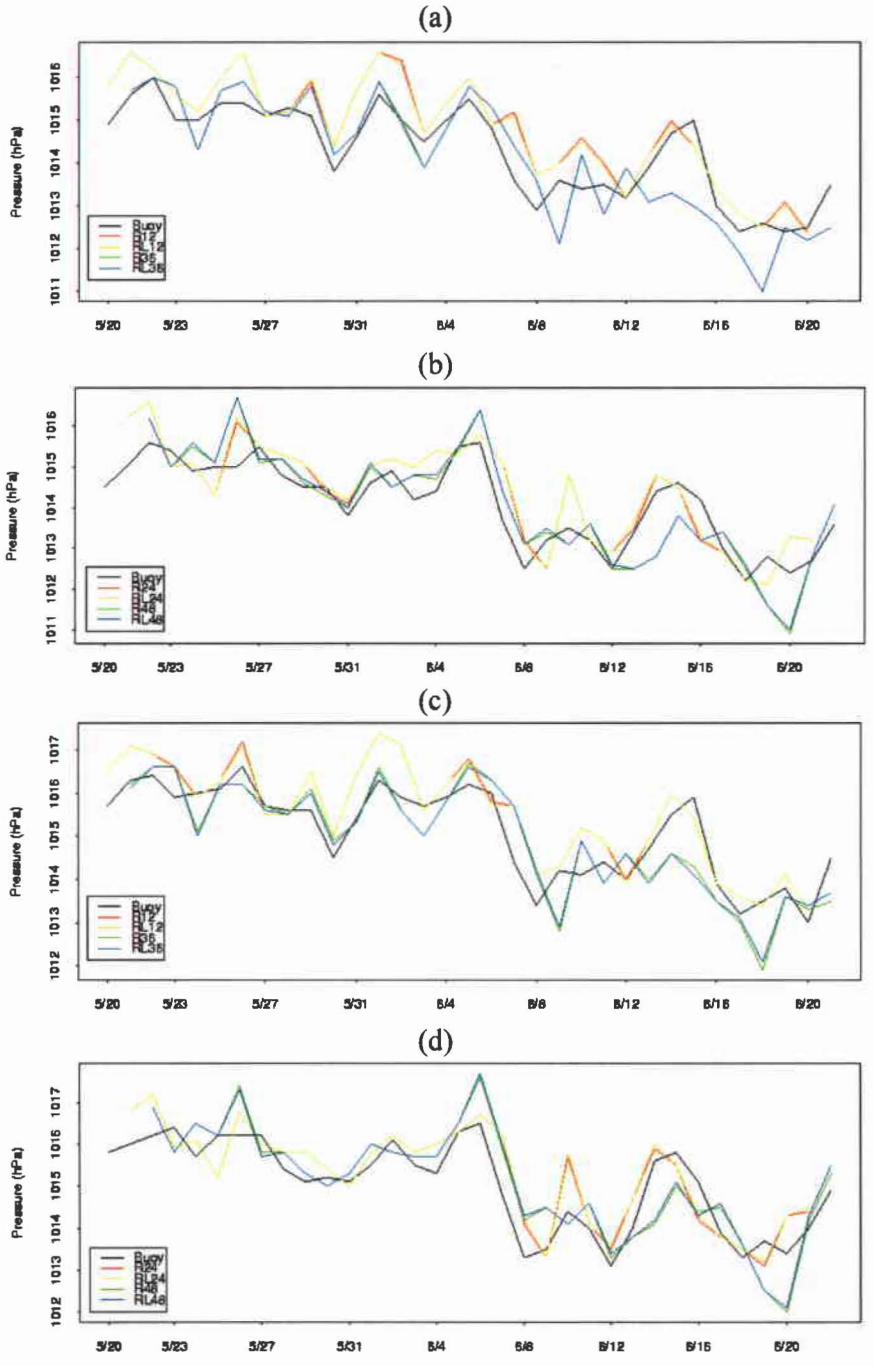

Figure 3.2. Observed and RSM, RSM/LSM forecasted surface pressure (hPa) at buoy station 51002 valid at (a) 0200 HST and (b) 1400 HST, and at buoy station 51003 valid at (c) 0200 HST and (d) 1400 HST. "Buoy" refers to observations and is denoted by black lines. In (a) and (c), "R12" ("RL12") and "R36" ("RL36") refer to the 12-h and 36-h forecasts by the RSM (RSM/LSM), denoted by red (yellow) lines and green (blue) lines, respectively. In (b) and (d), "R24" ("RL24") and "R48" ("RL48") refer to the 24-h and 48-h forecasts by the RSM (RSM/LSM), denoted by red (yellow) lines and green (blue) lines, respectively. The RSM and RSM/LSM runs were initialized at 1400 HST.

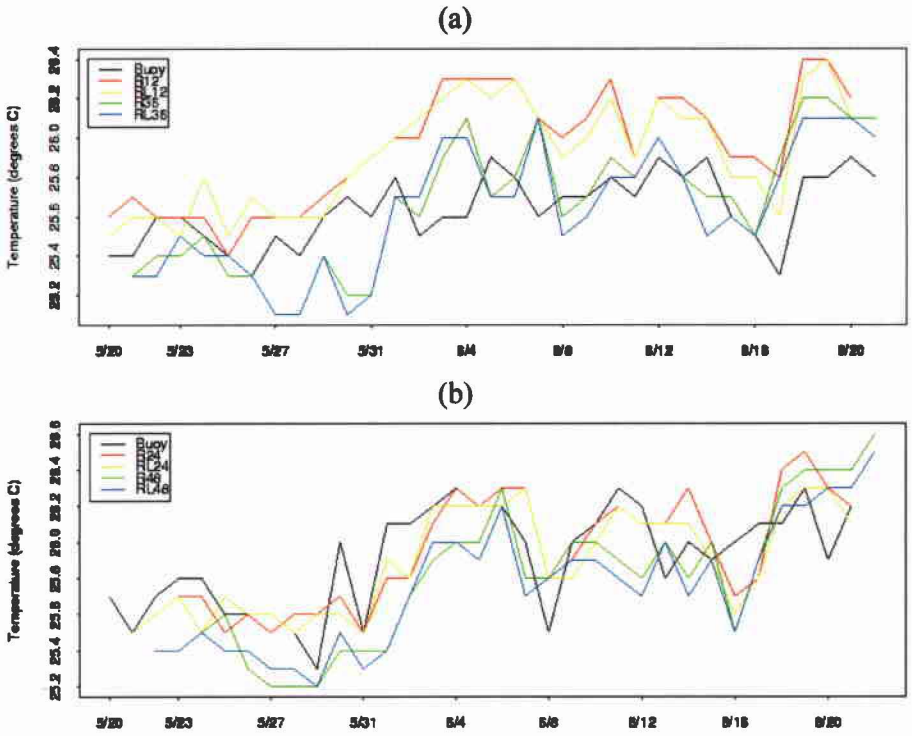

Figure 3.3. Observed and RSM, RSM/LSM forecasted 2-m temperature (°C) at buoy station 51002 valid at (a) 0200 HST and (b) 1400 HST. Legend notation as in Fig. 3.2.

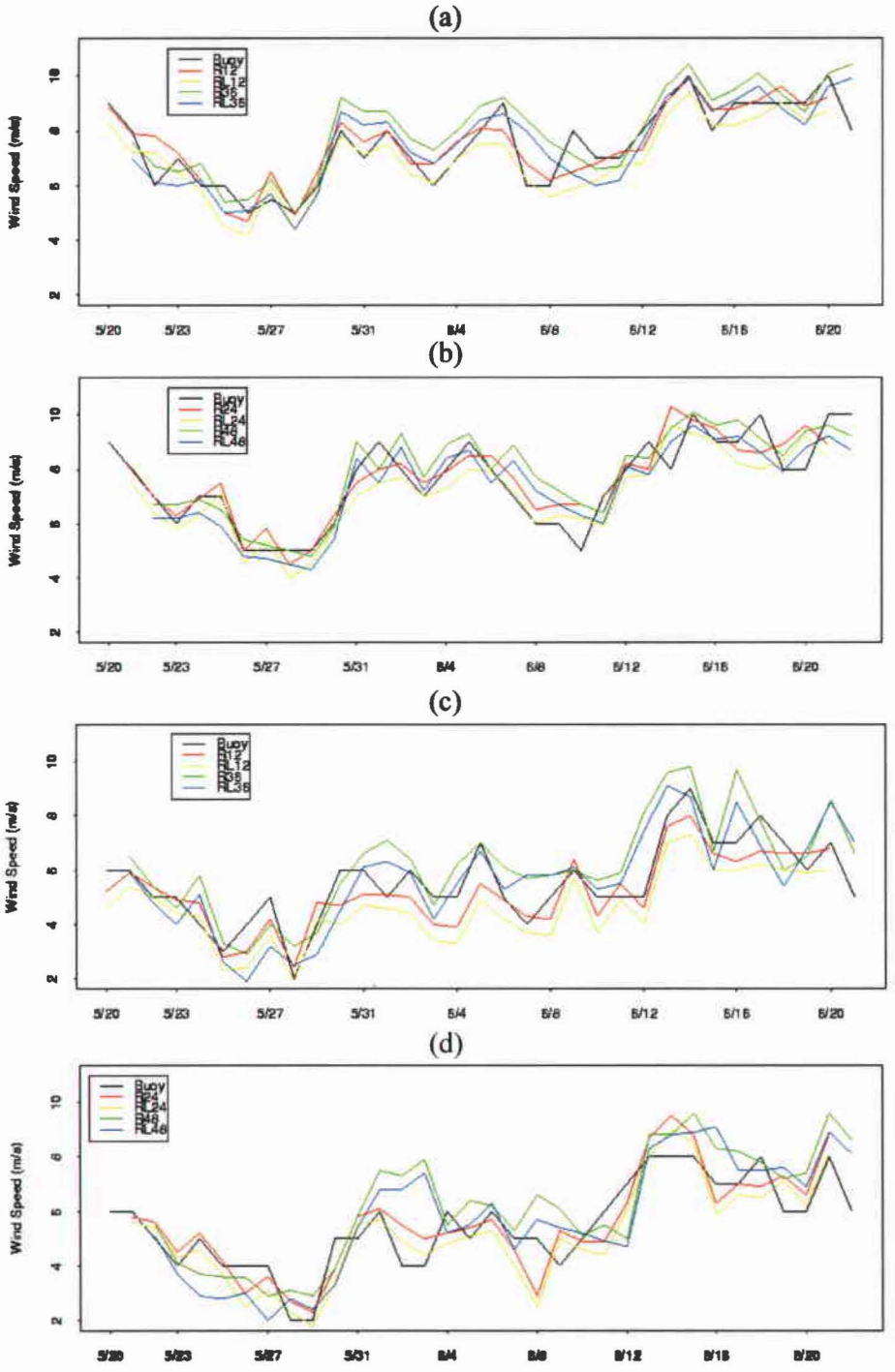

Figure 3.4. As in Fig. 3.2 except for 10-m wind speed (m s^{-1}).

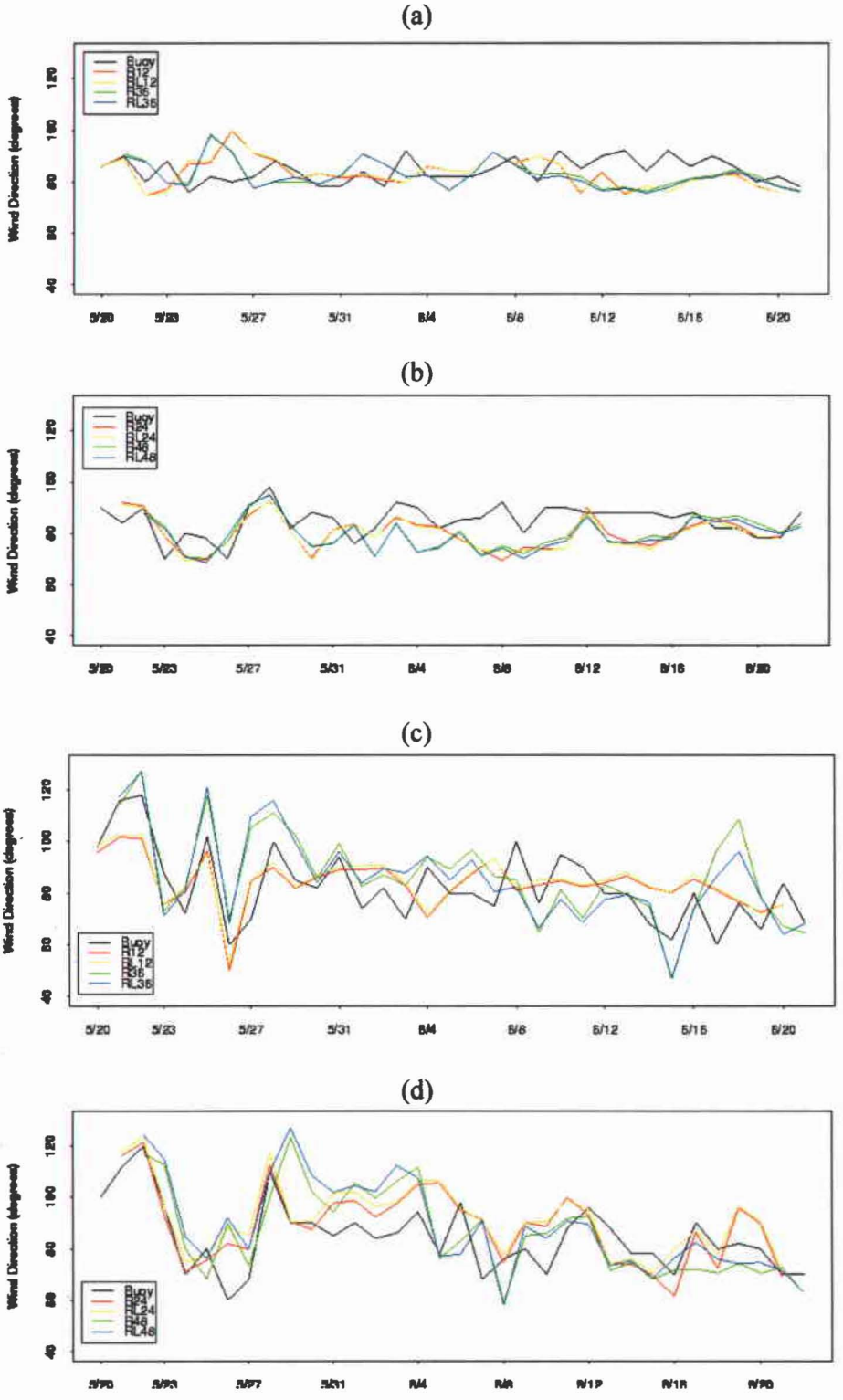

Figure 3.5. As in Fig. 3.2 except for 10-m wind direction (degrees).

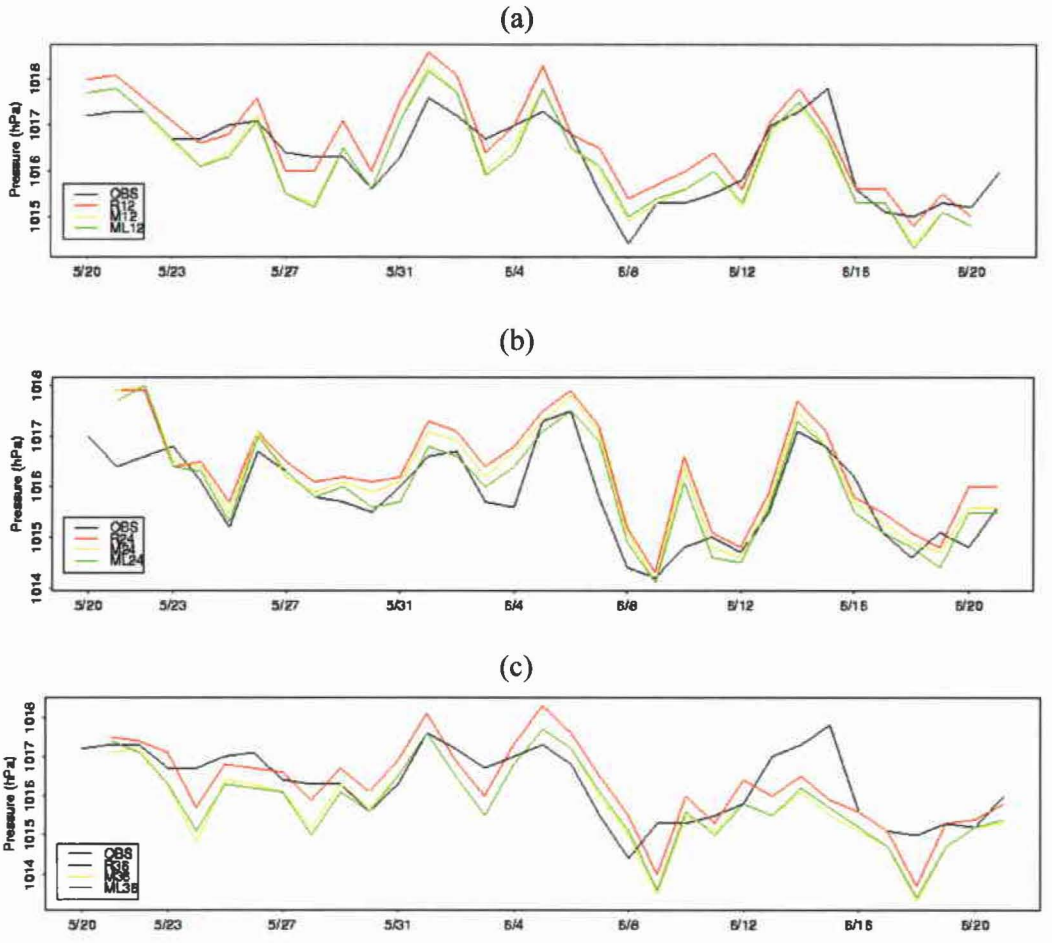

Figure 3.6. Observed and RSM, MSM and MSM/LSM forecasted sea level pressure (hPa) at PHNL valid at (a) 0200 HST (12-h model forecast), (b) 1400 HST (24-h model forecast), and (c) 0200 HST (36-h model forecast). "OBS" refers to observations and is denoted by black lines. "R12" ("M12", "ML12"), "R24" ("M24", "ML24"), and "R36" ("M36", "ML36") refer to the 12-h, 24-h, and 36-h forecasts by the RSM (MSM, MSM/LSM), respectively. "R12", "R24" and "R36" are denoted by red lines. "M12", "M24" and "M36" are denoted by yellow lines. "ML12", "ML24" and "ML36" are denoted by green lines. The RSM, MSM and MSM/LSM runs were initialized at 1400 HST.

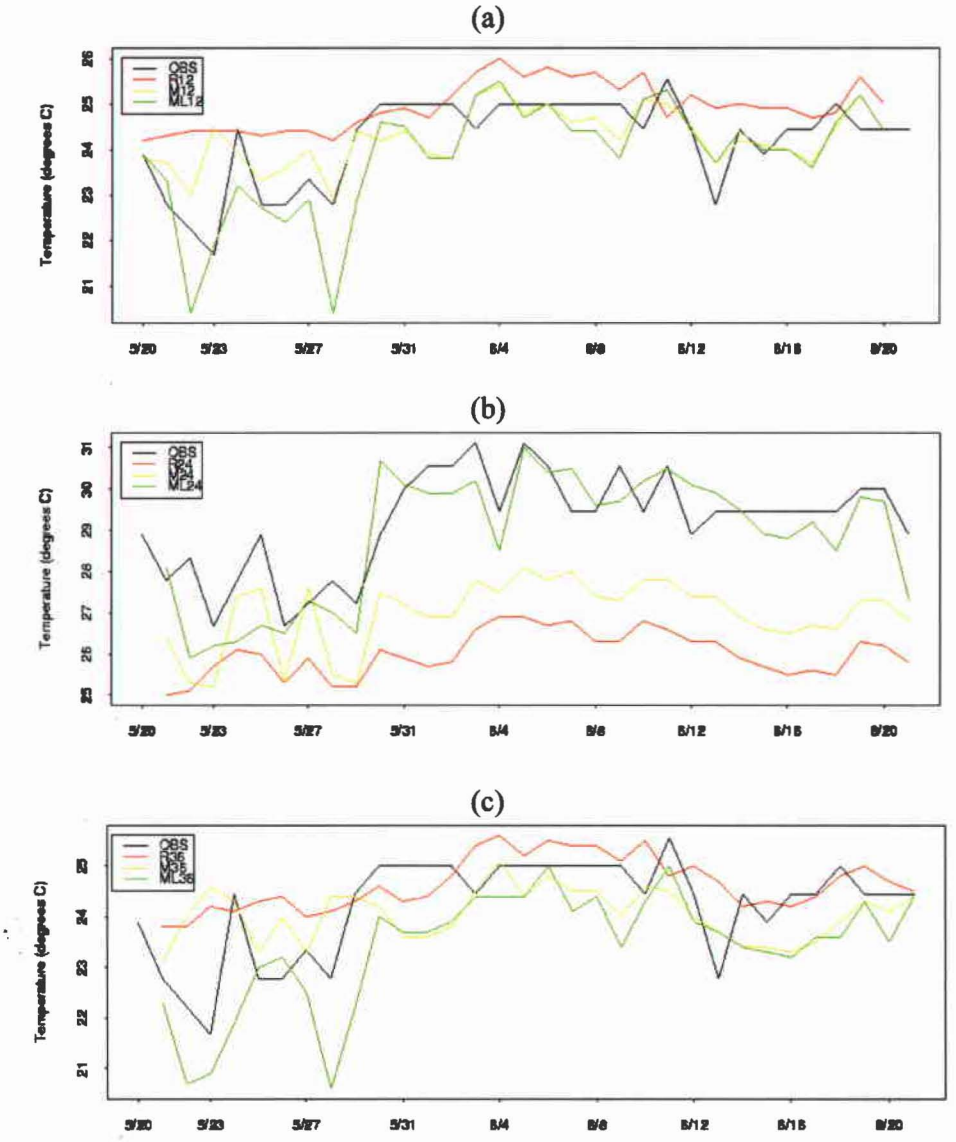

Figure 3.7. As in Fig. 3.6 except for 2-m temperature (°C).

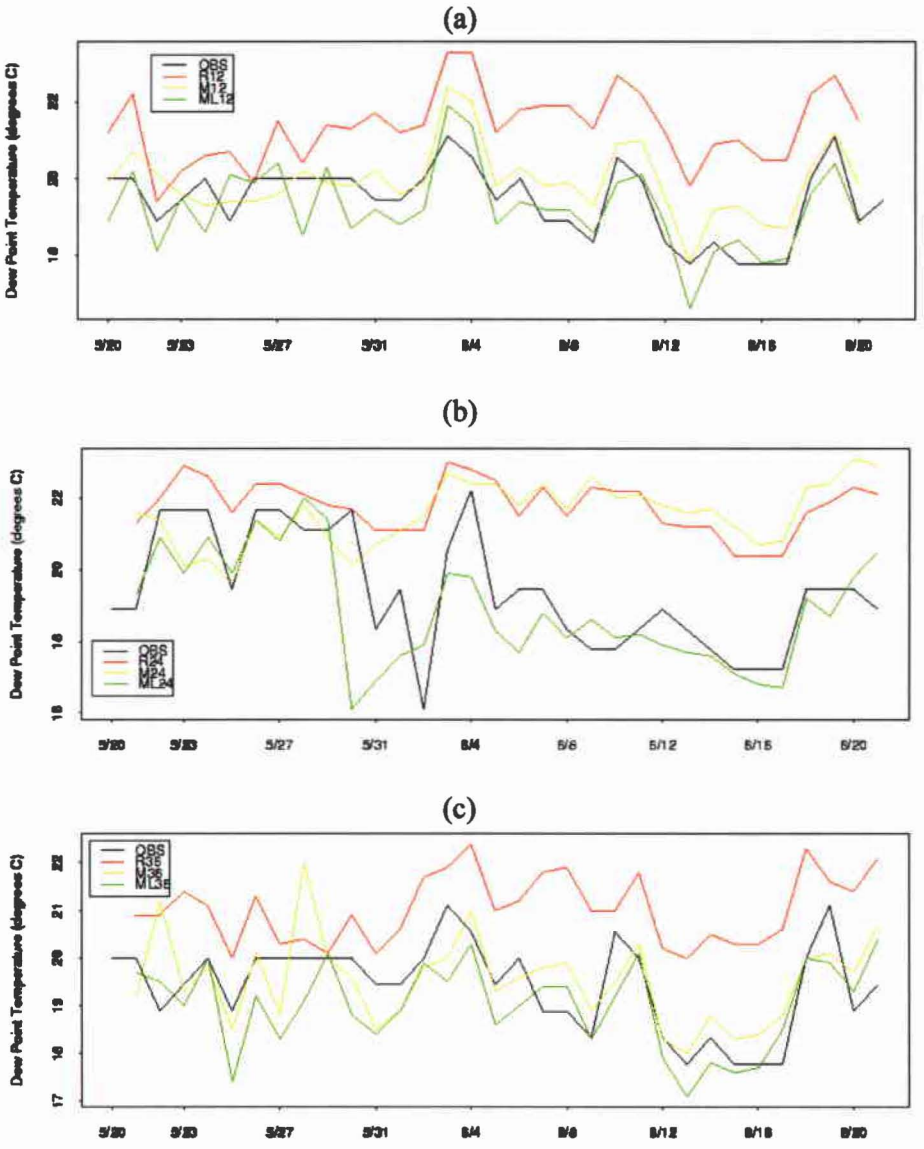

Figure 3.8. As in Fig. 3.6 except for 2-m dew point temperature (°C).

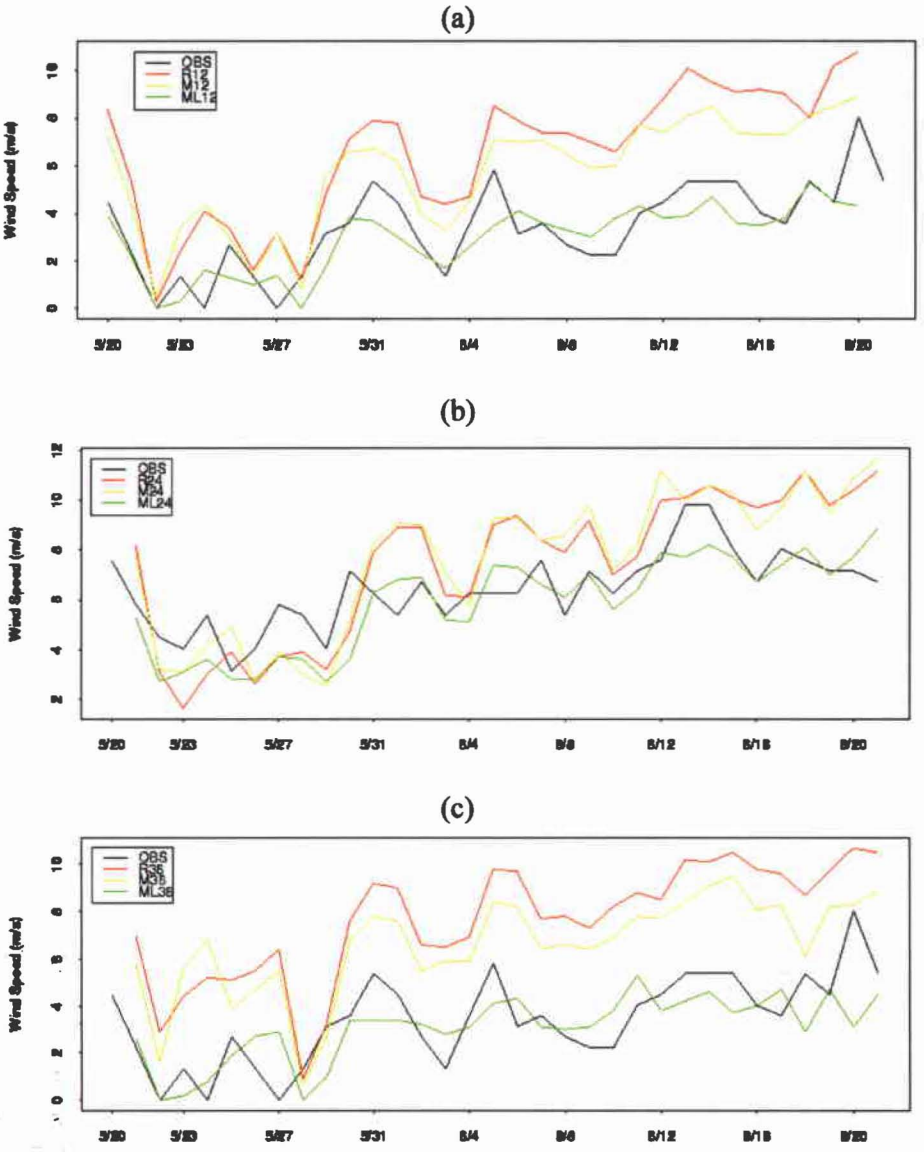

Figure 3.9. As in Fig. 3.6 except for 10-m wind speed (m s^{-1}).

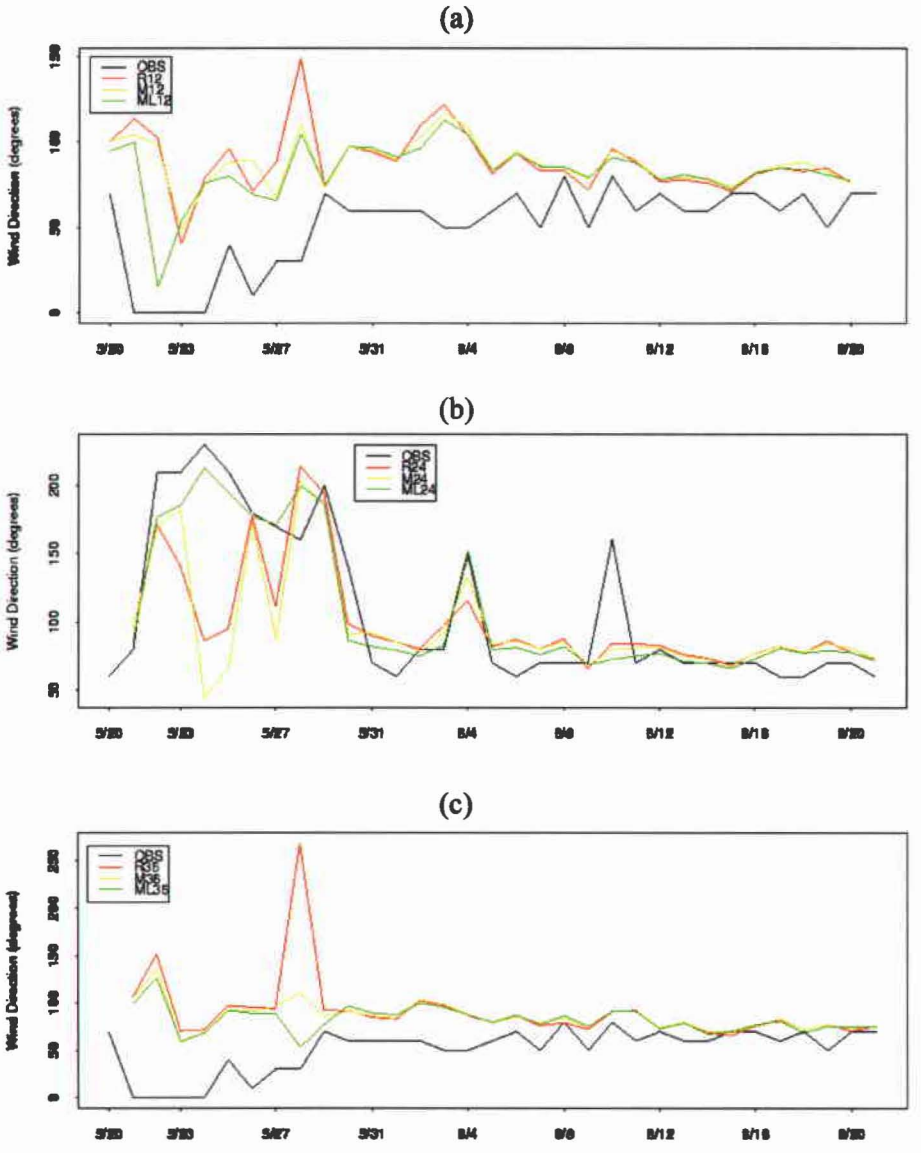

Figure 3.10. As in Fig. 3.6 except for 10-m wind direction (degrees).

(a)

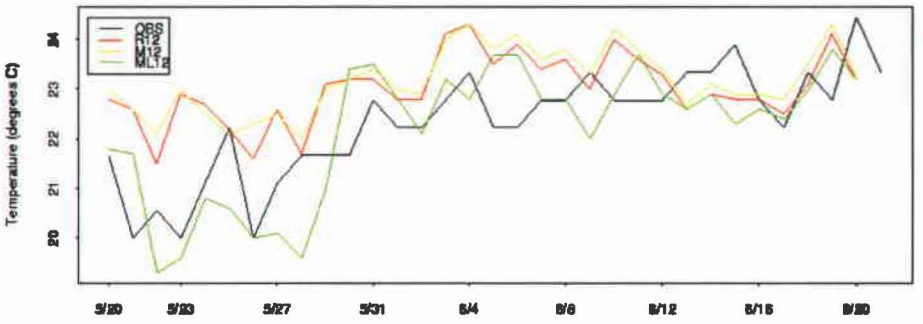

(b)

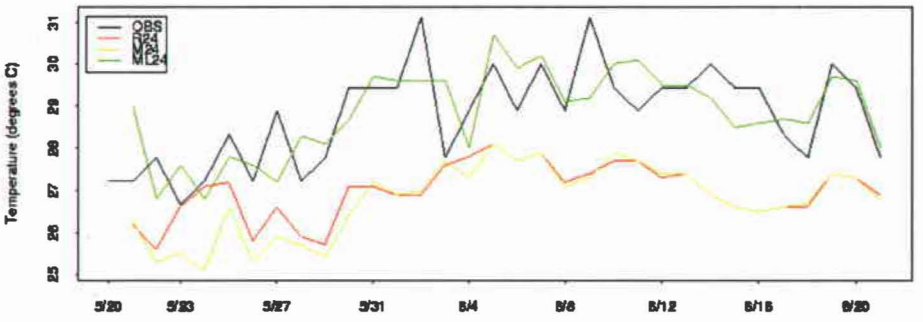

(c)

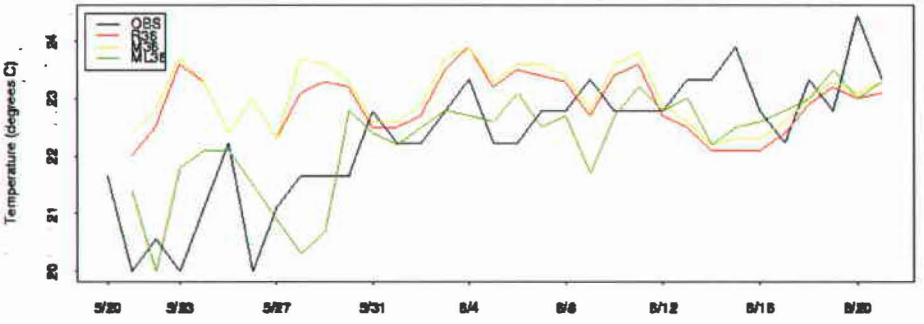

Figure 3.11. As in Fig. 3.7 except at PHJR.

(a)

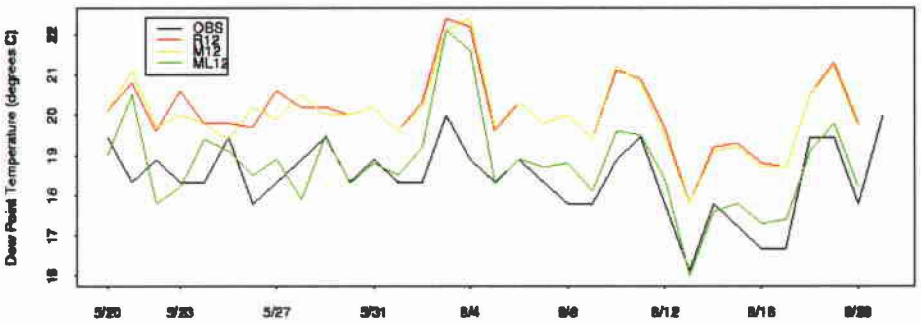

(b)

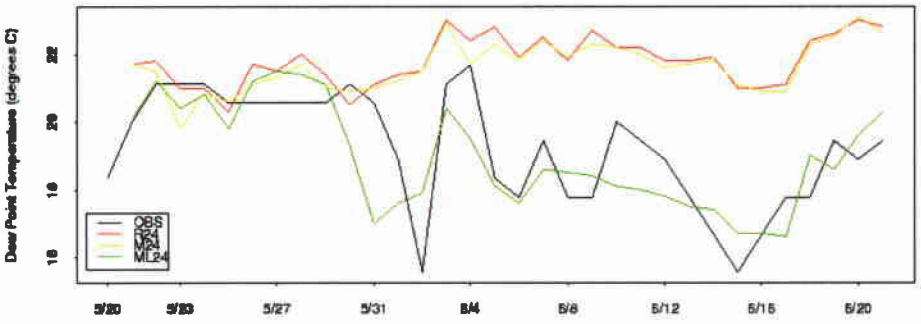

(c)

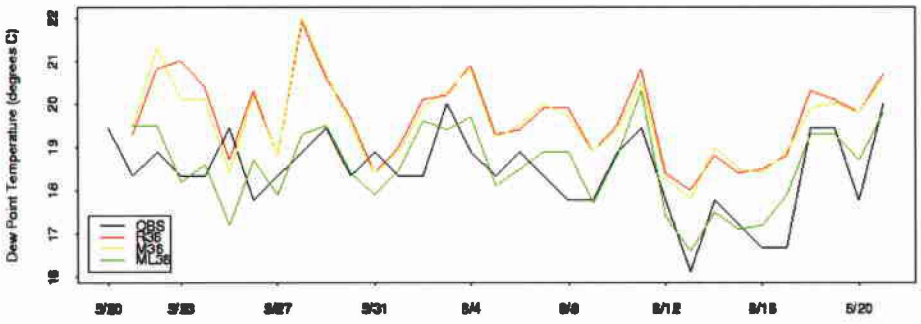

Figure 3.12. As in Fig. 3.8 except at PHJR.

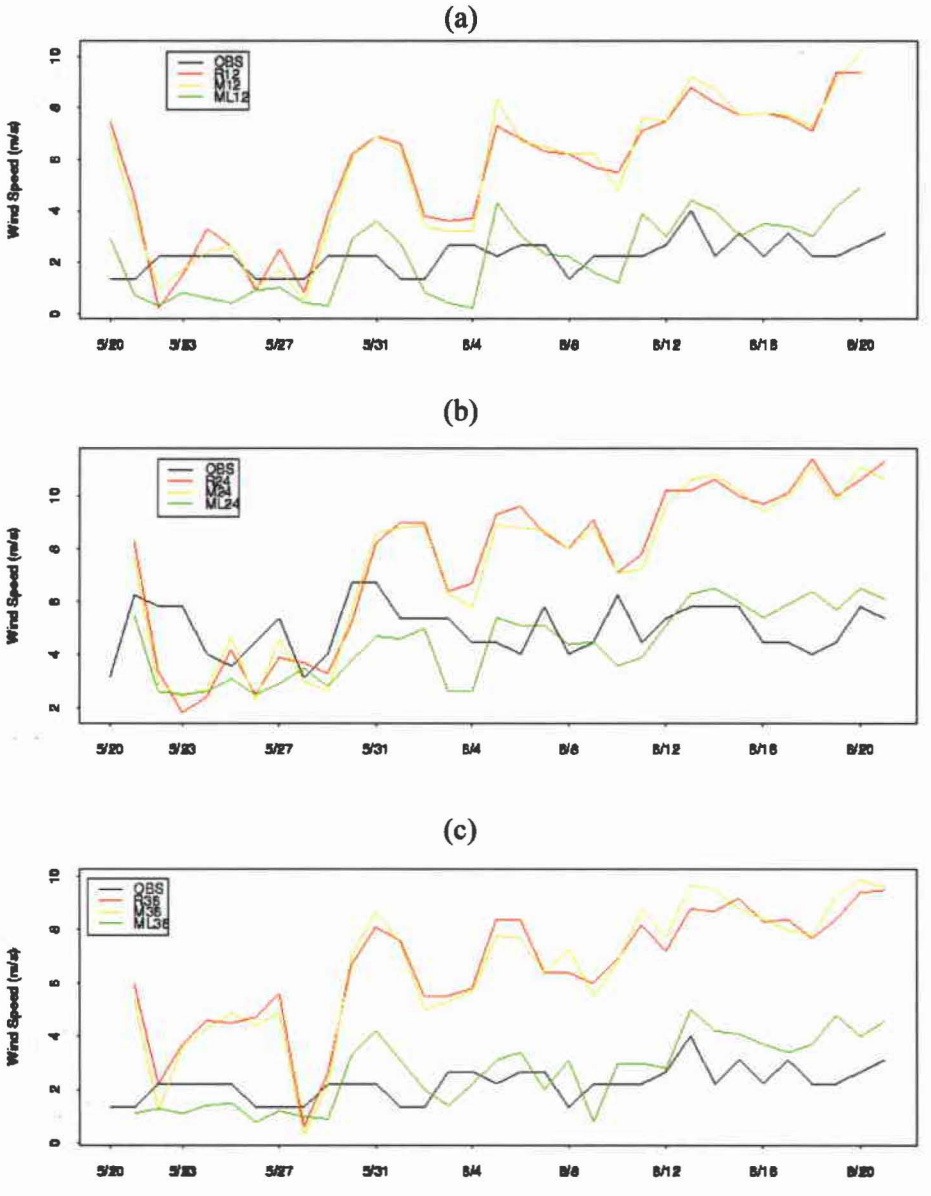

Figure 3.13. As in Fig. 3.9 except at PHJR.

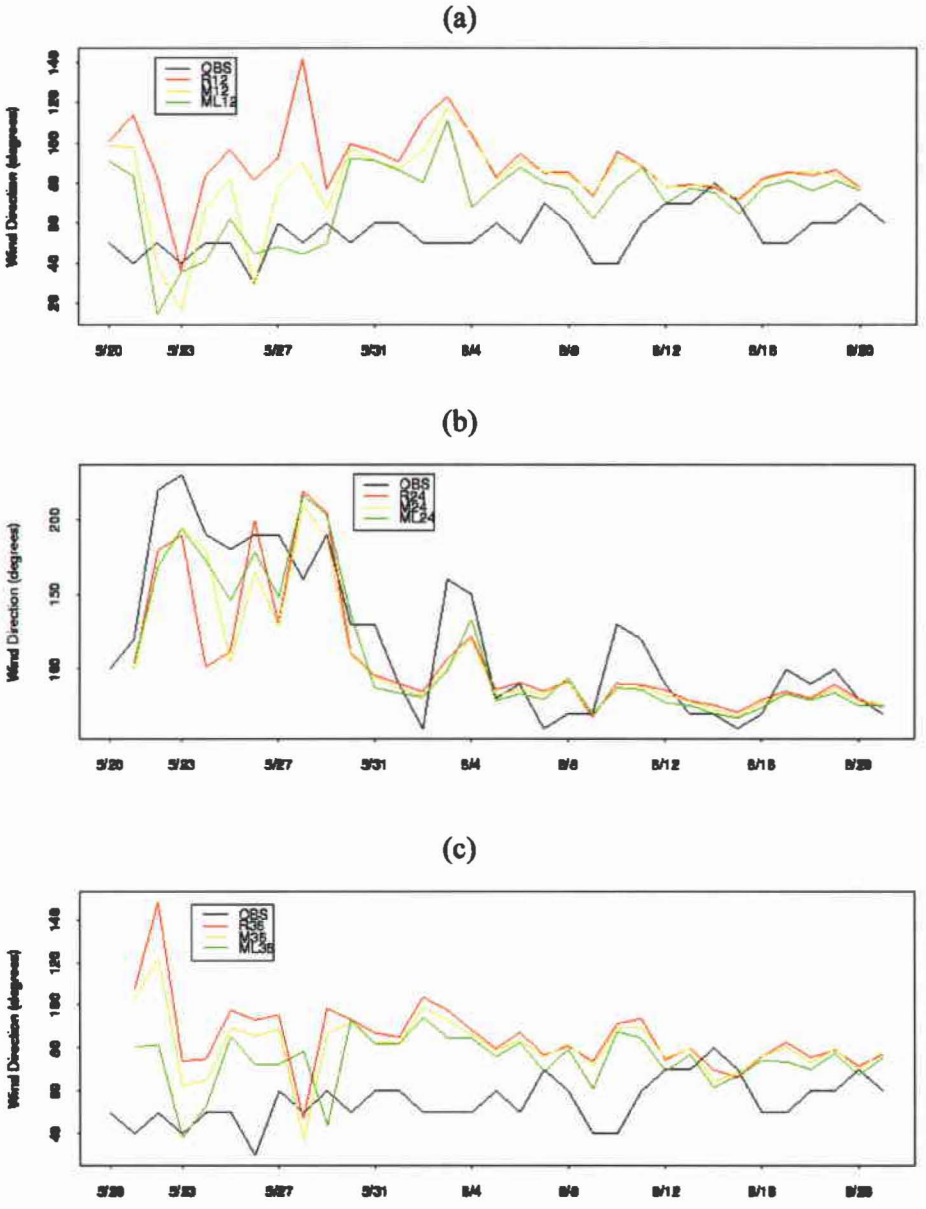

Figure 3.14. As in Fig. 3.10 except at PHJR.

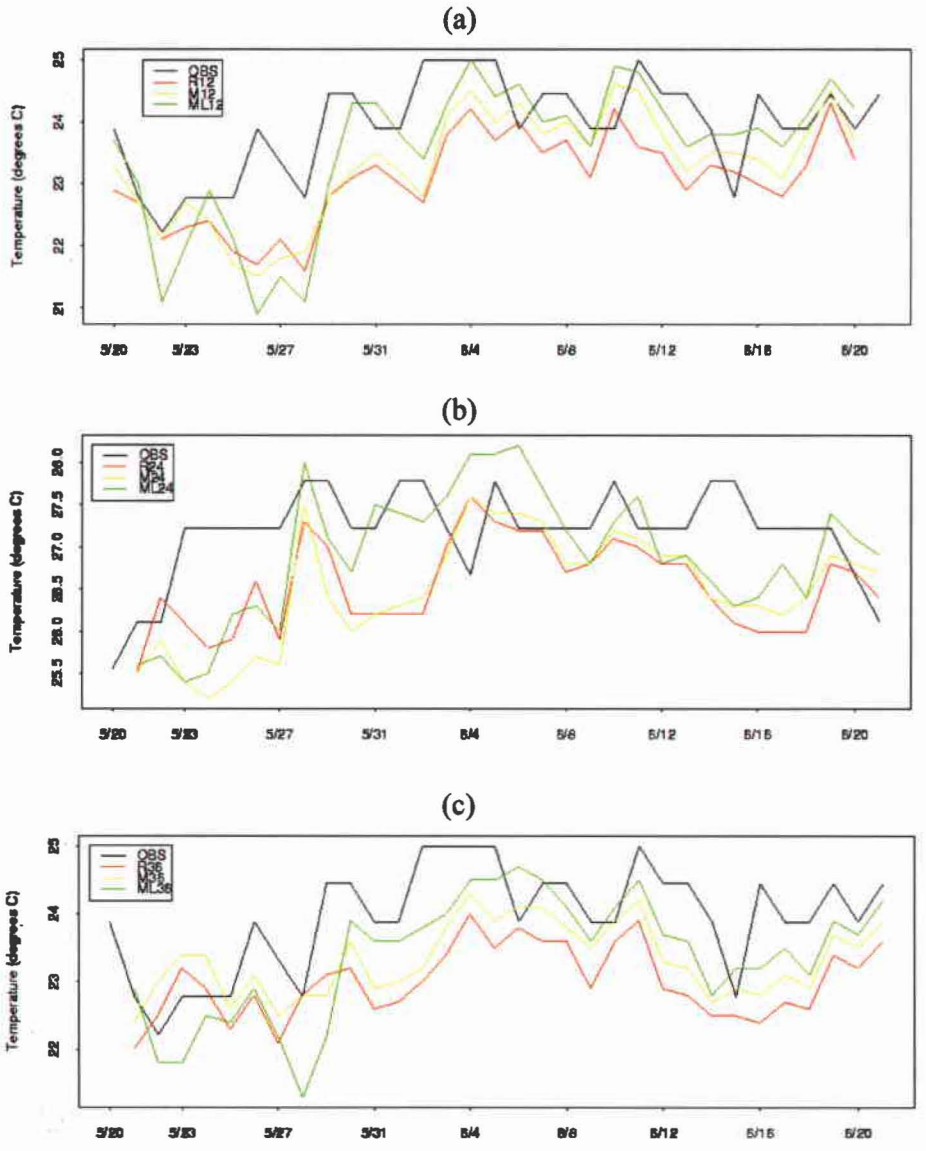

Figure 3.15. As in Fig. 3.7 except at PHNG.

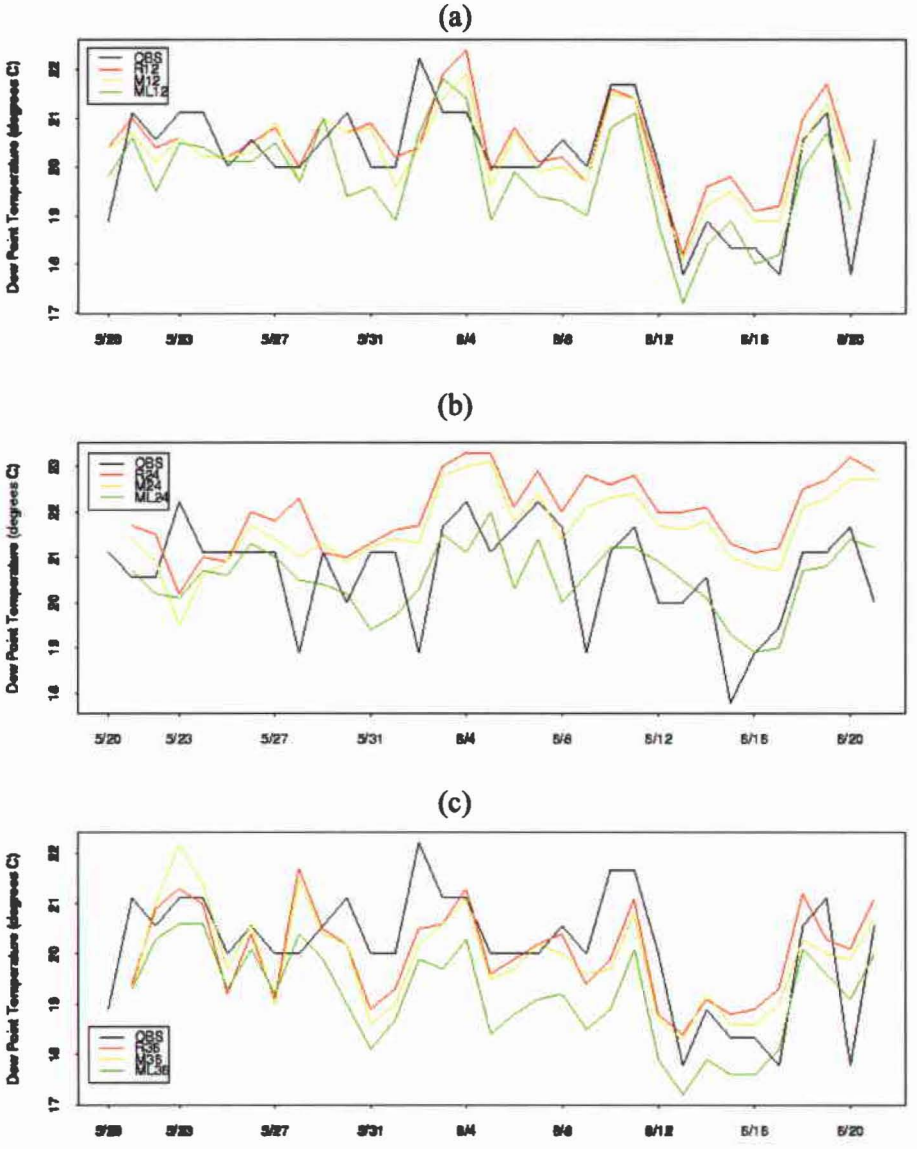

Figure 3.16. As in Fig. 3.8 except at PHNG.

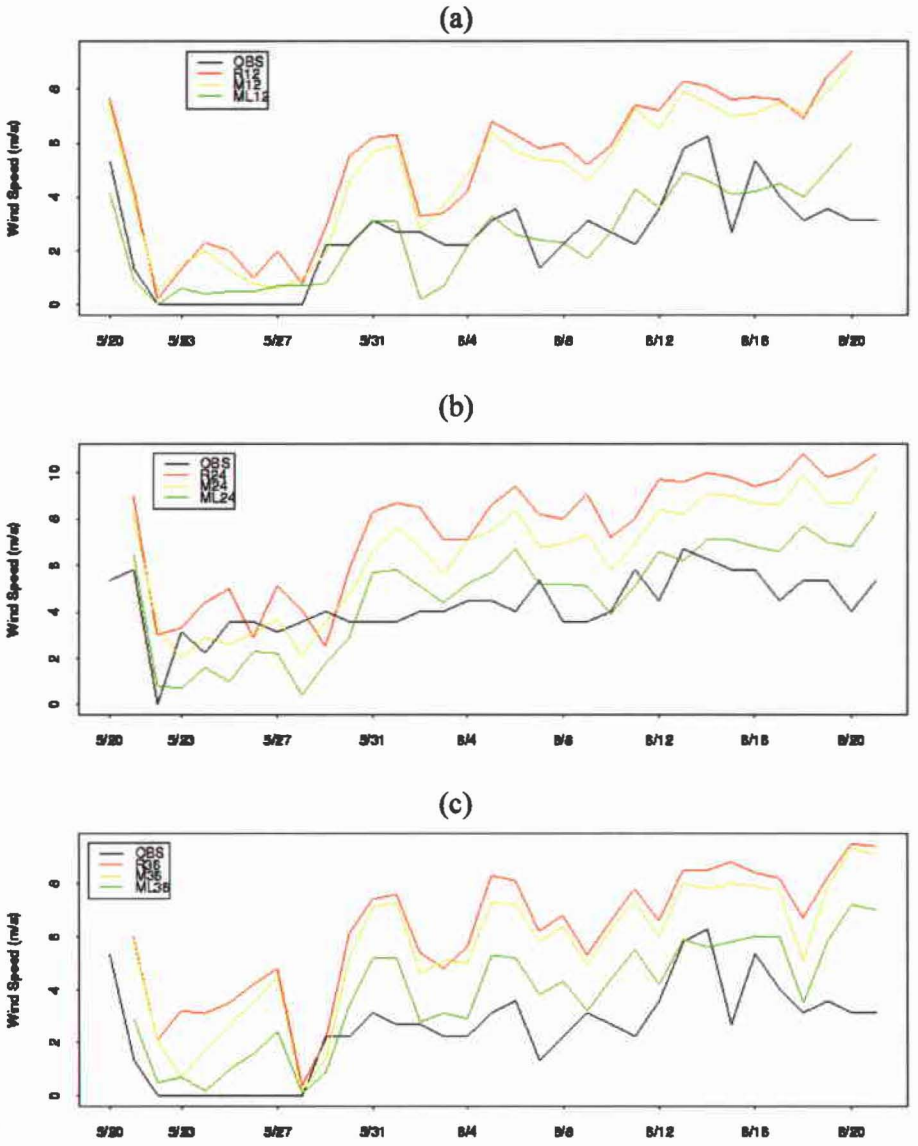

Figure 3.17. As in Fig. 3.9 except at PHNG.

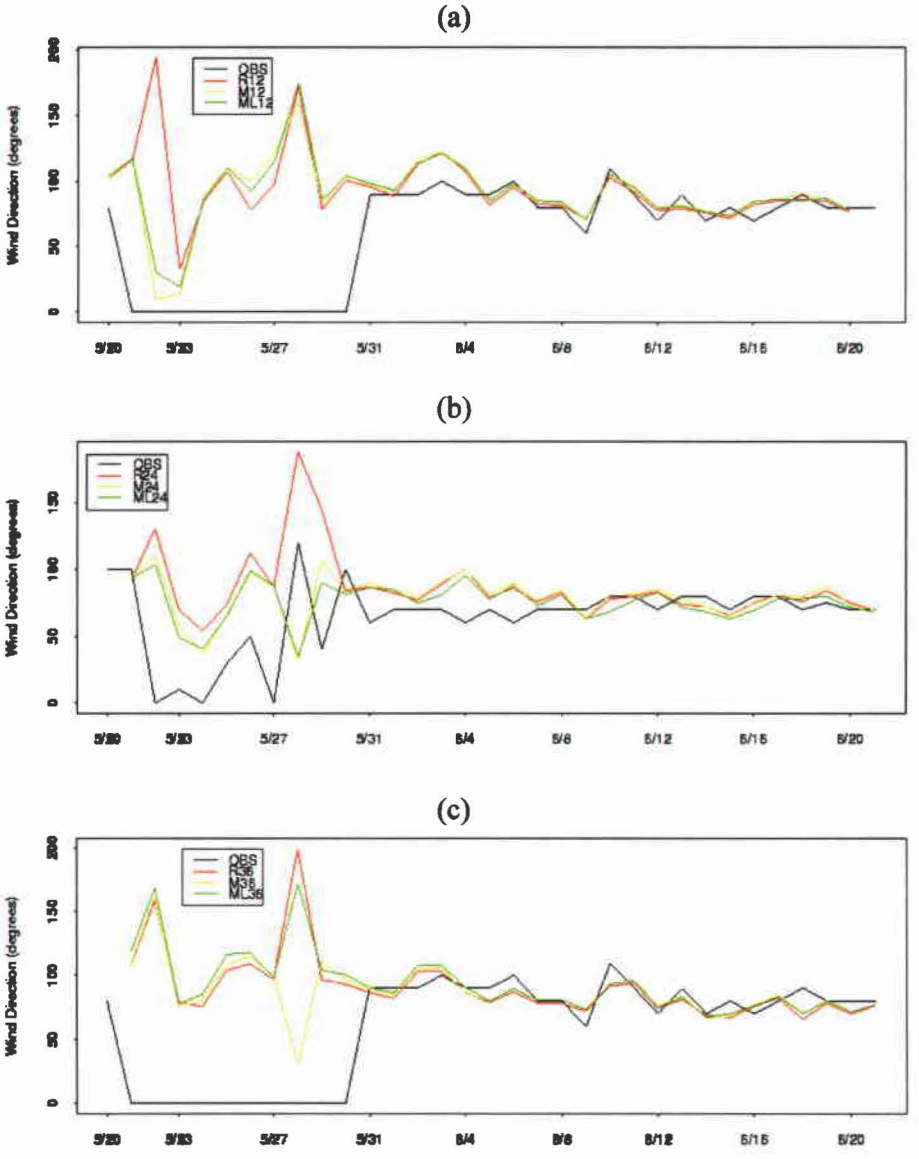

Figure 3.18. As in Fig. 3.10 except at PHNG.

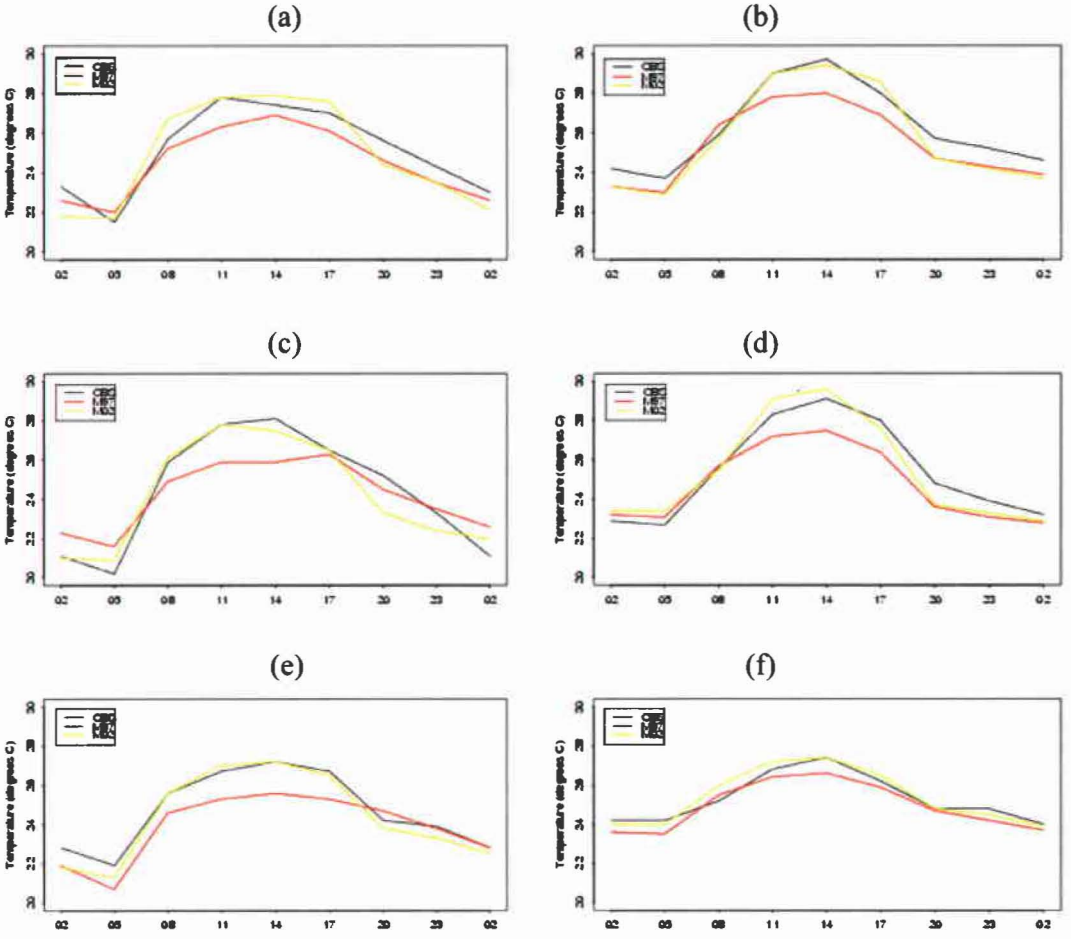

Figure 3.19. Observed, MSM and MSM/LSM composite diurnal cycles of 2-m temperature (°C) at PHNL (a, b), PHJR (c, d), and PHNG (e, f) during the weak trade wind days (left column) and the strong trade wind days (right column). "OBS" refers to observations (black lines); "M97" refers to the uncoupled MSM forecasts (red lines); and "M02" refers to the coupled MSM/LSM forecasts (yellow lines). Time is in HST. The MSM and MSM/LSM runs were initialized at 1400 HST. Selection of weak and strong trade wind days is described in the text.

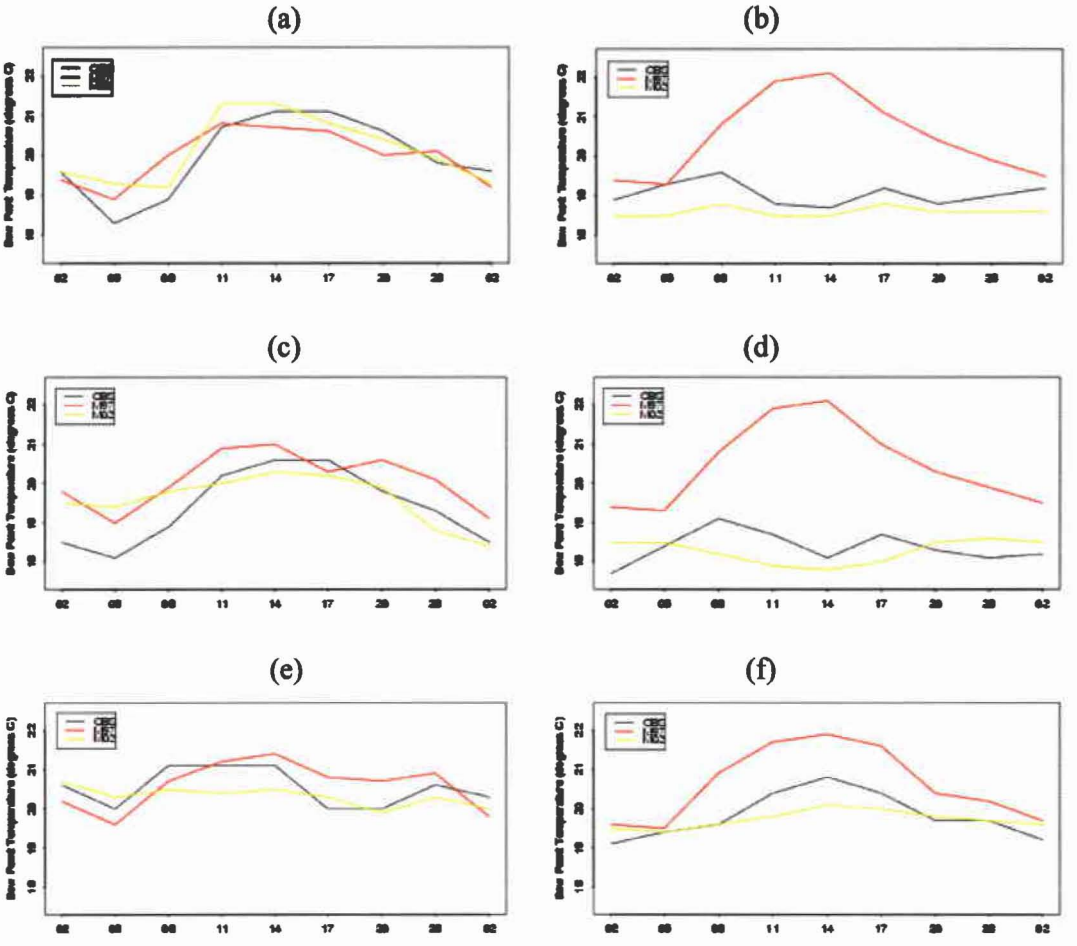

Figure 3.20. As in Fig. 3.19 except for 2-m dew point temperature (°C).

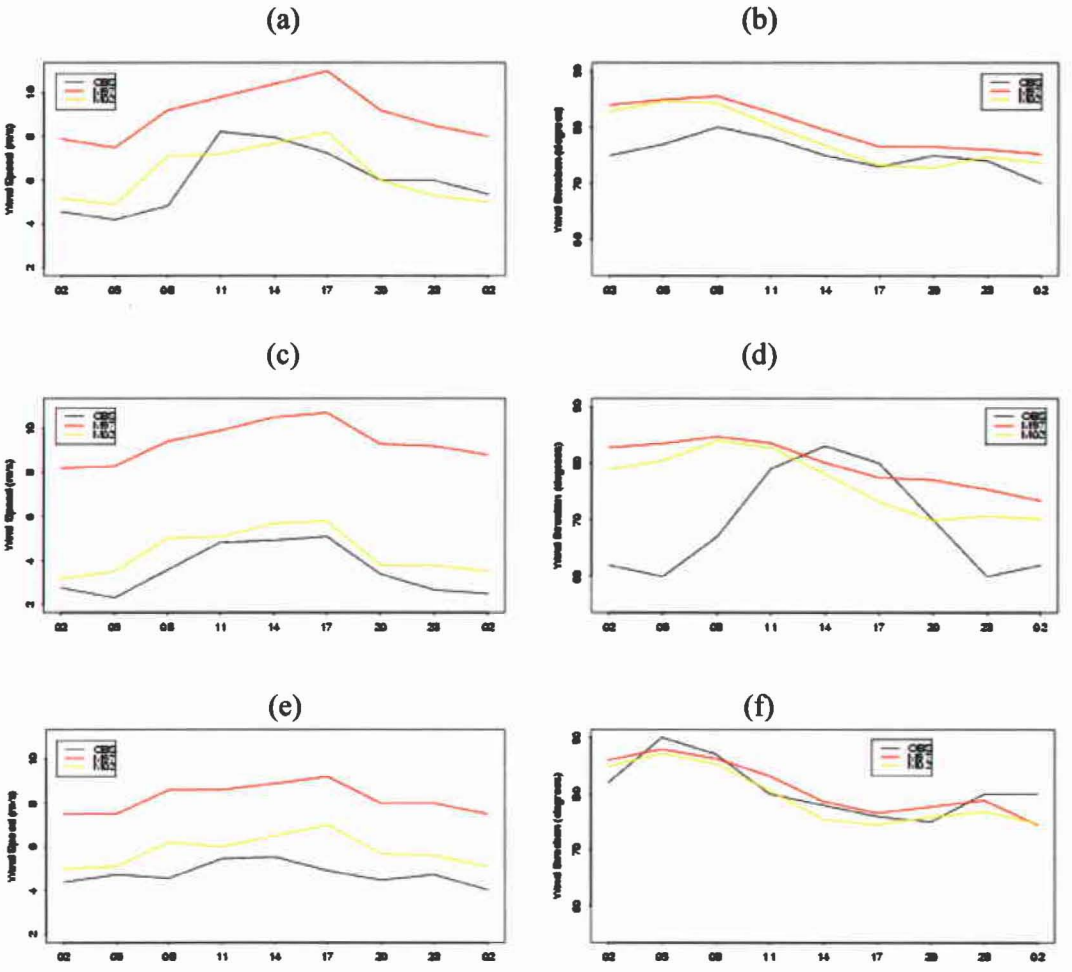

Figure 3.21. Observed and MSM, MSM/LSM simulated composite diurnal cycles of 10-m wind speed (m s^{-1}, left column) and 10-m wind direction (degrees, right column) at PHNL (a, b), PHJR (c, d), and PHNG (e, f) during the strong trade wind days. The legend as in Fig. 3.19.

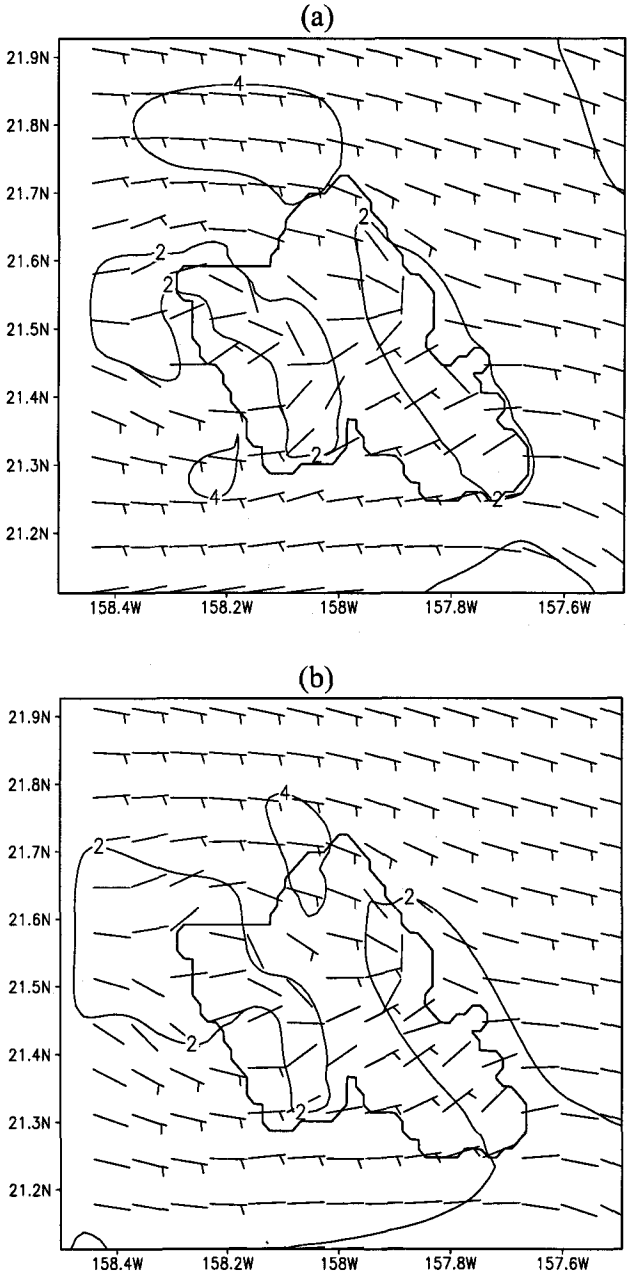

Figure 3.22. Composite horizontal maps of 10-m wind (m s^{-1}) in the Oahu domain forecasted by (a) the MSM/LSM and (b) the MSM valid at 0500 HST (15-h model forecasts) for the weak trade wind days. The MSM/LSM and MSM runs were initialized at 1400 HST the previous day. Isotachs are drawn every 2 m s^{-1}. The half barb and full barb denotes 5 m s^{-1} and 10 m s^{-1}, respectively.

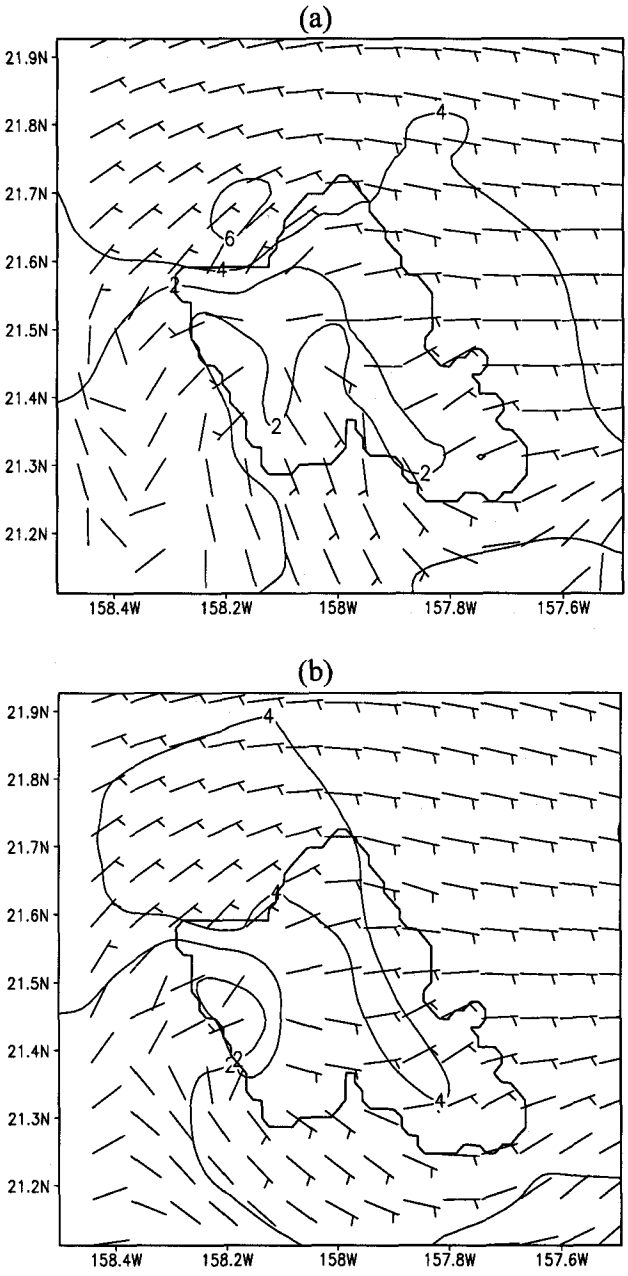

Figure 3.23. As in Fig. 3.22 but for the 24-h model forecasts valid at 1400 HST.

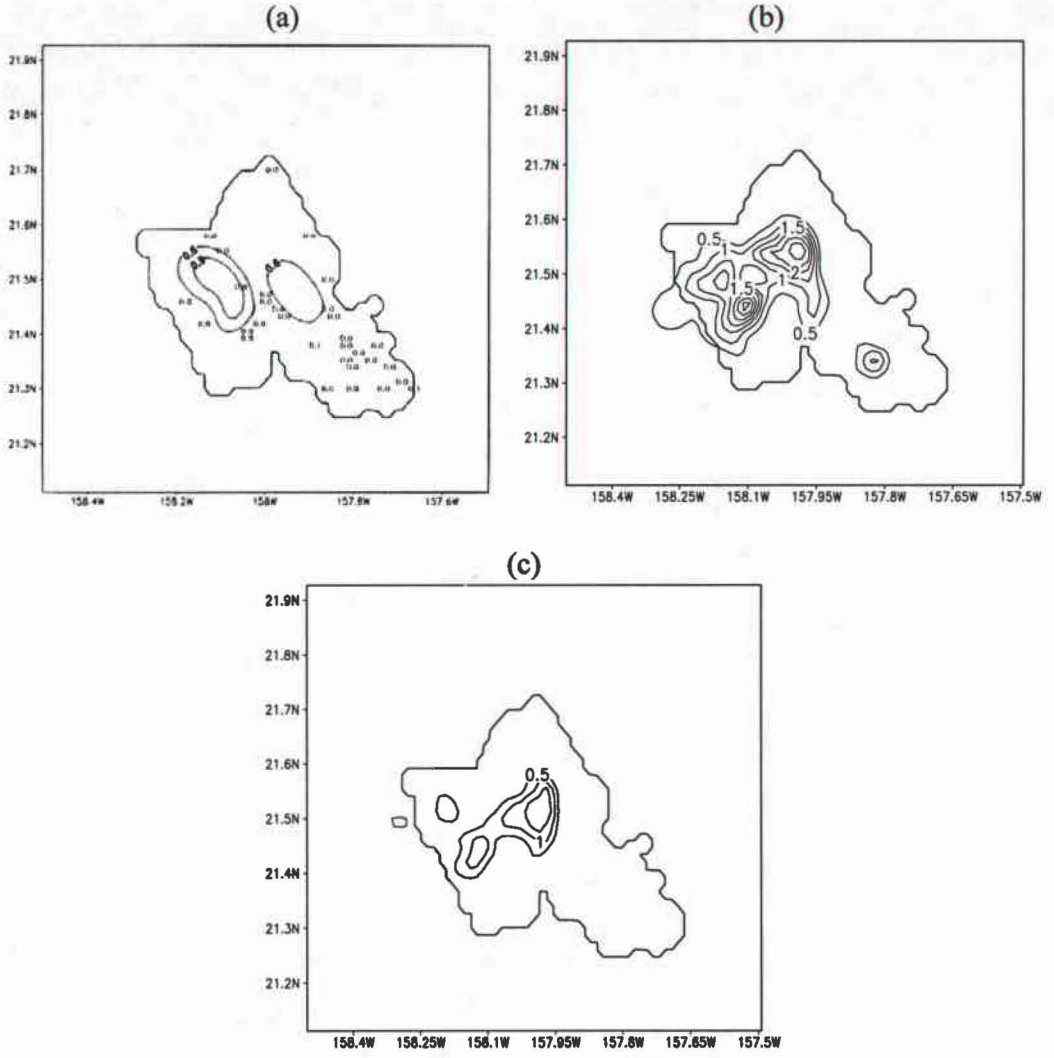

Figure 3.24. Composite horizontal maps of 6-h accumulated rainfall (mm) for the afternoon period of 1100 HST – 1700 HST from (a) observations, (b) MSM/LSM forecasts, and (c) MSM forecasts for the weak trade wind days. The MSM/LSM and MSM runs were initialized at 1400 HST the previous day. Contour interval is 0.3 mm in (a) and 0.5 mm in both (b) and (c). Station values are also included in (a).

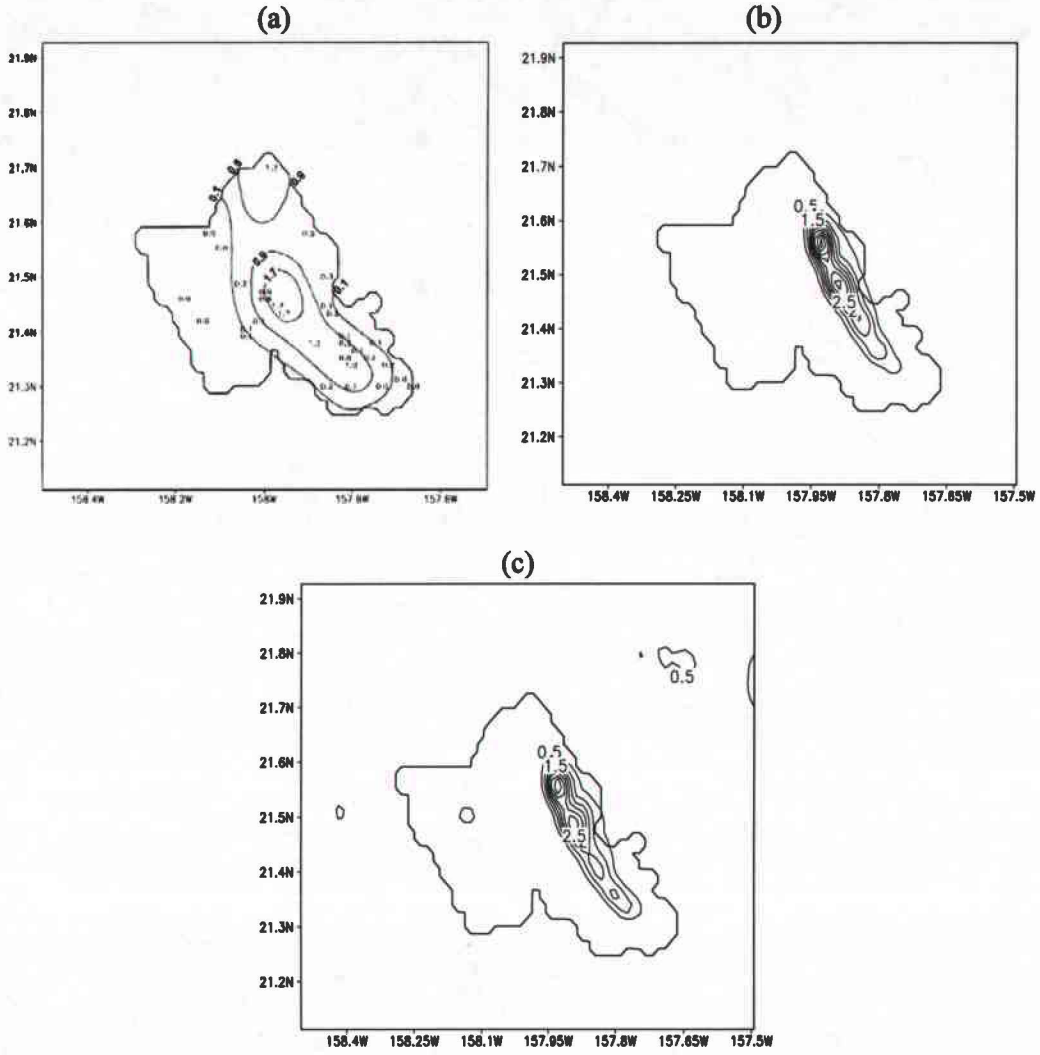

Figure 3.25. As in Fig. 3.24 except for the morning period of 0200 HST – 0800 HST for the strong trade wind days. Contour interval is 0.8 mm in (a) and 0.5 mm in both (b) and (c).

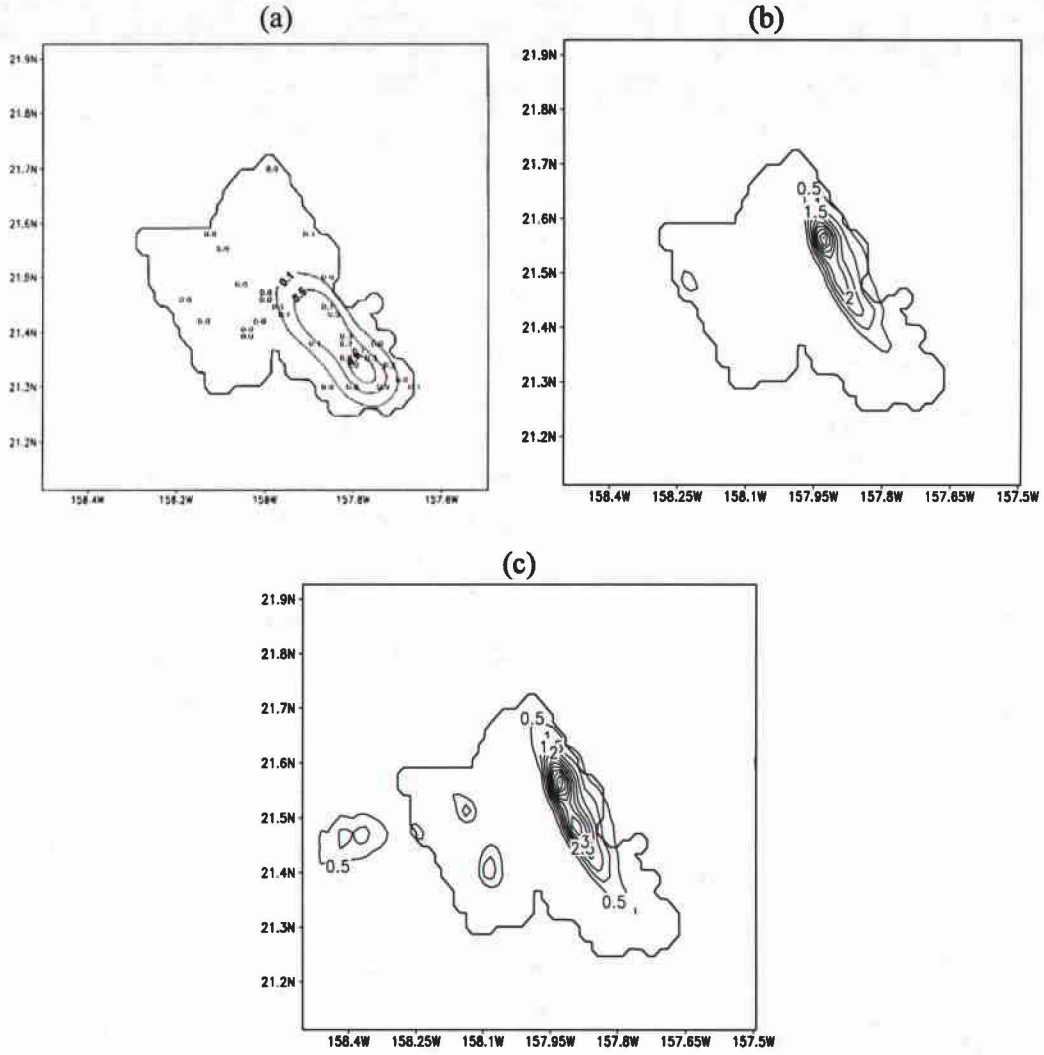

Figure 3.26. As in Fig. 3.24 except for the strong trade wind days. Contour interval is 0.4 mm in (a) and 0.5 mm in both (b) and (c).

CHAPTER 4

Sea breeze simulations over northwest Hawaii

4.1 Introduction

Sea- and land-breeze circulations are frequent phenomena over the Hawaiian Islands (Leopold 1949; Eber 1957; Lavoie 1967; Mendonca 1969; Garrett 1980; Schroeder 1981; Chen and Nash 1994; Wang and Chen 1995; Austin et al. 1996; Carbone et al. 1998; Yang and Chen 2003). As mentioned before, these thermally driven diurnal circulations may contribute to rainfall by reinforcing trade-wind orographic lifting (Garrett 1980), generating areas of low-level convergence when interacting with the prevailing trade winds (Leopold 1949, and the others), or initiating orographic lifting of onshore flow in areas not exposed to trade winds (Yang and Chen 2003). The cloud and precipitation patterns developed by these diurnal circulations are important local weather, and can affect local temperatures, humidity, and rainfall. Local rainshowers also affect the surface airflow (Chen and Wang 1994; Wang and Chen 1995; Carbone et al. 1995, 1998). Such local weather must be taken into account during the forecast process. The ability of these thermally driven circulations to trap and distribute pollutants from agricultural burning (Schroeder 1993) or volcanic smog (Hollingshead et al. 2003) also makes them a feature of importance to forecasters.

The global model output distributed by NCEP is too coarse to resolve the local circulations in Hawaii (Kodama and Businger 1998). Wang et al. (1998) examined the operational NCEP RSM (Juang and Kanamitsu 1994) simulations at a 10-km resolution

in resolving mesoscale weather over the Hawaiian Islands. They noted that while the RSM showed significant improvement over the NCEP global model in forecasting the local weather, there were still large discrepancies between the RSM simulations and observations. They went on to suggest that higher resolutions ($\leq$ 3 km) and nonhydrostatic models are needed to resolve the local circulations resulting from the effects of orography. As computational resources have now become cheaper and more powerful, it is highly desirable to use a high-resolution mesoscale model to explore the feasibility of high resolution guidance in improving local weather forecasting. In doing this, the very important first step is to examine the performance of high-resolution models in representing the local circulations such as the sea breeze.

To date, there have been no comprehensive simulations of the sea breezes over the Hawaiian Islands. Lavoie (1974) performed the first numerical simulation of trade wind weather on Oahu with 3 km × 3 km horizontal grids. He proposed that his model was able to simulate the sea breezes although there were no observations presented alongside to confirm. Smolarkiewicz et al. (1988), Rasmussen et al. (1989), and Rasmussen and Smolarkiewicz (1993) investigated the dynamics of the Hawaiian cloud bands using a numerical model in conjunction with observational analyses. Their focuses were on the formation and development of the cloud bands upstream of the Big Island. Recent modeling work (Chen and Feng 2001; Feng and Chen 2001) studied the effects of the diurnal heating cycle on airflow and cloud distributions over the Big Island. They were concerned mainly with the offshore cloud lines and nocturnal flow regime without extending to the simulations of the sea breezes.

Schroeder (1981) examined meteorological data collected during the period 23-28 June 1978 at six stations arranged in a nearly linear transection extending from the coast at Anaehoomalu to Waimea Airport, 25 km inland and 800 m higher over the northwestern part of the Big Island (Fig. 4.1). This experiment is likely the only one over the Hawaiian Islands that provides a detailed portrayal of the sea breezes along a nearly linear transection. Three different types of sea breeze development were identified: (1) short-lived afternoon sea breezes that barely advance inland against strong trade winds, (2) longer lasting sea breezes which appear in mid-morning and persist through the afternoon, and (3) sea breezes that develop inland past 300 m mean sea level (MSL). Schroeder (1981) further suggested that sea breeze variability is related to both synoptic-scale clouds and winds and to the thermal properties of the underlying surface along the transection. These three types of sea breeze development are typical sea breeze scenarios over the Hawaiian Islands, though variations in duration and wind speeds can be encountered in various parts of the island chain. Using aircraft data and portable automated mesonet (PAM) data, Yang and Chen (2003a) studied the circulation and rainfall on the lee side of the Big Island during the Hawaiian Rainband Project (HaRP). They noted that because of the presence of opposing trade winds the sea-breeze duration in the northwestern and southwestern leeside areas of the island is short compared to the central leeside coast (e.g., Kona coast; see Fig. 2.1c).

Over the northwestern part of the Big Island, the Kohala mountains, the Waimea Saddle, and the Mauna Kea mountain are located. The Waimea Saddle is one of the windiest places in Hawaii (Ramage 1979) while thermally driven circulations prevail on the leeside of the Kohala and Mauna Kea mountains (Chen and Nash 1994). It appears

that a constant battle is going on in that region between the strong winds out of the Waimea Saddle and the thermally driven sea breezes. How far the sea breezes can penetrate inland depends not only on synoptic winds but also on the strength of the Waimea Saddle winds. The farther the sea breezes advance, the more precipitation they will likely produce in that normally dry region. Temperature and humidity distributions are also intriguing in that region, too. When the downslope winds out of the Waimea Saddle are strong, adiabatic warming and evaporation in association with the descending flow would be enhanced (Chen and Wang 1994). This will result in relatively higher surface air temperature and lower humidity along the lowland. On the other hand, when the downslope winds out of the Waimea Saddle are weak, surface air temperature would be lower and humidity would be higher along the lowland when compared to the days with strong winds. These features suggest that the northwestern part of the Big Island is a good testing area for the performance of mesoscale models in resolving the intriguing local weather.

This chapter re-visits Schroeder's (1981) sea-breeze cases using the NCEP Mesoscale Spectral Model (MSM) (Juang 2000) coupled with the modified Oregon State University Land Surface Model (LSM) originally developed by Pan and Mahrt (1987) (Chen et al. 1996; Chen and Dudhia 2001). The questions we would like to address are (1) can the coupled MSM/LSM reproduce these three types of sea breeze development identified in Schroeder (1981) and (2) to what extent do the surface thermal properties influence the simulated sea breeze characteristics?

The rest of the chapter is organized as follows. Section 4.2 contains a brief description of the surface properties along the transection and model initialization. Model simulations

for the period of 23-28 June 1978 are examined and compared with observations in section 4.3. Conclusions and discussions are presented in section 4.4.

4.2 Surface properties along the transection and model initialization

4.2.1 Surface properties along the transection

Within the transection over northwest Big Island, unweathered lava flows dominate the coast while sparsely vegetated uplands support some livestock grazing (Schroeder 1981). In our compiled datasets from the USGS 1:100,000-scale Land Use Land Cover Level II data for Hawaii, vegetation types near the coast along the transection are bare soil with scattered broadleaf shrubs dominating uplands. Vegetation fraction is zero near the coast while it is small (< 10%) in the uplands. The reason for this discrepancy between our compiled datasets and the actual is that in the USGS Land Use Land Cover datasets for Hawaii, the lava rocks are categorized as barren land. The black lava rocks are dry with little or no soil moisture, low albedo, and low heat capacity as compared to barren land. Thus, using bare soil to represent the lava rocks may underestimate the daytime sensible heat fluxes over the surface covered by lava rocks.

4.2.2 Model initialization

The 3-km MSM/LSM was initialized every day at 2000 HST by the 10-km RSM/LSM simulations and was run for a 36-h simulation. The RSM/LSM boundary conditions consisted of the NCEP/NCAR reanalysis data with a 2.5° resolution. The increment hour for restart from the coarse-resolution model to the fine-resolution model (i.e., the nesting period) is 3-h from the RSM/LSM to MSM/LSM and 6-h from the reanalysis data to the RSM/LSM. The MSM/LSM data were output for every hour during 23-28 June 1978.

In order to obtain a more realistic soil moisture field, we started the RSM/LSM and MSM/LSM runs one month earlier, i.e., on 23 May 1978. From 24 May on, we used the 24-h forecasts of the previous RSM/LSM (MSM/LSM) run to provide the initial soil conditions (soil temperature and soil moisture) for new RSM/LSM (MSM/LSM) run. It is evident that the areas with smaller (larger) volumetric soil moisture content in the MSM/LSM simulations (Fig. 4.2a) correspond rather well to the climatologically drier (wetter) areas over the Molokai-Maui-Hawaii domain (Giambelluca et al. 1986). Using the 24-h simulations of the previous MSM/LSM run to provide the initial soil conditions for the one-month simulation removes excessive soil moisture (i.e., has a drying effect) especially over the areas with climatologically less rainfall (Fig. 4.2b).

4.3 Results

June 1978 typified early summer trade-wind weather. The Tropical Upper Tropospheric Trough (TUTT) (Sadler 1967) was established by 15 June (Schroeder 1981). Surface wind steadiness (defined as resultant speed/mean speed) exceeded 90% at first-order stations (Lihue on the island of Kauai; Honolulu on the island of Oahu; and Kahului on the island of Maui) (Schroeder 1981).

4.3.1 Surface winds and temperatures

In this section, the MSM/LSM simulated surface winds and temperatures during 23 June through 28 June 1978 along the transection are compared with observations from Schroeder (1981). A brief description of the synoptic-scale conditions and the observed weather along the transection for each day during the 6-day period is provided before the discussions of model simulations.

a. 23 June

A strong subtropical high was located to the north of the Hawaiian Islands at 0200 HST 23 June (Fig. 4.3) and sustained moderate trade winds over the island chain. Trade winds exceeded gale force in the uplands along the transection (Fig. 4.4a). Loose connection on direction channel at Beach contaminated the observations for this day; however, pilot balloon launches recorded weak sea breezes (1-2 m s^{-1}) at Beach that lasted briefly (Schroeder 1981). The sea breeze front barely moved ashore. Skies along the transection were nearly cloudless owing to strong subsidence on the leeward slopes in association with the strong trade winds channeling through the Waimea Saddle.

The MSM/LSM simulates weak (0.5-2 m s^{-1}) southwesterly and northwesterly onshore flow between 1100 HST and 1400 HST at Beach (Fig. 4.4b). At the other stations, consistent with the observations, moderate (~ 8 m s^{-1}) northeasterly trades channel through the Waimea Saddle and prevail for most times of the day along the transection in the model simulations. However, the model simulated trade-wind speeds are about 3-4 m s^{-1} weaker than that observed. The discrepancies are even larger (~ 8-10 m s^{-1}) especially around local noon time. The MSM/LSM runs are initialized by the NCEP/NCAR reanalysis data. As noted by Yang and Chen (2003b), the low-level winds at Hilo are strongly affected by island blocking and diurnal heating cycle. They do not represent the trade-wind flow over the open ocean. Since there are no routine soundings upstream of the Hawaiian Islands, including the Hilo wind data (see Fig. 2.1c for the location of Hilo) in the analysis would give rise to spurious weak low-level winds over Hawaii in the NCEP/NCAR reanalysis. This is indicated in the reanalysis low-level winds valid at 1400 HST 23 June (Fig. 4.5a) which shows relatively weak winds (~ 6 m s^{-1}) over the entire

Big Island. In the composite reanalysis low-level winds for the period of 23 June through 28 June (Fig. 4.5b), the Big Island and the adjacent areas correspond to a spurious minimum (≤ 5 m s^{-1}) in wind speed.

The observed surface temperature distribution is reproduced by the MSM/LSM on 23 June (solid lines in Figs. 4.4a and 4.4b). Notable diurnal variation in surface temperature is evident at Beach and Lava Flow both in model simulations and in observations. Upland of the transection, the diurnal variation in the surface air temperature is relatively small probably due to the effects of vegetation there. One major deficiency in the model simulations is that during the daytime the model-simulated temperature at Beach and Lava Flow is about 2.5 °C lower than that observed. This is likely related to the fact that we have used bare soil to represent lava rocks in the model which could have underestimated daytime heat flux over the surface covered by lava rocks. Sensitivity tests with vegetation and soil parameters are presented in section 4.3.4 for further investigation. Weak low-level winds in the NCEP/NCAR reanalysis data could also be an issue since with weak winds adiabatic warming along the lowlands on the leeside of mountains would be small (Chen and Wang 1994). Too much vertical mixing associated with the MRF diffusion scheme (Hong and Dudhia 2003) may also contribute to the simulated temperature deficiency by bringing down excessive cool and dry air aloft. Mendonca (1969) showed rapid heating over the surface covered by lava rocks near Mauna Loa Observatory after sunrise. Schroeder (1993) showed a diurnal temperature range of 35 °C (9 °C) at a 6 mm (165 mm) depth in ash at the Mauna Kea summit on a clear day in June 1980. The observed rapid heating at Beach and Lava Flow is not indicated in the MSM/LSM simulations (Fig. 4.4b).

b. 24 June

A cyclonic cell within the TUTT approaching from the northeast influenced the Big Island weather on 24 June (Fig. 4.6). This cyclonic cell slowly drifted northward and moved out of the island chain within the next 48 hours. Decreased stability and weak vertical shear of the horizontal wind observed in both the Hilo soundings and pilot balloon ascents (Farrell 1980) contributed to the development of convective showers over the semi-arid desert over northwest Hawaii. The total rainfall (~ 20 mm) exceeded monthly medium. The subtropical high for 24 June was slightly weaker (not shown) than one day ago, likely due to the effect of the upper-level cyclonic cell. Long-lasting sea breezes were recorded at Beach and Lava Flow for this day (Fig. 4.7a). The sea breeze front advanced to between Lava Flow and Puu Nui.

The MSM/LSM reproduces the observed long-lasting sea breezes between 1000 HST and 1800 HST at Beach and Lava Flow (Fig. 4.7b), though the model-predicted sea breeze speed (2-4 m s^{-1}) is about 2-3 m s^{-1} lower with farther penetrations than observations. The MSM/LSM also simulates the observed northeasterly trades at coastal stations during nighttime and along upslopes most times of the day. However, the model underestimates the trade wind speeds by more than 4 m s^{-1}. This underestimation of the trade wind speeds by the model appears to be responsible for the farther penetration of the simulated sea breezes than that observed, since strong trades oppose the development and inland movement of the sea breezes (Schroeder 1981).

Rapid heating of the surface covered by lava rocks after sunrise (Mendonca 1969) is evident in the observed surface air temperature (Fig. 4.7a). The MSM/LSM simulates a slower increase in surface air temperature at coastal stations after sunrise (Fig. 4.7b) as

compared with observations. Elsewhere along the transection, the MSM/LSM-simulated surface air temperature is generally consistent with observations.

c. 25 June

At 0200 HST 25 June, the northward drifting upper-level cyclonic cell further eroded the subtropical high over the Hawaiian Islands (not shown). Weaker trade winds were blowing along the transection on 25 June (Fig. 4.8a) than on 24 June. The sea breezes moved upslope of Puu Nui where it merged with the anabatic flow of Mauna Kea (Fig. 4.8a). Showers developed along the slopes, within 5 km of Puu Nui.

The MSM/LSM simulates sea breezes between 0900 HST and 1800 HST that reach Waimea Airport at 1400 HST (Fig. 4.8b). Observations also show long-lasting sea breezes during the same period that pass Puu Nui but do not reach Top and Waimea Airport (Fig. 4.8a). Since the trade winds along the upslopes are more than 3 m s^{-1} weaker in the model simulations than in observations, the model-simulated sea breezes are able to penetrate further inland than that observed.

d. 26 June

The subtropical high located to the northeast of the Hawaiian Islands sustained moderate trade winds over the island chain on 26 June (Fig. 4.9). The trade winds along the transection for this day were slightly stronger (Fig. 4.10a) than for 25 June (Fig. 4.8a). Longer lasting sea breezes appeared in mid-morning and persisted through the afternoon (Fig. 4.10a). The sea breeze front advanced beyond Lava Flow. Cumulus developed along the sea breeze front but did not develop sufficiently to produce rain.

The MSM/LSM simulates sea breezes between 1000 HST and 1800 HST that develop inland past Waikoloa Office (Fig. 4.10b), in good agreement with observations (Fig.

4.10a). The model-simulated temperature distributions are also consistent with observations.

e. 27 June

The synoptic-scale pressure gradient at surface over the Hawaiian Islands was slightly increased due to the southward shift of the subtropical high (not shown). The trade winds exceeded gale force in the uplands along the transection (Fig. 4.11a), although the winds were slightly weaker than 23 June (Fig. 4.4a). Sea breezes were observed at Beach between 1400 HST and 1600 HST (Fig. 4.11a). The sea breeze front moved ashore but did not advance beyond Lava Flow.

On 27 June, the model simulates sea breezes between 1000 HST and 1600 HST that develop past Puu Nui (Fig. 4.11b); however, observations show sea breezes only at Beach (Fig. 4.11a). Again, this discrepancy is primarily related to the underestimation of the trade wind speeds in the model. Observations for 27 June indicate that the trade winds blow at gale force most times of the day and effectively prevent the development of sea breezes (Schroeder 1981).

f. 28 June

The remnant of Hurricane Carlotta (Gunther 1979) completely disrupted local circulations as she passed the Big Island on the night of 27 June (Fig. 4.12). Heavy rains fell on the island of Kauai and Oahu with light showers over the Big Island as subsidence on Carlotta's periphery suppressed the convection there. Onshore winds blew at Beach between 2200 HST 27 June and 0300 HST 28 June (Schroeder 1981). Weak southeasterly synoptic flow prevailed behind Carlotta. Since the transection is sheltered

from southeasterlies by Mauna Kea and Mauna Loa (see Fig. 2.1c), anabatic winds developed unhindered, reaching Waimea Airport by 0900 HST 28 June (Fig. 4.13a).

On 28 June, the MSM/LSM simulates the observed weak surface winds along the transection (Fig. 4.13b). The model also simulates the observed longer-lasting, further-penetrating anabatic flow (sea breezes) between 0900 HST and 1800 HST that reach Waimea Airport. However, surface temperatures simulated by the MSM/LSM appear to contain some warm biases around noontime. As will be discussed in the next section, the warm biases may be related to the absence of precipitation in the model in contrast to the observed rain showers associated with the anabatic flow. Also note that the simulated duration of the anabatic winds at Top and Waimea Airport is shorter than that observed with a later onset time as compared to observations (Fig. 4.13).

g. Forecasting errors

Based on observations and the MSM/LSM simulations, the forecasting errors for surface temperature are computed at the observation stations for each day during 23 June to 28 June 1978. They are summarized in Table 4.1. The forecasting error is defined as

$$fe = \frac{\sum_{i=1}^{N} \left| A_o^i - A_m^i \right|}{N} \tag{4.1}$$

where A refers to surface temperature, N is the number of times of observations at each station (N = 17, 0600 HST to 2200 HST), subscripts o and m respectively denote observations and MSM/LSM simulations, and superscript i ranges from 1 to 17. Temperatures were not recorded at Waimea Airport. Since the original data were not available, the observed surface temperatures were directly read from the figures.

The largest forecasting errors for temperature (~ 3 °C) occur at Beach for two strong trade wind days (23 and 27 June) (Table 4.1). For the rest of the observation period, the forecasting errors for temperature range from 0.8 °C for 28 June and 0.9 °C for 26 June to 1.6 °C for both 24 June and 25 June at Beach. It appears that the MSM/LSM significantly underestimates the adiabatic warming associated with strong downslope winds under strong trade wind conditions (Chan and Wang 1994) due to the weak low-level winds in the reanalysis data. The forecasting errors for temperature at the other stations (Lava Flow, Puu Nui, and Top) are relatively small when compared to those at Beach except for 28 June when the forecasting errors at Puu Nui and Top are twice as many as at Beach.

In summary, it is evident that the coupled MSM/LSM reproduces the observed sea breeze development along the transection during 23 June to 28 June 1978. Except for 27 June, the simulated onset time and duration of the sea breezes agree with observations reasonably well. Major deficiencies in the model simulations include (1) sea breeze speeds are about 2-3 m s^{-1} lower than observations, and (2) horizontal penetration of sea breezes along the transection is generally overestimated. Statistics evaluations reveal large forecasting errors for surface temperature especially at the coastal stations under strong trade wind conditions. These deficiencies in the model simulations are likely related to (1) underestimation of daytime heat flux due to the representation of the surface covered by lava rocks as bare soil, and (2) underestimation of the trade wind speeds from the NCEP/NCAR reanalysis data. Too much vertical mixing associated with the MRF boundary layer parameterization scheme (Hong and Dudhia 2003) may also contribute to the model deficiencies by bringing down excessive cool and dry air aloft.

4.3.2 Precipitation

Observations from Schroeder (1981) showed that convective showers occurred within or adjacent to the transection on three of the six complete observation days. In two instances (25 and 28 June), weak showers developed in shallow clouds which formed upslope in anabatic currents and drifted downslope as the anabatic winds subsided and the trade winds returned. On 26 June, cumuli developed along the sea breeze front but did not produce rain.

On 24 June, tall cumuli developed at the sea breeze front producing showers at Beach and Lava Flow (Schroeder 1981). The model simulates light rainfall (0.1-0.2 mm hr^{-1}) at Beach and Lava Flow with appreciable rainfall (1.5-2.1 mm hr^{-1}) further inland between 0800 HST and 1600 HST (Fig. 4.14a). On 25 June, the MSM/LSM simulates appreciable rainfall (0.5-3.0 mm hr^{-1}) along the transection (Fig. 4.14b) which is consistent with the observed weather. The onset of the sea breeze showers during the early morning hours with ensuing development along the upslopes and then downslope drifting during the late afternoon hours (Schroeder 1981) are captured by the model.

The MSM/LSM reproduces the observed sea breezes on 26 June (Fig. 4.10) without producing any rainfall along the transection, in good agreement with observations. However, in contrast to observations, the MSM/LSM simulations for 28 June indicate no rainfall within the transection (not shown). This may also partially explain the noontime warm biases identified in the MSM/LSM simulations for 28 June (Fig. 4.13b), since without rain the simulated air temperature would be warmer. For both 26 and 28 June (Figs. 4.10b and 4.13b), the simulated diurnal ranges in the surface air temperature are slightly larger than days with rainfall simulated.

4.3.3 Vertical extent of the sea breeze

The observed vertical extent of the sea breeze during the period 23-28 June 1978 was summarized in Schroeder (1981) based on pilot balloon data. The results indicated a maximum depth of the sea breezes around 1400 HST at Beach ranging from 300 m on 23 June to 1500 m on 28 June (Table 4.2). In comparison, the MSM/LSM captures the observed vertical extent of the sea breezes well, as demonstrated in the transection-height cross sections (Fig. 4.15). On 24 June and 27 June (Figs. 4.15a and 4.15c), the simulated depth of the sea breezes is about 900 m which is close to the observed values of 800 m on 24 June and 750 m on 27 June. On 25 June and 28 June (Figs. 4.15b and 4.15d), the simulated depth of the sea breezes is about 1000 m and 1500 m, respectively. On 23 June, the MSM/LSM simulations indicate shallow (~ 400 m) sea breezes at Beach (not shown) while the observations also show shallow (300-500 m) sea breezes at Beach. There were no successful pilot balloon launches on 26 June (Schroeder 1981). The model simulated sea breezes for 26 June show a vertical depth of 700 m at Beach (not shown).

4.3.4 Sensitivity tests

Soil properties and insolation (i.e., cloudiness) regulate surface heating, which in turn regulates the characteristics of sea breezes (Schroeder 1981). More cloudiness would result in less surface heating, which in turn would inhibit further development of sea breezes. Several modeling studies (McCumber 1980; Garrett 1982; and Yamada 1982) have shown that sharp horizontal changes in the character and type of the vegetation cover would induce mesoscale circulations. Observational studies by Segal et al. (1988) also showed noticeable air temperature differences due to the effect of vegetation cover

under the same environmental conditions. In the case of Hawaii, there are few studies on the effects of soil properties on sea breeze behavior using high-resolution models.

The black lava rocks are dry with little soil moisture, low albedo, and low heat capacity as compared to surfaces with ground cover. In the USGS datasets for Hawaii, the lava rocks are categorized as bare soil as previously mentioned. Bare soil is relatively wet (reference soil moisture content = 0.108) and has relatively high albedo (~ 0.238) when compared to the lava rocks. Thus, using bare soil to represent the lava rocks would underestimate the daytime sensible heat flux. We performed sensitivity tests for June 28 using the MSM/LSM with reduced soil moisture and albedo for the surface covered by the lava rocks while keeping all other configurations the same as in the control run. June 28 is chosen for these sensitivity tests mainly because the surface winds were weak on this day, and both observations and model results show well developed sea breezes along the transection. Our model simulations (not shown) indicate minor modulation of soil moisture on the sea breeze development within the transection. This could be due to the fact that soil moisture is already small in that area after being kept updated for one month (Fig. 4.2a) and further reduce does not produce many differences. Reducing albedo only slightly affects the surface temperature distributions without bringing in significant impact on the sea breeze development.

We further performed sensitivity tests with thermal conductivity and heat capacity. Thermal conductivity is dependent on volumetric soil moisture with less soil moisture corresponding to lower thermal conductivity (McCumber and Pielke 1981). Based on the fact that the lava rocks have little or no soil moisture, we reduced the thermal conductivity by a factor of 10 (from 3.45 to 0.34 W m^{-1} K^{-1}) for the surface covered by

the lava rocks. This appears to be justified based on Chen and Dudhia (2001). The model simulations are presented in Figure 4.16a. Onshore wind speeds at Beach and Lava Flow for 28 June increase from 1-2 m s^{-1} in the control run (Fig. 4.13b) to 5 m s^{-1} (Fig. 4.16a) between 1300 HST and 1400 HST. Rapid heating after sunrise over the surface covered by lava rocks is also indicated (Fig. 4.16a) when compared to the control run (Fig. 4.13b). Another sensitivity test involves reducing (a) the surface albedo by 90%, and (b) the thermal conductivity by a factor of 10 for the surface covered by the lava rocks. The results (Fig. 4.16b) show relatively longer temporal duration of the strengthened sea breezes and the 30 °C isotherm when compared to the sensitivity test with the thermal conductivity the only changing parameter (Fig. 4.16a). The explanation for this is that reducing the thermal conductivity inhibits the energy transfer to deep soil which in turn promotes heating of the surface layer. Our sensitivity tests with varying heat capacity (reduced by a factor of 5 up to 10, not shown) produce similar model simulations with the control run. This could be related to the fact that heat capacity is already small along the coastal stations within the transection due to little soil moisture there (Fig. 4.2a).

We also examine how the model initialization processes affect the simulated sea breeze characteristics for 28 June. With the initial soil conditions interpolated from the RSM/LSM simulations rather than updating the surface conditions using the 24-h simulations of the previous MSM/LSM run for one month, the simulated sea breezes (Fig. 4.17a) display much smaller extent in both horizontal penetration and spatial scale than in the control run (Fig. 4.13b) and compare less favorably with observations (Fig. 4.13a). The simulated temperature distribution (Fig. 4.17a) also differs from the observations. These deficiencies in the simulations are related to the relatively higher soil moisture in

the model in the semi-arid region without considering the amount of prior precipitation (Fig. 4.17b). The soil moisture depends not only on the ground cover and surface properties but also on the amount of precipitation in the past.

In the original version of the MSM, the surface conditions are initiated by one soil type (sandy clay loam) and one vegetation type (broadleaf trees) over the entire model domain with a constant vegetation fraction of 70%, resulting in a rather uniform distribution of soil moisture content ~ 0.33 over northwest Hawaii (Fig. 4.18b). Using the original version of the MSM, the simulated maximum temperature along the transection is lower than in the control run especially in the semi-arid region on the lower slopes and along the coast (Fig. 4.18a). With a 70% surface vegetation cover in the model, the air temperature decreases at a slower rate after sunset as compared with the control run. As a result, the ending time of the sea breezes occurs slightly later on the upper slopes (Fig. 4.18a).

4.3.5 Higher-resolution (1 km) simulation

Our discussions presented so far are based on model simulations from the 3-km MSM/LSM runs. It would be desirable to conduct higher-resolution (1 km) simulations to investigate if additional improvements could be achieved by a better representation of the local terrain. Earlier studies on sea breezes (e.g., Estoque 1962; Neumann and Mahrer 1971; Lambert 1974) indicate that greater horizontal resolution is necessary to achieve more accurate predictions. Case et al. (2002) perform verifications of high-resolution Regional Atmospheric Modeling System (RAMS) forecasts over East-Central Florida during the 1999 and 2000 summer months. They note that the skill scores of the RAMS sea breeze predictions over central Florida improve using 1.25 km grid spacing compared

to 5 km grid spacing. Analysis of the individual sea breeze cases in New England (Colby 2004) also shows that with higher-resolution grids, his model has the capability to resolve realistic details in the sea breeze circulation that are missed by coarser-resolution grids. For this purpose, we ran the MSM/LSM for northwestern Hawaii at a 1-km resolution for 27 June. June 27 is chosen because the 3-km MSM/LSM simulates longer lasting and farther penetrating sea breezes than that observed (see Fig. 4.11). The initial conditions and the time-dependent base fields for the 1-km MSM/LSM run are provided by the 10-km RSM/LSM simulations. Juang (2000) showed that the MSM can be successfully nested into the hydrostatic model at 10- to 20-fold differences in horizontal resolution within a small domain due to the well-behaved perturbation nesting over flat plains, coastal oceans, as well as steep mountains.

The time section constructed from the MSM/LSM simulations at a 1-km resolution for 27 June are presented in Figure 4.19a. The simulated sea breezes barely move ashore with short temporal duration (1200 HST – 1700 HST), in good agreement with observations (Fig. 4.11a). With a 1-km resolution, the simulated trades channeling through the Waimea Saddle along the transection are slightly stronger and penetrate farther downstream than the 3-km MSM/LSM (Figs. 4.19a and 4.11b). The stronger trades simulated in the 1-km MSM/LSM in turn oppose the inland penetration of the sea breezes. Nevertheless, deficiencies in the 1-km MSM/LSM simulations are noted that include (a) lower surface temperatures at Beach and Lava Flow, and (b) weaker sea breezes and weaker trades as compared with observations. After reducing the thermal conductivity and surface albedo by a factor of 10 in the 1-km MSM/LSM, surface temperatures at Beach and Lava Flow are increased by ~ 2.5 °C with a slight increase in

the sea breeze speeds at Beach (Fig. 4.19b) when compared to Figure 4.19a. This appears to suggest that representing the lava rocks with bare soil may underestimate the daytime surface heating. We also ran the 1-km MSM/LSM for 23 June (not shown) with similar results.

Though the 1-km runs show improvements over the 3-km MSM/LSM in reproducing the observed sea breezes, the forecasting errors for surface temperature (Table 4.1) for 23 June and 27 June from the 1-km runs with the original surface parameters do not indicate appreciable improvements when compared with the 3-km MSM/LSM simulations. A realistic specification of surface parameters appears to be one issue. How well the model physics (e.g., parameterizations of the planetary boundary layer and surface heat and moisture budget parameterizations on smaller scales) works at higher resolutions may be another issue. Mass et al. (2002) also show that decreasing grid spacing in mesoscale models generally improves the realism of the results but does not necessarily significantly improve the objectively scored accuracy of the forecasts.

4.4 Conclusions

Schroeder's (1981) sea breeze cases over northwest Hawaii are simulated using the coupled MSM/LSM. The model reproduces the observed sea breeze development along the transection during 23 June to 28 June 1978. Except on 27 June, the model-predicted onset time, duration and vertical extent of the sea breezes agree with observations reasonably well. The largest forecasting errors for surface temperature occur at the coastal stations under strong trade wind conditions. The simulated rainfall distribution in association with sea breeze fronts is consistent with observations.

Sensitivity tests using the MSM/LSM demonstrate the non-trivial effects of surface properties and initialization processes on sea breeze behavior. Higher-resolution (1 km) MSM/LSM simulations show improvements over the 3-km MSM/LSM in reproducing the observed sea breezes on 27 June through a better representation of the local terrain and a better simulation of the orographically enhanced trades through the Waimea Saddle. However, objective analyses at the observation stations do not indicate significant improvement of the 1-km simulations over the 3-km simulations.

Deficiencies in the model simulations are noted and include (1) sea breeze speeds are more than 2-3 m s^{-1} lower than observations, and (2) horizontal penetration of sea breezes within the transection is overestimated. These deficiencies in the model simulations appear to be related to two factors: the underestimation of the trade wind speeds from the NCEP/NCAR reanalysis data used in the model and the underestimation of daytime heat flux due to the specification of the surface covered by the lava rocks as bare soil. The former promotes the farther penetration of the sea breezes while the latter affect the surface temperatures and sea breeze speeds. There are also known deficiencies in the MRF boundary layer parameterization scheme used. Too much vertical mixing associated with this scheme could bring down excessive cool and dry air aloft and affect the sea breeze development. Testing of a revised vertical diffusion algorithm in the boundary layer (Hong and Dudhia 2003) will be performed in the future.

In addition to better representation of the terrain with a higher horizontal resolution, additional improvements could be made by including unconventional data in the initial conditions (Wang et al. 1998). These include the satellite-derived cloud drift and surface winds, the ACARS (Aircraft Communications Addressing and Reporting System)

soundings, radar-derived winds, and satellite-derived water vapor. Deployment of boundary layer wind profilers over the Hawaiian Islands is also desirable to provide additional data for model initialization. Incorporating unconventional wind data would help to alleviate weak low-level winds over the Hawaiian Islands given by the NCEP/NCAR reanalysis data.

Table 4.1. Forecasting error (°C) of 2-m temperature at four observation stations along the transection. Computation of the forecasting error is given by equation (4.1) in the text.

		Beach	Lava Flow	Puu Nui	Top
0623	3 km	2.92	1.37	1.12	1.48
	1 km	3.35	1.68	0.80	1.24
0624		1.62	0.99	0.80	1.12
0625		1.63	0.94	1.25	1.12
0626		0.96	0.55	1.07	0.65
0627	3 km	3.12	2.06	1.42	1.18
	1 km	2.94	1.32	2.02	2.39
0628		0.84	0.72	1.87	2.13

Table 4.2. Sea breeze vertical extent based on pilot balloon data (from Schroeder 1981).

Date	Time (HST)	Depth of sea breeze (m)	Comments
23 June	1430 1450 1600	300 500 0	Brief advance in afternoon after early downslope gales
24 June	0900 1030 1400	0 600 800	Several balloons set for zero buoyancy sank in showers upslope
25 June	0920 1000 1030 1400 1625	350 600 600 1000 700	Well-developed onshore flow
26 June			No successful launches
27 June	0830 1030 1450	0 0 750	On 1450 ascent balloon rose to 14 m s^{-1} over 60 s; apparently an updraft at the front
28 June	1400 1615	1500 1500	Strong onshore flow

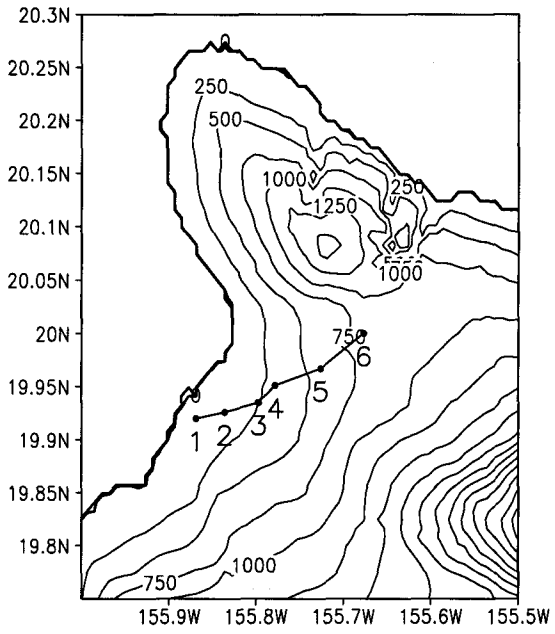

Station names:
1. Beach
2. Lava Flow
3. Waikoloa Office
4. Puu Nui
5. Top
6.Waimea Airport

Figure 4.1. Map of the northwestern Big Island showing major geographic features and the location of the transection with the station names located to the right of the map. Waikoloa Office only collects the insolation data. The terrain contour interval is 250 m. High-resolution (~ 1 km) Navy-NCAR terrain data for the Hawaiian Islands are used.

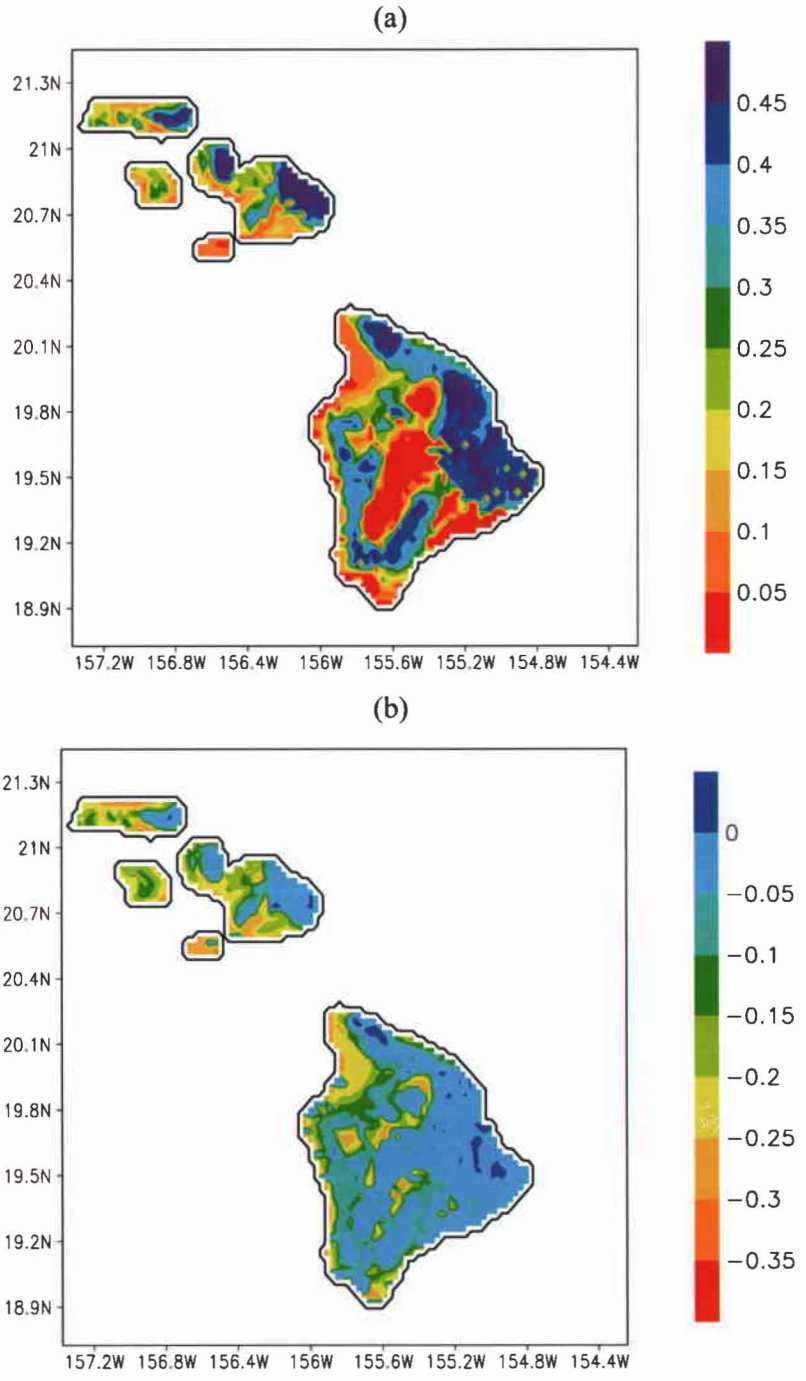

Figure 4.2. The MSM/LSM simulated first-layer (0-200 mm) (a) volumetric soil moisture content (fraction) with the MSM/LSM runs started one month earlier and with the soil conditions kept updated for one month, and (b) volumetric soil moisture content difference (fraction) between the MSM/LSM one-month simulations and the MSM/LSM 24-h simulations, valid at 2000 HST 23 May 1978.

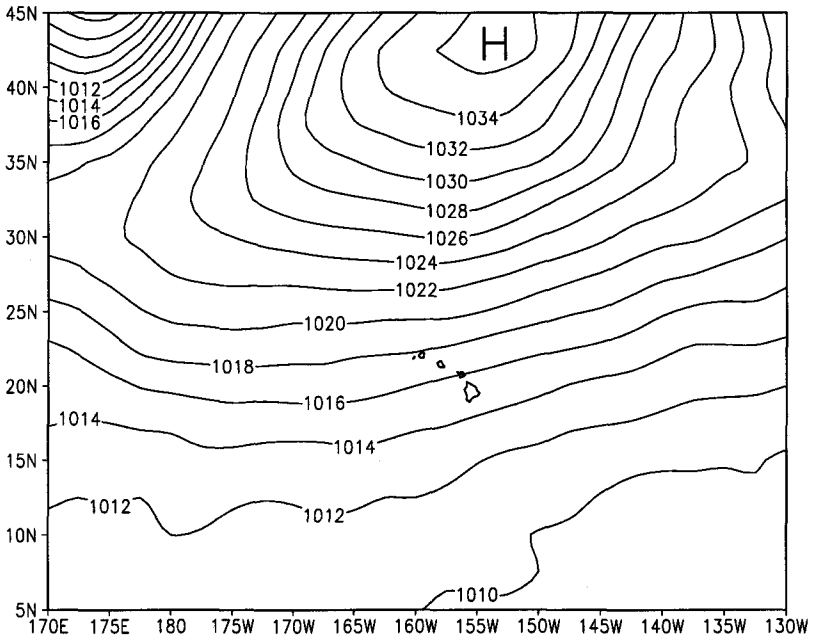

Figure 4.3. Sea level pressure (hPa) valid at 0200 HST 23 June 1978 based on the NCEP/NCAR reanalysis data. The contour interval is 2 hPa.

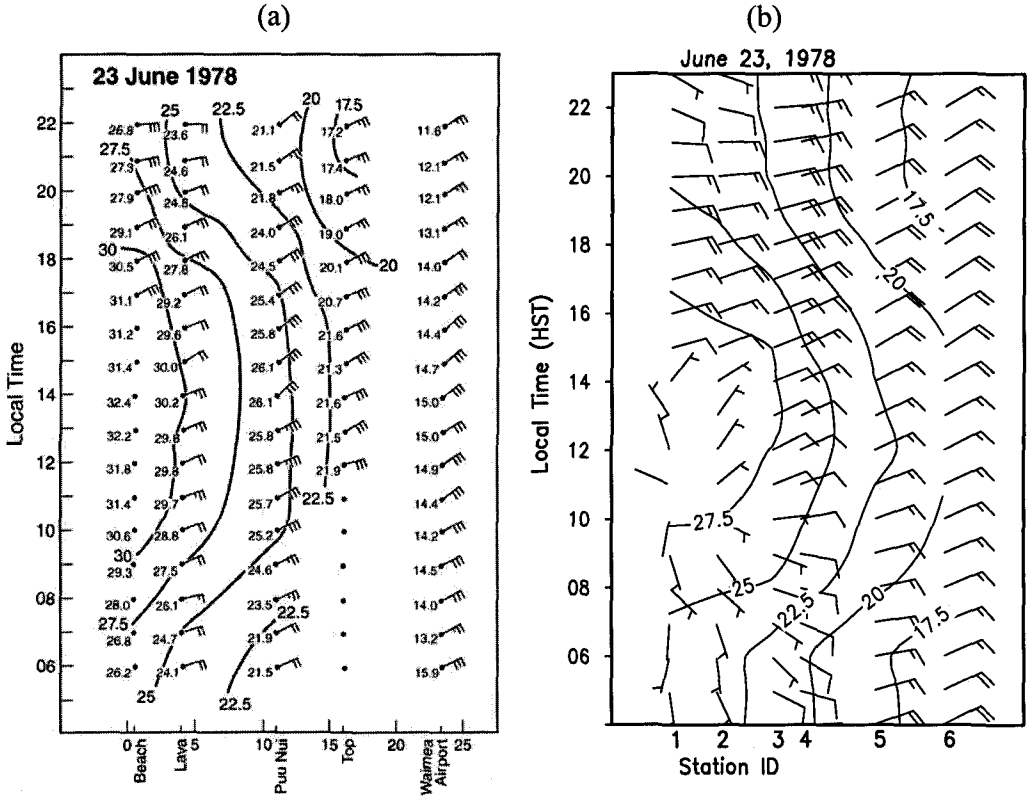

Figure 4.4. Time section along the transection from 0600 to 2200 HST 23 June 1978 for (a) observations (from Schroeder 1981), and (b) the 3-km MSM/LSM simulations, showing surface wind speeds (m s^{-1}, barbs) and temperature (°C, solid lines). Data in observations are means for the hour ending at indicated time. Isotherms are analyzed in 2.5 °C intervals. One full barb and half barb denote 5 m s^{-1} and 2.5 m s^{-1}, respectively. "Hand-held" and "Hand" hereafter indicate observations made with a hand-held anemometer; solid triangle indicates rain shower. The MSM/LSM runs were initialized at 2000 HST the previous day. Refer to Fig. 4.1 for the transection location and station names.

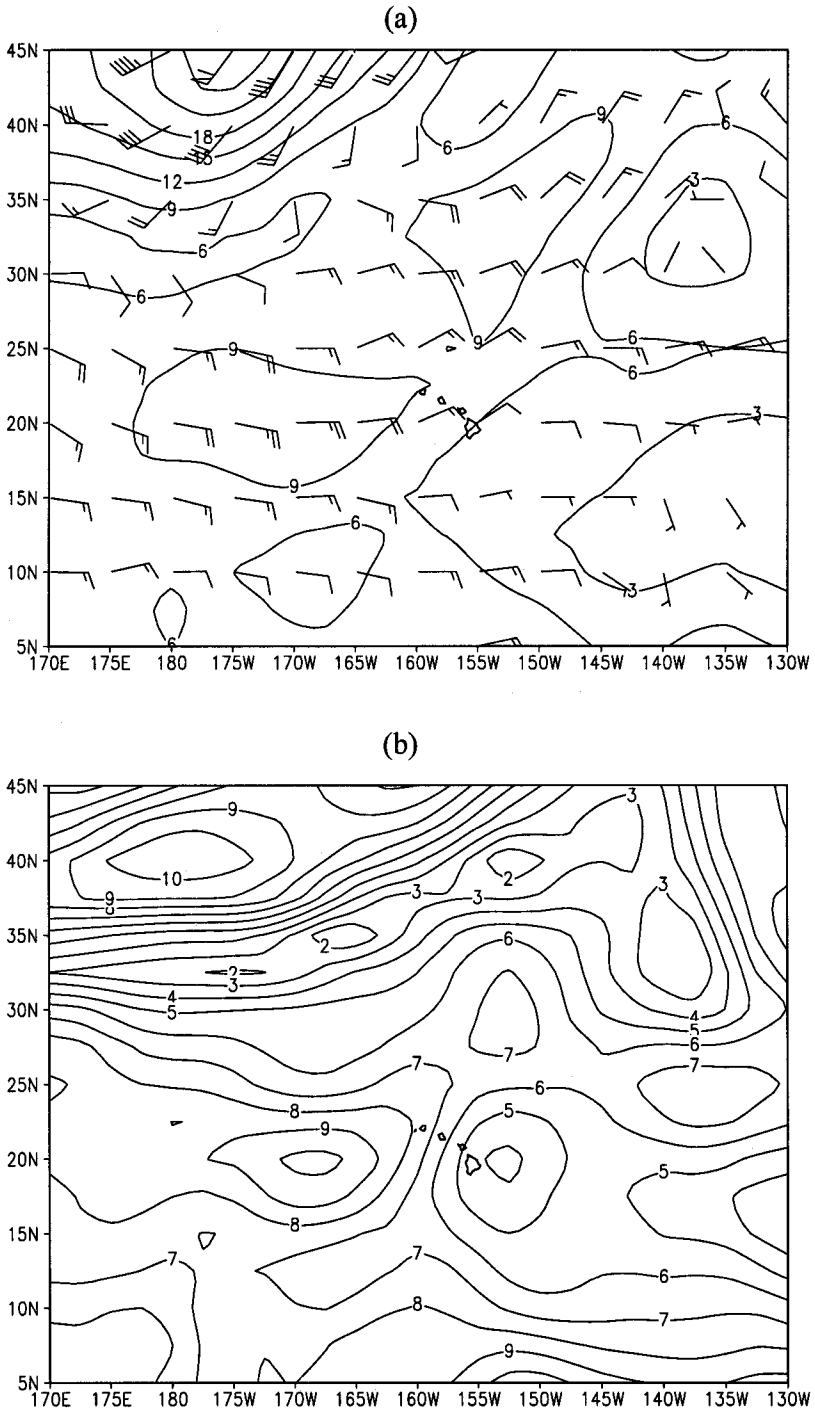

Figure 4.5. (a) horizontal wind speed (m s^{-1}) at 850 hPa valid at 0200 HST 23 June, and (b) composite wind speed (m s^{-1}) valid at 0200 HST for the period of 23 June through 28 June 1978, based on the NCEP/NCAR reanalysis data. Contour interval is 3 m s^{-1} in (a) and 1 m s^{-1} in (b). The wind barbs in (a) are the same as in Fig. 4.4.

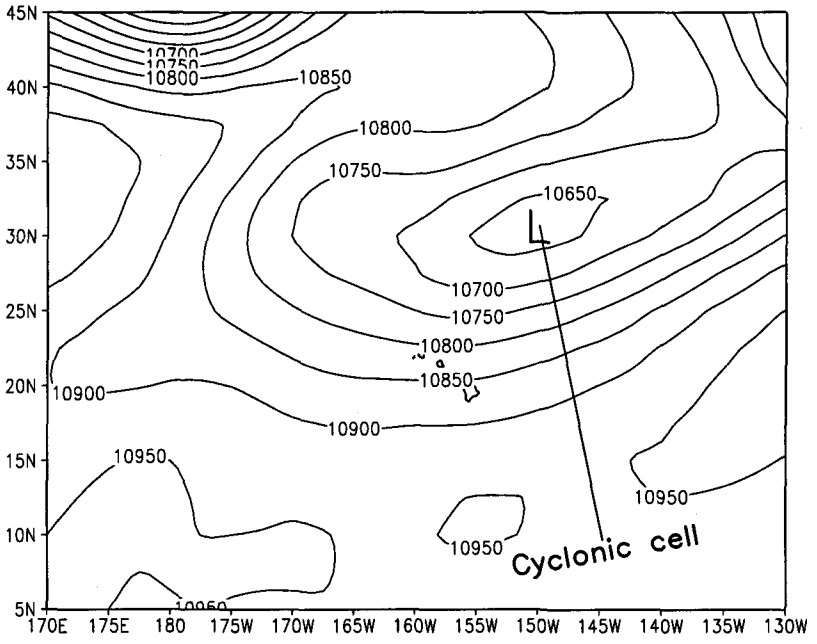

Figure 4.6. 250-hPa geopotential height (gpm) analyses valid at 0200 HST 24 June 1978 based on the NCEP/NCAR reanalysis data. The contour interval is 50 gpm.

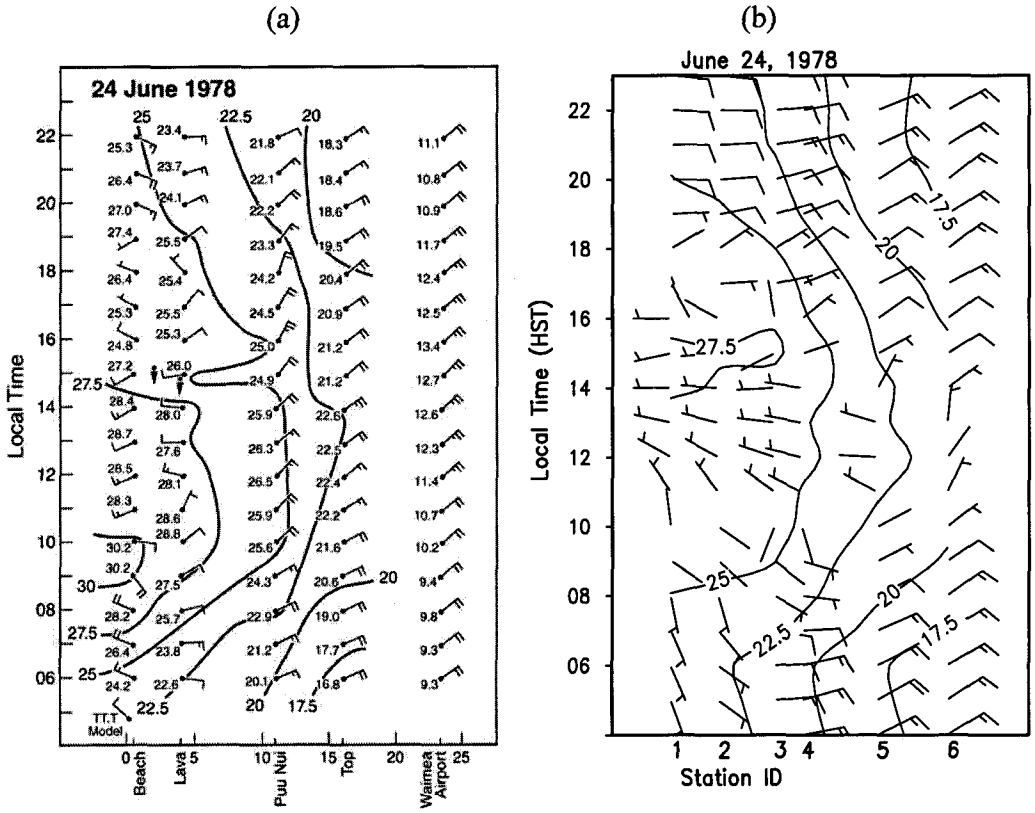

Figure 4.7. As in Fig. 4.4 except for 24 June 1978.

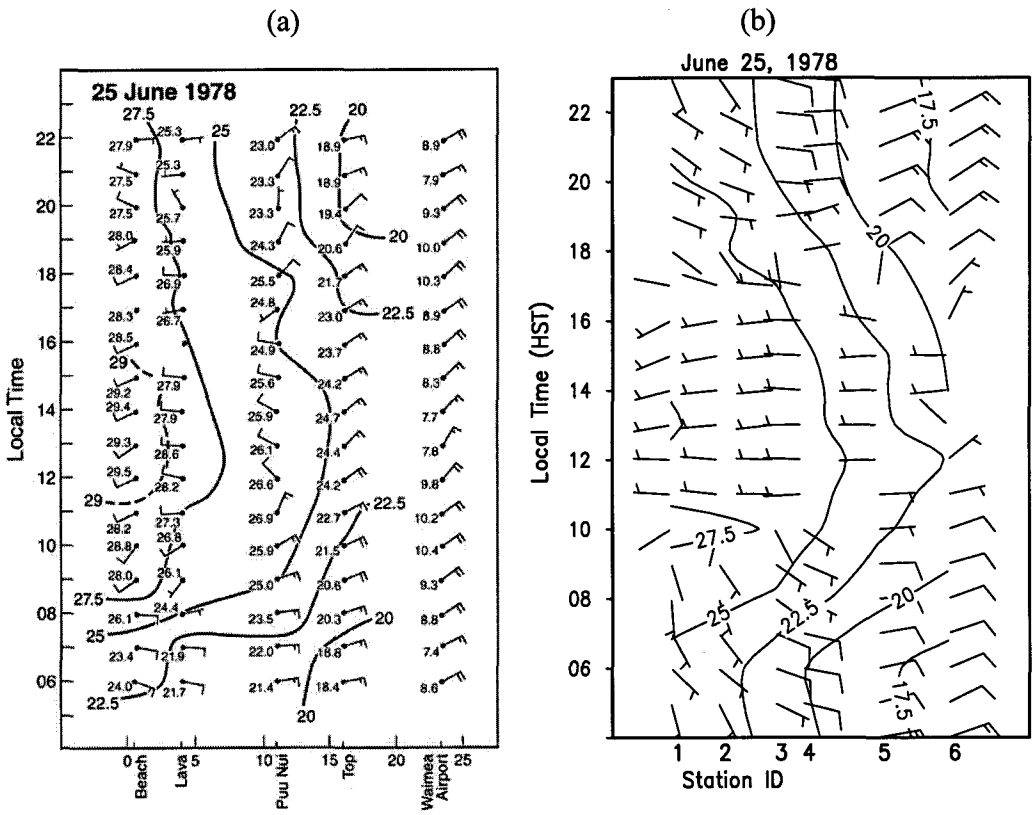

Figure 4.8. As in Fig. 4.4 except for 25 June 1978.

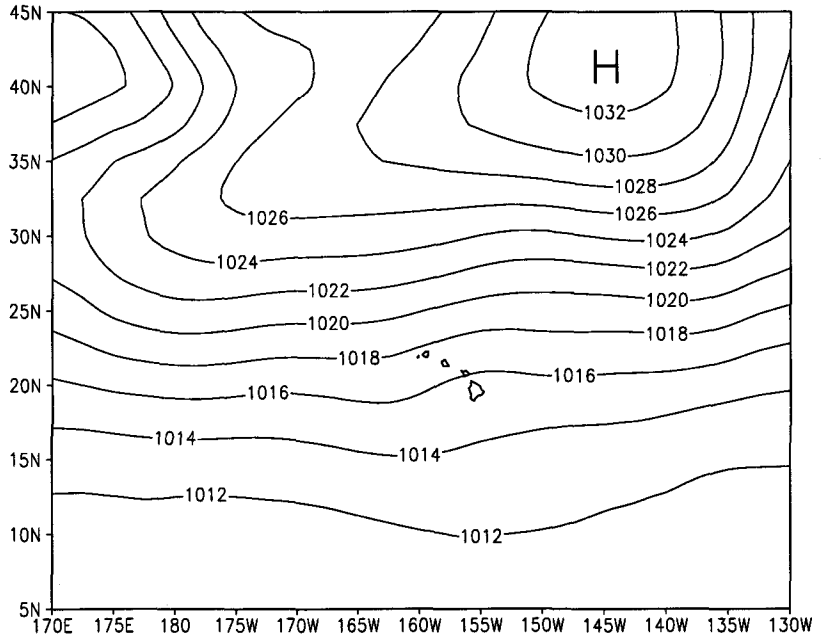

Figure 4.9. Sea level pressure (hPa) valid at 0200 HST 26 June 1978 based on the NCEP/NCAR reanalysis data. The contour interval is 2 hPa.

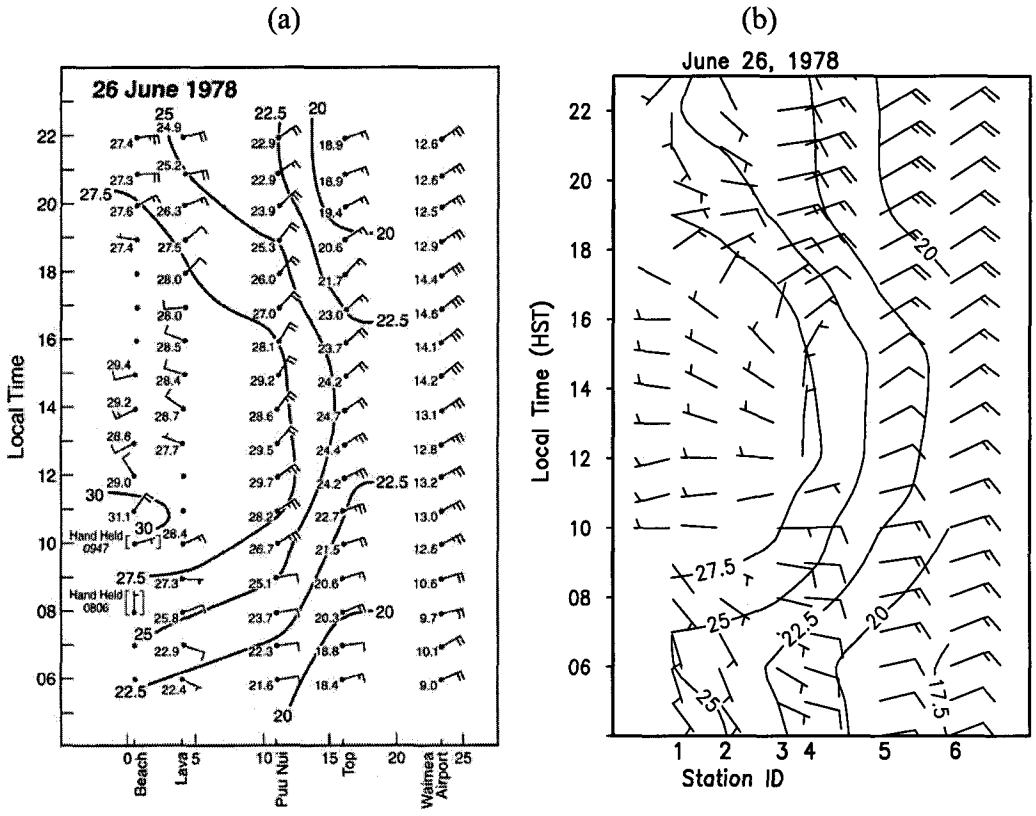

Figure 4.10. As in Fig. 4.4 except for 26 June 1978.

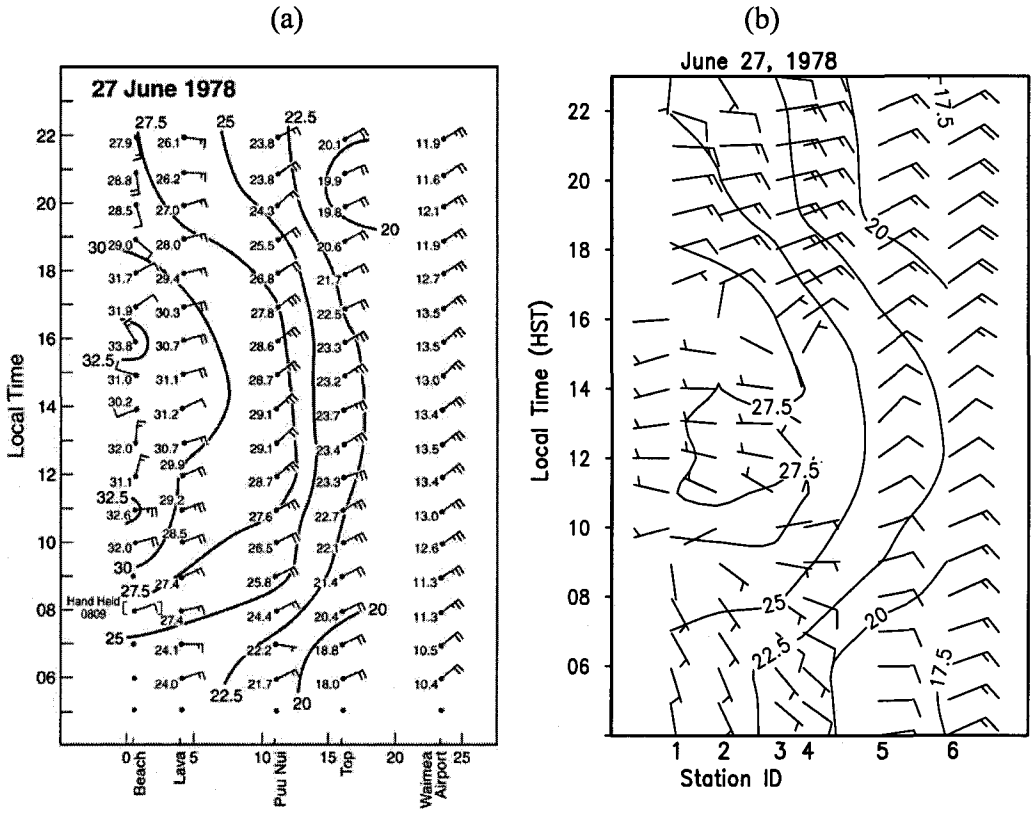

Figure 4.11. As in Fig. 4.4 except for 27 June 1978.

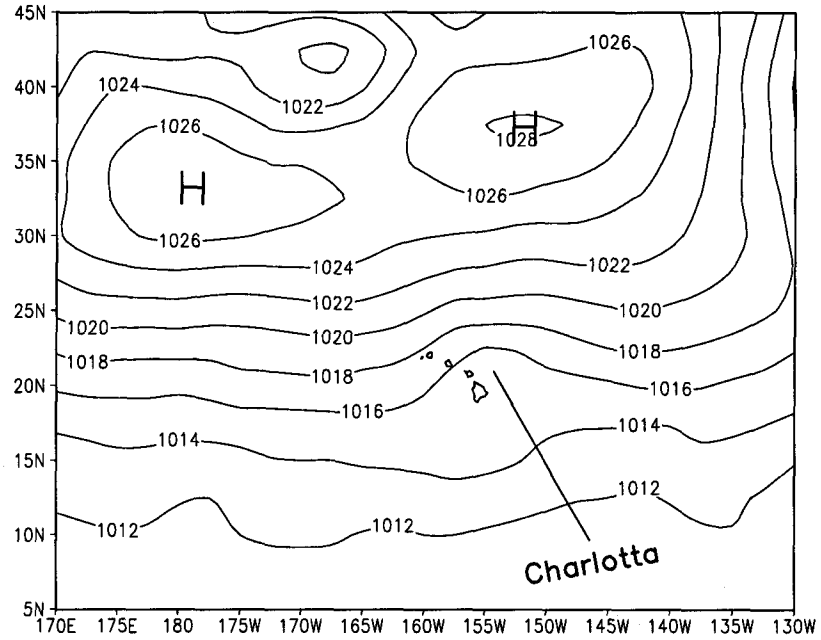

Figure 4.12. Sea level pressure (hPa) valid at 0200 HST 28 June 1978 based on the NCEP/NCAR reanalysis data. The contour interval is 2 hPa.

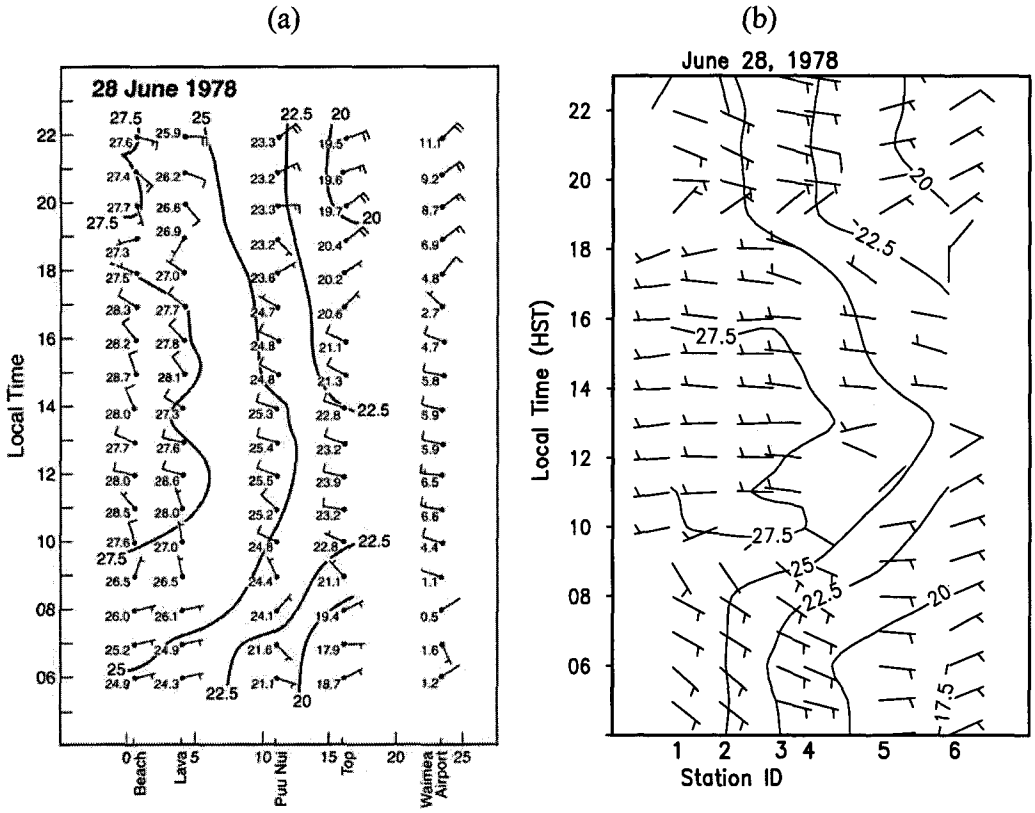

Figure 4.13. As in Fig. 4.4 except for 28 June 1978.

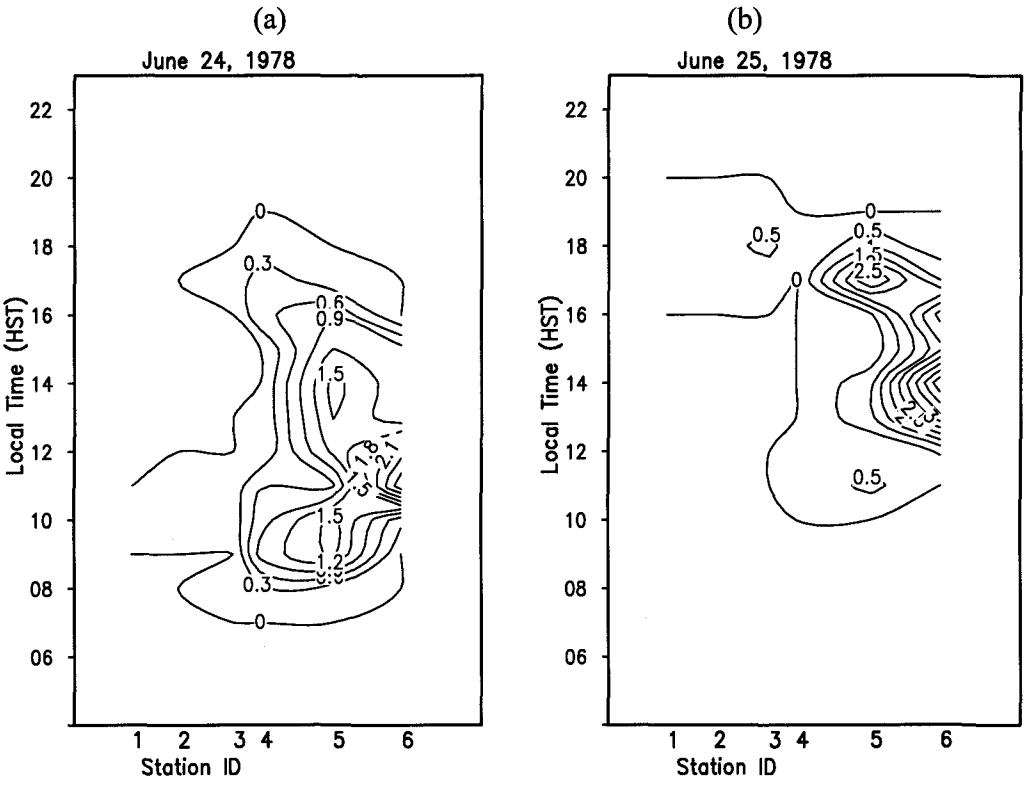

Figure 4.14. Time section along the transection from 0600 to 2200 HST for (a) 24 June and (b) 25 June 1978 showing hourly total precipitation (mm) simulated by the 3-km MSM/LSM. Contour interval is 0.3 mm in (a) and 0.5 mm in (b). The MSM/LSM runs were initialized at 2000 HST 23 June in (a) and 2000 HST 24 June in (b).

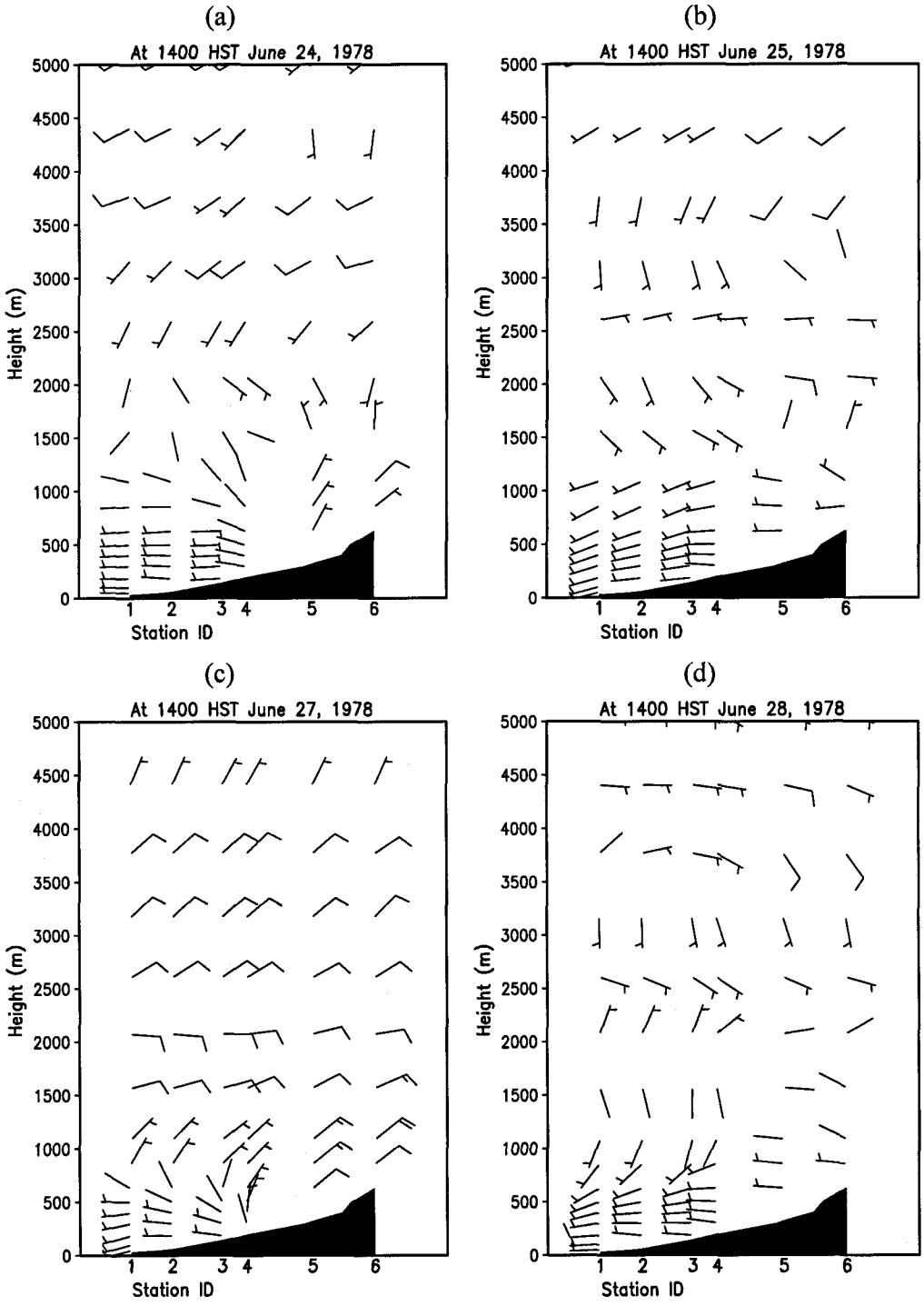

Figure 4.15. Vertical cross section along the transection showing horizontal wind (m s^{-1}) valid at 1400 HST (a) 24 June, (b) 25 June, (c) 27 June, and (d) 28 June 1978 simulated by the 3-km MSM/LSM. Wind barbs as in Fig. 4.4. The MSM/LSM runs were initialized at 2000 HST the previous day.

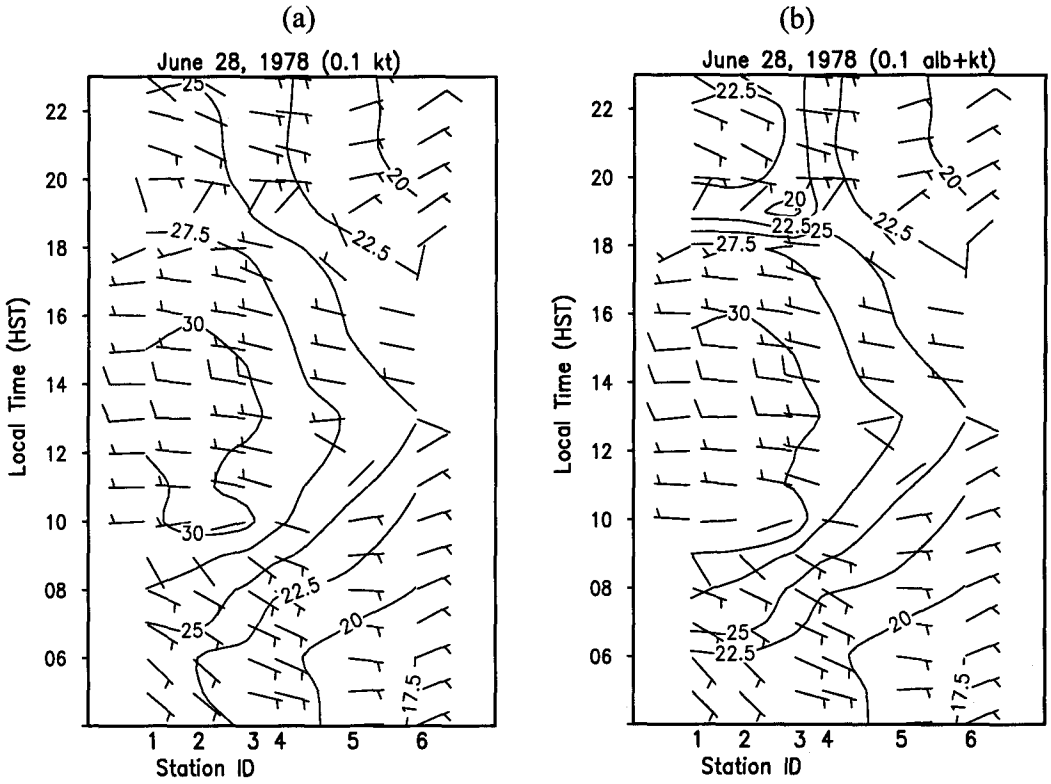

Figure 4.16. Time section along the transection from 0600 HST to 2200 HST 28 June 1978 showing surface wind speeds (m s^{-1}) and temperature (°C) simulated by the 3-km MSM/LSM with (a) thermal conductivity reduced by a factor of 10, and (b) surface albedo reduced by 90% and thermal conductivity reduced by a factor of 10 for the surface covered by lava rocks. The isotherms are drawn for every 2.5 °C. Wind barbs are the same as in Fig. 4.4. The MSM/LSM runs were initialized at 2000 HST 27 June.

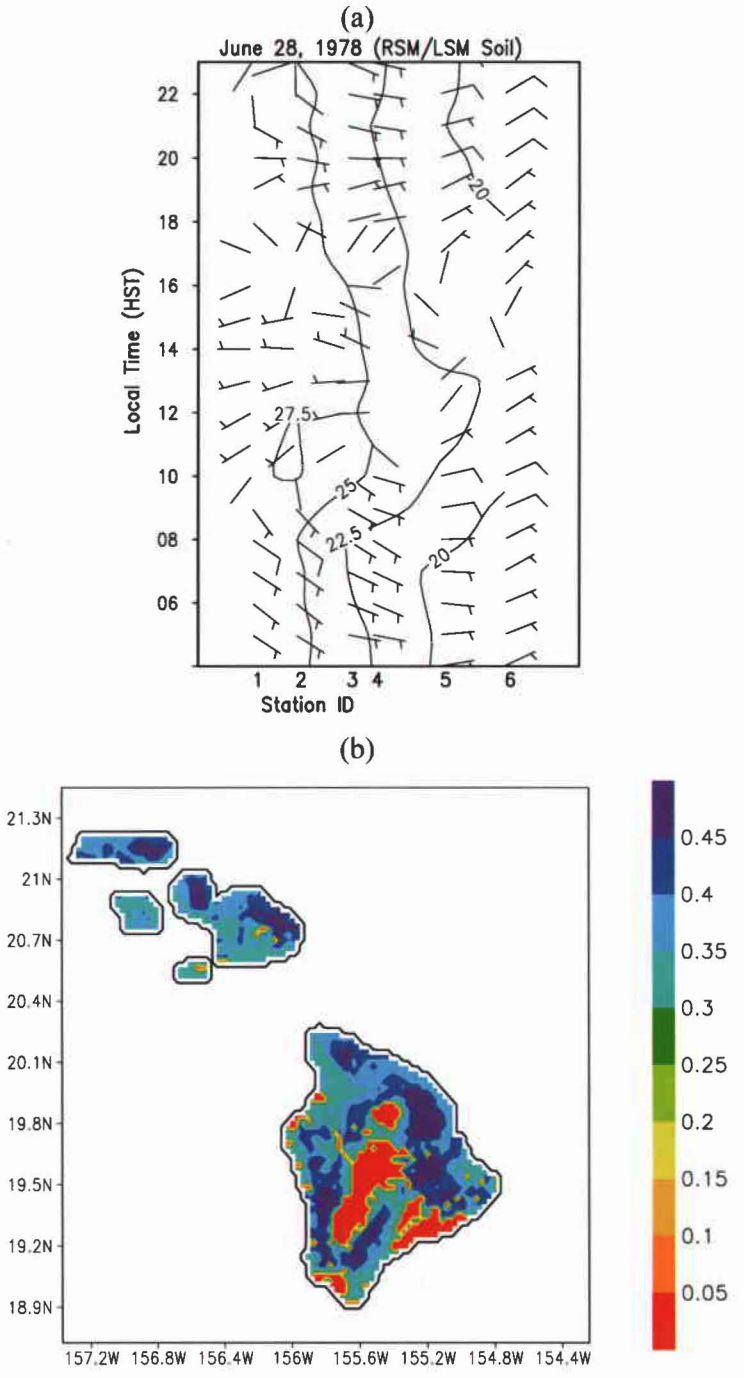

Figure 4.17. (a) Time section from 0600 to 2200 HST 28 June showing winds (m s^{-1}, barbs) and temperature (°C, solid lines), and (b) first-layer (0-200 mm) volumetric soil moisture content (fraction) valid at 2000 HST 28 June simulated by the MSM/LSM, with the initial soil conditions interpolated from the RSM/LSM simulations without being updated for one month. The MSM/LSM was initialized at 2000 HST 27 June 1978.

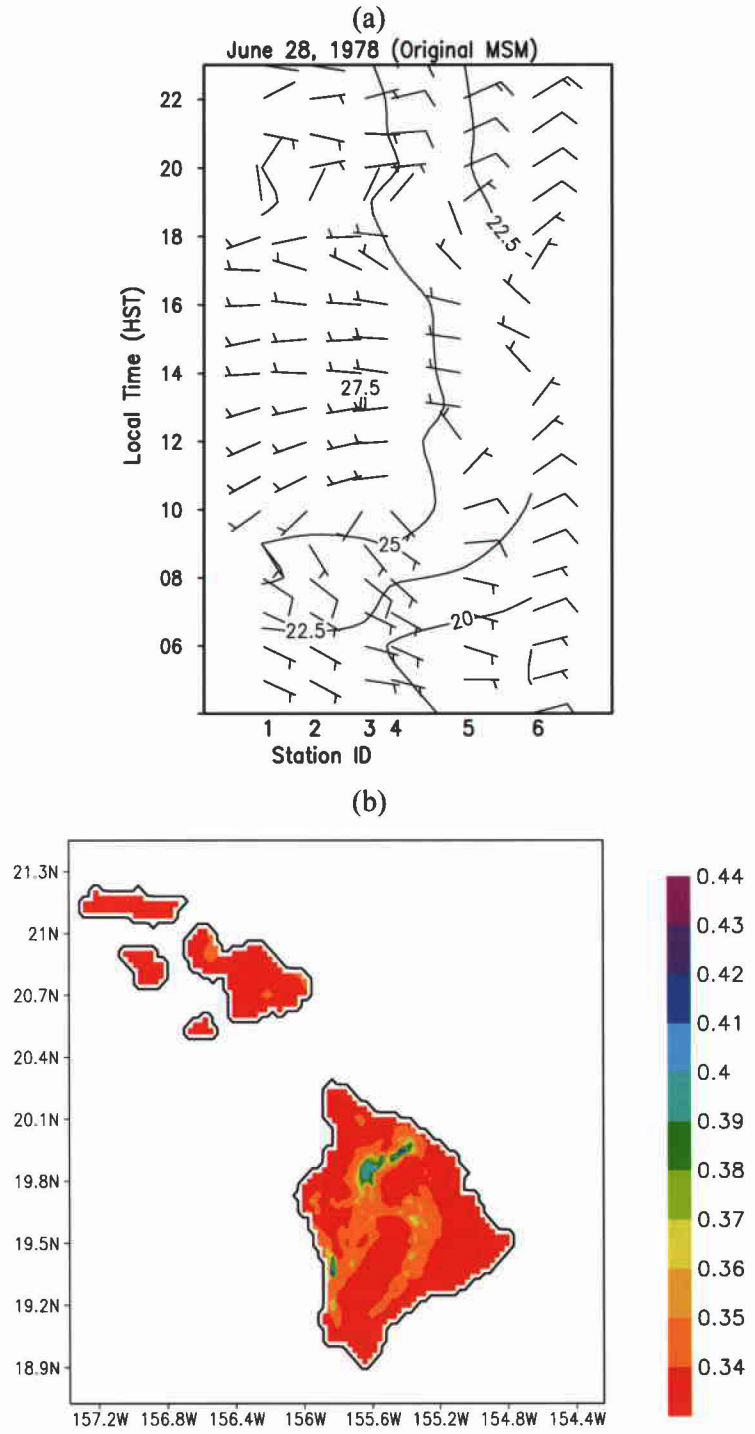

Figure 4.18. Same as Fig. 4.17 except by the original MSM. The MSM was initialized at 2000 HST 27 June 1978.

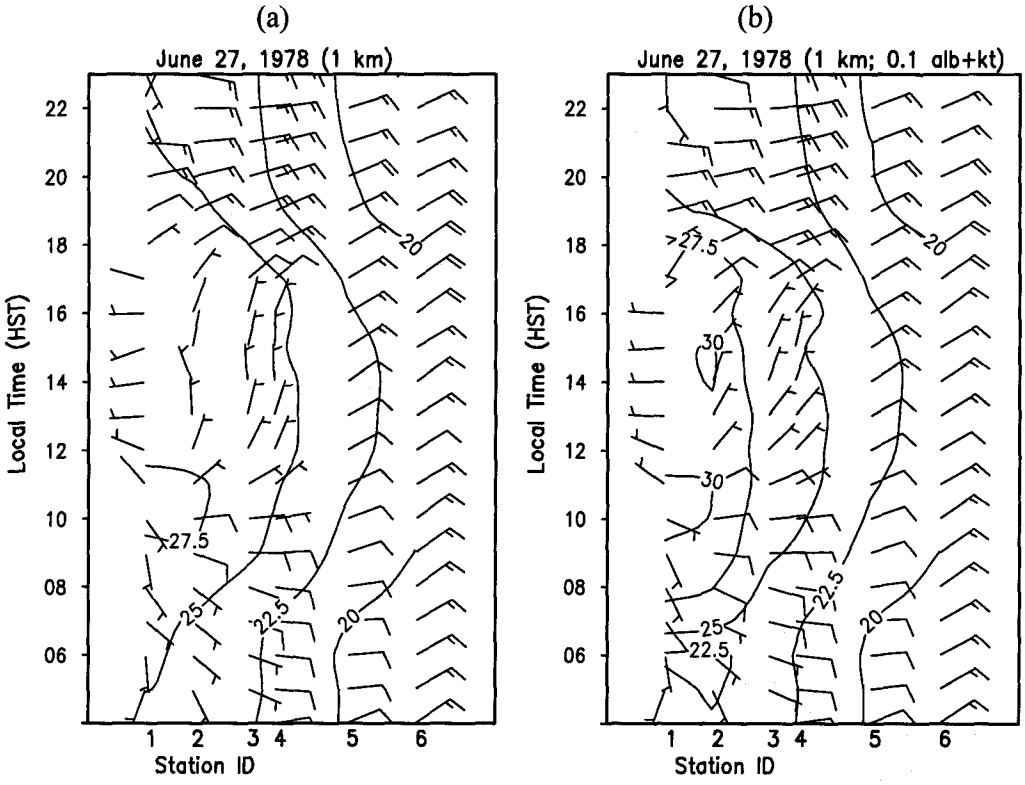

Figure 4.19. Time section from 0600 to 2200 HST 27 June 1978 showing surface winds (m s^{-1}, barbs) and temperature (°C, solid lines) valid at 1400 HST 27 June simulated by the 1-km MSM/LSM with (a) the original surface parameters and (b) the thermal conductivity reduced by a factor of 10 and the surface albedo by 90%. Isotherms are drawn for every 2.5 °C. Barbs are the same as in Fig. 4.4. The MSM/LSM runs were initialized at 2000 HST 26 June 1978.

CHAPTER 5

Heavy rainfall events

5.1 Introduction

Chapter 3 demonstrates that local circulation and island weather are reasonably well simulated by the coupled MSM/LSM under summer trade wind conditions with weak synoptic-scale forcing. Chapter 4 further shows that the MSM/LSM-predicted onset time, duration, and vertical extent of the sea breezes over northwest Hawaii agree reasonably well with observations. It is necessary to evaluate the performance of the MSM/LSM in simulating high-impact weather (e.g., heavy rainfall and high wind) over the Hawaiian Islands. The purpose of simulating high-impact weather is two-fold: (1) to understand the possible mechanisms for the occurrence and development of high-impact weather, and (2) to explore the benefit of high-resolution forecast guidance in simulating heavy rain and high wind events.

Blumenstock and Price (1967) identify four types of synoptic-scale systems which could produce heavy rain over the Hawaiian Islands: (a) cold frontal passages across the island chain; (b) kona storms (Simpson 1952; Ramage 1962); (c) tropical upper tropospheric troughs (TUTT) (Sadler 1967); and (d) tropical cyclones. With the exception of tropical cyclones, the majority of heavy rain events over the Hawaiian Islands occur during the cool season (October – April) (Schroeder 1977). During the cool season, extratropical and subtropical weather systems are able to penetrate southward and affect the weather of the Hawaiian island chain (Schroeder 1983).

This chapter documents the evaluations of the coupled MSM/LSM simulations for four heavy rainfall events over the Hawaiian Islands. The RSM/LSM forecasts are presented alongside the MSM/LSM simulations for comparison. Heavy rainfall events associated with tropical cyclones are not included in this study, but will be the focus of future work. The structure of this chapter is as follows: Model simulations from the MSM/LSM and the RSM/LSM are compared with observations in section 5.2. Conclusions and discussion are presented in section 5.3.

5.2 Case studies

5.2.1 5 -6 June 2001 summer thunderstorm on the island of Oahu

During the period of 5 – 6 June 2001, an upper-level low first situated to the northeast of the island of Oahu (Fig. 5.1a) drifted slowly west southwest, eventually moving out the island chain. An associated upper-level trough was evident far northeast of the Hawaiian Islands on 5 June 2001 (Fig. 5.1a). At the surface (Fig. 5.1b), moderate easterly trade winds of 7 m s^{-1} prevailed across the Hawaiian Islands owing to a high pressure system located northeast of the islands. An inverted trough associated with the upper-level low was evident at surface to the northeast of Oahu. The northeasterly winds ahead of the inverted trough converged with the easterly trade winds just northeast of Oahu.

The heaviest rainfall was recorded over the southeastern portion of the island of Oahu between 0800 HST and 2000 HST 5 June 2001, with a maximum of 90 mm reported at Manoa Lyon on the lee side of the Koolau Range (Fig. 5.2a). Appreciable rainfall ($\geq$ 10 mm) was also recorded along the windward side of the Waianae Range. The GOES-10 infrared image at 1530 HST 5 June shows a line of convective clouds with an east-west

orientation spanning southern Oahu and its adjacent waters (Fig. 5.2b). In addition to heavy rainfall, this rare early summer thunderstorm event also filled Oahu's skies with thunder and lighting. The heavy rainfall flooded a number of freeways and streets and triggered brief power failures for thousands of customers on the island.

There are no soundings taken routinely on the island of Oahu. Thus, the sounding from Lihue, Kauai (~ 130 km northwest of Oahu), taken at 0200 HST 5 June (Fig. 5.3) was used to represent the prestorm environment. This thermodynamic profile shows a weak trade-wind inversion between 850 hPa and 800 hPa. The level of free convection is near 900 hPa with positive buoyancy up to the tropopause. The lifted index of -2.6 °C and the Total Totals index of 44.8 °C are indicative of thunderstorm potential.

This summer thunderstorm case occurred from the combined effect of the decreased atmospheric stability in association with the upper-level low, and the orographic lifting of the easterly trade winds along the windward sides of the island of Oahu. Ramage (1971) and Schroeder (1977) suggest that heavy rain systems are frequently "anchored" to the mountainous terrain of the islands by a discontinuity in surface roughness – usually a coastline or mountain range. With easterlies in the low layer coupled with westerlies in the upper layer, the "anchoring" mechanism (Schroeder 1977) appears to be at work for this case because of persistent orographic lifting along the windward sides of the island at the low levels. The synoptic-scale system was well resolved by the AVN but the localized heavy rainfall on Oahu was not predicted.

The 10-km RSM/LSM and the 1.5-km MSM/LSM simulations for this case were initialized at 0200 HST 5 June 2001, ~ 10 hours prior to the heaviest rainfall. The simulated 12-h rainfall accumulation between 0800 HST and 2000 HST 5 June by the 10-

km RSM/LSM (Fig. 5.4a) shows heavy rains on the windward side of the island of Oahu, in agreement with the observations. However, the maximum rainfall total (~ 50 mm) is less than observed (~ 90 mm) and the location of the maximum rainfall is also displaced slightly northward as compared with observations. In addition, the RSM/LSM fails to provide the observed appreciable rainfall along the windward side of the Waianae Range. These discrepancies are related to the poor representation of the island's terrain by the RSM/LSM with a 10-km grid. In the RSM/LSM domain (Fig. 2.1a), the island of Oahu is represented as a single mountain with peak heights of 0.3 km, whereas in reality the island comprises two mountain ranges with peak heights in excess of 0.9 km. This results in erroneous forecasts by the RSM/LSM for the location of orographic lifting associated with the Waianae Range. The 10-m wind pattern in the RSM/LSM simulations is also rather uniform over entire Oahu (Fig. 5.4b).

The 1.5-km MSM/LSM reproduces the observed heavy rains on the eastern part of the island of Oahu (Fig. 5.5a). The model-predicted heaviest rainfall is comparable to that observed (100 mm in the model forecasts versus 90 mm in observations); but it is located on the windward side of the Koolau Range instead of the lee side as in observations. Appreciable rainfall (~ 20 mm) is also predicted along the windward side of the Waianae Range, consistent with observations (Figs. 5.2a and 5.5a). The rainfall amount over the Waianae Range is much less than that along the windward side of the Koolau Range. During the passage over the Koolau Range the easterly trade flow precipitates out considerable part of its moisture on the windward slopes and near the mountain ridge (Schroeder et al. 1977). Thus, the moisture content is relatively low by the time the

easterly trade flow reaches the Waianae Range with much less rainfall as compared with the rainfall along the Koolau Range (Fig. 5.2a).

Figure 5.5b shows the MSM/LSM simulated 10-m wind valid at 0800 HST 5 June. Easterly trade flow is prevalent over the entire domain. Trade wind speeds are reduced along the windward side of the Koolau Range and Waianae Range due to blocking, and are amplified along the lee slopes of both mountain ranges.

We have constructed longitude-height cross sections along 21.5 °N using the RSM/LSM and the MSM/LSM forecasted zonal wind speed and pressure vertical velocity (Fig. 5.6). With a single low mountain (~ 0.3 km high) in the RSM/LSM domain, winds are rather uniform with relatively weak vertical motions (Fig. 5.6a). In the MSM/LSM simulations (Fig. 5.6b), on the other hand, flow deceleration on the windward coast and amplification on the lee side of both mountain ranges are significant. Additionally, upward motion in the MSM/LSM is larger along the windward side of both mountain ranges than in the RSM/LSM. It appears that orographic lifting and feedback effects of convection are more significant with a high horizontal resolution.

5.2.2 Frontal system of 12 – 13 November 1996 on the island of Oahu

During the period of 1400 HST 12 November through 1400 HST 13 November 1996, a cold front extending from an extratropical low intensified as it moved southeastward towards the Hawaiian Islands (Wang et al. 1998). At 1400 HST 13 November, the extratropical low, with a central pressure of 975 hPa, was centered at 34 °N, 163 °W (Fig. 5.7a), and the associated cold front was east of the island of Kauai. The subtropical ridge, situated off the west coast of the United States, sustained moisture-laden southerly flow over the Hawaiian Islands. A persistent convective cloud band with a northeast-southwest

orientation in the prefrontal region (not shown) brought heavy rainfall to portions of the islands of Kauai and Oahu. The heaviest rainfall occurred on the island of Oahu. The 24-h rain totals between 1400 HST 12 November and 1400 HST 13 November exceeded 75 mm over most of the island. Over the southeastern and northwestern parts of the island that lie almost perpendicular to the prevailing southwesterly flow ahead of the cold front, the 24-h rainfall totals exceeded 100 mm (Fig. 5.7b). The large-scale low-level convergence associated with the frontal passage combined with the enhanced orographic lifting and abundant moisture from the south produced the heaviest rains in these areas.

For this case, the AVN provided reasonably good 24-h forecasts of the development and propagation of the cold front (Wang et al. 1998). Nevertheless, the coarse horizontal resolution prevented an accurate portrayal of the mesoscale structure associated with the prefrontal convection and the interaction between airflow and the island topography. As a result, the AVN did not predict the localized heavy rainfall in association with this frontal passage.

In our study, the 10-km RSM/LSM and the 1.5-km MSM/LSM were initialized at 1400 HST 12 November 1996. The 24-h RSM/LSM-forecasted 10-m wind (Fig. 5.8a) shows that the southwesterly flow associated with the cold front converges with the southeasterly flow from the subtropical ridge east of the island of Kauai. The wind pattern over the island of Oahu is rather uniform (Fig. 5.8a). The simulated 24-h rainfall accumulation between 1400 HST 12 November and 1400 HST 13 November by the RSM/LSM shows heavy rain (~ 90 mm) only over the southern part of Oahu (Fig. 5.8b). This is the region where orographic lifting of the southerly flow would occur with only a single mountain range in the model domain. The RSM/LSM also simulates heavy rains

over the southern parts of Kauai and Maui, related to orographic lifting of the southerly flow.

The 24-h MSM/LSM-forecasted 10-m wind valid at 1400 HST 13 November (Fig. 5.9a) shows southwesterly winds over the entire Oahu domain with apparent orographic lifting along the south sides of the Koolau and Waianae Ranges over the southeastern and northwestern parts of the island. The simulated 24-h rainfall accumulation ending at 1400 HST 13 November by the 1.5-km MSM/LSM (Fig. 5.9b) shows heavy rain over the entire island with the heaviest rainfall along the south sides of the Koolau and Waianae Ranges. This is consistent with the observed rainfall distribution. The model-predicted heaviest rainfall amount is 150 and 90 mm over the northwestern and southeastern parts of the island, respectively. These values are comparable to the observed rainfall amount. The model also simulates appreciable rainfall amounts over the central part of the Koolau Range.

5.2.3 1 – 2 November 2000 flood on the island of Hawaii

During 1–2 November 2000 a line of thunderstorms with a northeast-southwest orientation brought heavy rains to the island of Hawaii. Between 1400 HST 1 November and 1400 HST 2 November, the southeastern part of the island and the Hilo area reported rainfall of more than 700 mm with amounts reaching nearly 1000 mm recorded at Kapapala Ranch on the east rift of the Mauna Loa (Fig. 5.10a). In the composite radar image from 0912 HST 2 November (Fig. 5.10b) an area of deep convection was observed to extend from the southwestern to the northeastern part of the island. This was an extreme rain event that impacted the south and east sides of the island of Hawaii. Maximum hourly rain rates were over 100 mm h^{-1}, with a 24-h accumulation that fell just

short of setting a state record. Stream gauge records show that this was the most intense, widespread rain event in 20 years for Hawaii. At several sites, the maximum streamflow from this storm established records. The extensive flash floods that resulted are estimated to have caused $70M property damage while the impact on roads and other infrastructure persisted for weeks.

The 250-hPa height and wind analyses for 1400 HST 1 November 2000 (Fig. 5.11a) showed a trough and a low center to the west of the Hawaiian Islands. A subtropical westerly jet stream with maximum wind speed in excess of 40 m s^{-1} was evident to the east of the low. The low drifted slowly westward and eventually moved away from the island chain. The surface analysis at 1400 HST 1 November showed the establishment of an inverted trough over the Hawaiian Islands in association with the upper-level low (Fig. 5.11b). Also evident in Figure 4.11b was a mid-latitude cold front located about 800 km to the northwest of the island of Kauai.

Southeasterly winds of 5 m s^{-1} prevailed over the state of Hawaii (Fig. 5.11b). Convergence over a deep layer (1000 hPa – 400 hPa) and strong divergence between 300 hPa and 100 hPa were present over the Hawaiian Islands (Fig. 5.12), with high relative humidity at both the 300-hPa (Fig. 5.13a) and the 850-hPa levels (Fig. 5.13b). The Hawaiian Islands were on the anticyclonic side of the jet entrance region and to the east of the mid-latitude trough in the upper troposphere. At low levels, they were under the influence of the southeasterly flow.

The sounding taken at Hilo on the island of Hawaii at 0200 HST 1 November 2000 (Fig. 5.14) is used to examine the pre-storm environment. This sounding shows a weak trade-wind inversion at ~ 800 hPa. A moist layer is evident between 650 and 600 hPa.

The rain storms were also fueled by the remnants of tropical storm Paul, which developed in the monsoon trough off the west coast of Mexico on 22 October 2000. Surface analyses and satellite images (not shown) indicate that Paul became a tropical storm on 26 October and dissipated by 29 October, after traveling about halfway to the Hawaiian Islands. Its remnants continued westward and, as they approached the island of Hawaii on 1 November, were amplified by the aforementioned upper-level system. The high relative humidity seen over the island of Hawaii at 850 hPa in Figure 5.13b is related to the remnants of Paul. For this flash flood case, the synoptic-scale pattern was well predicted by the AVN, but the observed excessive localized rainfall, > 700 mm in 24 h, was completely missed.

The 10-km RSM/LSM and the 3-km MSM/LSM simulations for this case were initialized at 0200 HST 1 November 2000, ~ 17 hours prior to the heaviest rainfall. Figure 5.15a shows the RSM/LSM-forecasted 24-h rainfall accumulation between 1400 HST 1 November and 1400 HST 2 November. Heavy rains are predicted toward the lee sides of the two mountain tops (Mauna Kea and Mauna Loa) on the island of Hawaii with a maximum rainfall total of 230 mm. This is only one fourth of the recorded maximum rainfall total of 900 mm. In the RSM/LSM domain with a 10-km grid (Fig. 2.1a), Mauna Kea and Mauna Loa have peak heights of 2.4 km and 2.7 km, respectively. These heights are about 1.7 km lower than the actual heights for both mountain peaks. Thus, orographic lifting of the southeasterly flow along the windward slopes of these two mountain peaks is less. Also due to the lower terrain height in the model, the RSM/LSM is able to bring the precipitation to the top of the mountains under a weak trade-wind inversion (see Fig. 5.14). The RSM/LSM also simulates appreciable rainfall over the eastern part of the

island, but the rainfall total is much less than the observed total (120 mm versus 700 mm). The RSM/LSM-simulated 10-m winds valid at 1400 HST 2 November (Fig. 5.15b) show that the eastern part of the island is on the windward side of the prevailing southeasterly flow.

In comparison, the 3-km MSM/LSM reproduces the observed heavy rainfall over the southeastern part and the Hilo area on the island of Hawaii (Fig. 5.16a). The model-forecasted maximum rainfall amount is 600 mm for both areas. This amount is about 300 mm and 100 mm smaller than that observed for the southeastern part of the island and the Hilo area, respectively. The MSM/LSM also produces a considerable amount of rainfall over the northeastern part and the western part (Kona area) of the island, consistent with the observed rainfall distribution. However, the model overestimates the maximum rainfall total by about 200 mm for these two areas (Figs. 5.10a and 5.16a). In the corresponding 10-m wind field valid at 1400 HST 2 November (Fig. 5.16b), orographic lifting is apparent over the southeastern part and the Hilo area on the island of Hawaii. Orographic lifting is also important in producing appreciable rainfall over the northeastern part of the island as the southeasterly winds are forced to rise along the windward slopes of the Kohala Mountains.

5.2.4 2 – 3 November 1995 heavy rainfall on the island of Kauai

During the late morning hours of 3 November 1995, a line of thunderstorms with a northeast-southwest orientation in association with a kona low system (Fig. 5.17) brought heavy rainfall to the island of Kauai. Between 1400 HST 2 November and 1400 HST 3 November, the north and east sides of the island recorded rainfall of 150 – 220 mm, while the south and west sides of the island received 50 – 100 mm of rain (Fig. 5.18). The

heavy rain caused flooding in several areas of the northern and eastern portions of the island, resulting in road closures and evacuations. Low ceiling, poor visibility, and strong winds during this event resulted in the cancellation of 17 scheduled airline flights between the islands of Kauai and Oahu.

The synoptic and mesoscale environment associated with the severe weather brought by this kona low have been discussed by Businger et al. (1998). Wang et al. (1998) compare the AVN forecast and the nested RSM forecast for this heavy rainfall event. They note that while the RSM output provides much better 24-h forecast guidance than the AVN, the rainfall amount simulated by the RSM is only about one-third of that observed. Additionally, the area of heavier rainfall is simulated over the southern half of the island instead of the northeastern part of the island, as observed. They suggest that the localized rainfall resulting from the interaction between the large-scale flow and the island terrain is not well simulated by the RSM at a resolution of 10-km.

Our 10-km RSM/LSM and 1.5-km MSM/LSM simulations for this case were initialized at 1400 HST 2 November 1995, ~ 18 h prior to the heaviest rainfall. The RSM/LSM simulated 24-h rainfall accumulation between 1400 HST 2 November and 1400 HST 3 November have totals similar to Wang et al. (1998). Heavy rains are forecasted mainly over the southern half of the island with a maximum rainfall amount of 100 mm, ~ 120 mm lower than observations (Fig. 5.19a). The simulated 10-m wind (Fig. 5.19b) shows relatively uniform southerly flow for entire Kauai. With a peak height of 0.7 km for Kauai in the RSM/LSM domain at a 10-km grid (Fig. 2.1a), ~ 0.8 km lower than the actual height, orographic lifting is only partially resolved.

In comparison, the 1.5-km MSM/LSM provides a rainfall pattern much closer to observations with rainfall totals of 150 – 200 mm on the eastern part of the island of Kauai and 100 – 150 mm on the southern part of the island (Fig. 5.20a). These values are in good agreement with observations. The rainfall maximum on the eastern part of the island occurs where the low-level deflected flow merges with the air flow passing through the Kauai Channel to the east of the island (Fig. 5.20b). The southern part of the island is on the windward side of the large-scale southerly flow (Fig. 5.20b). Orographic lifting appears to be important for the production of rainfall there. Heavy rainfall is also evident over the southern part of the island of Niihau (~ 200 mm) which is on the windward side and over the ocean channel between the islands of Niihau and Kauai (~ 120 mm) where the deflected air flows by both islands converge (Fig. 5.20a). The WSR-88D radar image at 1400 HST 3 November 1995 (Fig. 7 in Businger et al. 1998) also indicates convective activity in these areas. One deficiency in the MSM/LSM simulations for this case is that, in contrast to observations, the MSM/LSM predicts little rainfall over the northern part of the island of Kauai (Figs. 5.18 and 5.20a).

5.3 Conclusions and discussion

We have simulated four heavy rainfall cases over the Hawaiian Islands using the MSM/LSM with resolutions $\leq$ 3 km and the RSM/LSM with a 10-km resolution. Observations show large spatial variability in rainfall distribution in association with these heavy rainfall events, related to the complex terrain and local winds. For these heavy rainfall events, the synoptic-scale pattern was reasonably well predicted by the

operational AVN runs but the observed localized heavy rains were poorly predicted due to its coarse horizontal resolution.

The 10-km RSM/LSM shows improvement over the AVN in simulating localized heavy rain associated with these events. The main improvements are seen in the location of heavy rainfall and the impact of terrain on local weather. Even though improvements are noticed, there are still appreciable discrepancies between the RSM/LSM simulations and observations. The major problems are due to the inadequate resolution and its inability to accurately represent the local terrain. The peak heights of the mountains on the islands of Oahu, Hawaii, and Kauai in the model domains are only about 30%, 60% and 50% of their actual heights, respectively. This implies that the Froude number (Fr = U/Nh, where U is the upstream wind speed, N is the Brunt-Väisälä frequency, and h is the height of the mountain) is overestimated by a factor of 3.0, 1.7 and 2.0 for Oahu, Hawaii and Kauai, respectively, under the same large-scale environment. Thus, the actual flow regime may be different from that forecasted by the RSM/LSM. In the Oahu domain, the 10-km RSM/LSM resolves only one mountain instead of two mountain ranges. This results in erroneous forecasts associated with the location of orographic lifting. Due to the presence of complex island terrain with heterogeneous surface properties, Chen et al. (2003) show that it is necessary to use a high-resolution mesoscale model with improved surface boundary conditions to better capture the diurnal cycles of surface variables and local winds in Hawaii.

The high-resolution MSM/LSM has better capability in simulating localized rainfall distributions and airflows associated with these heavy rainfall events than the 10-km RSM/LSM. The peak heights of the mountains on the islands of Oahu, Hawaii, and Kauai

in the MSM/LSM domains are about 70%, 90% and 90% of their actual heights, respectively. As a result, the interaction of large-scale airflow with local terrain, such as orographic lifting and enhancement of precipitation, would be better resolved by the MSM/LSM than the RSM/LSM. This is clearly illustrated in the four cases presented here. For the 5 – 6 June 2001 summer thunderstorms on Oahu, the MSM/LSM not only simulates the observed heavy rain along the windward side of the Koolau Range, but also produces appreciable rainfall along the windward side of the Waianae Range. For the frontal case of 12 – 13 November 1996 on Oahu, the MSM/LSM replicates the observed heavy rain over the northwestern and the southeastern parts of the island. For the 1 – 2 November 2000 flash flood case over the island of Hawaii, heavy rain (> 600 mm) over the southeastern part of the island and the Hilo area are simulated by the MSM/LSM. The model is also successful in reproducing the observed heavy rain over the eastern and southern parts of the island of Kauai for the kona storm case of 2 – 3 November 1995.

Despite the encouraging performance of the MSM/LSM in simulating these heavy rainfall events, deficiencies in the model simulations are noted. For the summer thunderstorm case on Oahu and the November 2 – 3 1995 flood case on Kauai, the model simulated rainfall is not well distributed in accordance with observations. For the 1 – 2 November 2000 flash flood case on the island of Hawaii, the model underestimates the heavy rainfall over the southeastern part of the island and the Hilo area.

A new precipitation physics package has been developed at the Yonsei University in Korea (Hong et al. 2003) and has recently been incorporated into the RSM and MSM. Sensitivity tests of the precipitation schemes using the MSM/LSM are underway. Additional improvements could be made by including remotely sensed data from radar

and satellites in the initial conditions (Wang et al. 1998). These include the satellite-derived moisture, satellite-derived cloud drift and surface winds, the low-level wind profiles and rain rates from a network of four WSR-88D radars in Hawaii, and the Global Positioning System (GPS)-integrated water vapor data (Foster et al. 2003).

Kuo et al. (1993) use a simple method to assimilate precipitable water measurements into a mesoscale model. They show that the improved analysis due to assimilation leads to improved short-range precipitation forecasts. Guo et al. (2000) perform a series of real-data assimilation experiments using the MM5 four-dimensional variational data assimilation (4DVAR) system with a full physics adjoint. The real data consist of GPS precipitable water, surface dewpoint, rainfall, and wind profiler data. Their system is able to reproduce the observed precipitation pattern and amount. Zou and Kuo (1996) and Xiao et al. (2000) also show improved model forecasts by incorporating the Special Sensor Microwave/Imager (SSM/I)-measured precipitable water and rain rate into a mesoscale model, especially over the data-sparse oceanic regions.

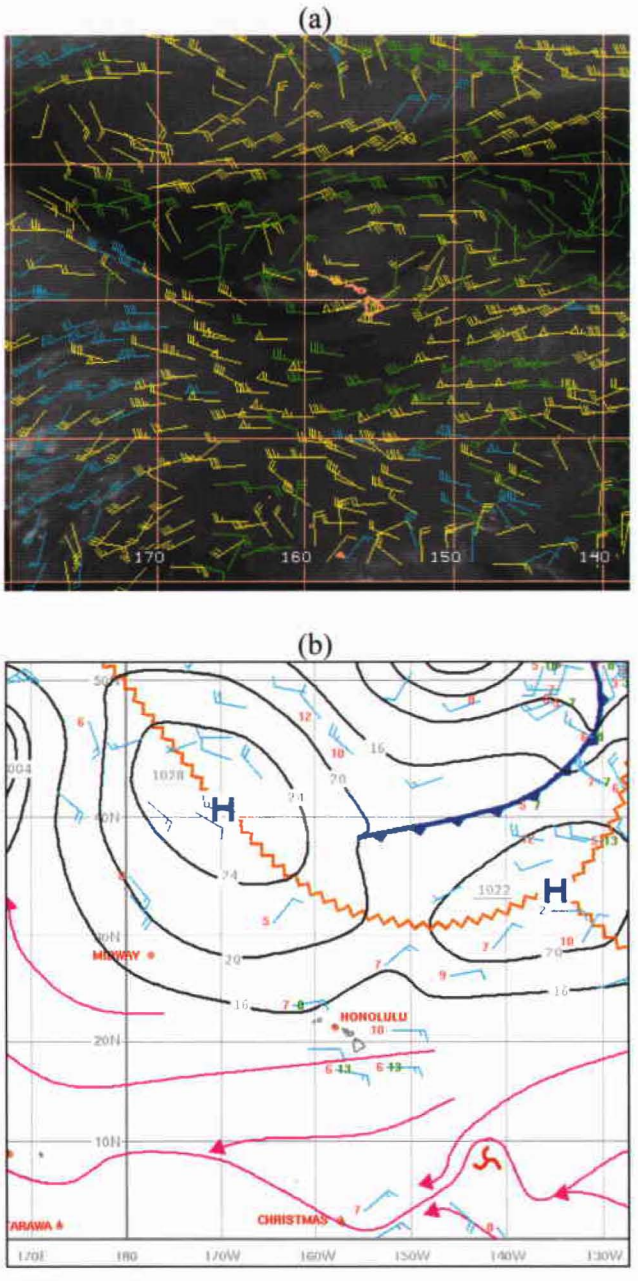

Figure 5.1. (a) GOES-10 mid-upper level wind analyses (blue, yellow, and green barbs refer to the mean winds within 100 to 250 hPa, 251 to 350 hPa, and 351 to 500 hPa, respectively) from 0500 HST June 5 2001 (Courtesy of the University of Wisconsin-Madison); and (b) surface chart at 0200 HST June 5 2001 (adapted from the subjective analyses by forecasters at the Weather Forecast Office Honolulu). In (a), conventional wind barbs (pennants = 25 m s^{-1}, long barbs = 5 m s^{-1}, and short barbs = 2.5 m s^{-1}) are used. In (b), isobars are plotted every 4 hPa.

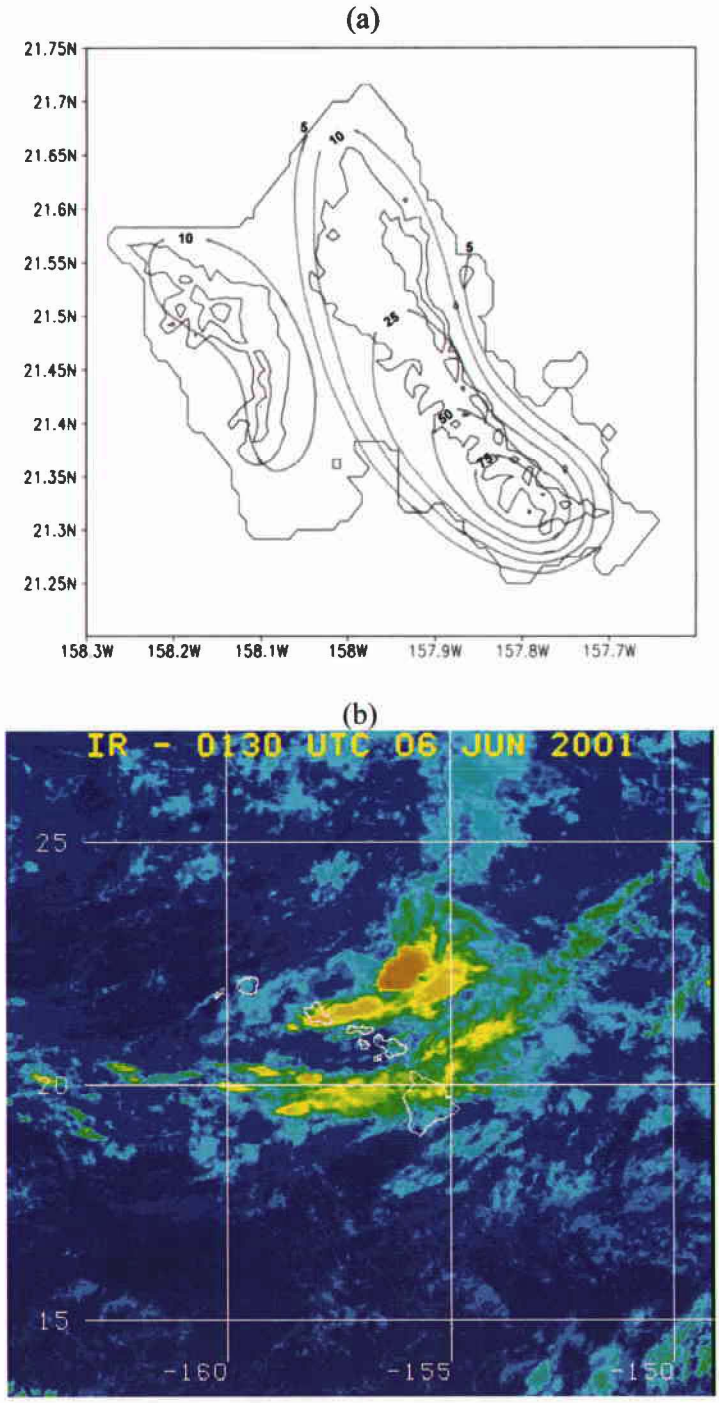

Figure 5.2. (a) 12-h accumulated rainfall from 0800 HST to 2000 HST 5 June 2001 (unit: mm), with the contours plotted for 5, 10, 25, 50 and 75 mm; and (b) GOES-10 infrared satellite image from 1530 HST 5 June 2001.

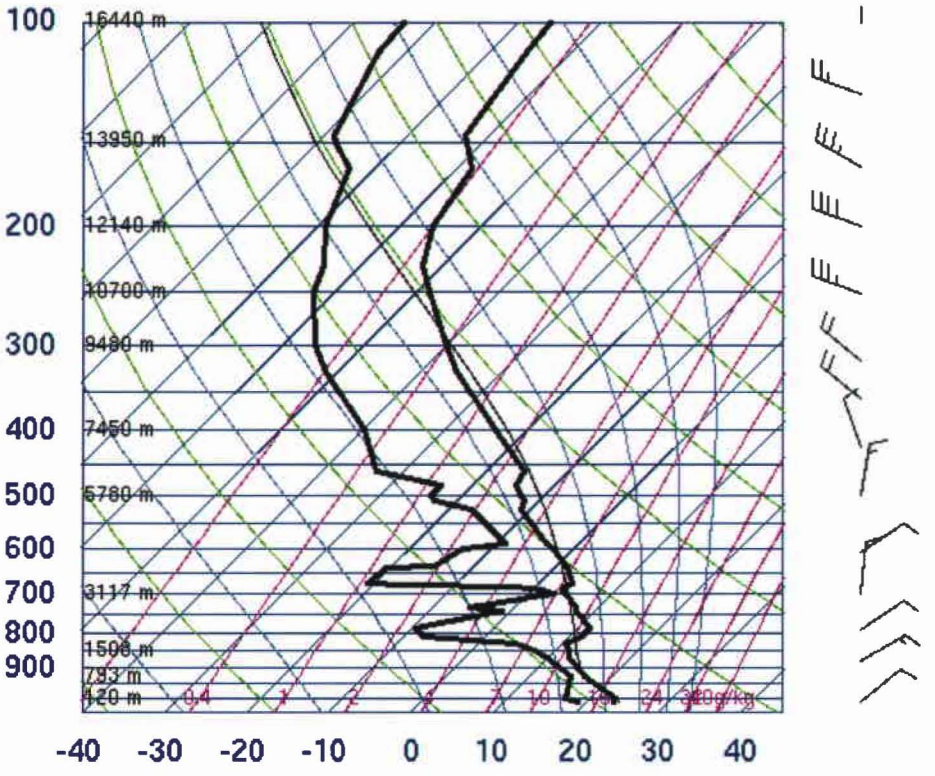

Figure 5.3. Temperature, dew point, and wind profiles from Lihue, Kauai (PHLI), from 0200 HST 5 June 2001 (courtesy of the University of Wyoming). Wind barbs follow the same convention as Fig. 5.1a.

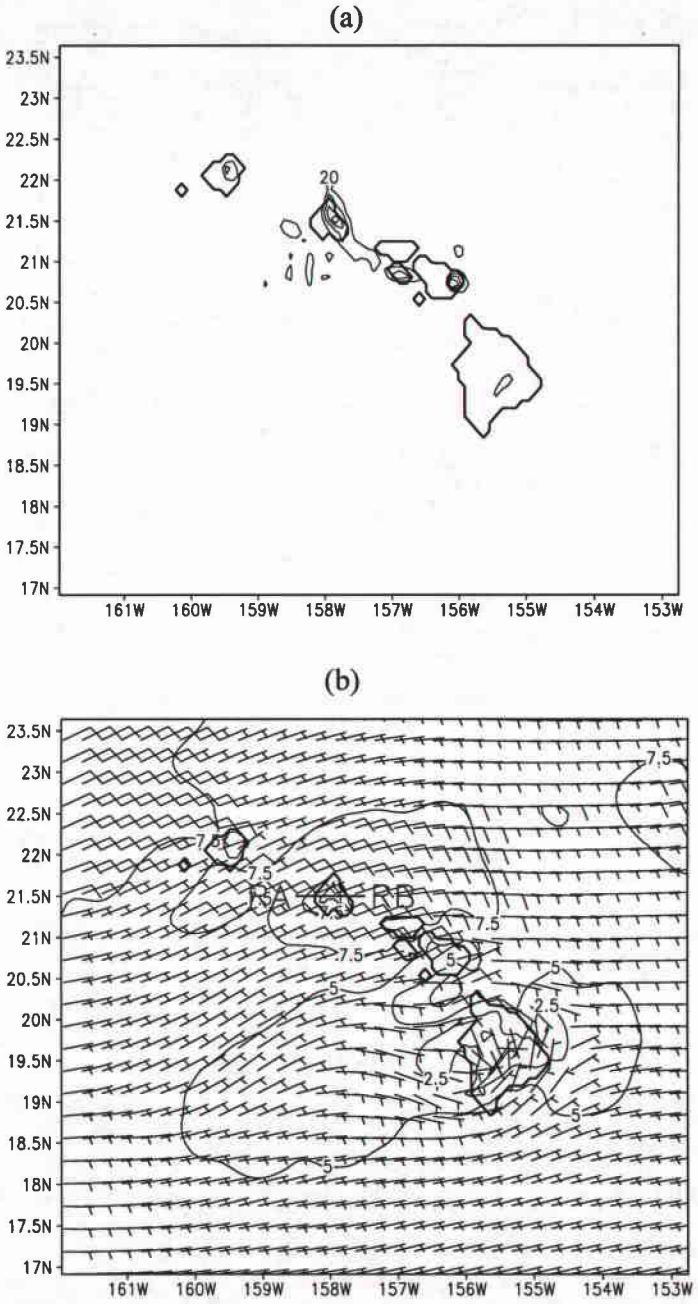

Figure 5.4. RSM/LSM-simulated (a) 12-h accumulated rainfall (mm) from 0800 HST to 2000 HST 5 June 2001 with a contour interval of 10 mm; and (b) 10-m wind (m s^{-1}) valid at 0800 HST 5 June 2001 with a contour interval 2.5 m s^{-1}. The wind barbs in (b) are drawn every three grid points in both directions. The line, RA-RB, in (b) denotes the position of the longitude-height cross section shown in Fig. 5.6a. Full barb and half barb represent 10 and 5 m s^{-1}, respectively. This same notation for wind barbs is used hereafter unless otherwise specified. The RSM/LSM run was initialized at 0200 HST 5 June 2001.

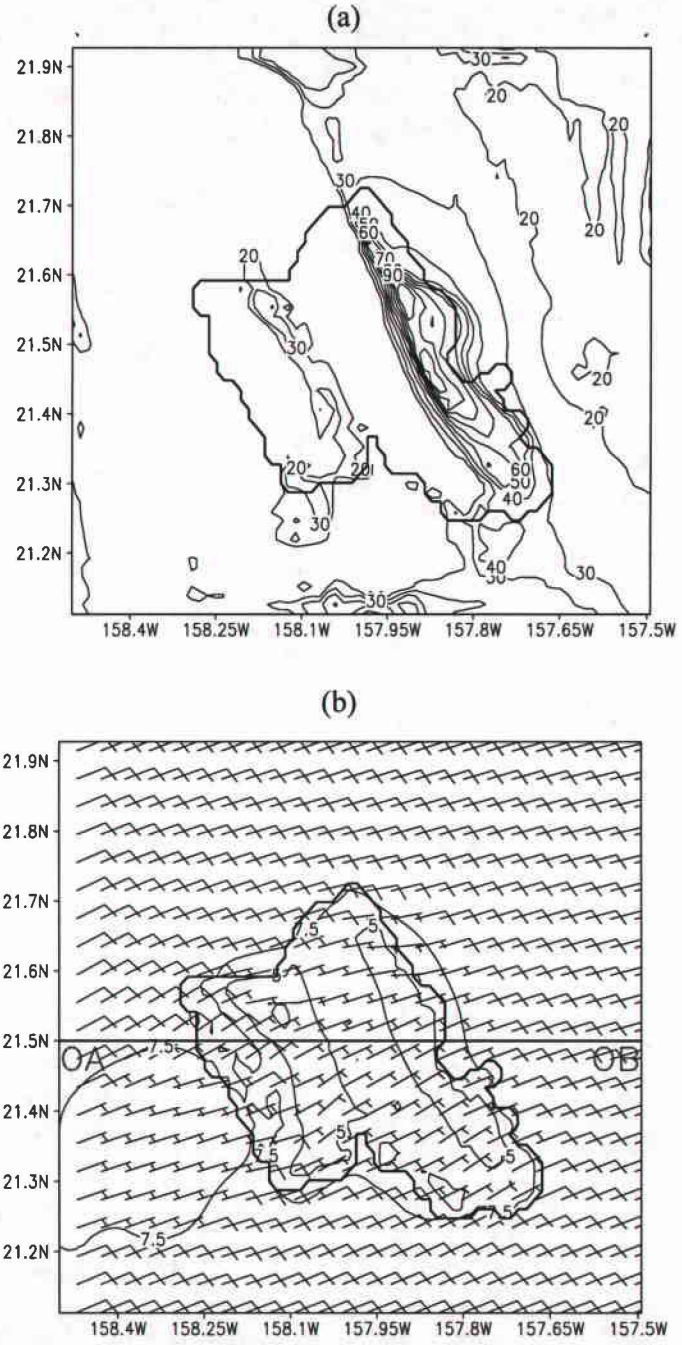

Figure 5.5. MSM/LSM-simulated (a) 12-h accumulated rainfall (mm) from 0800 HST to 2000 HST 5 June 2001 with a contour interval of 10 mm; and (b) 10-m wind (m s^{-1}) valid at 0800 HST 5 June 2001 with a contour interval of 2.5 m s^{-1}. The wind barbs in (b) are drawn every three grid points in both directions. The line, OA-OB, in (b) denotes the position of the longitude-height cross section shown in Fig. 5.6b. The MSM/LSM run was initialized at 0200 HST 5 June 2001.

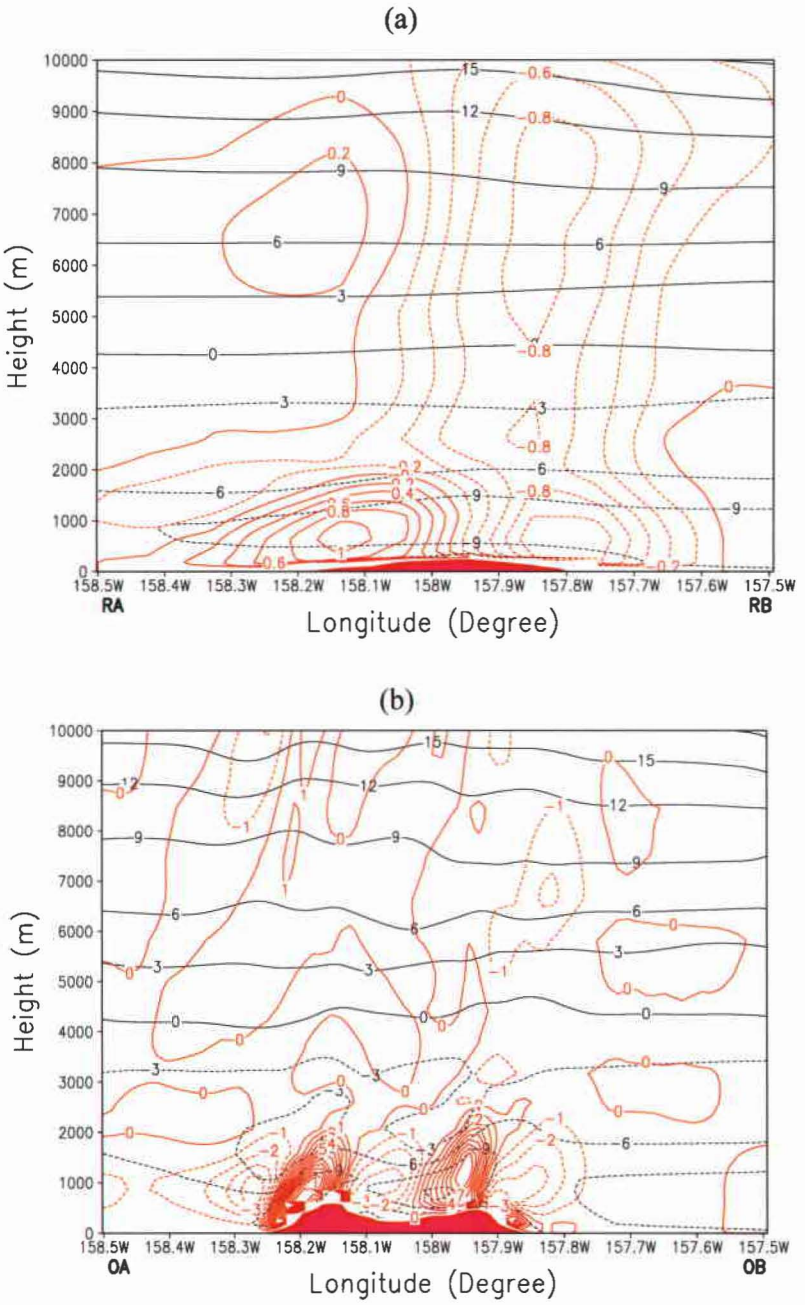

Figure 5.6. Longitude-height cross section along 21.5 °N constructed from (a) the RSM/LSM and (b) the MSM/LSM-forecasted zonal wind speed (m s^{-1}, black lines) and pressure vertical velocity (Pa s^{-1}, red lines) valid at 0800 HST 5 June 2001. Contours for zonal wind speed are drawn for every 3 m s^{-1}. Contour interval for pressure vertical velocity is 0.2 Pa s^{-1} in (a) and 1 Pa s^{-1} in (b). The locations of the cross section, RA-RB and OA-OB, are indicated by solid lines in Figs. 5.4b and 5.5b, respectively. The RSM/LSM and the MSM/LSM runs were initialized at 0200 HST 5 June 2001.

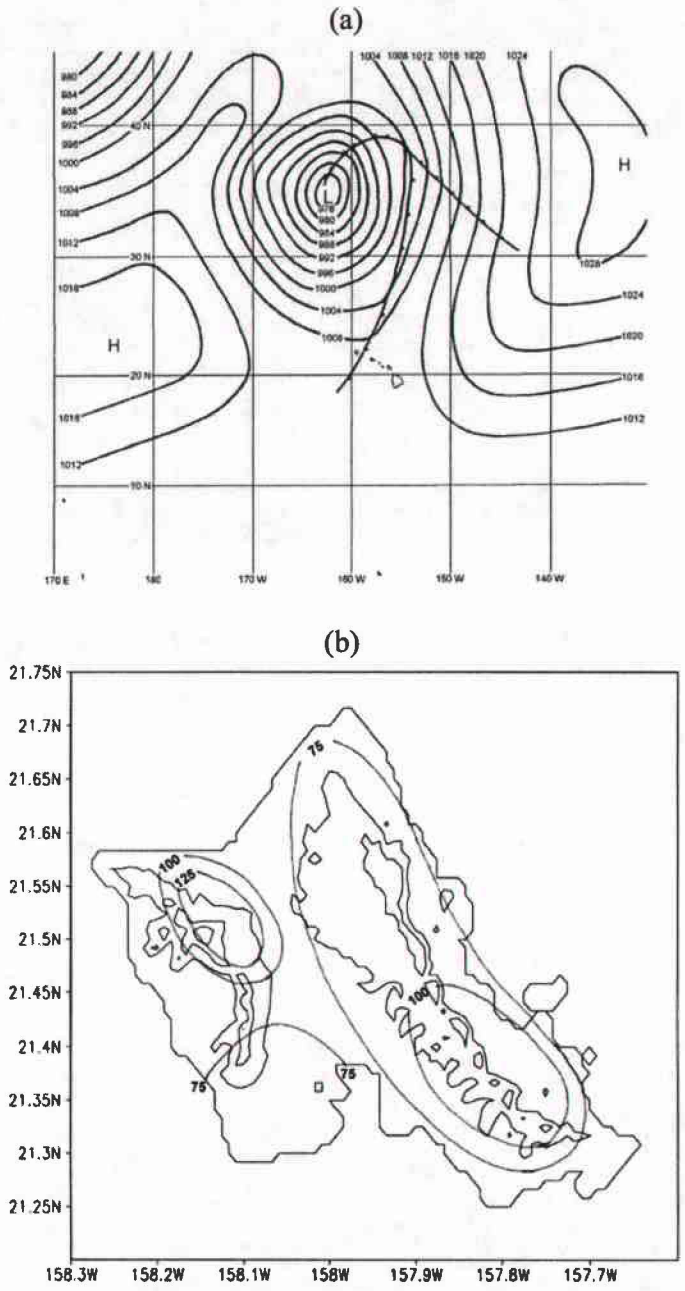

Figure 5.7. (a) Surface chart at 1400 HST 13 November 1996 with isobars plotted every 4 hPa (from Wang et al. 1998); and (b) 24-h accumulated rainfall (mm) from 1400 HST 12 November to 1400 HST 13 November 1996. Rainfall contours are drawn for every 25 mm.

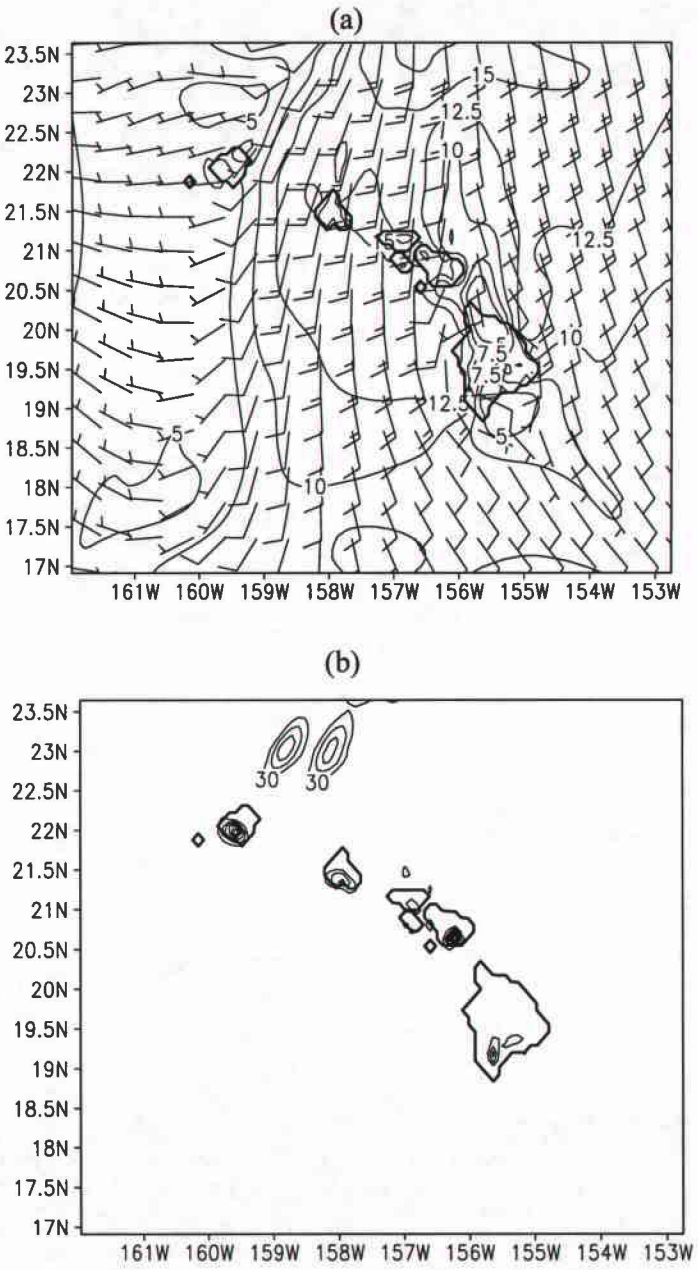

Figure 5.8. RSM/LSM-predicted (a) 10-m wind (m s^{-1}) valid at 1400 HST 13 November 1996 with a contour interval of 2.5 m s^{-1}; and (b) 24-h accumulated rainfall (mm) ending at 1400 HST 13 November 1996 with a contour interval of 30 mm. The wind barbs in (a) are drawn every five grid points in both directions. The RSM/LSM run was initialized at 1400 HST 12 November 1996.

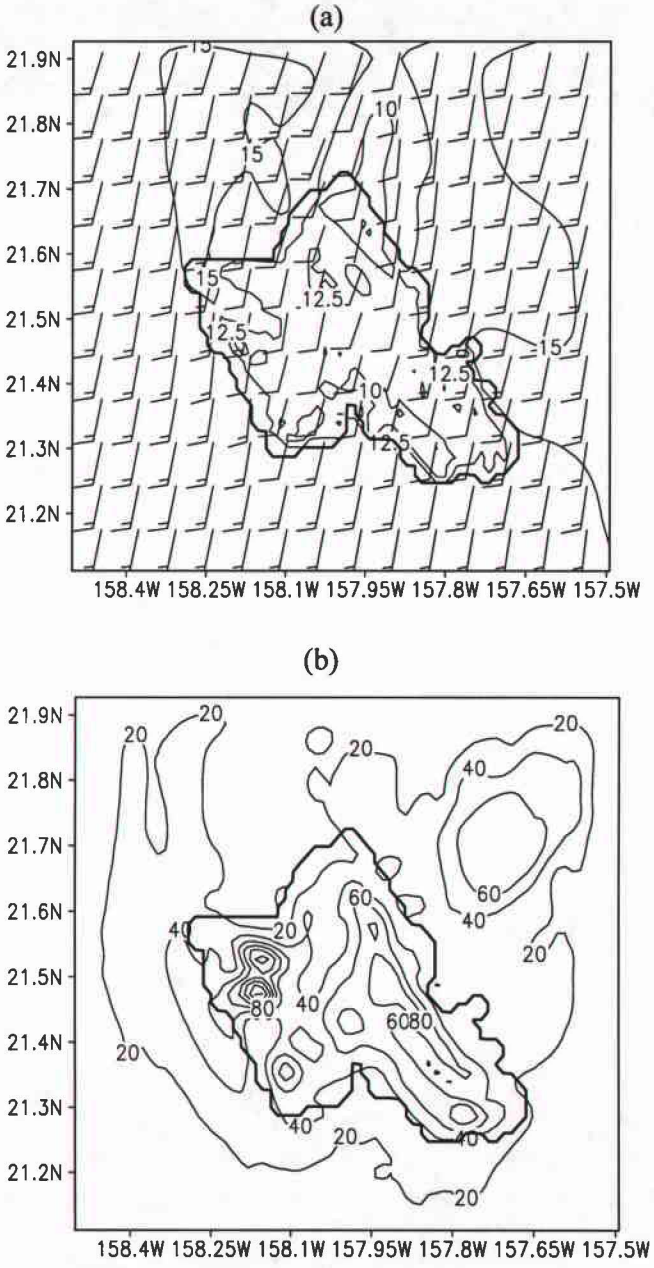

Figure 5.9. Same as Fig. 5.8 except for the MSM/LSM simulations. Contour interval is 20 mm in (b). The MSM/LSM run was initialized at 1400 HST 12 November 1996.

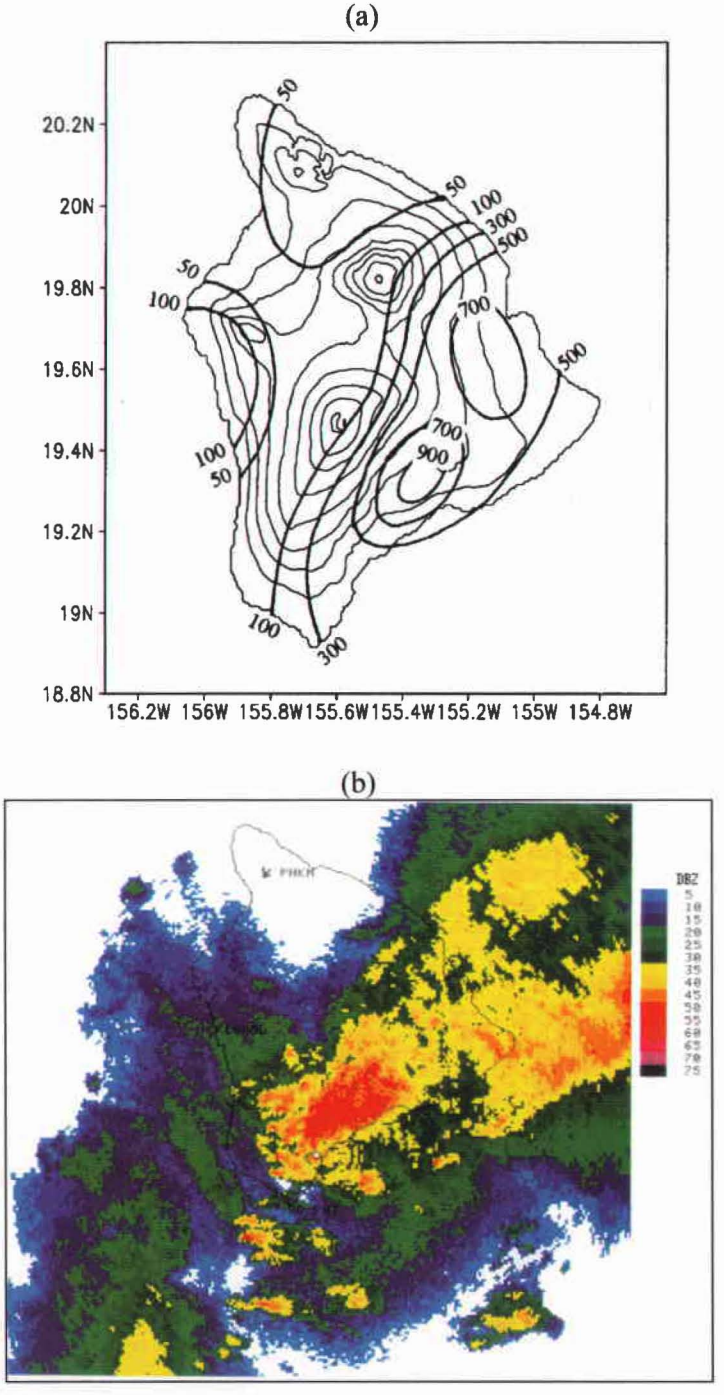

Figure 5.10. (a) 24-h accumulated rainfall (mm) from 1400 HST 1 November to 1400 HST 2 November 2000 over the island of Hawaii; and (b) composite radar image at 0912 HST 2 November 2000 obtained by the WSR-88D Radar installed at the South Point of the island of Hawaii. In (a), rainfall isopleths are plotted for 50, 100, 300, 500, 700, and 900 mm.

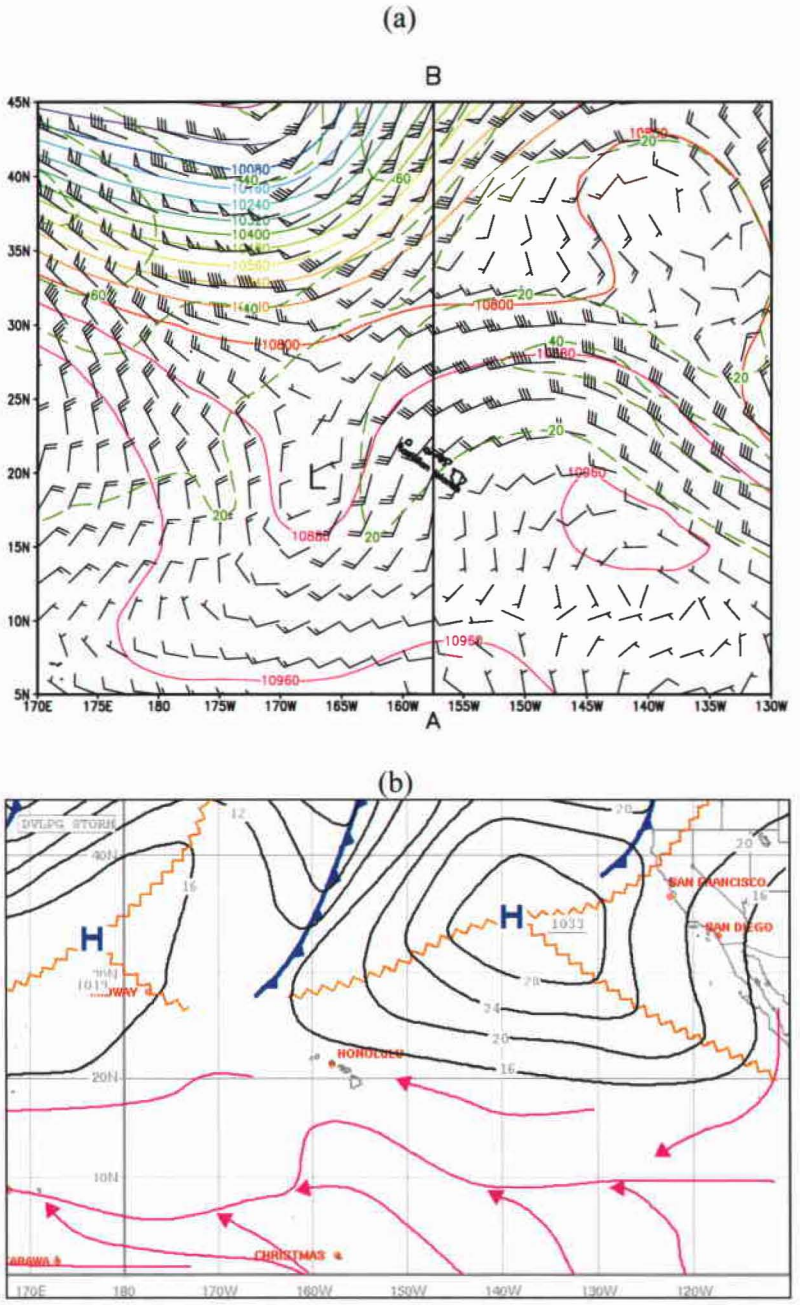

Figure 5.11. (a) 250-hPa geopotential height (gpm, solid lines) and horizontal winds (m s^{-1}, barbs and dashed lines) based on the NCEP/NCAR Reanalysis data, and (b) surface analyses (adapted from the subjective analyses by forecasters at the Weather Forecast Office Honolulu) for 1400 HST 1 November 2000. Isotachs are plotted every 20 m s^{-1} in (a) with one pennant, full barb and half barb representing 50, 10 and 5 m s^{-1}, respectively. In (b), isobars are plotted every 4 hPa. The line, A-B in (a), denotes the location of the cross section in Fig. 5.12.

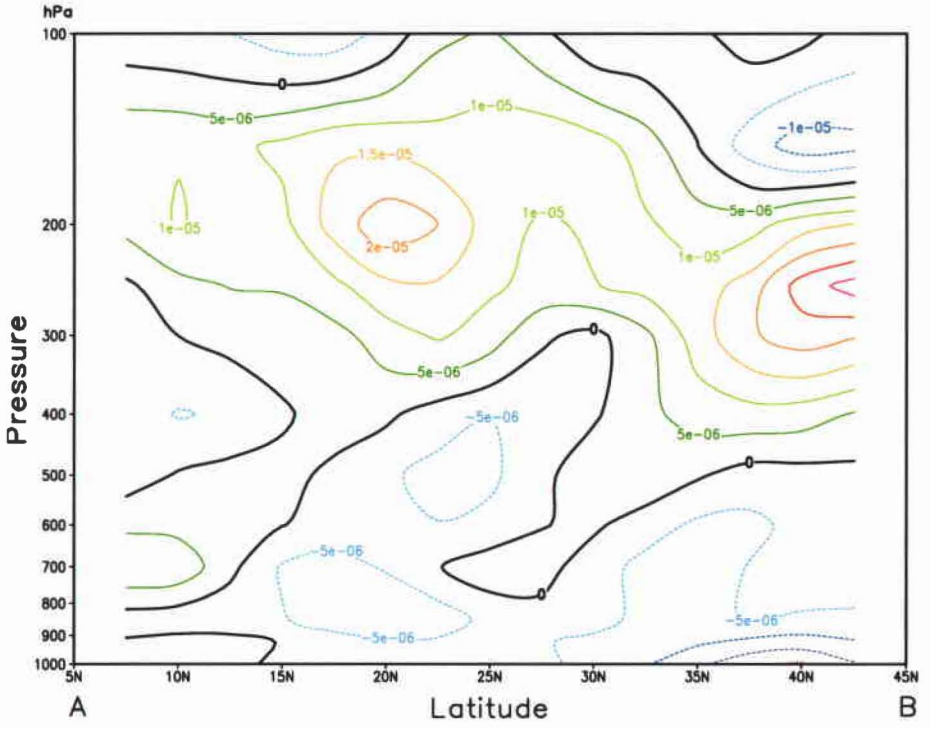

Figure 5.12. Latitude-height cross section along 157.5 °W showing the horizontal divergence (s^{-1}) based on the NCEP/NCAR reanalysis data. The contour interval is 5×10^{-6} s^{-1}. The position of the cross section, A-B, is shown in Fig. 5.11a.

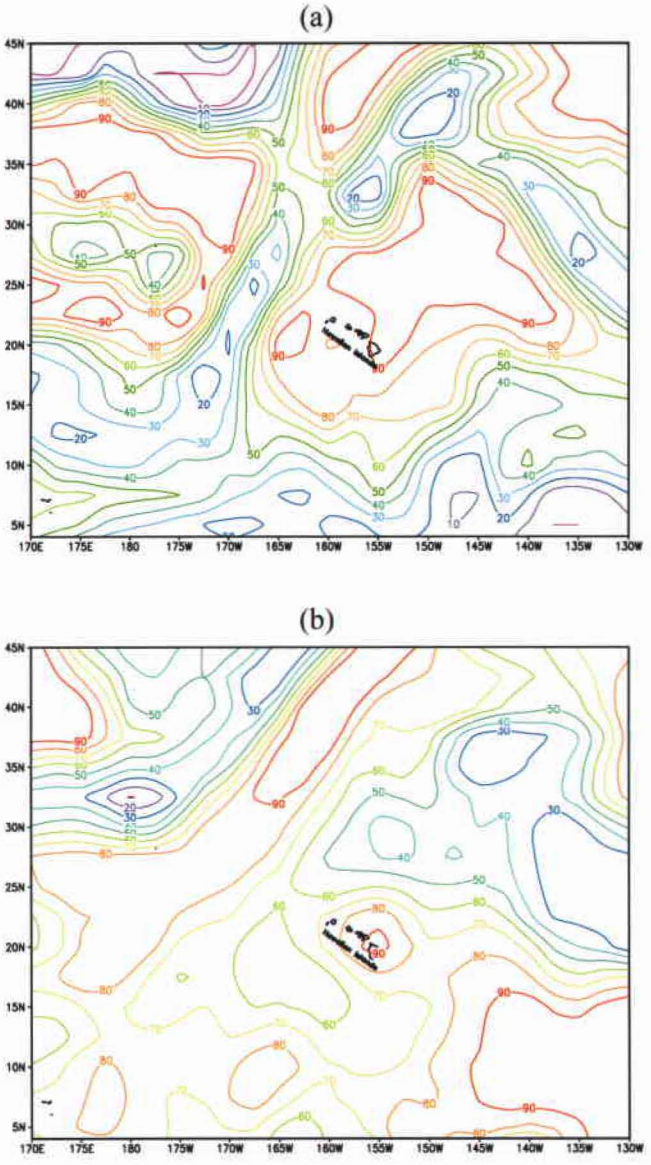

Figure 5.13. Relative humidity (%) at (a) 300 hPa and (b) 850 hPa for 1400 HST 1 November 2000 based on the NCEP/NCAR reanalysis data. Contours are plotted for every 10%.

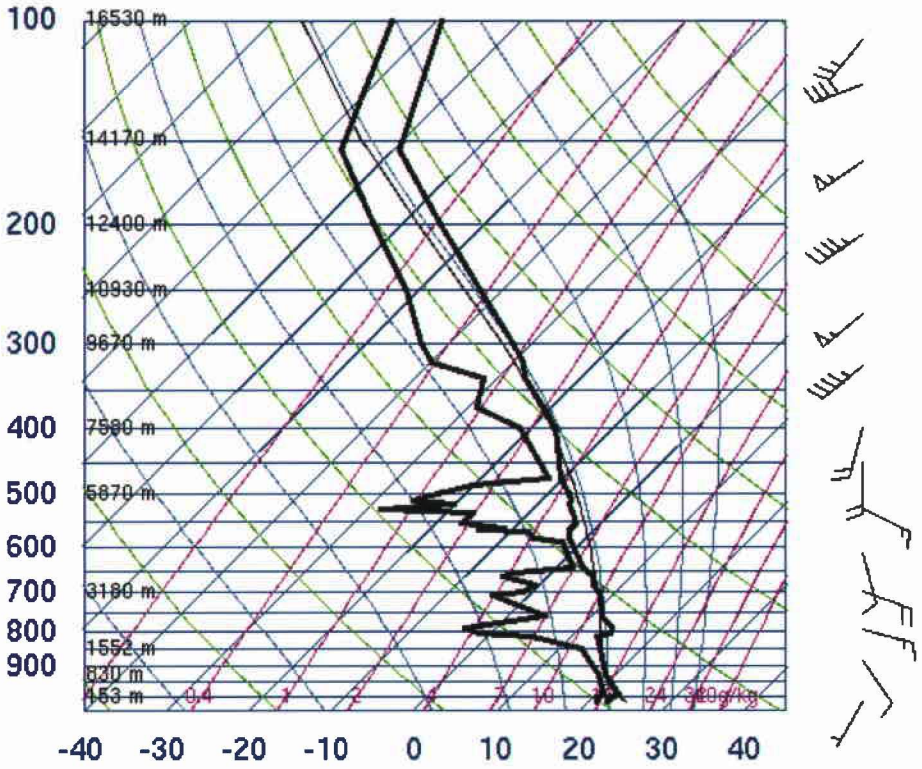

Figure 5.14. Temperature, dew point, and wind profiles from Hilo, island of Hawaii (PHTO), from 0200 HST 1 November 2000 (courtesy of the University of Wyoming). The convention of wind barbs is the same as in Fig. 5.1a.

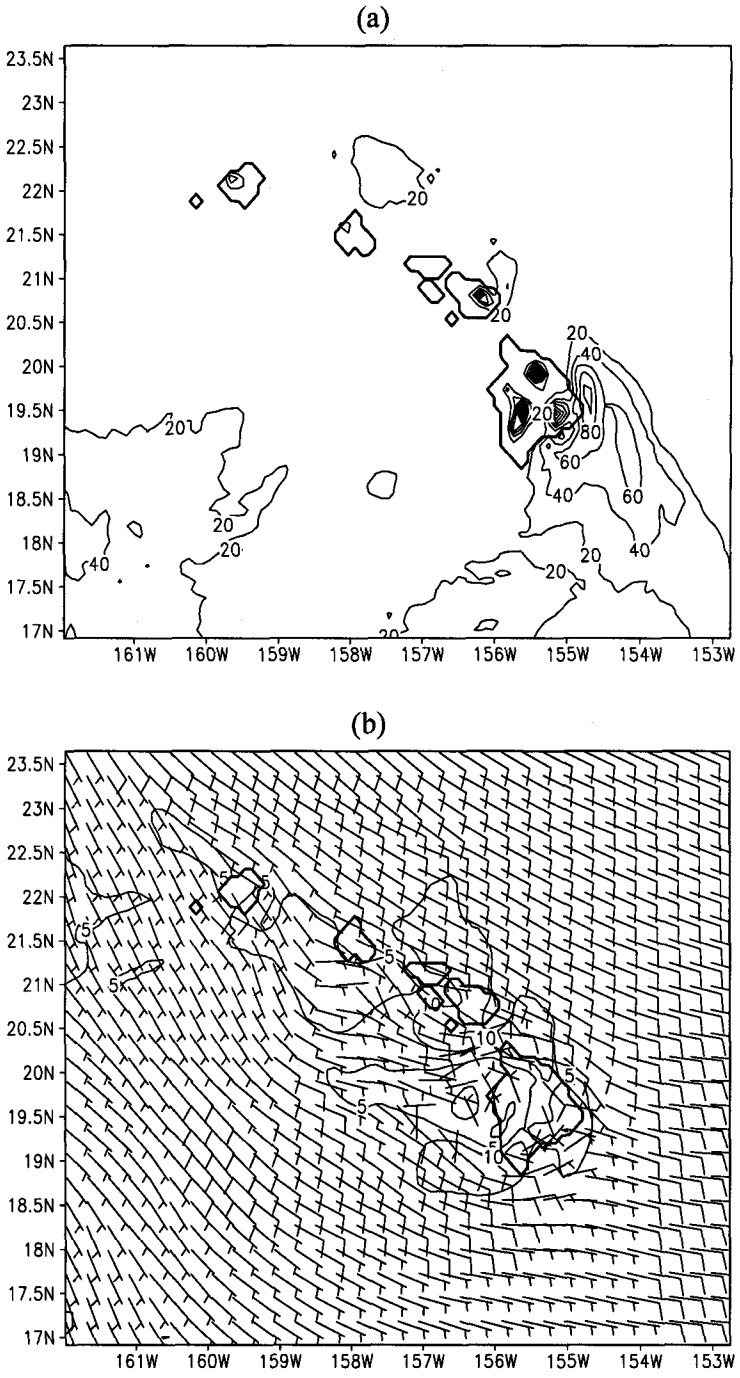

Figure 5.15. RSM/LSM-simulated (a) 24-h accumulated rainfall (mm) from 1400 HST 1 November to 1400 HST 2 November 2000 with a contour interval of 20 mm; and (b) 10-m wind (m s^{-1}) valid at 1400 HST 2 November 2000 with a contour interval of 5 m s^{-1}. The wind barbs in (b) are drawn every three grid points in both directions. The RSM/LSM run was initialized at 0200 HST 1 November 2000.

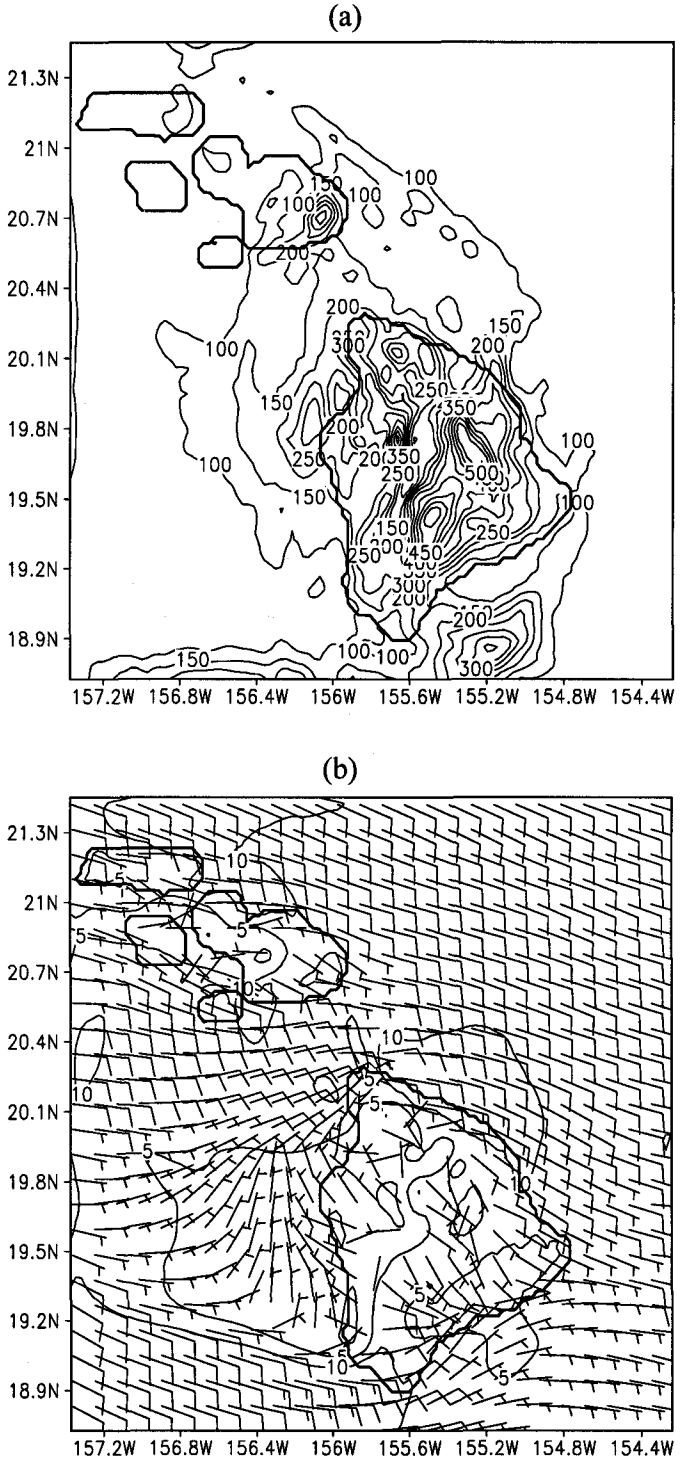

Figure 5.16. Same as Fig. 5.15 except for the MSM/LSM simulations. Contour interval is 50 mm in (a) and the wind barbs are drawn every four grid points in both directions in (b). The MSM/LSM run was initialized at 0200 HST 1 November 2000.

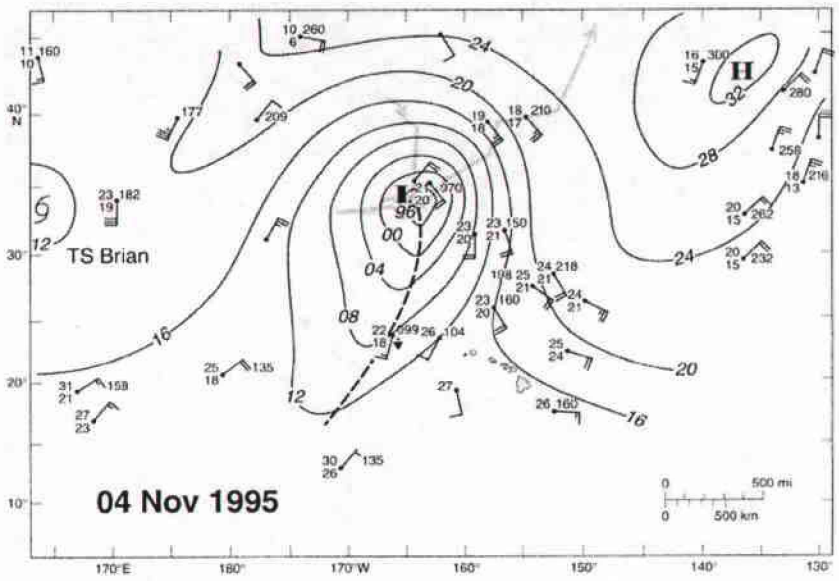

Figure 5.17. Sea level pressure (hPa) analyses for 0000 UTC on 4 November 1995 (from Businger et al. 1998). Ship observations are ± 6 h from valid time and use standard plotting convections. The 48-h track of the surface low starting at 1200 UTC 2 November is given by the gray line.

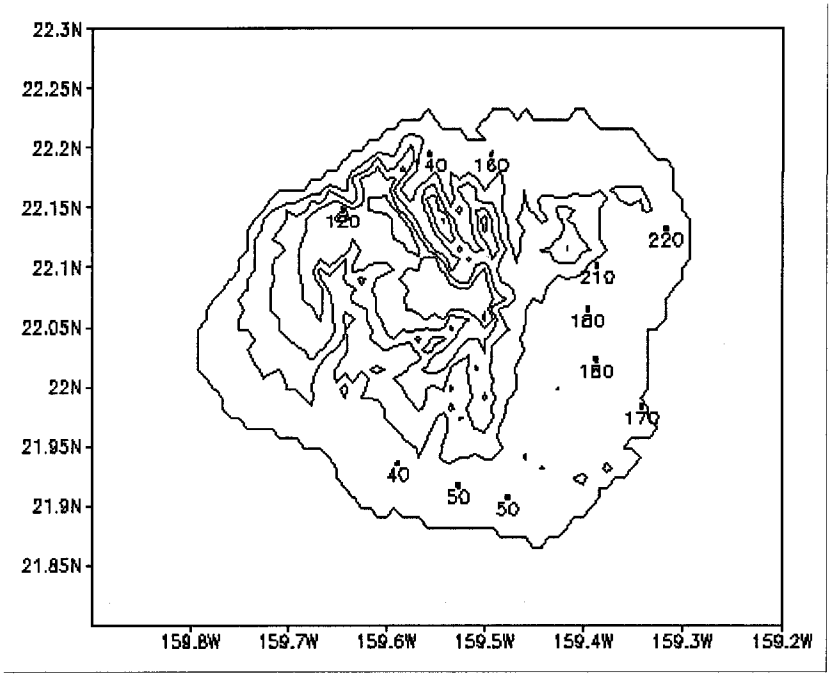

Figure 5.18. 24-h accumulated rainfall (mm) from 1400 HST 2 November to 1400 HST 3 November 1995 on the island of Kauai. Only station values are plotted.

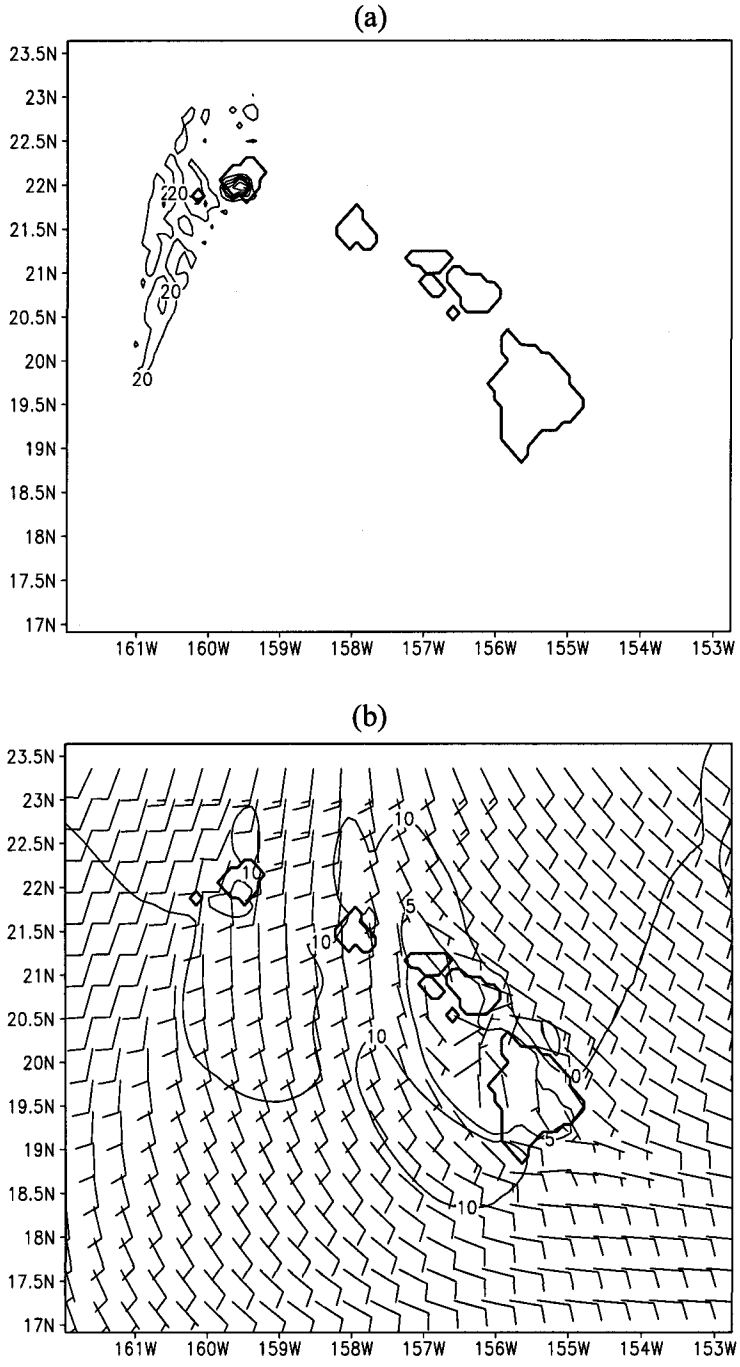

Figure 5.19. RSM/LSM-simulated (a) 24-h accumulated rainfall (mm) from 1400 HST 2 November to 1400 HST 3 November 1995 with a contour interval of 20 mm; and (b) 10-m wind (m s^{-1}) valid at 1400 HST 3 November 1995 with a contour interval of 5 m s^{-1}. The wind barbs in (b) are drawn every four grid points in both directions. The RSM/LSM run was initialized at 1400 HST 2 November 1995.

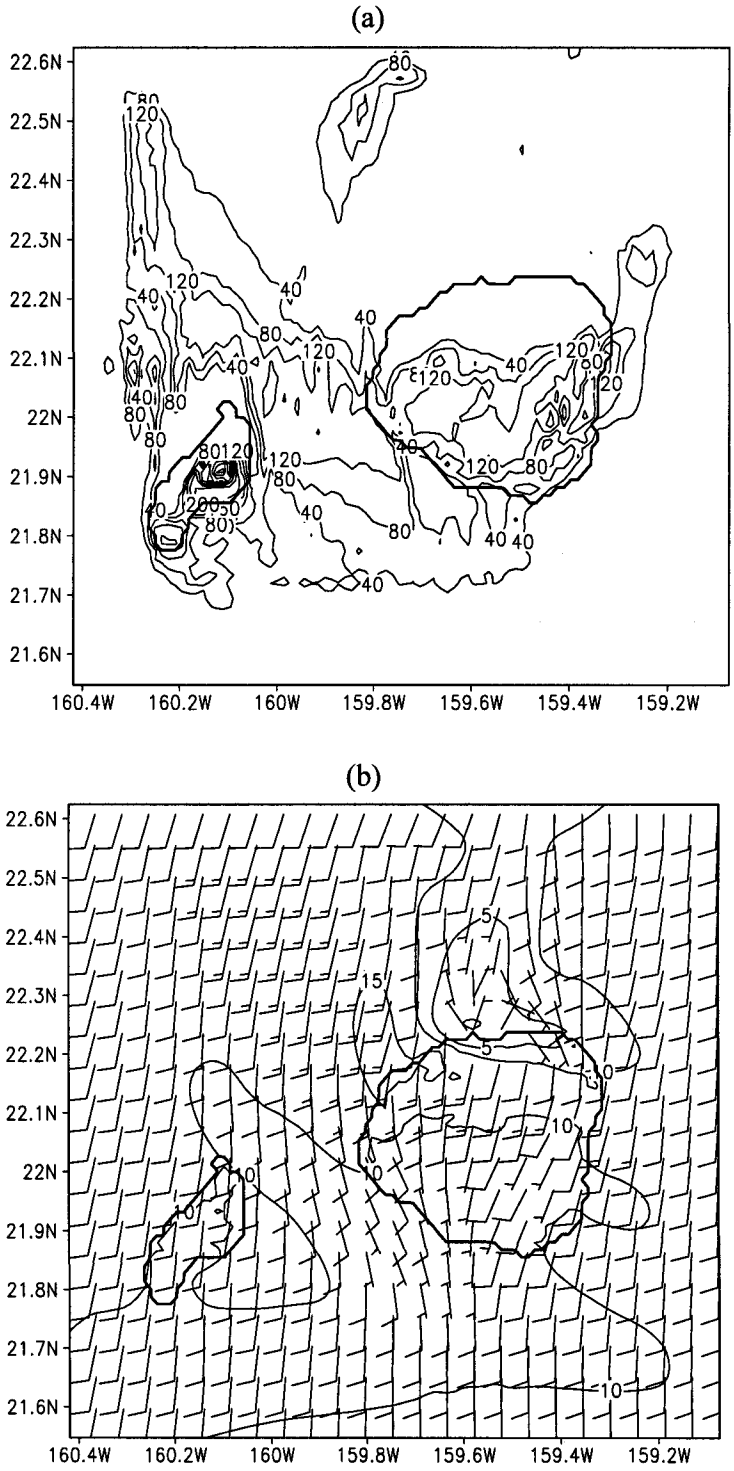

Figure 5.20. Same as Fig. 5.19 except for the MSM/LSM simulations. The contour interval is 40 mm in (a). The MSM/LSM run was initialized at 1400 HST 2 November 1995.

CHAPTER 6

A high wind event

6.1 Introduction

Severe downslope winds frequently occur over the Hawaiian Islands due to combined effects from large-scale synoptic forcing and complex local terrain (Schroeder 1977). There are generally two types of synoptic disturbances that bring high winds to the Hawaiian Islands: cold fronts and kona storms. Heavy rains and strong southerly winds frequently occur in the pre-frontal zone; whereas strong, gusty northeasterly trade winds dominate after the frontal passage as the post-frontal high pressure system merges with the semi-permanent subtropical high and centers just to the north of the Hawaiian Islands (Schroeder 1993). A kona storm (Simpson 1952; Ramage 1962) is a low-pressure system which develops in the upper troposphere, gradually extends to lower altitudes, and eventually appears as a low at the surface. If such a system develops to the west of the Hawaiian Islands, moist, showery southerly winds may persist for an extended period of time. Historically, the southerly winds in association with an advancing cold front and kona storm have caused greater devastation than trade winds (Schroeder 1977).

Local terrain plays a critical role in determining the area of high winds (Ramage et al. 1977; Schroeder 1977). For the eight major islands in the Hawaiian chain (Hawaii, Maui, Kauai, Oahu, Molokai, Lanai, Kahoolawe, and Niihau), this terrain is mountainous and complex. Noteworthy is the fact that 50% of the land is above 600 m mean sea level (MSL) (Blumenstock and Price 1967). The summit elevations of the western islands (i.e.,

Kauai and Oahu) are from 1 to 1.5 km. The eastern islands of Maui and Hawaii consist of massive mountains with summit elevations of 3 – 4 km. Lee wind maxima are frequently recorded on Oahu and Kauai (Morrow 1974). The northern and southern corners of the major Hawaiian Islands are places with frequent occurrences of high winds. Gaps between mountains and channels between islands are also prominent places of high winds (Patzert 1969; Smith and Grubišić 1993; Chen and Nash 1994; Lumpkin 1998).

Mountain wave activities in the vicinity of the Hawaiian Islands have been documented (Burroughs and Larson 1979). Ramage et al. (1977) discuss possible local topographic influences on winds over the Hawaiian Islands. These include (1) leeside disturbances due to the presence of mountain barriers, (2) aerodynamic channeling through gaps in the mountains, along valleys, and around the corners of the island, and (3) aerodynamic channeling between islands. Schroeder (1977) suggests that leeslope windstorms in Hawaii result mainly from development of orographic wave disturbances with additional enhancement from local aerodynamic effects. He notes that (1) the coupled surface high-pressure systems and the upper tropospheric troughs give rise to winds which blow normal to the mountain ranges through a deep layer; and (2) the bottom of a subsidence layer lies near the mountain crests. Lavoie (1974) shows a mild hydraulic jump over Oahu under normal trade wind conditions using a mesoscale numerical model with a horizontal resolution of 3 km.

Forecasting the location and magnitude of high winds is challenging in Hawaii due to sparse surface and upper-air observations in the mid-Pacific. With a 10-km horizontal resolution, the operational RSM is unable to resolve fine flow structures and pinpoint the locations where high winds are expected to occur. In this study, the coupled MSM/LSM

is used to simulate a high wind event over the Hawaiian Islands which occurred during 14-15 February 2001 in association with a cold front passage. We would like to study to what extent the localized high winds over the island chain could be predicted using a high resolution model. The 10-km RSM/LSM simulations are presented alongside the MSM/LSM simulations for comparison. Furthermore, the possible mechanisms for the development of downslope windstorms at various locations over the Hawaiian Islands will also be examined. This chapter is organized as follows. Section 6.2 contains a brief overview of gap winds and downslope windstorms. Synoptic conditions in association with this high wind event are discussed in section 6.3. Model simulated flow patterns over the Hawaiian Islands are examined in section 6.4. Section 6.5 validates the MSM/LSM and RSM/LSM predicted surface winds and precipitation using observations. Conclusions and discussion are given in section 6.6.

6.2 An overview of gap winds and downslope windstorms

6.2.1 Gap winds

Gap winds (Reed 1931) are driven by the imposed gap-parallel pressure gradient. They are in approximate ageostrophic equilibrium between the inertia term and the pressure gradient force. Overland and Walter (1981) specify this balance of forces in the along-gap direction as

$$\frac{d}{dx}\left(\frac{u^2}{2}\right) = -\frac{1}{\rho}\frac{\partial p}{\partial x} \qquad (6.1)$$

where u is the velocity, ρ is the density, and $\partial p/\partial x$ is the gap-parallel pressure gradient. In integrated form, this gives the Bernoulli equation

$$\frac{u^2}{2} = \frac{u_0^2}{2} - \frac{\Delta p}{\rho} \qquad (6.2)$$

where u_0 is the initial velocity and Δp is the pressure difference. Equation (6.2) can be used to estimate u at any point in the gap. Qualitatively, wind speeds increase along the gap and reach their maximum near the exit. However, the effects of surface drag and vertical entrainment can reduce the acceleration in the along-gap direction by almost 50% (Lackmann and Overland 1989). Bell and Bosart (1988) show that friction can strongly offset sustained accelerations during Appalachian cold-air damming events. Gap winds have been documented to occur in many areas such as the Strait of Juan de Fuca in Washington State (Reed 1931; Overland and Walter 1981), the Columbia River Gorge bordering Washington and Oregon (Cameron and Carpenter 1936), and the Shelikof Straits in Alaska (Lackman and Overland 1989).

6.2.2 Downslope windstorms

It is well established that many downslope windstorms are developed through mountain wave amplification. When an upward propagating wave encounters a region in which the Scorer parameter (Scorer 1949, 1954) changes rapidly, part of its energy is reflected back into a downward propagating mode and thereby increases the downward wave amplitude. Klemp and Lilly (1975) suggest that strong downslope winds occur when the atmosphere has a multilayer structure which produces a constructive superposition (reinforcement) of vertically propagating mountain waves reflected by variations in vertical static stability. Klemp and Lilly (1978) further note that reflections could occur due to the presence of critical levels (i.e., levels of zero wind or flow reversal). In a series of papers, Clark and Peltier (1977, 1984), Peltier and Clark (1979),

and Clark and Farley (1984) show that even without a critical level in the ambient flow, a growing wave may break and generate a "self-induced" critical level. Laprise and Peltier (1989) demonstrate that wave amplification could occur due to trapping and reflection of wave energy between the ground and the "self-induced" critical level.

Long's hydraulic theory (Long 1954) is another intriguing mechanism to account for strong downslope winds. According to the hydraulic theory, strong winds will occur along the lee slope when the fluid undergoes a transition from subcritical flow upstream to supercritical flow over the mountain. Smith (1985) and Durran (1986) show that the transition to supercritical flow is sensitive to the height of an elevated inversion. Removal of a crest-level inversion prevents the development of strong downslope winds. Smith and Sun (1987) develop generalized hydraulic solutions pertaining to severe downslope winds which show qualitative agreement with observations.

These theoretical ideas have been applied mainly to Colorado windstorms. Observations of the strongest events with peak gusts in the 50-60 m s^{-1} have been collected by aircraft (Lilly and Zipser 1972) and recently using Doppler lidar (Neiman et al. 1988). These studies clearly show surface manifestations of amplified mountain waves which result in severe downslope windstorms. Brinkmann (1974) examines 20 Boulder windstorms and notes that favorable large-scale conditions for the development of windstorms are a stable layer or inversion level above mountain top and relatively strong winds at that level.

Amplification of mountain waves may also be important for windstorms at other locations. Colman and Dierking (1992) identify three necessary criteria for strong downslope winds (Taku winds) to occur in southeast Alaska as a manifestation of

amplified mountain waves. These include (1) an inversion at or just above ridgetop, somewhere between 1.5 and 2 km MSL, (2) strong cross-barrier flow near ridgetop, typically 15-20 m s^{-1} in geostrophic wind speed, and (3) cross-barrier flow decreasing with height to a critical level somewhere between 3 and 5.5 km MSL. Dierking (1998) documents a mountain wave windstorm which occurred in the Taku River Valley near Juneau, Alaska. Mass and Albright (1985) note substantial wave activity above the lee slopes of the Washington Cascade Mountains during an intense windstorm event.

Bora windstorms occur southwest of the Dinaric Alps along the Adriatic coast (Klemp and Durran 1987). A sharp drop in temperature usually accompanies these windstorms, whereas the downslope windstorms along the eastern side of the Rockies generally have chinook (warm) characteristics. Smith (1987) presents aerial observations of the Yugoslavian bora, with gusts sometimes approaching 50 m s^{-1}. Klemp and Durran (1987) suggest that mountain wave and hydraulic dynamics may be applied to bora windstorms. A bora-like windstorm is also documented in western Washington (Reed 1981).

6.3 Synoptic-scale conditions

During the period of 14-15 February 2001, a strong high-pressure cell moved to the north of the Hawaiian Islands following the passage of a cold front (Fig. 6.1a). This high cell reached its maximum strength of 1038 hPa by 1400 HST 14 February 2001 after merging with the semi-permanent subtropical high (Fig. 6.1b). At 500 hPa (Fig. 6.2), a NE-SW oriented trough was located northeast of the Hawaiian Islands. The strong surface high produced windy conditions across the state of Hawaii, with trees knocked down by high winds and power disrupted in many island communities. Most of the power

failures and damages occurred on the lee sides of mountain ranges on Kauai and Oahu as well as within gaps between mountain ranges. Gale warnings were issued at 0400 HST 14 February for all channels in Hawaiian coastal waters by the National Weather Service. In addition to high winds, rain showers were reported throughout the state of Hawaii except on the lee sides of high mountains of Maui and the Big Island. The Big Island got the heaviest rain, with more than 121 mm of rainfall recorded on the windward lower slopes in the 24-h period ending at 0000 HST 15 February. Up to a quarter meter of snowfall was also reported in some areas of Mauna Kea and Mauna Loa on the Big Island.

Atmospheric soundings are taken routinely at Lihue on Kauai and Hilo on the Big Island. Figure 6.3a shows the sounding from 1400 HST 14 February at Lihue. A weak trade-wind inversion is identifiable between 800 hPa and 700 hPa (2 – 3 km) which is just above the mountain ridges on Kauai and Oahu. The critical layer is located between 500 hPa and 400 hPa (5.5 – 7.5 km). Cross-barrier wind speed near ridgetop (1 – 1.5 km) is about 15 m s^{-1}. The northeasterly trades are strongest between surface and 2 km MSL.

Based on this sounding, we have computed the Scorer number (Scorer 1949) because of its implications for the occurrence of wave-induced downslope windstorms (Klemp and Lilly 1975). The Scorer number is given by

$$l^2 = \frac{g\beta}{U^2} - \frac{1}{U}\frac{\partial^2 U}{\partial z^2} \tag{6.3}$$

where g is the gravity, U is the horizontal wind speed, β is $(1/\theta)(\partial\theta/\partial z)$, and θ is the potential temperature. The first term on the right hand side (stability term) is generally much larger than the second term (shear term). Figure 6.3b shows the vertical profile of the Scorer number at Lihue at 1400 HST 14 February 2001. Notable features are that the

trade-wind inversion layer (800-700 hPa) and the critical layer (500-400 hPa) have large values of the Scorer number. The stability, β, is large within the trade-wind inversion. In the critical layer, the stability term is large because of weak wind speeds. Figure 6.3b also shows a rapid decrease (increase) in l^2 by a factor of two (five) between the layers of 750-700 hPa (550-500 hPa) and 700-650 hPa (500-450 hPa).

The atmospheric sounding and the vertical profile of the Scorer number at 1400 HST 14 February 2001 at Hilo are shown in Figures 6.4a and 6.4b, respectively. A weak trade-wind inversion is identifiable between 700 and 650 hPa (3 – 3.5 km) with the critical level located between 600 and 500 hPa (4 – 6 km) (Fig. 6.4a). The trade-wind inversion at Hilo is much weaker than that at Lihue, likely due to the mid-level trough which lies just ahead of the Big Island (see Fig. 6.2b).

Large values of the Scorer number are evident within the layers of 700 – 650 hPa and 600 – 500 hPa (Fig. 6.4b). These two layers correspond to the trade-wind inversion and the critical level, respectively. The largest increase in l^2 by a factor of three occurs between the layers of 750 – 700 hPa and 700 – 650 hPa. These sharp changes in l^2 vertical profile and the multilayer structure are favorable large-scale conditions for the development of wave-induced downslope winds on the lee sides of mountains with peaks below the trade-wind inversion (Klemp and Lilly 1975; Colman and Dierking 1992).

6.4 Horizontal and vertical structure of flow field

In this section, the horizontal and vertical distributions of the MSM/LSM forecasted flow field within each nested domain are examined for downslope windstorms and gap winds through channels and mountains and compared with the RSM/LSM forecasts. The

temporal evolution of the forecasted upstream surface winds along 154 °W by the 10-km RSM/LSM (Fig. 6.5) shows strong winds in the late afternoon and early evening hours of 14 February 2001, with a maximum around 1800 HST near 20.8 °N. Therefore, we will focus our discussion on the simulated wind fields at this time. Figure 6.5 also reveals that the zonal wind component is dominant (~ 95%) in the horizontal wind field.

The horizontal map of 10-m winds forecasted by the 10-km RSM/LSM valid at 1800 HST 14 February is shown in Figure 6.6. General features include (1) weaker winds on the windward sides of Maui and the Big Island due to island blocking; (2) wakes on the lee sides of Maui and the Big Island; (3) two vortexes with weak (2 – 4 m s^{-1}) return flow in between on the lee side of the Big Island; and (4) strong winds at the southern and northern corners of major islands as well as within the Alenuihaha Channel. Wind patterns on Kauai and Oahu are relatively uniform due to the coarse representation of the islands' terrain by the 10-km model grid.

6.4.1 Kauai domain

For the nested MSM/LSM Kauai domain with a 1.5-km horizontal resolution, relatively weak winds of 6 m s^{-1} are evident on the windward side with strong winds ($\geq$ 14 m s^{-1}) along the lee slopes (Fig. 6.7a). The wake of the island is located between its western coast and the island of Niihau with the wind speed as small as 2 m s^{-1}. Strong winds ($\geq$ 14 m s^{-1}) also prevail on the northwestern and southern corners of Kauai, consistent with damage reports of tiles blown off and tree limbs downed in those areas.

We constructed the longitude-height cross section along 22.13 °N (the solid line in Fig. 6.7a) showing the MSM/LSM forecasted zonal wind, equivalent potential temperature and pressure vertical velocity (Fig. 6.7b). This cross section features a mountain with a

peak height of 1.2 km, with a gentle eastern slope and a sharp western slope. This peak height is about 0.1-0.2 km lower than the actual height. Strong downslope winds (~ 24 m s^{-1}) are evident along the western slopes with downward motion reaching 25 Pa s^{-1} (Fig. 6.7b). These downslope flows extend past the coastline and, when combined with the strong winds deflected along the northwestern corner of the island (see Fig. 6.7a), form a low-level easterly jet with the strongest winds of 24 m s^{-1} located about 1 km above the surface. This low-level jet extends further downstream. The eastern slope of the mountain is characterized by decelerating, rising flows with surface wind speeds below 6 m s^{-1}. The critical level is located around 6 km.

Orographic lifting of the easterly trade flow is evident along the windward (eastern) slopes as the isentropic surfaces tilt upward toward the mountain ridge (Fig. 6.7b). Downward of the mountain ridge, a moderate hydraulic jump (Long 1954; Lavoie 1974) is evident.

Along the same latitude (22.13 °N) in the 10-km RSM/LSM domain (Fig. 6.7c), amplification of trade winds is evident towards the leeside of the mountain ridge. However, strong winds do not extend to the lee slopes of the mountain. In this cross section, the peak height of the mountain is 0.6 km, ~ 0.7 km lower than the actual height. Thus, orographic enhancement of the trade winds through mountain wave amplification is only partially resolved by the RSM/LSM.

6.4.2 Oahu domain

For the nested MSM/LSM Oahu domain with a 1.5-km horizontal resolution, relatively weaker winds (< 10 m s^{-1}) are found on the windward slopes of the Koolau and Waianae Ranges on Oahu (Fig. 6.8a). Except along the leeside coasts of the Waianae and Koolau

Ranges, strong winds (> 14 m s^{-1}) are found in the coastal areas with the strongest (> 16 m s^{-1}) immediately off the northern and southern coasts of the island. Surface winds are relatively weaker in the island interior due to surface friction.

Longitude-height cross section along MOA-MOB (21.45 °N) (Fig. 6.8b) is characterized by two mountain ranges, Koolau Range in the east and Waianae Range in the west, with a similar peak height of 0.6 km in the model. This height is about 0.2-0.3 km lower than the actual mountain height. Strong downslope winds (> 12 m s^{-1}) are evident along the lee slopes of both mountain ranges (Fig. 6.8b). This is consistent with reports that recorded damages mainly on the lee sides of both mountain ranges. The strongest winds with wind speeds in excess of 22 m s^{-1} are located about 200 m above the surface. Figure 6.8b also shows that the upward motion along the windward slope of the Koolau Range is larger than along the windward slope of the Waianae Range (10 Pa s^{-1} versus 5 Pa s^{-1}) because the orographic lifting there is enhanced by latent heat release. However, at the time when strong trades reach the Waianae Range, the moisture content is less because of the removal of water vapor on the windward slope of the Koolau Range by precipitation (Schroeder et al. 1977). The critical level is located at around 5.5 km. Weak hydraulic jumps are evident on the lee sides of both mountain ranges.

In contrast, in the RSM/LSM domain (Fig. 2.1a), the island of Oahu is represented as one mountain with a peak height of 0.3 km. This height is about 0.6 km lower than the actual height. Thus, orographic effect is not properly resolved by the RSM/LSM. Along the same latitude (21.45 °N) in the 10-km RSM/LSM domain (Fig. 6.8c), strong winds (~ 20 m s^{-1}) are predicted towards the lee side of the mountain ridge with relatively uniform flow immediately above the mountain surface. The isentropic surfaces are also nearly

horizontal. The vertical motion (1-2 Pa s^{-1}) is more than one order of magnitude smaller in the RSM/LSM than in the MSM/LSM. It is apparent that amplification of trade-wind flow on the lee slopes is not resolved by the RSM/LSM model.

6.4.3 Molokai-Maui-Hawaii domain

Figure 6.9a shows the 10-m winds predicted by the 3-km MSM/LSM for the Molokai-Maui-Hawaii domain valid at 1800 HST 14 February. Salient features in association with the Big Island include (a) decelerating and splitting flow along the windward side, (b) accelerating winds to the north and south of the island, (c) strong winds downstream of the Waimea Saddle (Waimea jet), and (d) a wake on the lee side of the island consisting of two elongated counterrotating eddies that give rise to a wide region (~ 60 km) of reverse flow along the wake axis. These flow features are generally consistent with the schematic diagram by Smith and Grubišić (1993) for the Big Island with one exception: a small Kohala wake observed by Smith and Grubišić (1993) is not identified in the MSM/LSM simulations. This is because Smith and Grubišić (1993) examine the flow features under normal trade wind conditions when weak winds are frequently recorded on the lee side of the Kohala Mountains (Schroeder 1981). For our high wind case, favorable large-scale conditions result in strong downslope winds through amplification of mountain waves on the lee side of the Kohala Mountains.

Along the Central Valley between the Haleakala Mountain and the west mountains on Maui, relatively weaker winds (~ 8 m s^{-1}) are predicted on the windward side with strong winds (~ 20 m s^{-1}) on the leeward side (Fig. 6.9a). This flow pattern agrees qualitatively with Daniels and Schroeder's (1978) findings based on low-level wind observations. The weaker winds on the windward side of the Central Valley are due to the island blocking,

whereas the strong winds along the leeward side of the Central Valley result primarily from the channeling effect. Strong winds are also predicted within the oceanic channels between the islands. A narrow wake on the lee side of the Haleakala Mountain is evident (Fig. 6.9a). This narrow wake delineates strong winds to the south of the island and strong winds along the leeward side of the Central Valley to the north. In contrast, the 10-km RSM/LSM resolves a broad wake on the lee side of Maui without predicting strong winds along the leeward side of the Central Valley (Fig. 6.6). This is likely due to the fact that the channeling effect along the Central Valley is not properly resolved by the RSM/LSM due to the lower (~ 0.2 km) mountain height on West Maui in the 10-km grid (see Fig. 2.1a).

Longitude-height cross sections are constructed from the MSM/LSM simulations to investigate the interaction of airflow with the complex terrain. The positions of these cross sections are shown in Figure 6.9b. The cross section along the Alenuihaha Channel is represented by MCA-MCB. MWA-MWB crosses the Waimea Saddle. MLA-MLB crosses a high mountain (Mauna Loa). The cross section, MSA-MSB, examines the airflow over the southern corner of the Big Island.

Across the Alenuihaha Channel (Fig. 6.10a), the airflow below 3 km starts to accelerate and descend in the entrance region and continues the acceleration and descent for nearly 100 km downstream. The strongest wind of 26 m s^{-1} is located at 0.8 km MSL. This flow pattern is consistent with Patzert's (1969) results based on cruise observations and Smith and Grubišić's (1993) findings based on aircraft observations. A moderate hydraulic jump is evident in the θ_e field at the exit region in accordance with the

strongest channel winds. In the 10-km RSM/LSM simulations (Fig. 6.10b), strong winds of 24 m s^{-1} are evident in the exit region; however, a hydraulic jump is not evident.

Like gap winds, channel winds are driven by the imposed channel-parallel pressure gradient (Overland and Walter 1981). Figure 6.11 shows a close correspondence between the temporal evolution of pressure difference and zonal wind difference across the channel. However, the existence of large mountains on either side of the channel adds complexity to the mechanisms of these strong channel winds. As noted earlier, a hydraulic jump is predicted by the MSM/LSM at the exit region of the channel.

Across the Waimea Saddle (Fig. 6.12a), relatively weaker winds (< 8 m s^{-1}) are predicted along the windward side with strong winds (> 24 m s^{-1}) on the lee side. The strongest winds of 30 m s^{-1} are located above the lee slopes. The downward motion in association with these strongest winds reaches 30 Pa s^{-1}. Ramage (1979) shows that the Waimea Saddle is one of the windiest sites on the Big Island. A low-level easterly jet of 22 m s^{-1} exists further downstream. A moderate hydraulic jump is evident above the lee slopes of the Waimea Saddle. The 10-km RSM/LSM predicts strongest winds (~ 24 m s^{-1}) along the leeside upper slopes of the Waimea Saddle (Fig. 6.12b). A weak hydraulic jump is also identified in the RSM/LSM simulations.

Gap winds and downslope winds are also known to occur simultaneously (Colman and Dierking 1992). This appears to be the case for the strong winds downstream of the Waimea Saddle (Waimea jet). Surface pressure differences across the saddle are on the order of 3-6 Pa $(100\ km)^{-1}$ in the MSM/LSM simulations (Fig. 6.13), with the zonal wind differences closely following the pressure pattern. It is, however, difficult to separate the relative contributions of gap winds and downslope winds to the Waimea jet.

Across the Mauna Loa volcano (Fig. 6.14a), weak westerly (upslope) winds (1-2 m s^{-1}) are evident along the lee slopes of the mountain. Because the mountain top of Mauna Loa (~ 4 km) is above the trade-wind inversion base (~ 3 km), the low-level strong trade-wind flow cannot pass over the mountain and descend on the lee side. Furthermore, the winds aloft at 4 km are relatively weak (< 5 m s^{-1}) (Fig. 6.4). Thus, neither downslope windstorms nor hydraulic jumps are present in the model simulations. Further downstream of the mountain, a return flow of 4 – 6 m s^{-1} is found between surface and 1 km MSL. This return flow originates near 157.2 °W, about 100 km west of the leeside coast, and extends eastward towards the mountain with an approximate north-south extent of 60 km at low levels (see Fig. 6.9a). Lumpkin (1998) and Xie et al. (2001) also suggest an origination point of the return flow at around 157 °W. Smith and Grubišić (1993) observe a broad region of reverse flow (5-10 m s^{-1}) in the lee of the island, spanning more than 80 km in crosswind direction under normal trade wind conditions. Nickerson and Dias (1981) estimate the north-south extent of the return flow around 60 km based on aircraft observations in June 1980. It is apparent that the MSM/LSM captures the return flow pattern reasonably well. In the 10-km RSM/LSM simulations (Fig. 6.14b), the horizontal extent of the return flow is less when compared to the MSM/LSM simulations.

Strong winds (24 m s^{-1}) are predicted above the lee slope along the southern corner of the Big Island by the MSM/LSM (Fig. 6.15a). The airflow descends along the lee slope and then abruptly ascends in a jump-like feature. The critical level is identified at 8 km MSL with less wave activities above it. Aerodynamic channeling (Ramage et al. 1977) also has some role in developing these strong winds as evident from the surface flow

predicted by the MSM/LSM (Fig. 6.9a). In contrast, the strong winds (~ 20 m s^{-1}) forecasted by the RSM/LSM are located above the mountain ridge, with an associated weak hydraulic jump (Fig. 6.15b). The magnitude of the vertical motion in the RSM/LSM simulations is about half of that predicted by the MSM/LSM. The terrain height in this cross section is 0.3 km in the RSM/LSM, about 0.2 km lower than the actual height. Thus, orographic effect is only partially resolved by the RSM/LSM.

In summary, downslope windstorms are predicted by the MSM/LSM along the lee slopes of Kauai and Oahu. These windstorms also display features of hydraulic jumps (Long 1954). At the exit region of the Alenuihaha Channel strong winds are forecasted with characteristics of gap winds (Reed 1931) and a hydraulic jump. The model also resolves the Waimea jet (Ramage 1979) with the strongest wind speed of 30 m s^{-1} above the lee slopes of the Waimea Saddle. A hydraulic jump is forecasted in association with the Waimea jet and the strong winds over the southern corner of the Big Island. In contrast, the 10-km RSM/LSM predicts uniform trade-wind flow for Kauai and Oahu, without large spatial variability in wind distributions related to complex local terrain.

6.5 Verifications of model forecasts

6.5.1 Surface winds

In this section, the forecasted surface winds from the RSM/LSM and MSM/LSM are validated at 10 surface sites over the Hawaiian Islands where hourly wind data are available. The 10 surface sites are Kahuku, Bellows, Wheeler AFS (Air Force Station) and Waialua on Oahu (Fig. 2.1b); Hana, Haleakala and Maalaea Bay on Maui (Fig. 2.1c); Honokaa, Kawaihae and Upolu AP (Airport) on the Big Island (Fig. 2.1c).

Figure 6.16 shows the observed and RSM/LSM, MSM/LSM forecasted 10-m wind speeds and wind directions at Kahuku, Bellows, Wheeler AFS, and Waialua on Oahu for the period of 0000 HST 14 February through 0000 HST 15 February 2001. The recorded gusty wind speeds are also shown. The observed wind speeds are 2-minute averaged values. Both models produce a gradual increase in the surface wind speeds during the day which is consistent with observations. The wind directions are well predicted at all four sites except at Wheeler AFS over central Oahu in the early morning hours (Fig. 6.16f). The observed strong winds at Kahuku (11-12 m s^{-1}) (Fig. 6.16a) and Bellows (11-14 m s^{-1}) (Fig. 6.16c) and relatively weaker winds (2-6 m s^{-1}) at Wheeler AFS and Waialua within the valley between the Koolau and Waianae Ranges (Figs. 6.16e and 6.16g) are reasonably well predicted by the MSM/LSM. The strong winds at Kahuku and Bellows are due to flow moving around the northeastern and southeastern corners of the island, respectively, under strong incoming northeasterly trades. In contrast, the RSM/LSM underestimates the strong winds at Bellows by about 2 m s^{-1} and overestimates the weak winds at Wheeler AFS and Waialua by about 2 m s^{-1} and 6 m s^{-1}, respectively. This is related to the fact that the mountain ranges are not well resolved by the RSM/LSM (Fig. 2.1a). It is apparent that the spatial variations in the surface winds are better resolved by the MSM/LSM than the RSM/LSM.

On Maui (Fig. 6.17), both the RSM/LSM and MSM/LSM reproduce the observed surface wind speeds at Hana reasonably well (Fig. 6.17a). At Haleakala (Fig. 6.17c), the MSM/LSM forecasted surface wind speed is rather consistent with the observations whereas the RSM/LSM forecasts are persistently 3-4 m s^{-1} higher than the observed. This is likely related to the fact that the terrain height of this site in the RSM/LSM domain is 1

km, ~ 2 km lower than the actual height. Atmospheric soundings at Lihue and Hilo (Figs. 6.3a and 6.4a) have indicated that the easterly trade winds are strongest between surface and 2 km but decrease upward. At Maalaea Bay (Fig. 6.17e), the MSM/LSM forecasted surface wind speed is consistent with observations before 1300 HST but overestimations of 5 m s^{-1} are noted after 1300 HST. Related to orographic amplification of trade-wind flow through the Central Valley (Daniels and Schroeder 1978; see Fig. 6.9a), the gusty wind speeds at Maalaea Bay are in excess of 15 m s^{-1} throughout the period. This is better resolved by the MSM/LSM than the RSM/LSM. In terms of the surface wind direction, the MSM/LSM simulations are consistent with observations at Maalaea Bay (Fig. 6.17f), but appreciable discrepancies are noted at Hana and Haleakala (Figs. 6.17b and 6.17d).

On the Big Island (Fig. 6.18), the RSM/LSM and MSM/LSM provide similar forecasts for wind speed and wind direction at all three sites. This is probably due to the similar location and terrain height for these sites in both model domains (Figs. 2.1a and 2.1c). Both models capture the strongest wind speed in the afternoon hours of 14 February at Honokaa and Upolu (Figs. 6.18a and 6.18e). These strongest afternoon winds are likely the combination of strong trades over the open ocean at this time and the downward transport of momentum due to vertical mixing as a result of solar heating in the afternoon hours (Schroeder 1981). The wind pattern reported at Kawaihae (Fig. 6.18c) is peculiar in the sense that the gusty wind speeds are much higher than the 2-minute averaged wind speeds. This is likely related to the fact that this surface site is located in a bay area on the lee side of the Kohala Mountains which experiences significant fluctuations in winds (Tyson 1968; Schroeder 1981). The RSM/LSM and MSM/LSM forecasted wind speeds at this site are much higher than the observed 2-minute averaged wind speeds; however,

they are rather consistent with the observed high gusty wind speeds there. The predicted surface wind directions from both models are generally consistent with observations at Honokaa and Upolu (Figs. 6.18b and 6.18f). However, large discrepancies occur at Kawaihae (Fig. 6.18d).

6.5.2 Precipitation

On Kauai, the coastal stations received less than 15 mm of rainfall during a 24-h period ending at 0000 HST 15 February (Fig. 6.19a). One station on the northwestern slope of the Waialeale Mountain recorded 45 mm of rainfall during the 24-h period. It is reasonable to infer that along the windward upper slopes of the mountain the rainfall amount could be more than 45 mm during the 24-h period due to the apparent orographic lifting to the northeasterly trade-wind flow. In the MSM/LSM simulations (Fig. 6.19b), heavy rains are predicted along the upper slopes of the Waialeale Mountain. Giambelluca et al. (1986) show that the Waialeale Mountain receives about 11,300 mm of rain annually, being one of the world's wettest spots. For the coastal stations, an overestimation of rain totals is evident in the MSM/LSM simulations.

Over Oahu, the Koolau Range received more than 30 mm of rainfall during the 24-h period with 44 mm of rain recorded on its southeastern section (Fig. 6.20a). The Waianae Range, on the other hand, recorded negligible rainfall for this event. In the MSM/LSM simulations (Fig. 6.20b), considerable rain (> 30 mm) is forecasted along the windward side of the Koolau Range with little rainfall along the windward side of the Waianae Range, in agreement with the observations. We have noted earlier that vertical motion in association with the Waianae Range is weaker than with the Koolau Range due to the effect of moisture-convection feedback (see Fig. 6.8b). The forecasted heaviest rainfall

total (40-60 mm) is also comparable to that observed; however, it is located along the upper slopes of the Koolau Range. Observations show the heaviest rainfall toward the lee side of the mountain ridge (Fig. 6.20a).

On the island of Maui (Fig. 6.21a), fewer station observations render it difficult to draw a detailed horizontal map of rainfall distribution. The MSM/LSM simulations show that the ridge of the West Maui Mountains and the windward slopes of the Haleakala Mountain on eastern Maui received the heaviest amount of rainfall as a result of orographic lifting (Fig. 6.21c).

More than 50 mm of rainfall was received on the lower slopes of the windward side of the Big Island during the 24-h period with an amount of 121 mm recorded in the Hilo area (Fig. 6.21b). The MSM/LSM simulations for the same period (Fig. 6.21c) are fairly consistent with observations both in rainfall distribution and rainfall amounts. In addition, the MSM/LSM predicts 0.14 to 0.2 meters of snowfall over the two mountain peaks (Mauna Loa and Mauna Kea), in agreement with the observed local weather. Rainfall on the windward side of the Kohala Mountains over northern Hawaii is also predicted in the model. These results compare favorably with observations.

The 10-km RSM/LSM also predicts appreciable rains along the windward sides of the major Hawaiian Islands (Fig. 6.22). However, the rainfall amount is largely underestimated in the RSM/LSM simulations. For example, along windward Oahu, less than 20 mm of rains are predicted by the RSM/LSM, in contrast to the observed total of more than 40 mm. For West Maui, the RSM/LSM predicts little rainfall since the mountain there is poorly resolved in the RSM/LSM domain (Fig. 2.1a). Along the

windward side of the Big Island, ~ 80 mm of rains are predicted by the RSM/LSM, about 40 mm less than the observations.

6.6 Conclusions and discussion

A high wind event (14-15 February 2001) over the Hawaiian Islands associated with a cold front is simulated using the coupled MSM/LSM. It occurred when a strong high-pressure cell moved to the northeast of the Hawaiian Islands following the passage of the cold front and merged with the semi-permanent subtropical high, which resulted in windy conditions across the state of Hawaii. Analyses of the routine atmospheric soundings at Lihue on Kauai and Hilo on the Big Island reveal sharp changes in the vertical profile of the Scorer number as well as a multilayer structure with a trade-wind inversion. These large-scale conditions are favorable for the development of wave-induced downslope winds on the lee sides of mountains with peaks below the trade-wind inversion.

The MSM/LSM forecasts reproduce the general flow features in association with the local complex terrain. These include (1) decelerating and deflecting flow in the immediate upstream of the islands, (2) wakes on the lee sides of major islands, (3) strong winds around the northern and southern corners of islands, and (4) strong winds within the oceanic channels between islands and within the gaps between mountains. The model also resolves two elongated counterrotating eddies in the wake of the Big Island that give rise to a wide region of reverse flow along the wake axis. The forecasted return flow originates at 157.2 °W with a north-south extent of 60 km and a depth of about 1 km.

Downslope windstorms are forecasted by the MSM/LSM on the lee sides of Kauai and Oahu. These windstorms display features of hydraulic jumps. Strong winds are also

forecasted at the exit region of the Alenuihaha Channel with characteristics of gap winds and a hydraulic jump. The model well resolves the Waimea jet above the lee slopes of the Waimea Saddle. A hydraulic jump is forecasted in association with the Waimea jet and the strong winds over the southern corner of the Big Island. In the case of high mountains with peak height above the trade wind inversion, weak winds are simulated on the lee side. This is due to the fact that trade-wind flow is unable to pass over the high mountains and descend on the lee sides because of the trade-wind inversion. In contrast, the 10-km RSM/LSM predicts uniform trade-wind flow over Kauai and Oahu. In addition, the RSM/LSM forecasted strong winds are mainly located above the mountain ridges without extending to the lee slopes.

Comparisons between observations and model simulations over 10 surface sites show that the MSM/LSM reproduces the spatial distribution and magnitude of the surface wind better than the RSM/LSM. This is largely due to the much improved representation of the local complex terrain by the high-resolution MSM/LSM. Observed rainfall patterns in association with this high wind event are reasonably well reproduced by the MSM/LSM for the major Hawaiian Islands, with comparable rainfall amounts over Oahu and the Big Island. The RSM/LSM also provides rains on the windward side of major islands; however, the predicted rainfall amount is less than that observed.

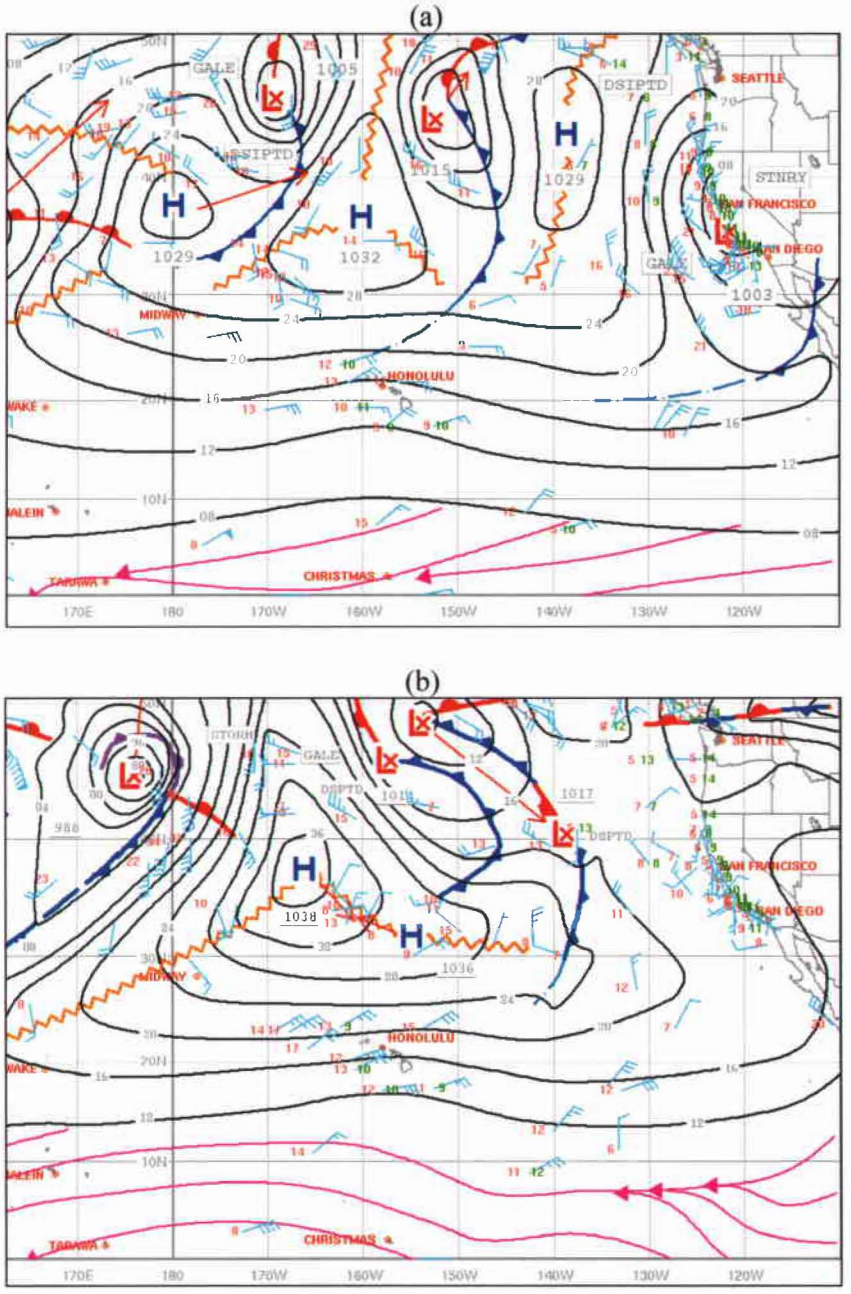

Figure 6.1. Surface analyses for 1400 HST on (a) 13 February and (b) 14 February 2001 (adapted from the subjective analyses by forecasters at the Weather Forecast Office Honolulu). Isobars are every 4 hPa.

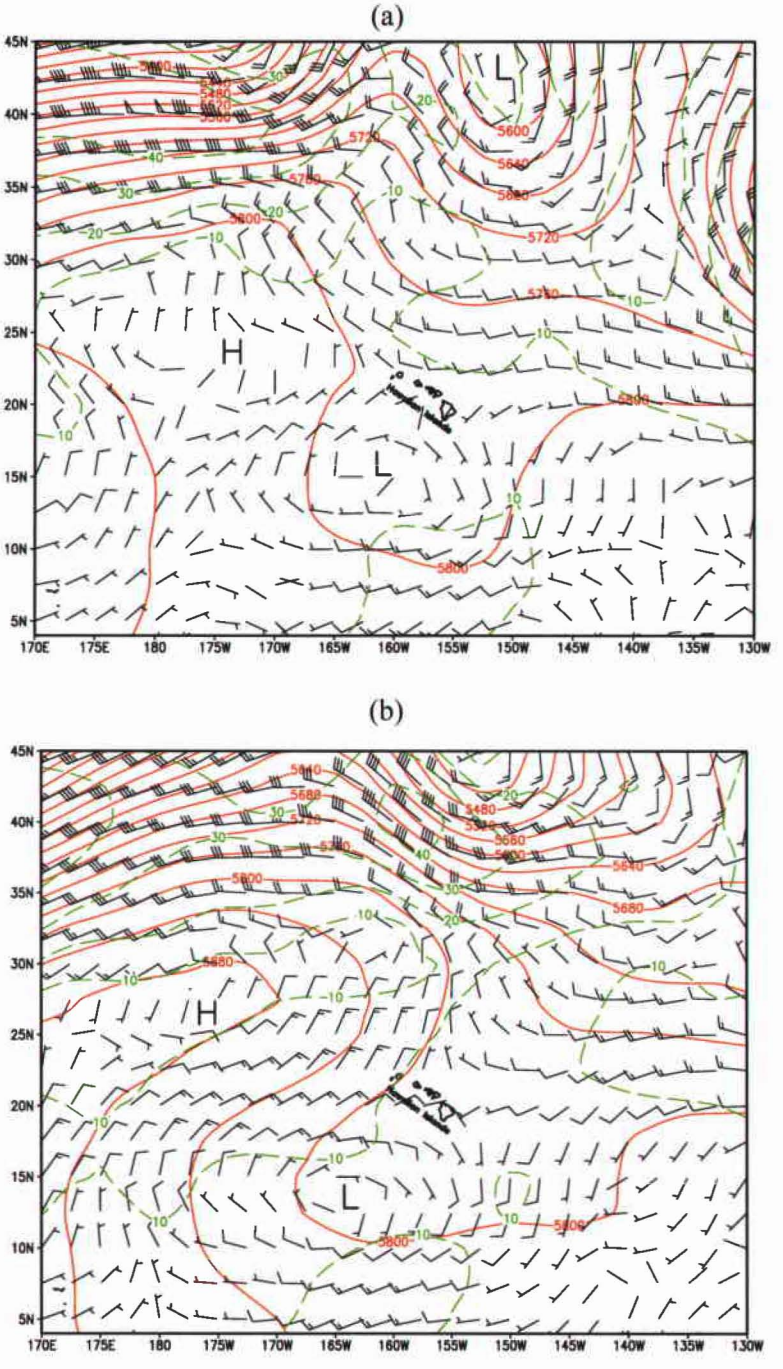

Figure 6.2. 500-hPa geopotential height (gpm, solid and red lines) and horizontal winds (m s^{-1}, dashed and green lines) based on the NCEP/NCAR Reanalysis data at 1400 HST on (a) 13 February and (b) 14 February 2001. Contours are every 40 gpm for geopotential height and 10 m s^{-1} for wind, respectively. One pennant, full barb and half barb represent 50, 10 and 5 m s^{-1}, respectively.

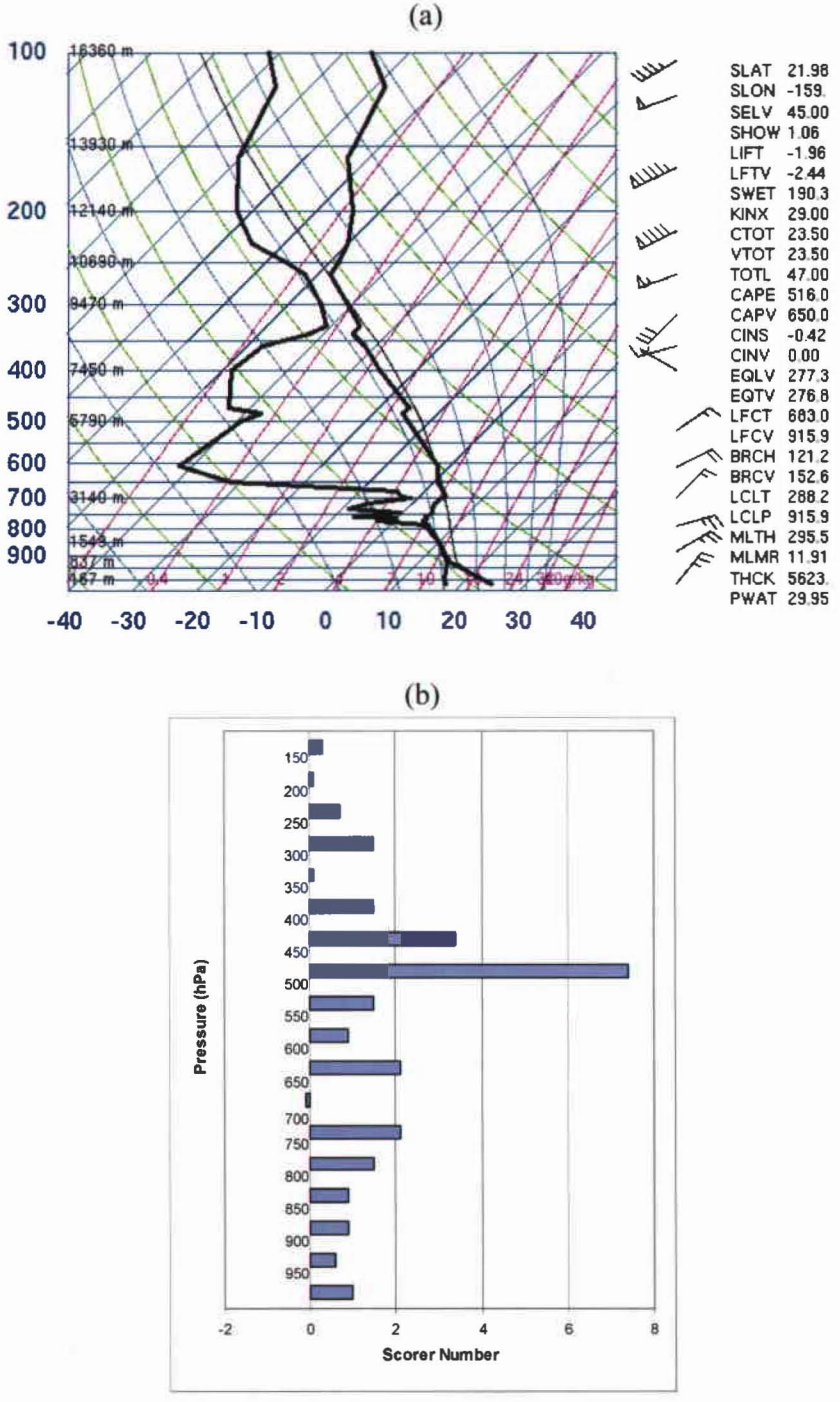

Figure 6.3. Skew-T chart (courtesy of the Department of Atmospheric Science, University of Wyoming; http://weather.uwyo.edu/upperair/sounding.html) (a) and vertical profile of the Scorer number (km^{-2}) (b) for Lihue, Kauai at 1400 HST 14 February 2001. Refer to Fig. 2.1d for the location of Lihue.

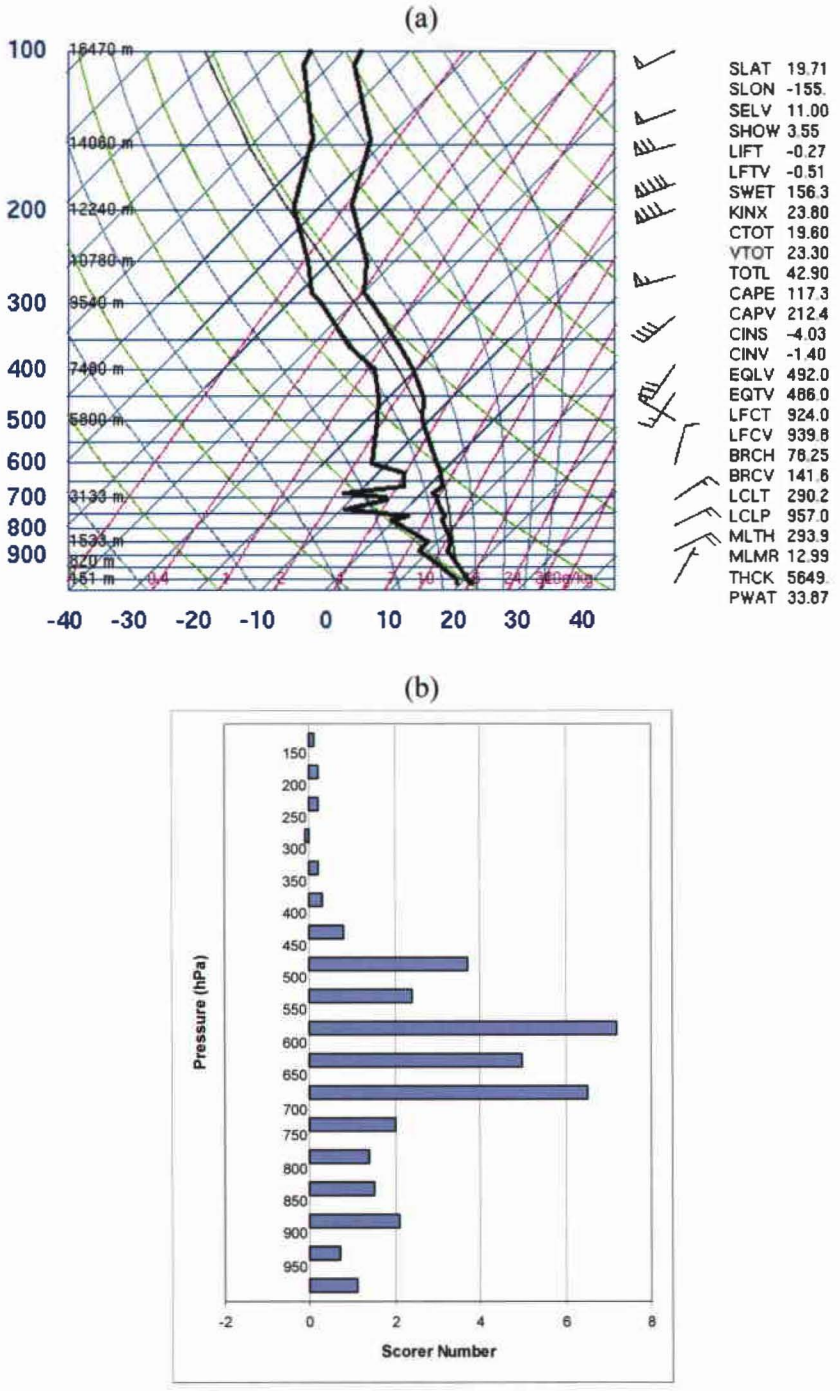

Figure 6.4. Same as Fig. 6.3 except for Hilo, Big Island. Refer to Fig. 2.1c for the location of Hilo.

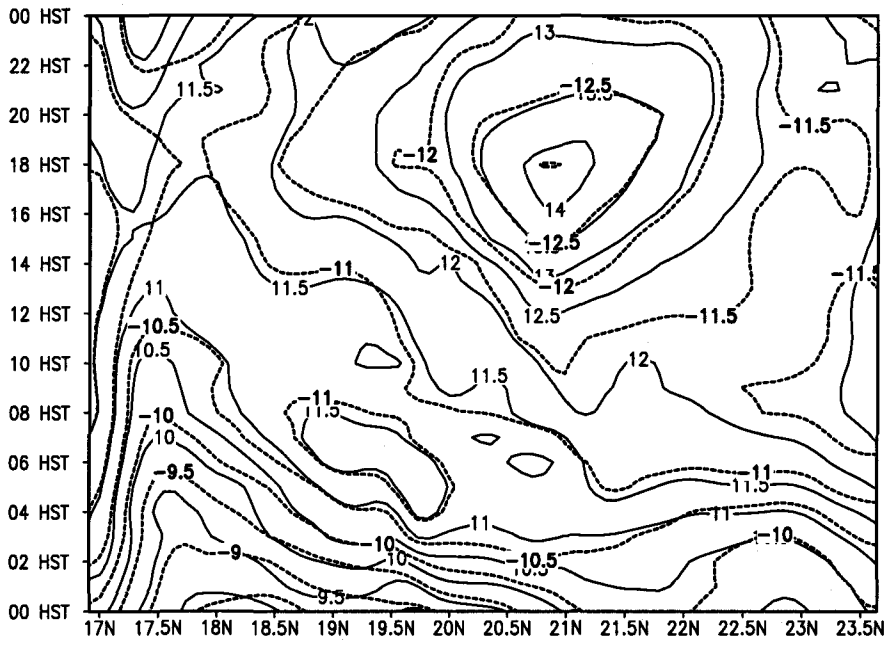

Figure 6.5. Latitude-time cross section along 154 °W featuring the RSM/LSM forecasted 10-m horizontal wind speeds (solid lines, m s^{-1}) and zonal wind component (dashed lines, m s^{-1}). Time goes from 0000 HST 14 February to 0000 HST 15 February. Isotachs are every 0.5 m s^{-1}. Negative values for zonal wind component denote winds from the east. The RSM/LSM was initialized at 1400 HST 13 February 2001.

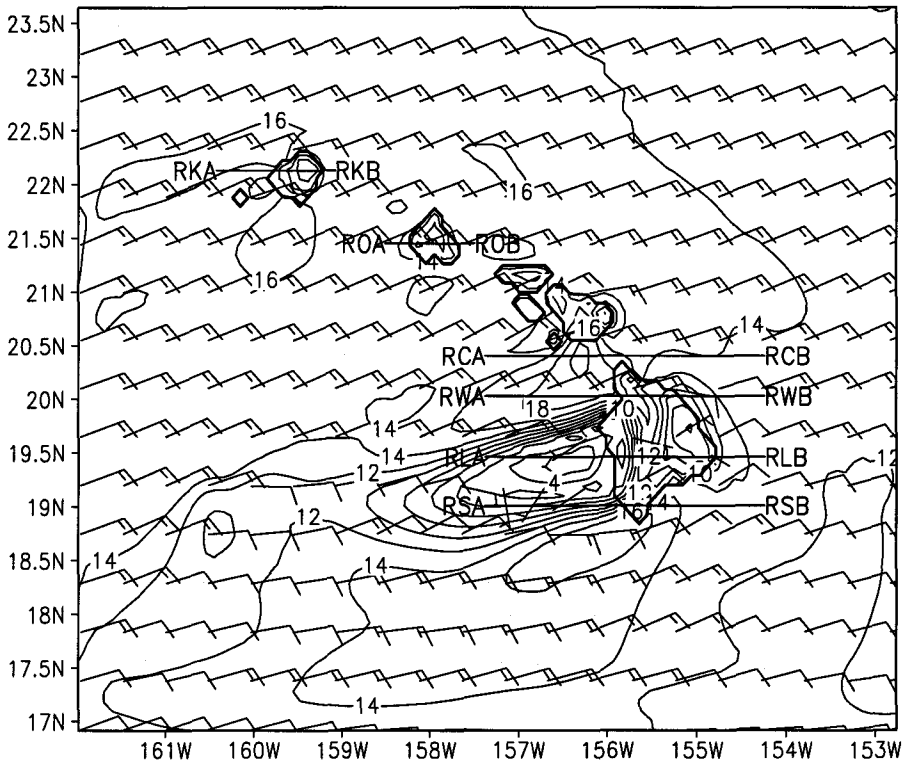

Figure 6.6. RSM/LSM 28-h forecasted 10-m winds (m s^{-1}) valid at 1800 HST 14 February 2001. Isotachs are every 2 m s^{-1}. Full barb and half barb represent 10 m s^{-1} and 5 m s^{-1}, respectively. The wind barbs are plotted every five grid points in both directions. The solid lines denote the locations of cross sections. The RSM/LSM was initialized at 1400 HST 13 February 2001.

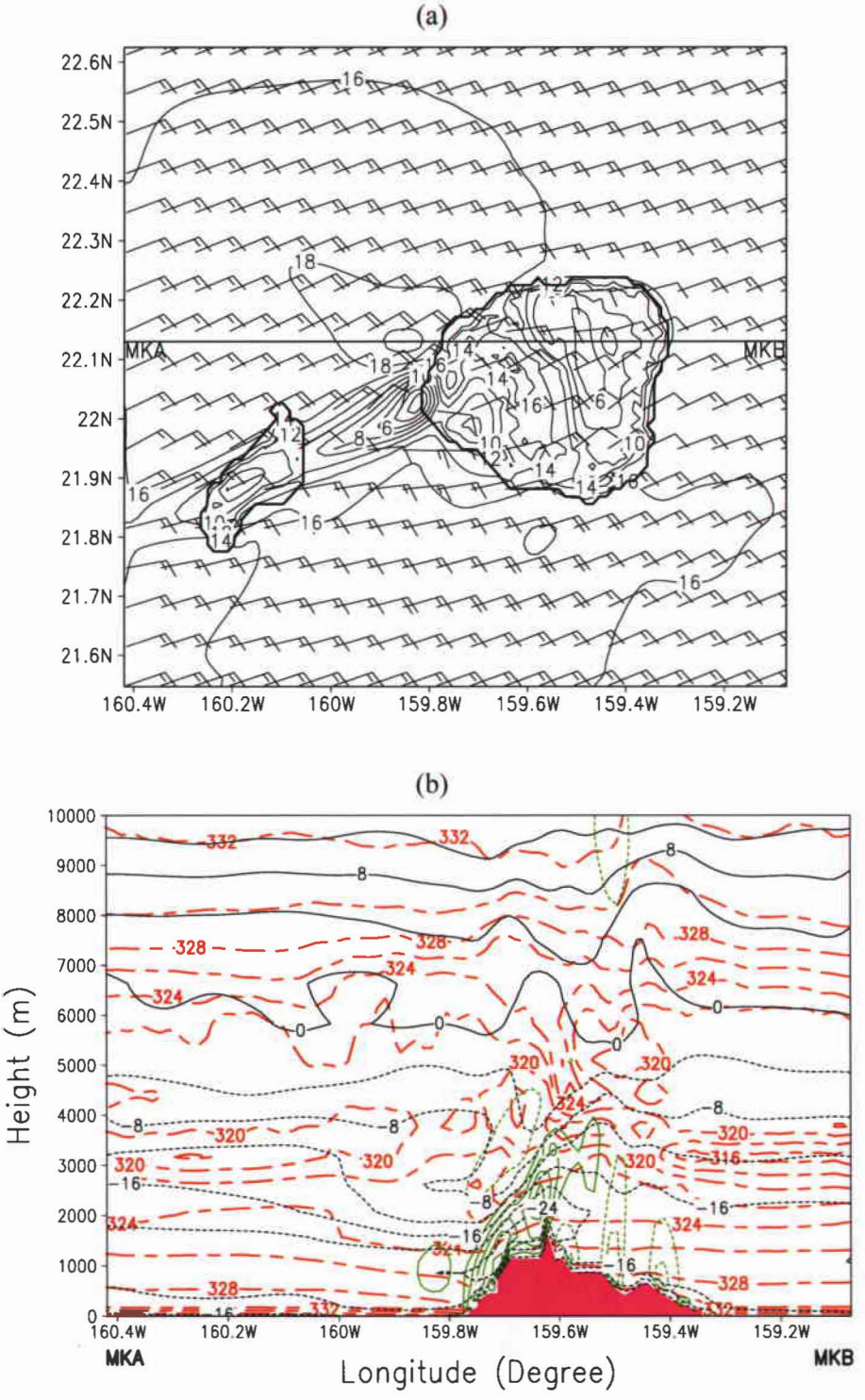
(a)
22.6N
22.5N
22.4N
22.3N
22.2N
22.1N
22N
21.9N
21.8N
21.7N
21.6N
MKA
MKB
160.4W
160.2W
160W
159.8W
159.6W
159.4W
159.2W
(b)
Height (m)
10000
9000
8000
7000
6000
5000
4000
3000
2000
1000
0
MKA
MKB
Longitude (Degree)

Figure 6.7. (a) (b)

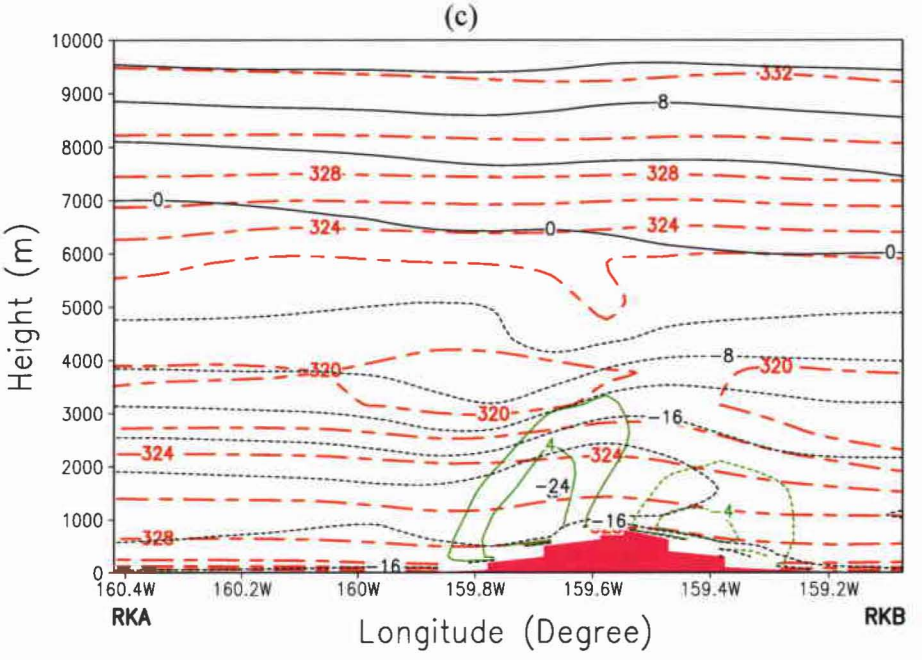

Figure 6.7. The MSM/LSM forecasted 10-m winds (m s^{-1}) over the Kauai domain (a), and longitude-height cross section along MKA-MKB (b) and RKA-RKB (c) showing zonal winds (black lines), equivalent potential temperature (red lines) and pressure vertical velocity (green lines) constructed from the respective MSM/LSM and RSM/LSM 28-h forecasts valid at 1800 HST 14 February. The isotachs are every 2 m s^{-1} in (a) and 4 m s^{-1} in (b) and (c). Isentropes are every 2 °K. Pressure vertical velocity is every 5 Pa s^{-1} in (b) and 2 Pa s^{-1} in (c). The wind barbs in (a) are plotted every 3 grid points in both directions. The 1.5-km MSM/LSM and 10-km RSM/LSM were initialized at 1400 HST 13 February 2001. The locations of the cross sections, MKA-MKB and RKA-RKB, are shown in Figs. 6.7a and 6.6, respectively.

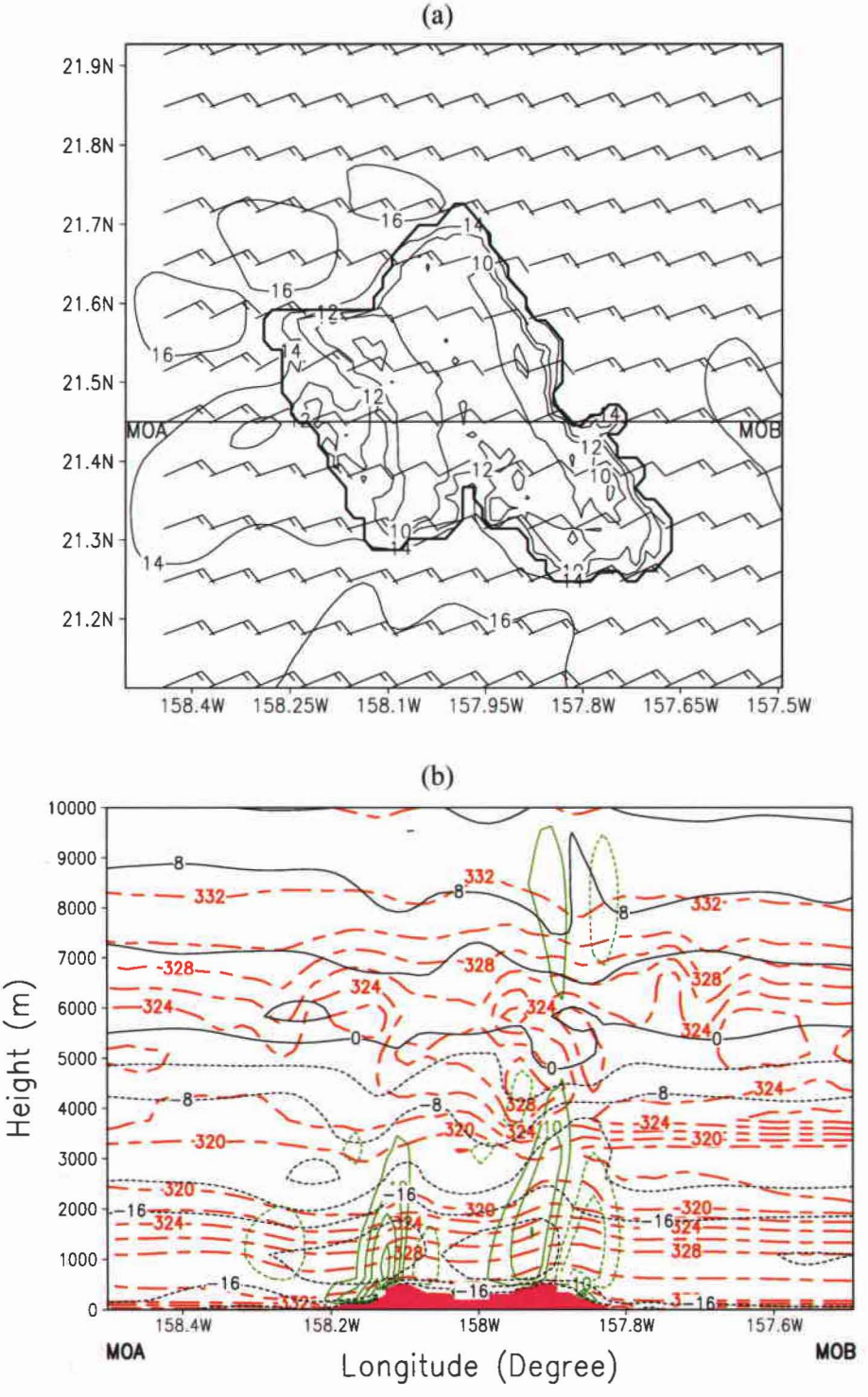
(a)
21.9N
21.8N
21.7N
21.6N
21.5N
21.4N
21.3N
21.2N
MOA
MOB
158.4W
158.25W
158.1W
157.95W
157.8W
157.65W
157.5W
(b)
Height (m)
10000
9000
8000
7000
6000
5000
4000
3000
2000
1000
0
158.4W
158.2W
158W
157.8W
157.6W
MOA
MOB
Longitude (Degree)

Figure 6.8. (a) (b)

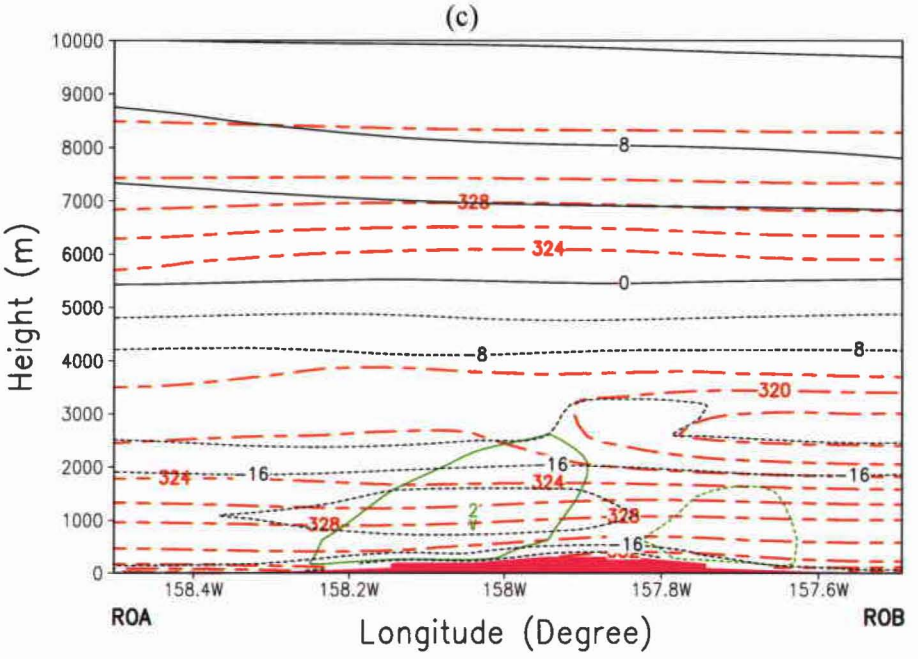

Figure 6.8. Same as Fig. 6.7 except for the Oahu domain and along MOA-MOB and ROA-ROB. Pressure vertical velocity is every 1 Pa s^{-1} in (c). The locations of MOA-MOB and ROA-ROB are shown in Figs. 6.8a and 6.6, respectively.

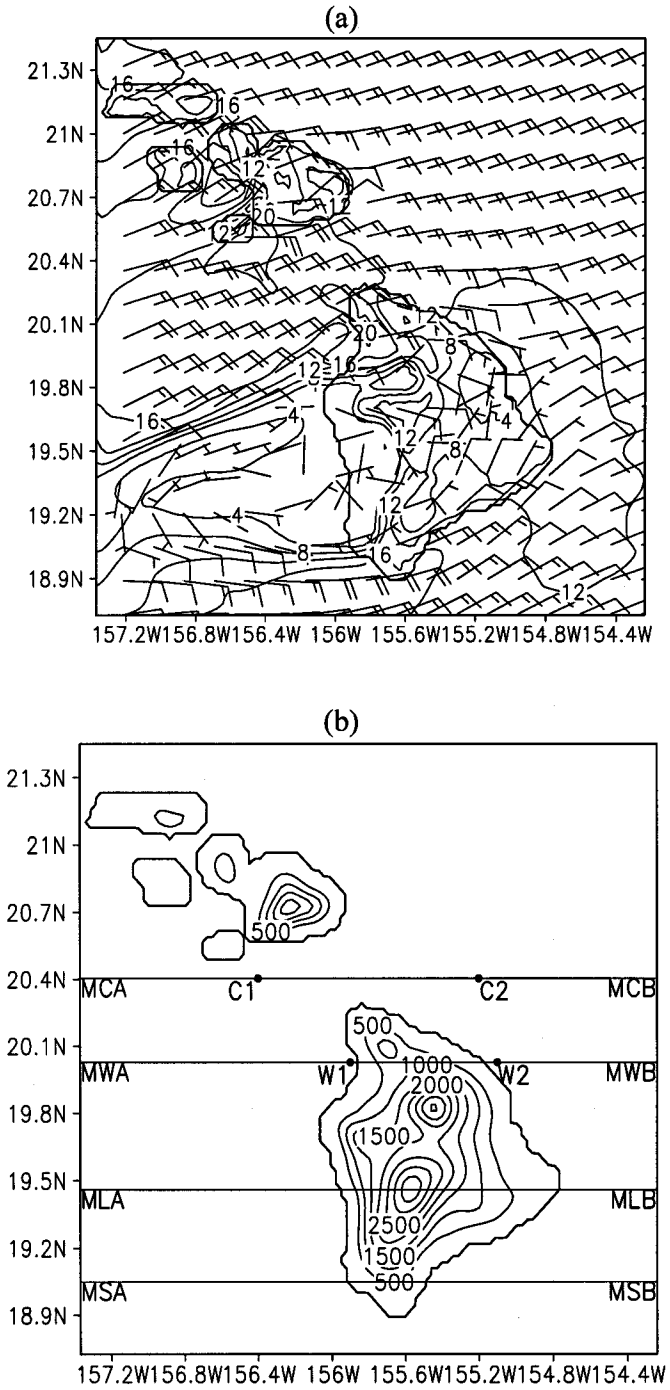

Figure 6.9. (a) The 3-km MSM/LSM 28-h forecasted 10-m wind (m s^{-1}) over the Molokai-Maui-Hawaii domain valid at 1800 HST 14 February 2001, and (b) positions of the longitude-height cross sections presented in the following. Isotachs in (a) are every 4 m s^{-1} with the wind barbs plotted every 5 grid points in both directions. The 3-km MSM/LSM was initialized at 1400 HST 13 February 2001.

(a)

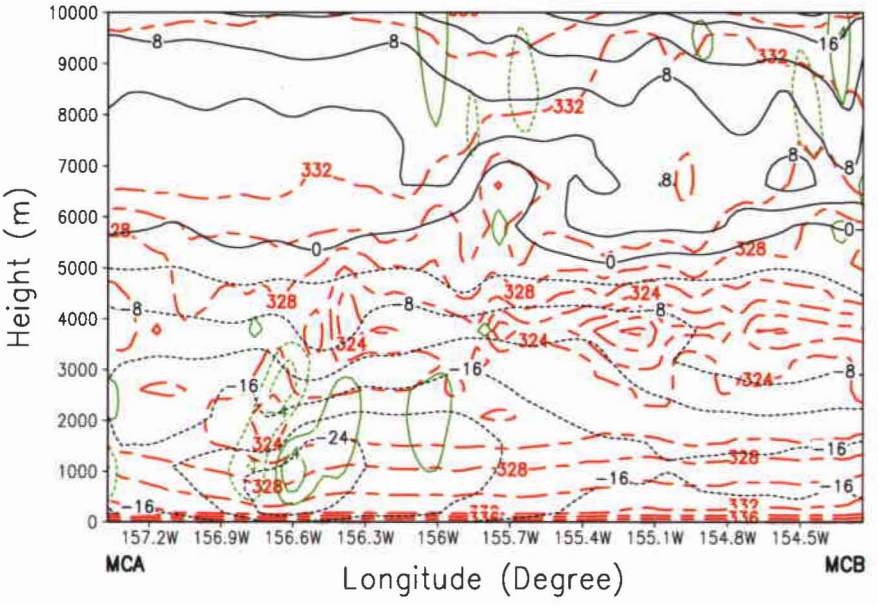

(b)

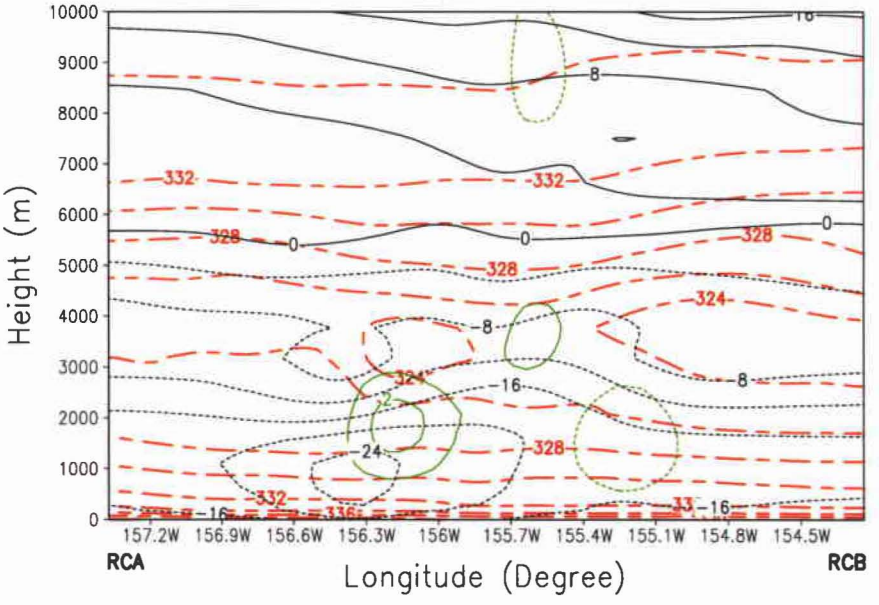

Figure 6.10. Longitude-height cross sections showing zonal winds (m s^{-1}, black lines), equivalent potential temperature (°K, red lines) and pressure vertical velocity (Pa s^{-1}, green lines) along the Alenuihaha Channel constructed from (a) 3-km MSM/LSM and (b) 10-km RSM/LSM forecasts valid at 1800 HST 14 February. Isotachs (isentropes) are every 4 m s^{-1} (2 °K). Pressure vertical velocity is every 2 Pa s^{-1} in (a) and 1 Pa s^{-1} in (b). The positions of the cross sections, MCA-MCB and RCA-RCB, are shown in Figs. 6.9a and 6.6, respectively. The MSM/LSM and RSM/LSM were initialized at 1400 HST 13 February 2001.

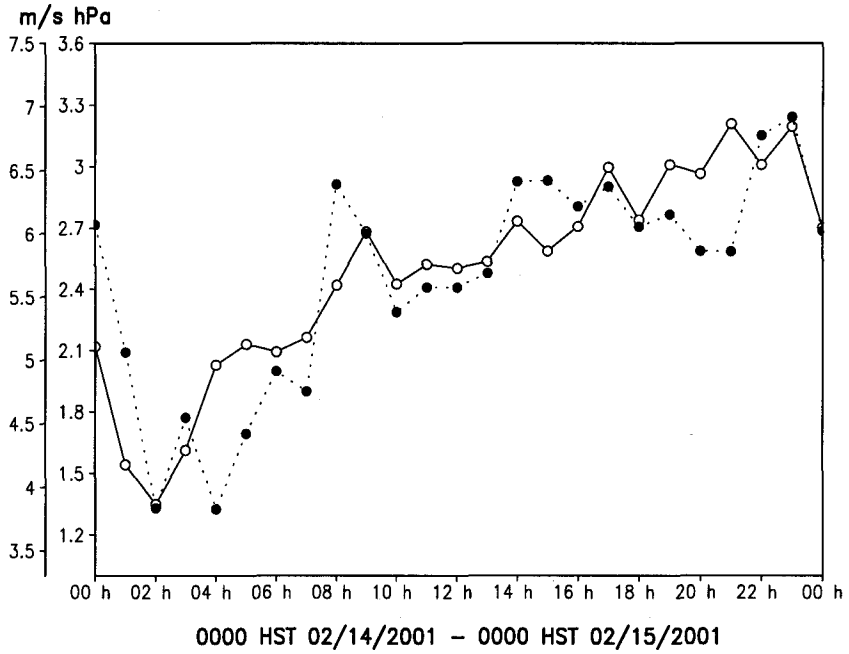

Figure 6.11. Hourly surface pressure differences (hPa, solid lines) and zonal wind speed differences (m s^{-1}, dashed lines) between the entrance region (C2) and exit region (C1) of the Alenuihaha Channel during 0000 HST 14 February and 0000 HST 15 February predicted by the 3-km MSM/LSM. The locations, C1 and C2, are shown in Fig. 6.9b. The MSM/LSM was initialized at 1400 HST 13 February 2001.

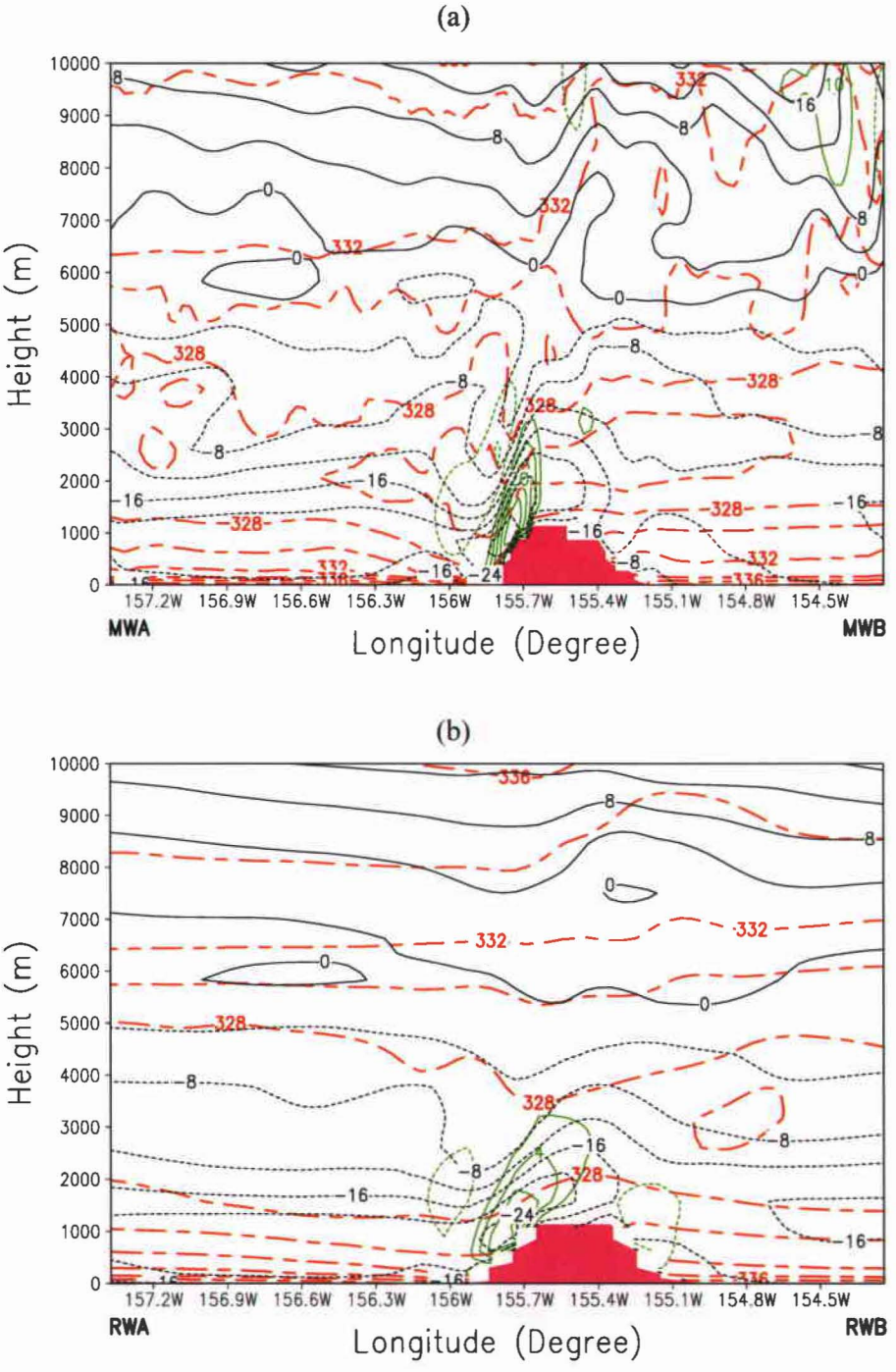

Figure 6.12. Same as Fig. 6.10 except for the cross sections along the Waimea Saddle, MWA-MWB and RWA-RWB. Pressure vertical velocity is every 5 Pa s^{-1} in (a) and 2 Pa s^{-1} in (b).

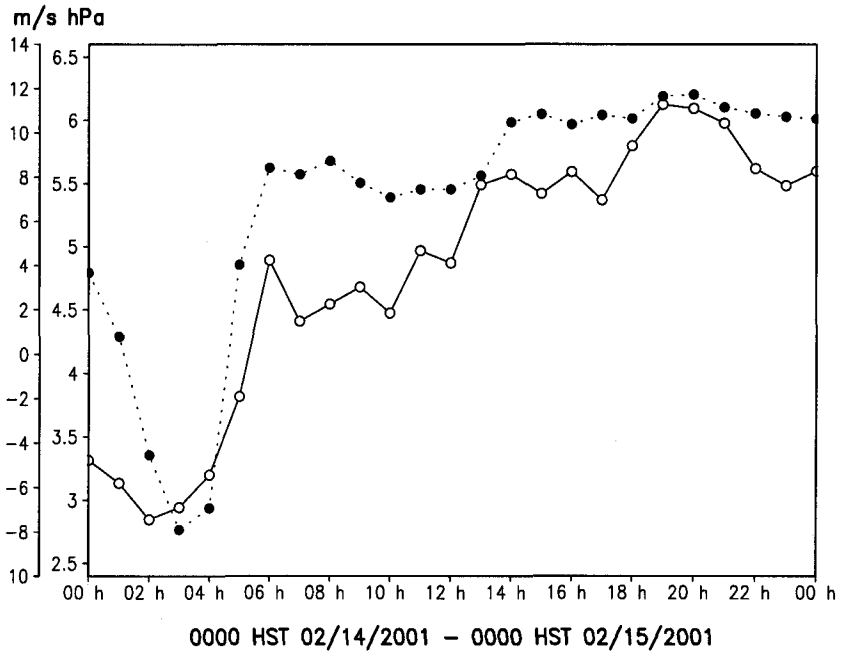

Figure 6.13. Same as Fig. 6.11 except for the Waimea Saddle between W1 and W2. The positions, W1 and W2, are shown in Fig. 6.9b.

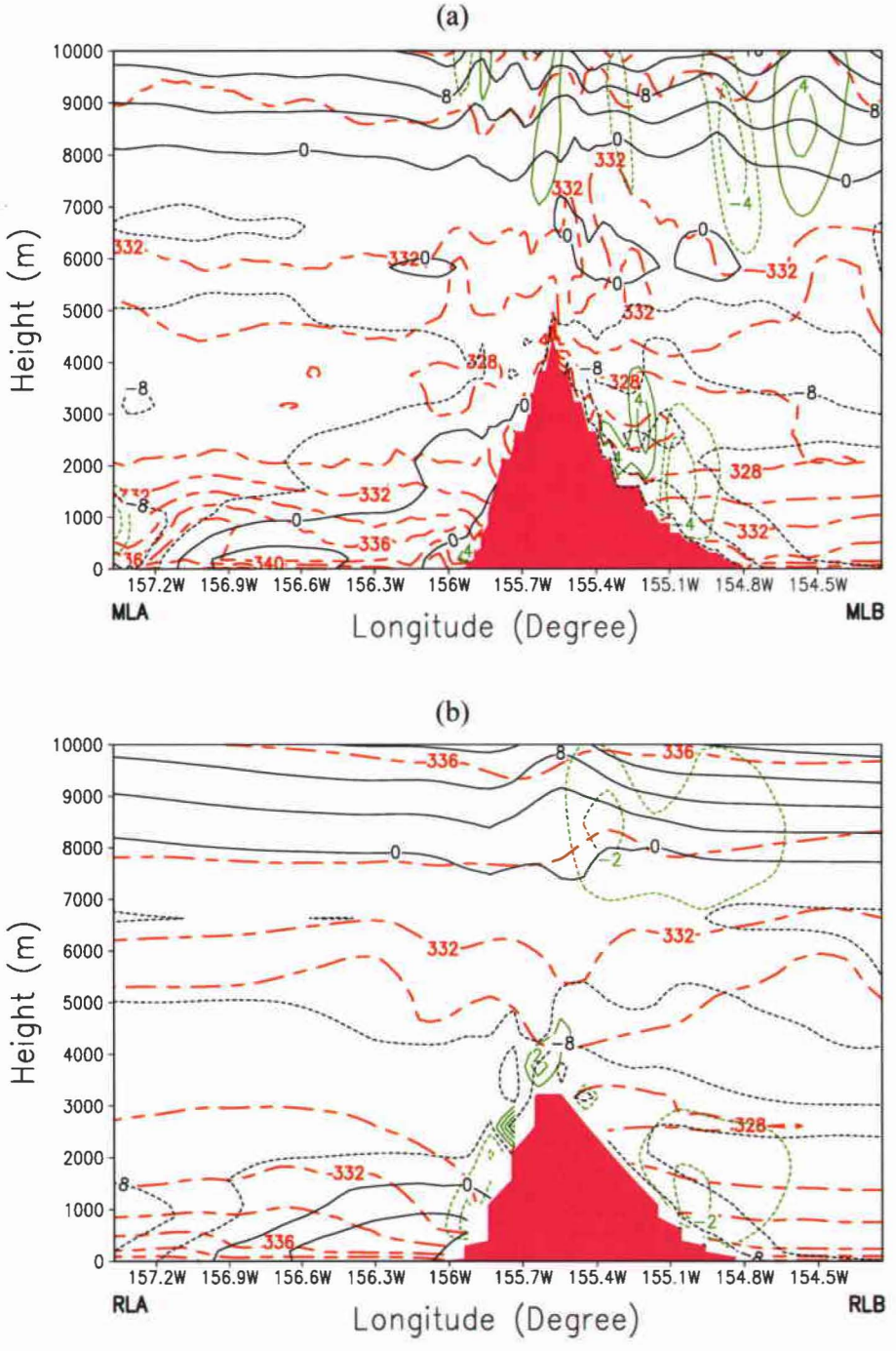

Figure 6.14. Same as Fig. 6.10 except for the cross sections along Mauna Loa, MLA-MLB and RLA-RLB. Pressure vertical velocity is every 2 Pa s^{-1} in (a) and 1 Pa s^{-1} in (b).

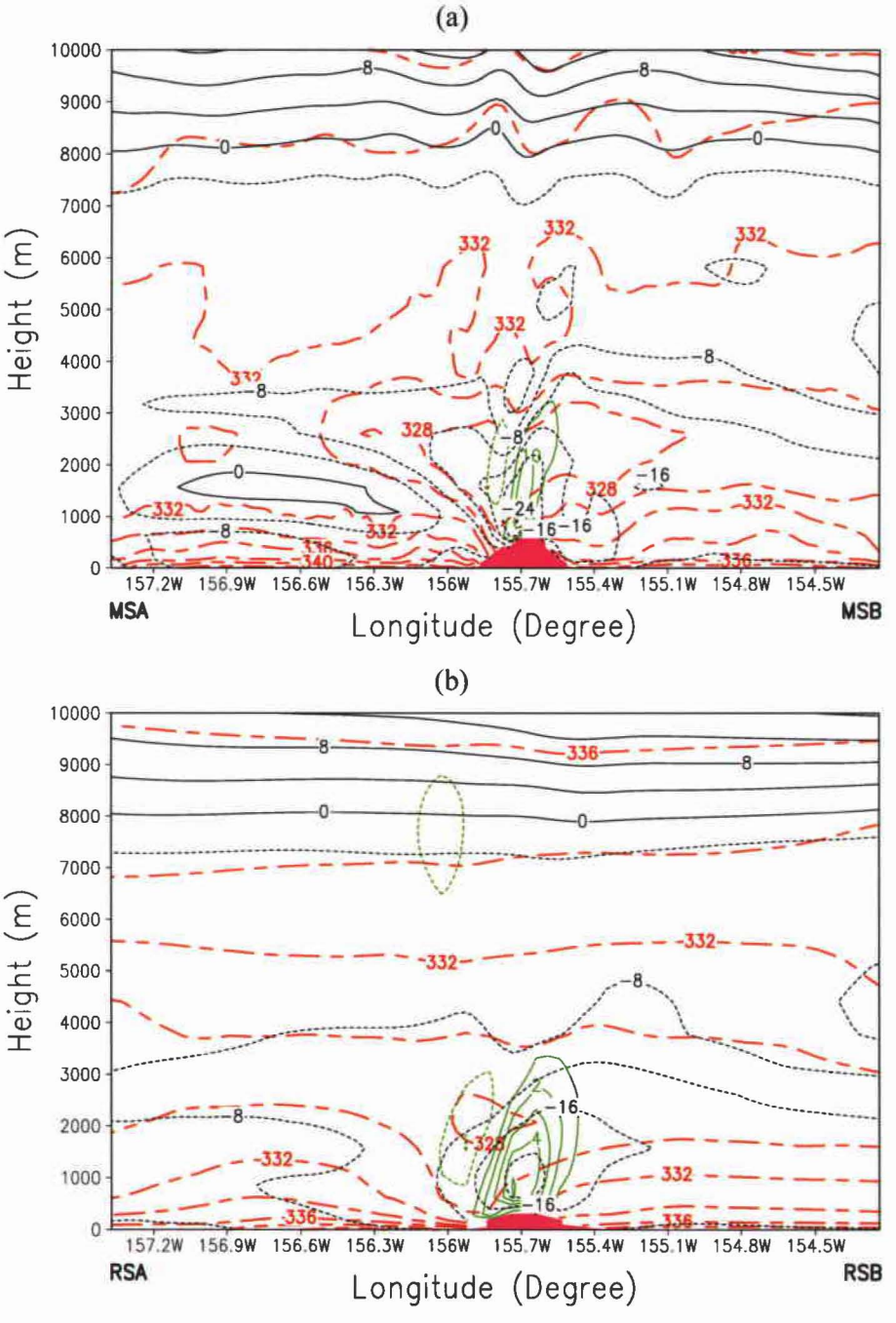

Figure 6.15. Same as Fig. 6.10 except for the cross sections along the South Corner of the Big Island, MSA-MSB and RSA-RSB. Pressure vertical velocity is every 5 Pa s^{-1} in (a) and 1 Pa s^{-1} in (b).

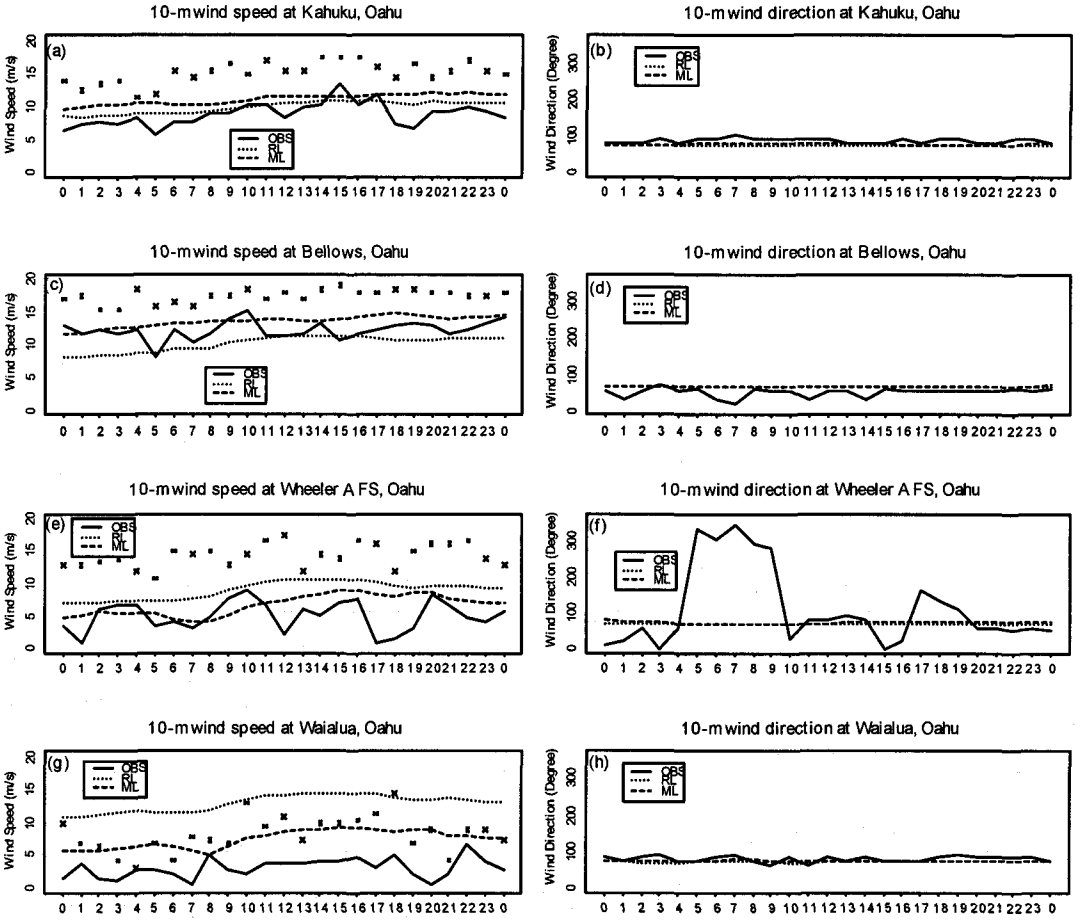

Figure 6.16. Observed and RSM/LSM, MSM/LSM simulated 10-m wind speeds (m s^{-1}) (left column) and wind directions (degrees) (right column) at Kahuku (a) (b), Bellows (c) (d), Wheeler AFS (e) (f), and Waialua (g) (h) on Oahu, during the period of 0000 HST 14 February through 0000 HST 15 February 2001. Solid, dotted and dashed lines refer to the observations, RSM/LSM and MSM/LSM simulations, respectively. Stars indicate the magnitude of reported wind gusts (m s^{-1}). Refer to Figs. 2.1a and 2.1b for the locations of these surface sites. The 10-km RSM/LSM and 1.5-km MSM/LSM runs were initialized at 1400 HST 13 February 2001.

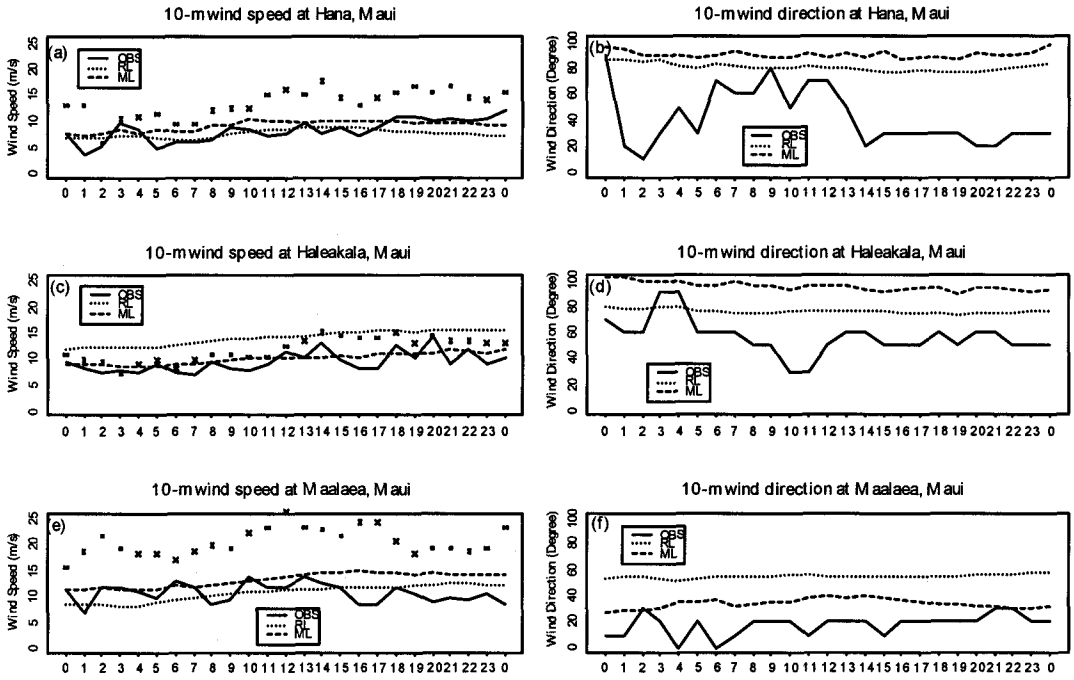

Figure 6.17. Observed and RSM/LSM, MSM/LSM simulated 10-m wind speeds (m s^{-1}) (left column) and wind directions (degrees) (right column) at Hana (a) (b), Haleakala (c) (d), and Maalaea Bay (e) (f) on Maui, during the period of 0000 HST 14 February through 0000 HST 15 February 2001. Solid, dotted and dashed lines refer to the observations, RSM/LSM and MSM/LSM simulations, respectively. Stars indicate the magnitude of reported wind gusts (m s^{-1}). Refer to Figs. 2.1a and 2.1c for the locations of these surface sites. The 10-km RSM/LSM and 3-km MSM/LSM runs were initialized at 1400 HST 13 February 2001.

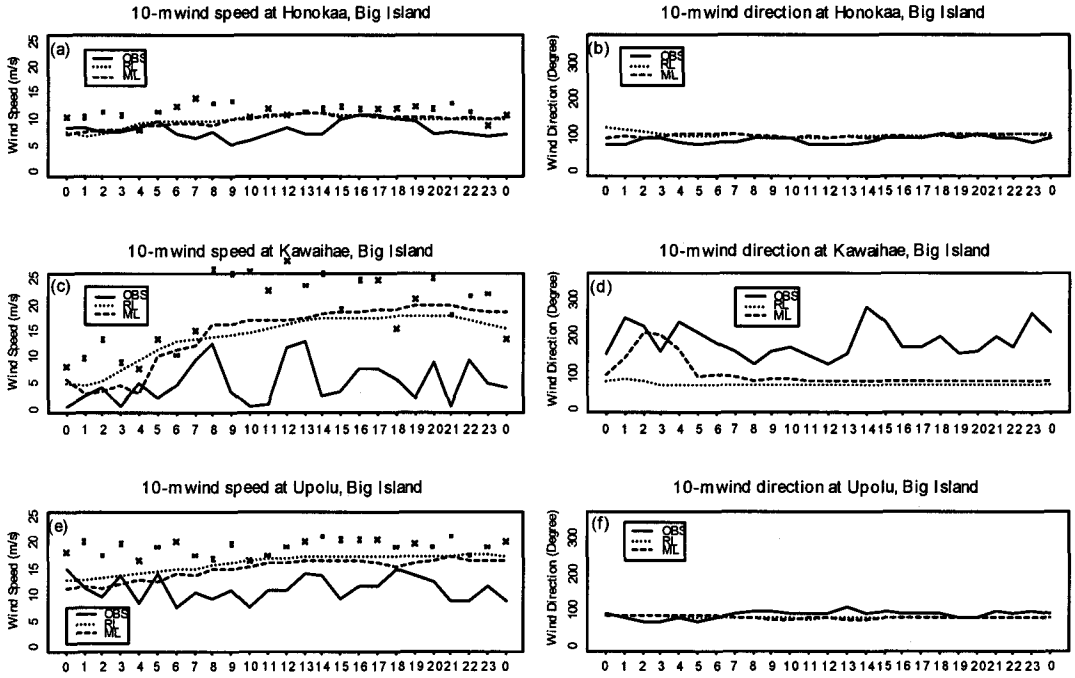

Figure 6.18. Observed and RSM/LSM, MSM/LSM simulated 10-m wind speeds (m s^{-1}) (left column) and wind directions (degrees) (right column) at Honokaa (a) (b), Kawaihae (c) (d), and Upolu AP (e) (f) on the Big Island, during the period of 0000 HST 14 February through 0000 HST 15 February 2001. Solid, dotted and dashed lines refer to the observations, RSM/LSM and MSM/LSM simulations, respectively. Stars indicate the magnitude of reported wind gusts (m s^{-1}). Refer to Figs. 2.1a and 2.1c for the locations of these surface sites. The 10-km RSM/LSM and 3-km MSM/LSM runs were initialized at 1400 HST February 13 2001.

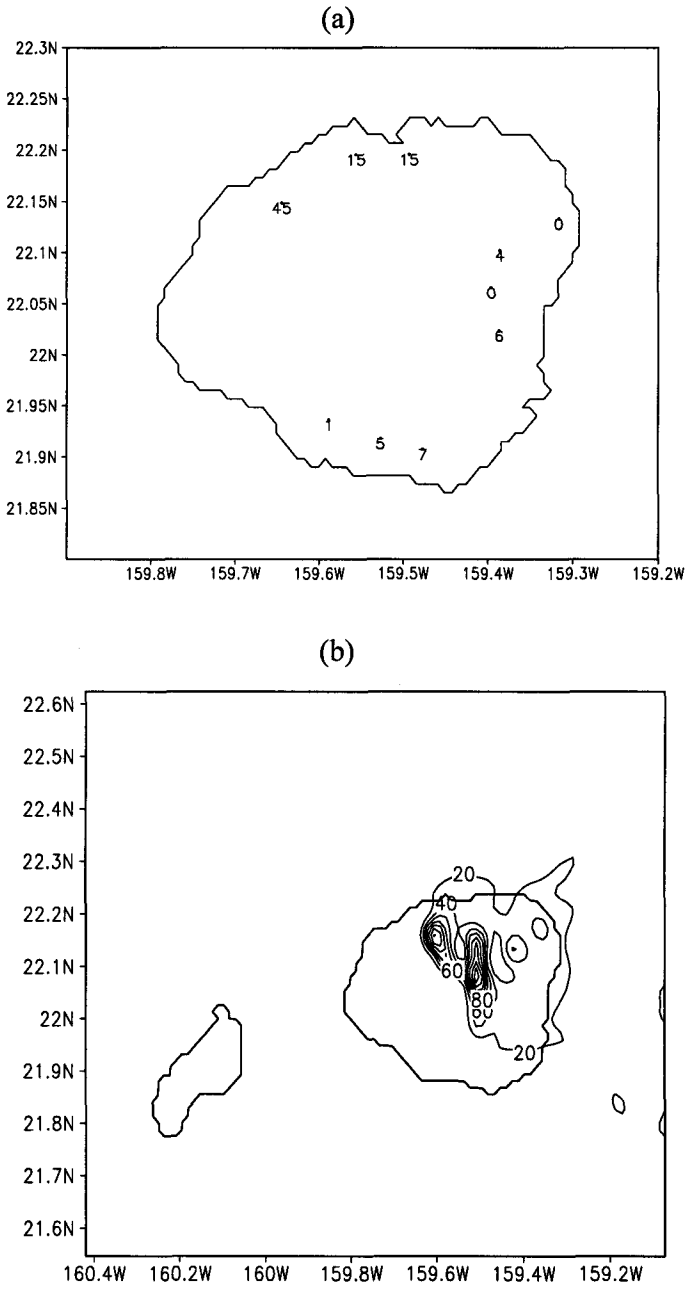

Figure 6.19. 24-h accumulated rainfall (mm) from 0000 HST 14 February to 0000 HST 15 February 2001 over the island of Kauai: (a) observed and (b) forecasted by the 1.5-km MSM/LSM. Only station values are shown in (a). In (b), contours are every 20 mm. The MSM/LSM was initialized at 1400 HST 13 February 2001.

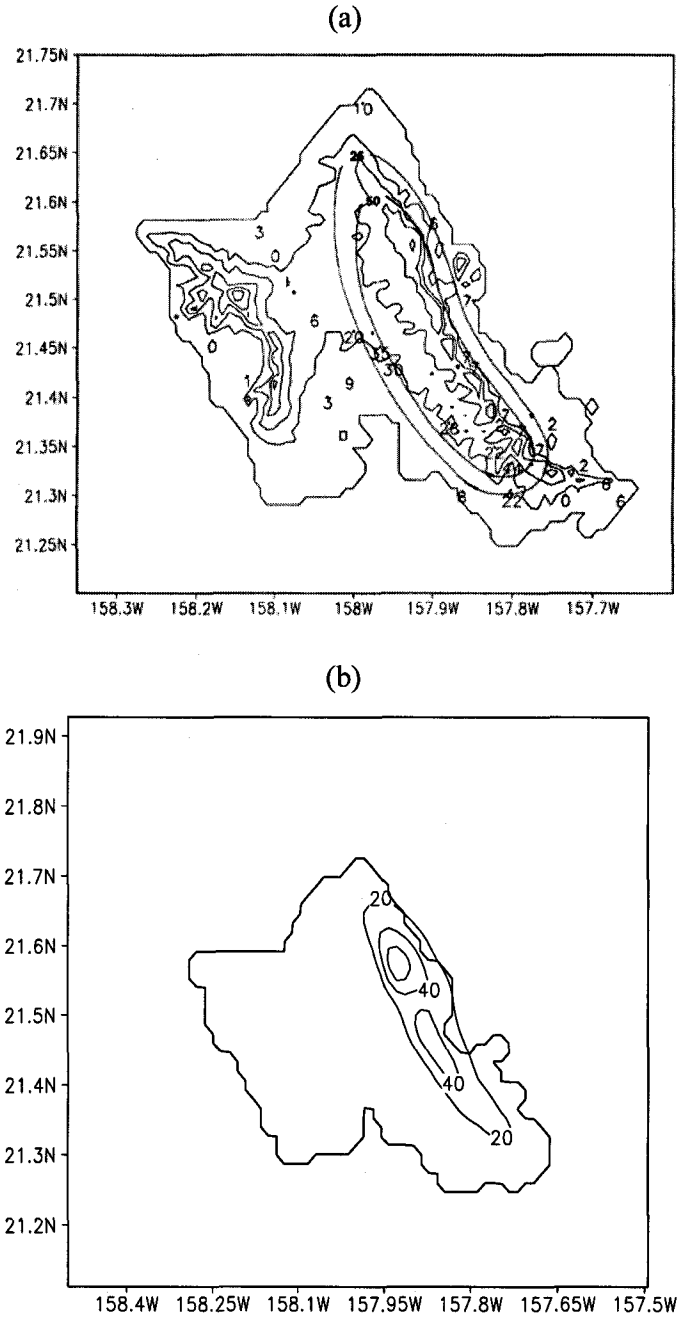

Figure 6.20. 24-h accumulated rainfall (mm) from 0000 HST 14 February to 0000 HST 15 February 2001 over the island of Oahu: (a) observed and (b) forecasted by the 1.5-km MSM/LSM. Contour interval is 25 mm in (a) and 20 mm in (b). The MSM/LSM was initialized at 1400 HST 13 February 2001.

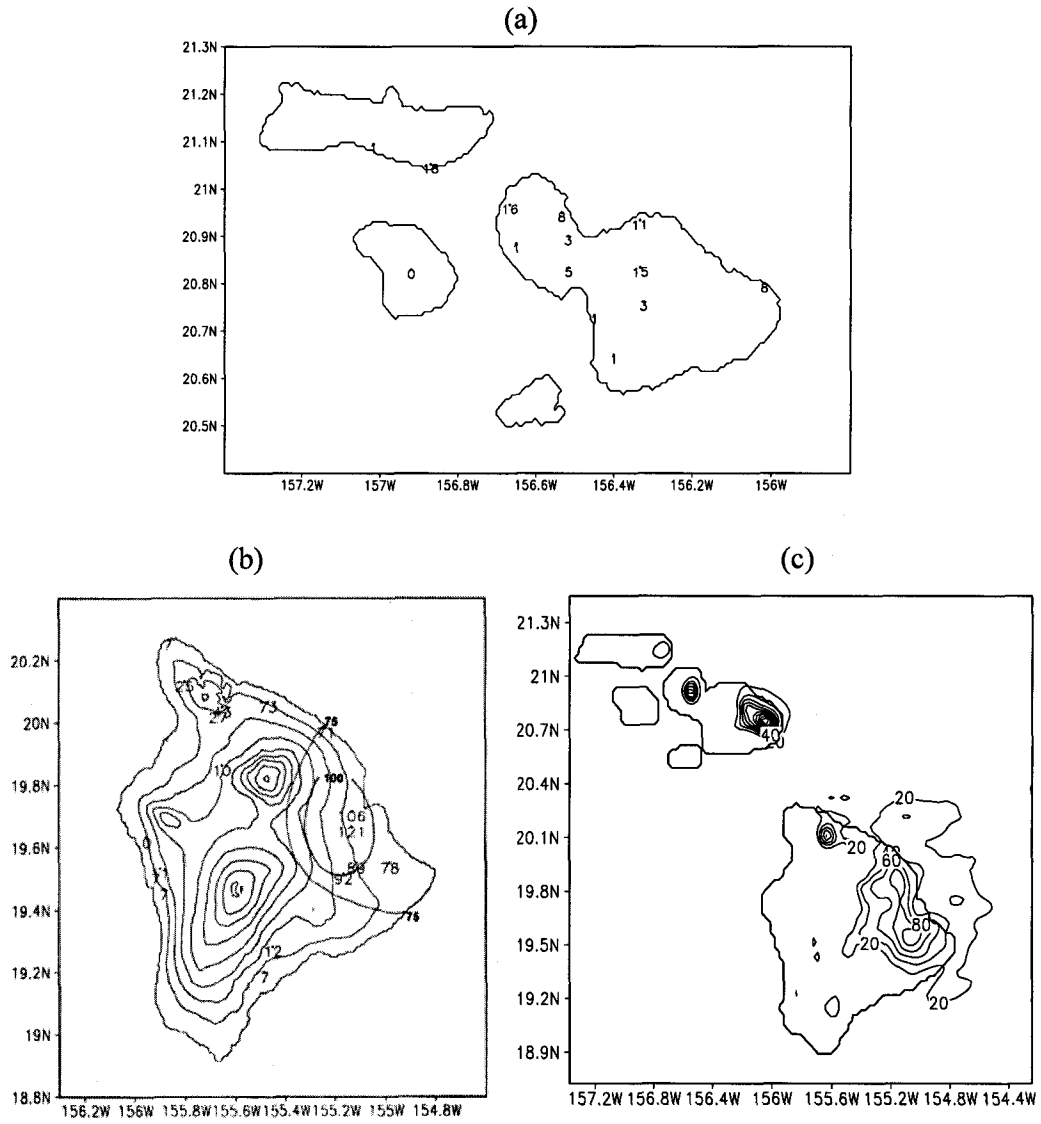

Figure 6.21. 24-h accumulated rainfall (mm) from 0000 HST 14 February to 0000 HST 15 February 2001: (a) observed over the Molokai-Maui domain, (b) observed over the Big Island, and (c) forecasted by the 3-km MSM/LSM for the Molokai-Maui-Hawaii domain. Only station values are shown in (a). Contour internal is 25 mm in (b) and 20 mm in (c). The MSM/LSM was initialized at 1400 HST 13 February 2001.

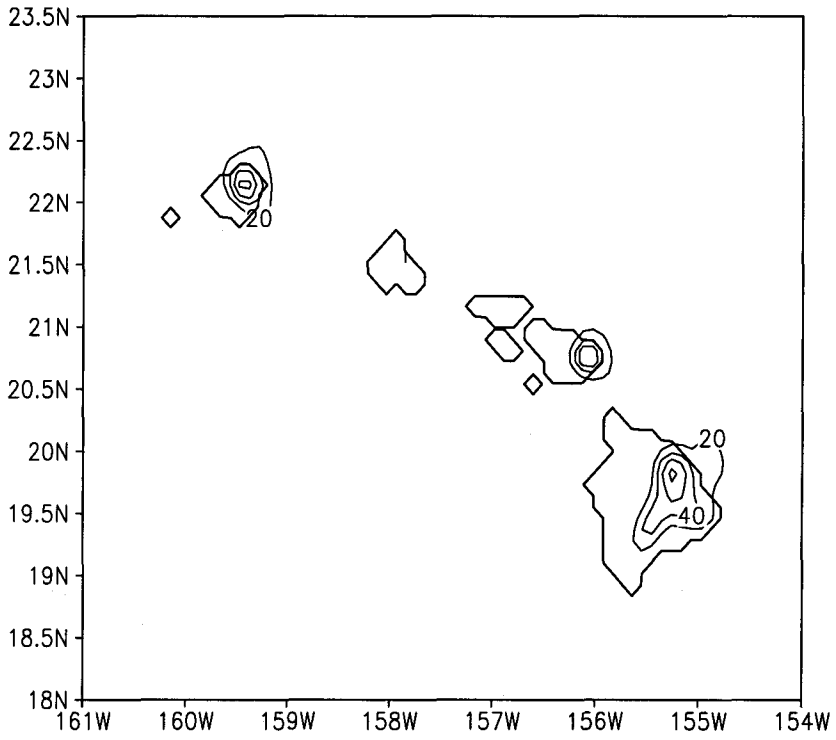

Figure 6.22. 24-h accumulated rainfall (mm) from 0000 HST 14 February to 0000 HST 15 February 2001 forecasted by the 10-km RSM/LSM. Contour internal is 20 mm. The RSM/LSM was initialized at 1400 HST 13 February 2001.

CHAPTER 7

Summary

7.1 Focuses of this study

In the preceding chapters, we have assessed the impact of the improved representation of island terrain and surface boundary conditions on simulating orographic and local effects under summer trade-wind conditions, localized heavy rainfall and orographically amplified high winds based on a few cases. The simulated surface variables both over land and over ocean, diurnal cycles of meteorological variables, sea-breeze circulations, rainfall distributions and wind patterns under undisturbed and disturbed synoptic conditions are validated using observations.

7.2 Major conclusions

The surface variables predicted by the RSM agree well with observations over the buoy stations deployed in the adjacent waters of the Hawaiian Islands. Over land with adequate representation of the terrain, the 1.5-km MSM provides better forecasts of surface variables than the 10-km operational RSM. However, there are still appreciable discrepancies between the MSM simulations and observations. Further improvements are achieved by coupling the MSM with the LSM. In particular, over-estimation of the surface wind speed and daytime cold biases experienced by the MSM are largely corrected in the coupled MSM/LSM.

Composite analyses of surface variables at the three surface sites on the island of Oahu are conducted for three week trade wind days (< 5 m s^{-1}) and five strong trade wind days (> 8 m s^{-1}) during the one-month period. The results show that the observed diurnal cycles in 2-m temperature, 2-m dew point temperature and 10-m wind are better forecasted by the MSM/LSM than the MSM. The observed daytime minima in 2-m dew point temperatures during the strong trade wind days at two urban sites are also reproduced by the MSM/LSM.

Additional evaluations of the coupled MSM/LSM simulations with a 3-km horizontal resolution are performed for Schroeder's (1981) sea breeze cases during 23 June to 28 June 1978 over northwest Hawaii. Except for 27 June, the model predicted onset time, duration and vertical extent of the sea breezes agree with observations reasonably well. The model simulated rainfall distribution in association with sea breeze fronts is largely consistent with observations. Sensitivity tests using the 3-km MSM/LSM demonstrate the strong modulation of sea breeze behavior by surface properties. High-resolution (1 km) MSM/LSM simulations for 27 June show improvements over the 3-km MSM/LSM in reproducing the observed sea breezes through a better representation of local terrain and a better simulation of orographically enhanced trades channeling through the Waimea Saddle.

Heavy rainfall events over the Hawaiian Islands display a large variability in rainfall distribution related to terrain and local winds. The RSM/LSM, having a coarser horizontal resolution than the MSM/LSM, does a reasonably good job in resolving regional-scale mesoscale features in association with these synoptic-scale systems but fails to accurately reproduce rainfall distribution and rate. The island terrain is not

adequately resolved by the RSM/LSM with its 10-km resolution. The MSM/LSM, with its higher resolution, has better capability in simulating localized rainfall distributions and airflows associated with these heavy rainfall events because the orographic effects related to terrain and local winds are better represented.

A high wind event (14-15 February 2001) over the Hawaiian Islands associated with a cold front is investigated using the coupled MSM/LSM. The model predicts downslope windstorms and hydraulic jumps on the lee sides of the islands of Kauai and Oahu. The highest peaks of both islands are below the trade-wind inversion (~ 2100 m). In the case of high mountains with a peak height above the trade-wind inversion, weak winds are simulated on the lee side. At the exit region of the Alenuihaha Channel between the islands of Maui and Hawaii with high mountains, strong winds are forecasted with characteristics of gap winds and a hydraulic jump. The model also resolves the Waimea jet above the lee slopes of the Waimea Saddle between Mauna Kea and the Kohala mountains of the Big Island. A hydraulic jump is forecasted in association with the Waimea jet and the strong winds over the southern corner of the Big Island. In contrast, the 10-km operational RSM coupled with the LSM predicts uniform trade-wind flow for Kauai and Oahu. In addition, the RSM/LSM forecasted strong winds are mainly located over the mountain ridges without extending to the lee slopes.

Comparisons between observations and model simulations at 10 surface sites during this high wind event show that the MSM/LSM reproduces the spatial pattern and magnitude of the surface wind better than the RSM/LSM. The observed rainfall distribution is reasonably well reproduced by the MSM/LSM for the major Hawaiian Islands, with comparable rainfall amount over Oahu and the Big Island. The RSM/LSM

also provides rains on the windward sides of major islands; however, the predicted rainfall amount is much less than that observed.

Major model bias is that the MSM/LSM produces excessive rainfall on the windward side of steep mountains with little rainfall downstream of the mountain ranges.

7.3 Future work

Model sensitivity tests of cloud and precipitation schemes will be performed to address the overestimation (underestimation) of precipitation on the windward (leeward) side of steep mountains. The Yonsei University diffusion scheme will be tested to address the problem of too much vertical mixing associated with the MRF scheme. It is also desirable to extend the experimental daily high-resolution ($\leq$ 3 km) forecasts to the other islands using the Weather Research and Forecasting (WRF) model. Since we have been archiving the model data (GFS, RSM/LSM and MSM/LSM) since summer 2002, it would be desirable to conduct local climate studies based on the archived model data. Our focuses will be on seasonal and interannual variability of local circulations, and the effect of El Niño on our local climate.

REFERENCES

Akaeda, K., J. Reisner, and D. Passons, 1995: The role of mesoscale and topographically induced circulations in initiating a flash flood observed during the TAMEX project. *Mon. Wea. Rev.*, **123**, 1720-1739.

Asselin, R. A., 1972: Frequency filter for time integration. *Mon. Wea. Rev.*, **100**, 487-490.

Austin, G. R., R. M. Rauber, H. T. Ochs III, and L. J. Miller, 1996: Trade-wind clouds and Hawaiian rainbands. *Mon. Wea. Rev.*, **124**, 2126-2151.

Avissar, R., and R. Pielke, 1989: A parameterization of heterogeneous land surfaces for atmospheric numerical models and its impact on regional meteorology. *Mon. Wea. Rev.*, **117**, 2113-2136.

Baines, P. G., 1980: The dynamics of southerly buster. *Aust. Meteor. Mag.*, **28**, 175-200.

Banta, R. M., 1990: The role of mountains in making clouds. Chapter 9. *Meteor. Monogr.*, **45**, Amer. Meteor. Soc., 229-284.

Bell, G. D., and L. F. Bosart, 1988: Appalachian cold-air damming. *Mon. Wea. Rev.*, **116**, 137-161.

Blumen, W., Ed., 1990: Atmospheric Processes over Complex Terrain. *Meteor. Monogr.*, **45**, Amer. Meteor. Soc., 323 pp.

Blumenstock, H. L., and S. Price, 1967: *Climates of the United States Hawaii.* Climatography of the United States 60-51, U.S. Dept. of Commerce, ESSA, 27 pp. [Available from the NOAA Central Library, 2nd Floor, SSMC3, 1315 East-West Highway, Silver Spring, MD 20910.]

Bowley, C. J., A. H. Glaser, R. J. Newcomb, and R. Wexler, 1962: Satellite observations of wake formation beneath an inversion. *J. Atmos. Sci.*, **19**, 52-55.

Briegleb, B. P., P. Minnis, V. Ramanathan, and E. Harrison, 1986: Comparison of regional clear-sky albedo inferred from satellite observations and model computations. *J. Appl. Meteor.*, **25**, 214-226.

Brinkmann, W. A. R., 1974: Strong downslope winds at Boulder, Colorado. *Mon. Wea. Rev.*, **102**, 592-602.

Burroughs, L. D., and R. N. Larson, 1979: Wave clouds in the vicinity of Oahu island, Hawaii. *Mon. Wea. Rev.*, **107**, 608-611.

Businger, S., T. Birchard Jr., P. A. Jendrowski, K. Kodama, J. N. Porter, and J. J. Wang, 1998: A bow echo and severe weather associated with a kona low in Hawaii. *Wea. Forecasting*, **13**, 579-591.

Cameron, D. C., and A. B. Carpenter, 1936: Destructive easterly gales in the Columbia river gorge, December 1935. *Mon. Wea. Rev.*, **64**, 264-267.

Carbone, R. E., W. A. Cooper, and W. C. Lee, 1995: Forcing of flow reversal along the windward slopes of Hawaii. *Mon. Wea. Rev.*, **123**, 3466-3480.

—, J. D. Tuttle, W. A. Cooper, V. Grubišić, and W.-C. Lee, 1998: Trade wind rainfall near the windward coast of Hawaii. *Mon. Wea. Rev.*, **126**, 2847-2863.

Case, J. L., J. Manobianco, A. V. Dianic, M. M. Wheeler, D. E. Harms, and C. R. Parks, 2002: Verification of high-resolution RAMS forecasts over East-Central Florida during the 1999 and 2000 summer months. *Wea. Forecasting*, **17**, 1133-1151.

Charnock, H., 1955: Wind stress on a water surface. *Quart. J. Roy. Meteor. Soc.*, **81**, 639-640.

Chen, F., and R. Avissar, 1994a: The impact of land-surface wetness on mesoscale heat fluxes. *J. Appl. Meteor.*, **33**, 1324-1340.

—, and —, 1994b: Impact of land-surface moisture variability on local shallow convective cumulus and precipitation in large-scale models. *J. Appl. Meteor.*, **33**, 1382-1401.

—, and J. Dudhia, 2001a: Coupling an advanced land surface – hydrology model with the Penn State – NCAR MM5 modeling system. Part I: Model implementation and sensitivity. *Mon. Wea. Rev.*, **129**, 569-585.

—, and —, 2001b: Coupling an advanced land surface – hydrology model with the Penn State – NCAR MM5 modeling system. Part II: Preliminary model validation. *Mon. Wea. Rev.*, **129**, 587-604.

—, K. Mitchell, J. Schaake, Y. Xue, H.-L. Pan, V. Koren, Q. Y. Duan, M. Ek, and A. Betts, 1996: Modeling of land-surface evaporation by four schemes and comparison with FIFE observations. *J. Geophys. Res.*, **101**, 7251-7268.

Chen, Y.-L., H.-M. H. Juang, P. A. Jendrowski and K. Kodama, 1999: Application of the NCEP nonhydrostatic spectral model to improve weather forecasting in Hawaii. The 1st Regional Spectral Model Workshop, Maui, Hawaii, 9-13 August, 1999.

—, and A. J. Nash, 1994: Diurnal variation of surface airflow and rainfall frequencies on the island of Hawaii. *Mon. Wea. Rev.*, **122**, 34-56.

—, and J.-J. Wang, 1994: Diurnal variations of surface thermodynamic fields on the island of Hawaii. *Mon. Wea. Rev.*, **122**, 2125-2138.

—, and J. Feng, 2001: Numerical simulations of airflow and cloud distributions over the windward side of the island of Hawaii. Part I: The effects of trade wind inversion. *Mon. Wea. Rev.*, **129**, 1117-1134.

Chopra, K. P., and L. F. Hubert, 1965: Meso-scale eddies in wake of islands. *J. Atmos. Sci.*, **22**, 652-657.

Clark, T. L., and W. R. Peltier, 1977: On the evolution and stability of finite mountain waves. *J. Atmos. Sci.*, **34**, 1715-1730.

—, and —, 1984: Critical level reflection and the resonant growth of nonlinear mountain waves. *J. Atmos. Sci.*, **41**, 3122-3134.

—, and R. D. Farley, 1984: Severe downslope windstorm calculations in two and three spatial dimensions using anelastic interactive grid nesting. A possible mechanism for gustiness. *J. Atmos. Sci.*, **41**, 329-350.

Colby, Jr., F. P., 2004: Simulations of the New England sea breeze: The effect of grid spacing. *Wea. Forecasting*, **19**, 277-285.

Colman, B. R., and C. F. Dierking, 1992: The Taku wind of southeast Alaska: Its identification and prediction. *Wea. Forecatsing*, **7**, 49-63.

Corby, G. C., 1954: The airflow over mountains: a review of the state of current knowledge. *Quart. J. Roy. Meteor. Soc.*, **80**, 491-521.

Cram, R. S., and H. R. Tatum, 1979: Record torrential rainstorms on the island of Hawaii, January-February 1979. *Mon. Wea. Rev.*, **107**, 1653-1662.

Daniels, P. A., and T. A. Schroeder, 1978: Air flow in the Central Valley of Maui, Hawaii. *J. Appl. Meteor.*, **17**, 812-818.

Dierking, C. F., 1998: Effects of a mountain wave windstorm at the surface. *Wea. Forecasting*, **13**, 606-616.

DOI USGS, 1986: Land Use Land Cover Digital Data from 1:250,000 and 1:100,000-Scale Maps. Data User Guide 4, U.S. Geological Survey, Reston, VA.

Dracup, J. A., E. D. H. Cheng, J. M. Nigg, and T. A. Schroeder, 1991: The New Year's Eve Flood on Oahu, Hawaii, December 31, 1987-January 1, 1988. *Natural Disaster Studies*. Vol. 1, National Academy Press, 72 pp.

Durran, D. R., 1986: Another look at downslope windstorms. Part I: On the development of supercritical flow in an infinitely deep, continuously stratified fluid. *J. Atmos. Sci.*, **43**, 2527-2543.

Eber, L. E., 1957: Upper air and surface wind observations in Project Shower. *Tellus*, **9**, 558-568.

Estoque, M. A., 1962: The sea breeze as a function of the prevailing synoptic situations. *J. Atmos. Sci.*, **19**, 244-250.

Farrell, R. W., 1980: A sea breeze shower over the Waikoloa desert of Hawaii. M.S. Thesis, Dept. of Meteorology, University of Hawaii, 114 pp.

Feng, J., and Y.-L. Chen, 2001: Numerical simulations of airflow and cloud distributions over the island of Hawaii. Part II: Nocturnal flow regime. *Mon. Wea. Rev.*, **129**, 1135-1147.

Foote, D. E., E. L. Hill, S. Nakamura, and F. Stephens, 1972: Soil survey of islands of Kauai, Oahu, Maui, Molokai, and Lanai, State of Hawaii. United States Department of Agriculture, Soil Conservation Service, in cooperation with the University of Hawaii Agricultural Experiment Station.

Foster, J., M. Bevis, Y.-L. Chen, S. Businger, and Y. Zhang, 2003: The Ka'u storm (November 2000): Imaging precipitable water using GPS. *J. Geophys. Res.*, **108**, 4585, 10.1029/2003JD003413.

Garrett, A. J., 1980: Orographic cloud over the eastern slopes of Mauna Loa volcano, Hawaii, related to insolation and wind. *Mon. Wea. Rev.*, **108**, 931-941.

—, 1982: A parameter study of interactions between convective clouds, the convective boundary layer, and forested surface. *Mon. Wea. Rev.*, **110**, 1040-1059.

Giambelluca, T. W., W. A. Nullet, and T. A. Schroeder, 1986: Rainfall Atlas of Hawaii. Honolulu, Hawaii. Dept. of Land and Natural Resources, Division of Water and Land Development (Report No. R76).

Gunther, E. B., 1979: Eastern North Pacific tropical cyclones of 1978. *Mon. Wea. Rev.*, **107**, 911-927.

Guo, Y.-R., Y.-H. Kuo, J. Dudhia, D. Parsons, and C. Rocken, 2000: Four-dimensional variational data assimilation of heterogeneous mesoscale observations for a strong convective case. *Mon. Wea. Rev.*, **128**, 619-643.

Haraguchi, P., 1977: Forecasting floods in Hawaii (excluding Hawaii Island). NOAA Tech. Memo. NWSTM PR-16, 30 pp. [Available from NOAA/PRH, Grosvenor Center Mauka Tower, 737 Bishop St. Suite 2200, Honolulu, HI 96813.]

Hollingshead, A. T., S. Businger, R. Draxler, J. Porter, and D. Stevens, 2003: Dispersion modeling of the Kilauea plume. *Bound.-Layer Meteor.*, **108**, 121-144.

Hong, S.-Y., and H.-L. Pan, 1996: Nonlocal boundary layer vertical diffusion in a medium-range forecast model. *Mon. Wea. Rev.*, **124**, 2322-2339.

—, and H.-L. Pan, 1998: Convective trigger function for a mass-flux cumulus parameterization scheme. *Mon. Wea. Rev.*, **126**, 2599-2620.

—, H.-M. H. Juang, and Q. Zhao, 1998: Implementation of prognostic cloud scheme for a regional spectral model. *Mon. Wea. Rev.*, **126**, 2621-2639.

—, J. Dudhia, and S.-H. Chen, 2003: A revised approach to ice-microphysical processes for the bulk parameterization of cloud and precipitation. *Mon. Wea. Rev.*, submitted.

—, and J. Dudhia, 2003: Testing of a new nonlocal boundary layer vertical diffusion scheme in numerical weather prediction applications. The 20th Conference on Weather Analysis and Forecasting/16th Conference on Numerical Weather Prediction, 12-15 January 2004, Seattle, Washington.

Hubert, L. F., and A. F. Krueger, 1962: Satellite pictures of meso-scale eddies. *Mon. Wea. Rev.*, **90**, 457-463.

Juang, H.-M. H., 2000: The NCEP mesoscale spectral model: A revised version of the nonhydrostatic regional spectral model. *Mon. Wea. Rev.*, **128**, 2329-2362.

—, 1992: A spectral fully compressible nonhydrostatic mesoscale model in hydrostatic sigma coordinates: Formulation and preliminary results. *Meteor. Atmos. Phys.*, **50**, 75-88.

—, and M. Kanamitsu, 1994: The NMC nested regional spectral model. *Mon. Wea. Rev.*, **122**, 3-26.

—, S.-Y. Hong, and M. Kanamitsu, 1997: The NCEP regional spectral model: An update. *Bull. Amer. Meteor. Soc.*, **78**, 2125-2143.

—, C.-T. Lee, Y. Zhang, Y. Song, M.-C. Wu, Y.-L. Chen, K. Kodama, and S.-C. Chen, 2004: Applying horizontal diffusion on pressure surface to mesoscale models on terrain-following coordinates. *Mon. Wea. Rev.*, in press.

Juvik, J. O., D. C. Singleton, and G. G. Clarke, 1978: Climate and water vapor on the island of Hawaii. Mauna Loa Observatory, Ed. J. Miller, Twentieth Anniversary

Report, U. S. Department of Commence, NOAA, Environmental Research Lab., 129-139.

Klemp, J. B., and D. K. Lilly, 1975: The dynamics of wave induced downslope winds. *J. Atmos. Sci.*, **32**, 320-339.

—, —, 1978: Numerical simulation of hydrostatic mountain waves. *J. Atmos. Sci.*, **35**, 78-107.

—, D. R. Durran, 1987: Numerical modeling of bora winds. *Meteor. Atmos. Phys.*, **36**, 215-227.

Kodama, K., and H.-M. H. Juang, 1999: An assessment of regional spectral model forecasts for the Hawaiian Islands. The 1st Regional Spectral Model Workshop, Maui, Hawaii, 9-13 August, 1999.

—, and G. M. Barnes, 1997: Heavy rain events over the south-facing slopes of Hawaii: Attendant conditions. *Wea. Forecasting*, **12**, 347-367.

—, and S. Businger, 1998: Weather and forecasting challenges in the Pacific region of the National Weather Service. *Wea. Forecasting*, **13**, 523-546.

Kuo, Ying-Hwa, Y.-R. Guo, and E. R. Westwater, 1993: Assimilation of precipitable water measurements into a mesoscale numerical model. *Mon. Wea. Rev.*, **121**, 1215-1238.

Lackmann, G. M., and J. E. Overland, 1989: Atmospheric structure and momentum balance during a gap-wind event in the Shelikof Strait, Alaska. *Mon. Wea. Rev.*, **117**, 1817-1833.

Lambert, S., 1974: High resolution numerical study of the sea-breeze front. *Atmosphere*, **12**, 97-105.

Laprise, R., and W. R. Peltier, 1989: The linear stability of nonlinear mountain waves: Implications for the understanding of severe downslope windstorms. *J. Atmos. Sci.*, **46**, 545-564.

Lavoie, R. L., 1974: A numerical model of trade wind weather on Oahu. *Mon. Wea. Rev.*, **102**, 630-637.

Leopold, L. B., 1949: The interaction of trade wind and sea breeze, Hawaii. *J. Meteor.*, **6**, 312-320.

Li, J., and Y.-L. Chen, 1998: Barrier jets during TAMEX. *Mon. Wea. Rev.*, **126**, 959-971.

—, —, and W.-C. Lee, 1997: Analysis of a heavy rainfall event during TAMEX. *Mon. Wea. Rev.*, **125**, 1060-1082.

Lilly, D. K., and E. J. Zipser, 1972: The Front Range windstorm of 11 January 1972. A meteorological narrative. *Weatherwise*, **25**, 56-63.

Long, R. R., 1954: Some aspects of the flow of stratified fluids. Part II: Experiments with a two fluid system. *Tellus*, **6**, 97-115.

Lumpkin, C., 1998: *Eddies and Currents of the Hawaiian Islands*. Ph. D. dissertation, School of Ocean and Earth Sciences and Technology, University of Hawaii, 271 pp.

Lyons, S. W., 1979: Summer weather on Haleakala, Maui. UH-MET 79-09, Dept. of Meteorology, University of Hawaii, 56 pp. [Available from Dept. of Meteorology, University of Hawaii, 2525 Correa Road, Honolulu, HI 96822]

Lyons, W. A., and T. Fujita, 1968: Meso-scale motions in oceanic stratus as revealed by satellite data. *Mon. Wea. Rev.*, **96**, 304-314.

Mahfouf, J. F., and J. Noilhan, 1991: Comparative study of various formulations of evaporation from bare soil using in situ data. *J. Appl. Meteor.*, **30**, 1345-1365.

Mahrt, L., and H.-L. Pan, 1984: A two layer model of soil hydrology. *Bound.-Layer Meteor.*, **29**, 1-20.

Mass, C. F., and M. D. Albright, 1985: A severe windstorm in the lee of the Cascade Mountains of Washington State. *Mon. Wea. Rev.*, **113**, 1261-1281.

—, D. Ovens, K. Westrick, and B. A. Colle, 2002: Does increasing horizontal resolution produce more skillful forecasts? *Bull. Amer. Meteor. Soc.*, **83**, 407-430.

McCumber, M. C., 1980: A numerical simulation of the influence of heat and moisture fluxes upon mesoscale circulations. Ph.D. dissertation, Department of Environmental Science, University of Virginia, Charlottesville, 255 pp.

—, and R. A. Pielke, 1981: Simulation of the effects of surface fluxes of heat and moisture in a mesoscale numerical model soil layer. *J. Geophys. Res.*, **86**, 9929-9938.

Mendonca, B. G., 1969: Local wind circulation on the slopes of Mauna Loa. *J. Appl. Meteor.*, **6**, 312-320.

Morrow, M. J., 1974: *Straight line wind variability over selected stations on leeward Oahu.* NOAA Tech. Memo., NWSTM PR-12, 27 pp.

Neiman, P. J., R. M. Hardesty, M. A. Shapiro, and R. E. Cupp, 1988: Doppler lidar observations of a downslope windstorm. *Mon. Wea. Rev.*, **116**, 2265-2275.

Neumann, J., and Y. Mahrer, 1971: A theoretical study of sea and land breezes. *J. Atmos. Sci.*, **34**, 1913-1917.

Nickerson, E. C., and M. A. Dias, 1981: On the existence of atmospheric vortices downwind of Hawaii during the HAMEC project. *J. Appl. Meteor.*, **20**, 868-873.

Overland, J. E., and B. A. Walter, Jr., 1981: Gap winds in the Strait of Juan de Fuca. *Mon. Wea. Rev.*, **109**, 2221-2233.

Pan, H.-L., and L. Mahrt, 1987: Interaction between soil hydrology and boundary layer developments. *Bound.-Layer Meteor.*, **38**, 195-202.

—, 1990: A simple parameterization scheme of evapotranspiration over land for the NMC medium-range forecast model. *Mon. Wea. Rev.*, **118**, 2500-2512.

Patzert, W. C., 1969: *Eddies in Hawaiian waters.* Technical Report 69-8, Hawaiian Institute of Geophysics, University of Hawaii.

Peltier, W. R., and T. L. Clark, 1979: The evolution and stability of finite-amplitude mountain waves. Part II: Surface wave drag and severe downslope windstorms. *J. Atmos. Sci.*, **36**, 1498-1529.

Ramage, C. S., 1962: The subtropical cyclone. *J. Geophys. Res.*, **67**, 1401-1411.

—, 1971: *Monsoon Meteorology.* Academic Press, 112 pp.

—, 1979: Prospecting for meteorological energy in Hawaii. *Bull. Amer. Meteor. Soc.*, **60**, 430-438.

—, P. A. Daniels, T. A. Schroeder, and N. J. Thompson, 1977: *Oahu Wind Survey, First Report.* UH-MET 77-01, Dept. of Meteorology, University of Hawaii. [Available from the Department of Meteorology, University of Hawaii, 2525 Correa Road, HI 96822, Honolulu.]

Rasmussen, R. M., and P. K. Smolarkiewicz, 1993: On the dynamics of Hawaiian cloud bands. Part III: Local aspects. *J. Atmos. Sci.*, **50**, 1560-1572.

—, —, and J. Warner, 1989: On the dynamics of Hawaiian cloud bands: Comparison of model results with observations and island climatology. *J. Atmos. Sci.*, **46**, 1589-1608.

Reed, R. J., 1981: A case study of a bora-like windstorm in western Washington. *Mon. Wea. Rev.*, **109**, 2383-2393.

Reed, T. R., 1931: Gap winds of the Strait of Juan de Fuca. *Mon. Wea. Rev.*, **59**, 373-376.

Sadler, J. C., 1967: *The Tropical Upper Tropospheric Trough as a secondary source of typhoons and a primary source of trade wind disturbances*. Rep. 67-12. Hawaii Institute of Geophysics, University of Hawaii, 44 pp.

Sato, H. H., W. Ikeda, R. Paeth, R. Smythe, and M. Takehiro, Jr., 1973: Soil survey of the island of Hawaii, State of Hawaii. United States Department of Agriculture, Soil Conservation Service, in cooperation with the University of Hawaii Agricultural Experiment Station.

Schär, C., and R. B. Smith, 1993: Shallow water flow past isolated topography. Part I: Vorticity production and wake formation. *J. Atmos. Sci.*, **50**, 1373-1400.

Schroeder, T. A., 1977a: Severe downslope winds on Oahu. Preprints, 10th Conference on Severe Local Storms, Omaha, NE, Amer. Meteor. Soc., 373-375.

—, 1977b: Meteorological analysis of an Oahu flood. *Mon. Wea. Rev.*, **105**, 458-468.

—, 1981: Characteristics of local winds in northwest Hawaii. *J. Appl. Meteor.*, **20**, 874-881.

—, 1993: *Climate Controls. Prevailing Trade Winds*. M. Sanderson, Ed., University of Hawaii Press, 12-36.

—, B. J. Kilonsky, and B. N. Meisner, 1977: Diurnal variation in rainfall and cloudiness. UH-MET 77-03, Dept. of Meteorology, University of Hawaii. [Available from the Department of Meteorology, University of Hawaii, 2525 Correa Road, HI 96822, Honolulu]

Scorer, R., 1986: *Cloud Investigation by Satellite*. Ellis Horwood, Chichester, Halsted Press, 300 pp.

Scorer, R. S., 1949: Theory of waves in lee of mountains. *Q. J. R. Met. Soc.*, **75**, 41-56.

—, 1954: Theory of airflow over mountains: III-airstream characteristics. *Quart. J. Roy. Meteor. Soc.*, **80**, 417-428.

—, 1978: *Environmental Aerodynamics*, Ellis Horwood Ltd, Chichester.

Segal, M., R. Avissar, M. C. McCumber, and R. A. Pielke, 1988: Evaluation of vegetation effects on the generation and modification of mesoscale circulations. *J. Atmos. Sci.*, **45**, 2268-2292.

Simpson, R. H., 1952: Evolution of the kona storm: A subtropical cyclone. *J. Meteor.*, **9**, 24-35.

Smolarkiewicz, P. K., R. M. Rasmussen, and T. L. Clark, 1988: On the dynamics of Hawaiian Cloud bands: Island forcing. *J. Atmos. Sci.*, **45**, 1872-1905.

Smith, R. B., 1979: The influence of mountains on the atmosphere. Advances in Geophysics, 21, Academic Press, 87-230.

—, 1985: On severe downslope winds. *J. Atmos. Sci.*, **42**, 2597-2603.

—, 1987: Aerial observations of the Yugoslavian bora. *J. Atmos. Sci.*, **44**, 269-297.

—, and J.-L. Sun, 1987: Generalized hydraulic solutions pertaining to severe downslope winds. *J. Atmos. Sci.*, **44**, 2934-2939.

—, and V. Grubišić, 1993: Aerial observations of Hawaii's wake. *J. Atmos. Sci.*, **50**, 3728-3750.

Tyson, P. D., 1968: Velocity fluctuations in the mountain wind. *J. Atmos. Sci.*, **25**, 381-384.

Wang, J.-J., H.-M. H. Juang, K. Kodama, S. Businger, Y.-L. Chen, and J. Partain, 1998: Application of the NCEP Regional Spectral Model to improve mesoscale weather forecasts in Hawaii. *Wea. Forecasting*, **13**, 560-575.

—, and Y.-L. Chen, 1995: Characteristics of near surface winds and thermal profiles on the windward slopes of the island of Hawaii. *Mon. Wea. Rev.*, **123**, 3481-3501.

Yamada, T., 1982: A numerical model simulation of turbulent airflow in and above canopy. *J. Meteor. Soc. Japan*, **60**, 439-454.

Yang, Y., and Y.-L. Chen, 2003a: Circulations and rainfall on the lee side of the island of Hawaii during HaRP. *Mon. Wea. Rev.*, **131**, 2525-2542.

—, and —, 2003b: High-resolution simulations of the island-induced circulations for the island of Hawaii during HaRP. The 5th Symposium on Fire and Forecast Meteorology, Ameri. Meteor. Soc., Orlando, Florida, 16-20 November 2003.

Yeh, H.-C., and Y.-L. Chen, 1998: Characteristics of the rainfall distribution over Taiwan during TAMEX. *J. Appl. Meteor.*, **37**, 1457-1469.

—, and —, 2002: The role of offshore convergence on coastal rainfall during TAMEX IOP2. *Mon. Wea. Rev.*, **130**, 2709-2730.

Zhang, Y., Y.-L. Chen, H.-M. H. Juang, S.-Y. Hong, K. Kodama, and R. Farrell, 2000: Validations and sensitivity tests of the Mesoscale Spectral Model simulations over the Hawaiian Islands. The 2nd Regional Spectral Model Workshop, Maui, Hawaii, 17-21 July, 2000.

Xiao, Q., X. Zou, and Y.-H. Kuo, 2000: Incorporating the SSM/I-derived precipitable water and rainfall rate into a numerical model: A case study for the ERICA IOP-4 cyclone. *Mon. Wea. Rev.*, **128**, 87-108.

Xie, S.-P., W. T. Liu, Q. Liu, and M. Nonaka, 2001: Far-reaching effects of the Hawaiian Islands on the Pacific Ocean-atmosphere. *Science*, **292**, 2057-2060.

Zou, X., and Y.-H. Kuo, 1996: Rainfall assimilation through an optimal control of initial and boundary conditions in a limited-area mesoscale model. *Mon. Wea. Rev.*, **124**, 2859-2882.